Multi-scales, multi-physics personalized HD-sEMG model for the evaluation of skeletal muscle aging

Inès Douania

▶ To cite this version:

Inès Douania. Multi-scales, multi-physics personalized HD-sEMG model for the evaluation of skeletal muscle aging. Biomechanics [physics.med-ph]. Université de Technologie de Compiègne, 2022. English. NNT : 2022COMP2679 . tel-04543036

HAL Id: tel-04543036
https://theses.hal.science/tel-04543036

Submitted on 11 Apr 2024

Par **DOUANIA Inès**

Multi-scales, multi-physics personalized HD-sEMG model for the evaluation of skeletal muscle aging

Thèse présentée
pour l'obtention du grade
de Docteur de l'UTC

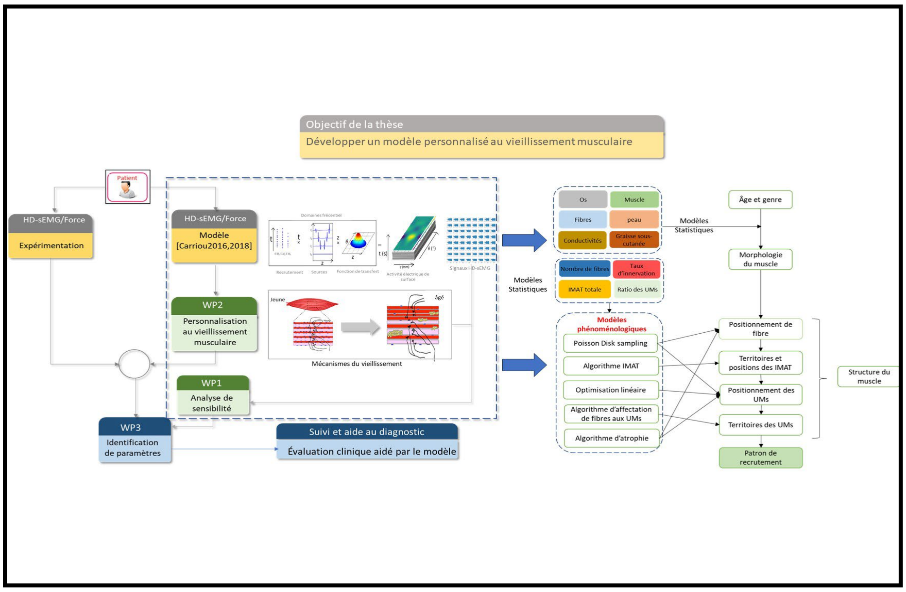

Soutenue le 3 juin 2022
Spécialité : Biomécanique, Bioingénierie : Unité de Recherche en Biomécanique et Bioingénierie (UMR-7338)

D2679

Université de Technologie de Compiègne
Ecole Doctorale
Rue Roger Couttolenc
60200 Compiègne

Multi-scales, multi-physics personalized HD-sEMG model for the evaluation of skeletal muscle aging

THESIS
PRESENTED TO

Sorbonne University, Université de Technologie de Compiègne Doctoral school « Sciences pour l'ingénieur »

FOR THE DEGREE OF

Doctor in Biomechanics and Bioengineering

Presented and publicly defended by:

DOUANIA Inès

June 03th 2022

Spécialité : Biomécanique, Bioingénierie

Jury members

Reviewers:
Mr. Alfredo I. HERNANDEZ, Research Director INSERM, Université de Rennes 1, LTSI
Mr. David GUIRAUD, Research Director INRIA - NEUROINNOV
Examiners:
Ms. Catherine MARQUE, Professor, Université de Technologie de Compiegne, BMBI
Ms. Virginie LE ROLLE , MCF, Université de Rennes 1, LTSI
Invited:
Ms. Kiyoka KINUGAWA BOURRON, Professor, Faculté de Médecine Sorbonne Université
Supervisors:
Mr. Sofiane BOUDAOUD, Professor, Université de Technologie de Compiègne, BMBI
Mr. Jérémy LAFORÊT, Research Engineer CNRS, Université de Technologie de Compiègne, BMBI

Publications

International journal papers:

- **I. Douania, J**. Laforêt, S. Boudaoud, "Improved Morris Sensitivity Analysis (IMSA) approach for the evaluation of a complex multi-scales and multi-physics neuromuscular model”, 2022, *Computer Methods and Programs in Biomedicine*, Elsevier Journal. In review (major revision).

International conference papers:

- **I. Douania**, J. Laforêt and B. Sofiane, "Personalized spatial recruitment model to motor unit type and number" *2021 Sixth International Conference on Advances in Biomedical Engineering (ICABME)*, 2021, pp. 155-158.
  Doi: 10.1109/ICABME53305.2021.9604890.
- **I. Douania**, J. Laforêt, S. Boudaoud, "New modeling approach of structural and morphological changes of fibers and motor units", *2020 Virtual Physiological Human conference.*
- **I. Douania**, J. Laforêt, S. Boudaoud and K. Kinugawa, "Assessment and sensitivity analysis of a motor units recruitment model during isometric contractions of the Biceps Brachii," *2019 Fifth International Conference on Advances in Biomedical Engineering (ICABME)*, 2019, pp. 1-4.
  Doi: 10.1109/ICABME47164.2019.8940248.

List Of Abbreviations

AP Action Potential.

ATP Adenosine TriPhosphate.

BB Biceps Brachii.

BC Best Candidate.

BF Biceps Femoris.

CNS Central Nervous System.

CSA Cross-Sectional Area.

CT Computational Time.

CTO Computer Tomography.

CV Conduction Velocity.

EE Elementary Effect.

EMG Electromyography.

ETC Excitation Contraction Coupling.

ETh Excitation Threshold.

FD Frequency Domain.

FF Fast Fatigable.

FI Fast Intermediate.

FPDS Fast Poisson Disk Sampling.

FR Fast Resistant.

GWAS Genome-Wide Association Studies.

HC High Contraction.

HD-sEMG High Density surface Electromyography.

IMAT Intra Muscular Adipose Tissue.

IMSA Improved Morris Sensitivity Analysis.

LC Low Contraction.

MAD Model Aided Diagnosis.

MN Motoneuron.

MRI Magnetic Resonance Imaging.

MSA Morris Sensitivity Analysis.

MU Motor Unit.

MUAP Motor Unit Action Potential.

MUMRI Motor Unit Magnetic Resonance Imaging.

MVC Maximal Voluntary Contraction.

MyHC Myosin Heavy Chain.

NMJ Neuromuscular Junction.

OM Old Men.

OW Old Women.

PDS Poisson Disk Sampling.

PNS Peripheral Nervous System.

PSD Power Spectral Density.

RMSA Root Mean Square of Amplitude.

S Slow.

SA Sensitivity Analysis.

sEMG surface Electromyography.

SF Subcutaneous Fat.

SFAP Single Fiber Action Potential.

SR Sarcoplasmic Reticulum.

TD Time Domain.

VL Vastus Lateralis.

WHO World Health Organization.

YM Young Men.

YW Young Women.

Contents

List of Tables

List of Figures

General introduction

Skeletal muscles are responsible of enabling and facilitating voluntary movement. They allow individuals to mobilize, manipulate their environment and live independently. The neuromuscular disorder is the most common disabling condition affecting people aged over 65 years. The non-exhaustive list of the age-related neuromuscular features includes the loss of Motor Units (MUs) and the expansion of that remain, the reduction in the number and size of muscle fibers, the increase of the intramuscular fat infiltration, and the disorder of the neural control. As a consequence, mechanical muscle performance is impaired with concurrent decreases in maximal muscle strength and power in the elderly population[1].

The increase in life expectancy is associated with a high risk of disability. Therefore, detecting an early decline in muscular functions during aging is of paramount importance. The muscle aging, as a disease entity, is known as sarcopenia. It is defined as a reduction of muscle strength accompanied by a loss of muscle mass and a decline in physical functions. The current methodologies used in clinical practice to assess this aging disease are rather limited to capturing the features of this decline at the macroscopic scale[2]. Factors such as the loss of MUs, the atrophy of fibers, and the neural recruitment pattern significantly influence muscular function. However, diagnosing sarcopenia by only measuring the muscle strength and/or muscle mass is not accurate enough and can not alert an early loss of muscular function. The inner scales (MU and fiber scale age-related changes) reflecting that loss of muscle mass and strength during aging are more interesting to exploit. Thus, in recent studies, some in our team, based on the surface Electromyography (sEMG) technique, have demonstrated the potential of this technique to be used as a biomarker to detect early signs of sarcopenic muscles.

In fact, the sEMG signal is the electrical response of the muscle activation managed by the Central Nervous System (CNS). It is measured at the skin surface using surface electrodes and can be correlated efficiently to the mechanical response of muscle activation. Moreover, mathematical models of sEMG signal can form a helpful alliance with sEMG experimental measures and processing to identify and/or quantify bio-indicators (i.e., anatomical and neural muscle parameters) of a healthy, early, accelerated, or sarcopenic muscle aging. Consequently, during the last years, the monitoring of these age-related alterations in the neuromuscular system from sEMG signals has expanded. Likewise, the modeling of sEMG signals has seen the same expansion.

Thanks to the thesis work of Dr. V. Carriou, under the supervision of Prof. S. Boudaoud and IR. J. Laforêt, a fast and optimized electrical model describing the electrical activity of the muscle at the skin surface using the High Density surface Electromyography (HD-sEMG) technique, was developed [1]. The reduced computational time of this model

---

[1] People aged over 65 years according to the World Health Organization (WHO)

[2] Diagnosis recommendations of the European Working Group on Sarcopenia of Older People EWG-SOP2

is the prominent key feature of identifying aging indicators using inverse methods and the HD-sEMG technique. However, this identification needs pre-aided methods such as sensitivity and identifiability analysis. Moreover, when dealing with this model, we have observed significant limitations such as the lack of physiological realism (e.g., MUs territories and the number of fibers per muscle), personalization (e.g., same recruitment pattern for the young and elder subject), and simplicity (e.g., adjustment of 50 model parameters according to age and gender). These limitations can restrain the use of this model in muscle aging diagnosis.
Therefore, we aimed in this thesis to address the limitations of model depicted in [1] and deliver a more realistic and user-friendly model to evaluate muscle aging. Based on all of the above, this manuscript is organized as follows:

- Chapter 1: in this chapter, we start the first section by introducing the aging problematic, its different trajectories, and the contribution of the neuromuscular system disorder in the increase of disability risks. In the second section, we introduce essential notions concerning the anatomy of the neuromuscular system and the mechanisms inducing electrical and mechanical muscle response to voluntary activation. Afterward, in the next section, we describe the age-related alterations of this anatomy and these mechanisms at the macroscopic scale (muscle mass and fat infiltration), at the microscopic scale (fiber and Motor Unit (MU)), and at the neural drive scale (recruitment pattern of sources generating electrical activity). We enclose this section by defining muscle aging as a disease entity (sarcopenia). In the next section, we present the diagnosis tools of muscle aging and discuss how their clinical use is limited to macroscopic measures, whereas they can provide more relevant information on the microscopic and neural scale. At the end of this section, we focus on the sEMG tool and its usefulness in detecting muscle aging changes. Therefore, afterward, we introduce the role played by models in enhancing the sEMG tool to detect these age-related changes. Wherein, we describe the HD-sEMG model depicted in [1] that will be performed in this thesis to simulate sEMG signal from specific physiological and neural configurations. Finally, we enclose this chapter by positioning the proposed thesis work in the face of diagnosing muscle aging and indicating the thesis's objectives and workflow.

- Chapter 2: in this chapter, we perform a global sensitivity analysis on the model [1], where the sensitivity of the statistics computed over the HD-sEMG signals is assessed according to the variation of the neuromuscular parameters. This analysis will help in identifying critical parameters of muscle aging. In fact, the sensitivity analysis will reduce/limit the identification problem to the parameters with large impact on the HD-sEMG signals. First, we will select the Morris Sensitivity Analysis (MSA) based on the complexity and the computational time of the HD-sEMG model. Second, we will improve this method for reliable parameter rankings. Finally, the Improved Morris Sensitivity Analysis (IMSA) will be performed on young and elder simulated subjects (at low and high force levels). The result will isolate the influential parameters for each age category, each force level, and each statistic feature computed over the HD-sEMG signals. A relationship will be built between ages, forces, neuromuscular parameters, and HD-sEMG signals. This relation will be helpful in the identifiability analysis (the cost function evaluation) and identification process on the one hand and will spotlight the model inaccuracies and limitations on the other hand. The latter fact will lead to achieving works in the next chapter.

- Chapter 3: in this chapter, we will address the limitations observed in the HD-sEMG model [1] and deliver a more realistic and user-friendly model to evaluate muscle aging. First, we will describe the modeling approach scheme as depicted in [1] and illustrate its limitations. Second, we will propose a new user-friendly scheme. In this new scheme, the 50 inputs will be fairly limited to the age and gender of the patient. We will propose descriptive and statistical models to estimate these 50 parameters, manually introduced in [1]. In fact, the statistical models will provide estimated neuromuscular parameters according to age and gender, such as the number and size of fibers and the intramuscular fat area. The descriptive models will define muscle morphology and structure based on age, gender, and estimated parameters from statistical models. These models describe the positioning of fibers, MUs, assignment of fibers to motoneurons, dispersion of intramuscular fat, and the neural drive. This mathematical description will be built regarding age-related changes depicted in chapter 1. Finally, we will discuss the usefulness of the new modeling approach to building a muscle aging diagnosis tool aided by the model.

Chapter 1

State of the art and problematic

Contents

1.1 Introduction

Movement is a capital sign of life; To move is to live. For a long time, this statement was evident. However, improved safety, health care, nutrition, and progress in medicine, science, and technology have increased the world population's life expectancy. This longevity of lifespan is not related necessarily to an impairment of movement capacities [2]. The rising in life expectancy, which is a human success story, is accompanied by a loss of functional performance capacities and a higher risk of falling, leading to a loss of autonomy and disability risks. Due to these changes, a significant clinical and economic burden for society exists. Therefore, detecting early declines in muscular function during aging and preventing the loss in functional performance is of paramount importance.

The primary factor contributing to poor healthcare outcomes for the elderly population is a general decline in physiological resilience, which is a crucial feature of frailty syndrome [3]. Frailty syndrome encompasses diseases of the immune, nervous, endocrine, skeletal, and muscular systems [3]. The neuromusculoskeletal disorder is the most common chronic disabling condition affecting people aged over 65 years [4]. Skeletal muscles enable and facilitate voluntary movement within this system and allow individuals to mobilize, manipulate their environment, and live independently.

However, during aging, skeletal muscles start their natural deteriorating process at the age of 35 years old [5]. The lean muscle mass and strength loss are the most notable features of this aging process [6]. The accelerated loss of lean muscle mass and function is known as sarcopenia, which is recognized as a disease entity by the World Health Organization (WHO) [7].

The current methodologies used in clinical practice to assess this aging disease are rather limited to capturing these features at the macroscopic scale, such as the diagnosis recommendations of the European Working Group on Sarcopenia of Older People EWGSOP2 [8]. Despite the collective effort, the diagnosis criteria of sarcopenia remain a major debate today among clinicians. The cut-off points of muscle mass and strength loss fixed through a statistical model using longitudinal studies among the elderly population are not accurate enough, robust, precise, and mutual between sarcopenia working groups. In addition, the recommended diagnosis tools/criteria are not reliable enough: (i) to differentiate between various aging stages (e.g., healthy, accelerated, pre-sarcopenic, several sarcopenic), and (ii) to predict and detect a presumed motor decline. For example, a method based on the sEMG processing [9] has demonstrated the great potential of this technique to be used as a biomarker to detect early signs of sarcopenic back muscle. To note, in this cited study [9], the younger and older groups have no significant difference in muscle strength.

Next to these limitations of macroscopic scale diagnosis of muscle aging, the inner scales reflecting that loss of muscle mass and strength during aging are more interesting to exploit. In fact, the increasingly enhanced technology and expertise dedicated to the functional evaluation of the neuro-musculo-skeletal system, such as the HD-sEMG technique and models, can boost the development of reliable devices able to assess motor decline and serve as an indicator in a prevention approach or functional rehabilitation. Following this idea, a recent European project (EIT Health CHRONOS project[1]) was granted in 2018, under the coordination of Prof. K. Kinugawa and Prof. S. Boudaoud, to develop a device able to assess muscle aging using HD-sEMG technique. Promising results were obtained through the thesis work of L. Imrani[10]. However, this work focused only

---

[1] www.eithealth.eu

on experimental data analysis without interaction with models.
Therefore, following the thesis purpose, this chapter aims to provide new insights into the muscle aging aided-diagnosis model by integrating macroscopic and microscopic observations of differences between the younger and older muscles. To begin with, we will introduce aging as a major health-related problem: the statistics and the different metrics of assessment. We will briefly introduce the human neuromuscular system anatomy and mechanisms of muscle contraction. After, we will review important literature which establishes age-related changes at the macroscopic scale (mass, size, morphology, fat, and strength of muscle), microscopic scale (fiber changes, motor unit changes), and neural scale (recruitment pattern changes). Then, after reviewing sarcopenia (definitions, criteria, and diagnosis tools), I will introduce the HD-sEMG technique and its usefulness in detecting age-related changes (healthy and sarcopenic). Furthermore, we will underscore key areas where the multi-scale and multi-physics HD-sEMG model [1, 11], developed in the team and improved during my thesis work, can enhance aided-diagnosis tools of muscle aging (eventually sarcopenic aging).

1.2 Aging: a health-related problem

As a time-related defective balance between cell-damage and cell-repair process, aging is accompanied by a loss of functional performance capacity and a higher risk of falling, leading to a loss of autonomy. In this section, we will first introduce the aging statistics in the world and the possible causes and reasons for the exponential statistic curves. Then, we will review the research efforts to achieve aging metrics and stages. In the last paragraph of this section, we will introduce the disability risks and the neuromusculoskeletal disorder for aging people.

1.2.1 Population aging statistics

The second half of the 20th century has seen the world population change. Improvements in safety, health care, nutrition, and progress in medicine, science, and technology, have increased the life expectancy of the world population. By 2050, according to the WHO statistics, the world's population of people aged 60 years and older will double (2.1 billion, 22% of the world human population). This phenomena, known as population ageing, is extending through the most planet countries (Fig. 1.1 (a) and (b)). The high income countries are much more impacted by this population aging: 65 year old and overs people should account around 36% of Southern European countries population and 38% of Japan's and South Korea's according to WHO statistics. Next to the growing number of older people aged above 60, there is a rapid increase in the number of very old people aged above 80 (their number should be triple according to the same source: WHO). This phenomenon is called "Silvering". In the United Kingdom, for example, the Office for National Statistics[2] (ONS) estimates that 50% of the population born after 2050 will survive to the age of 100 years (Fig. 1.2).
This demographic shift, beyond the major economic and societal challenges that implies, is a human success story: the health conditions and human safety are improved. However, is the life quality preserved for the aging and silvering population ?
Aging, as a biological definition, results from the impact of the accumulation of a wide

---

[2] www.ons.gov.uk

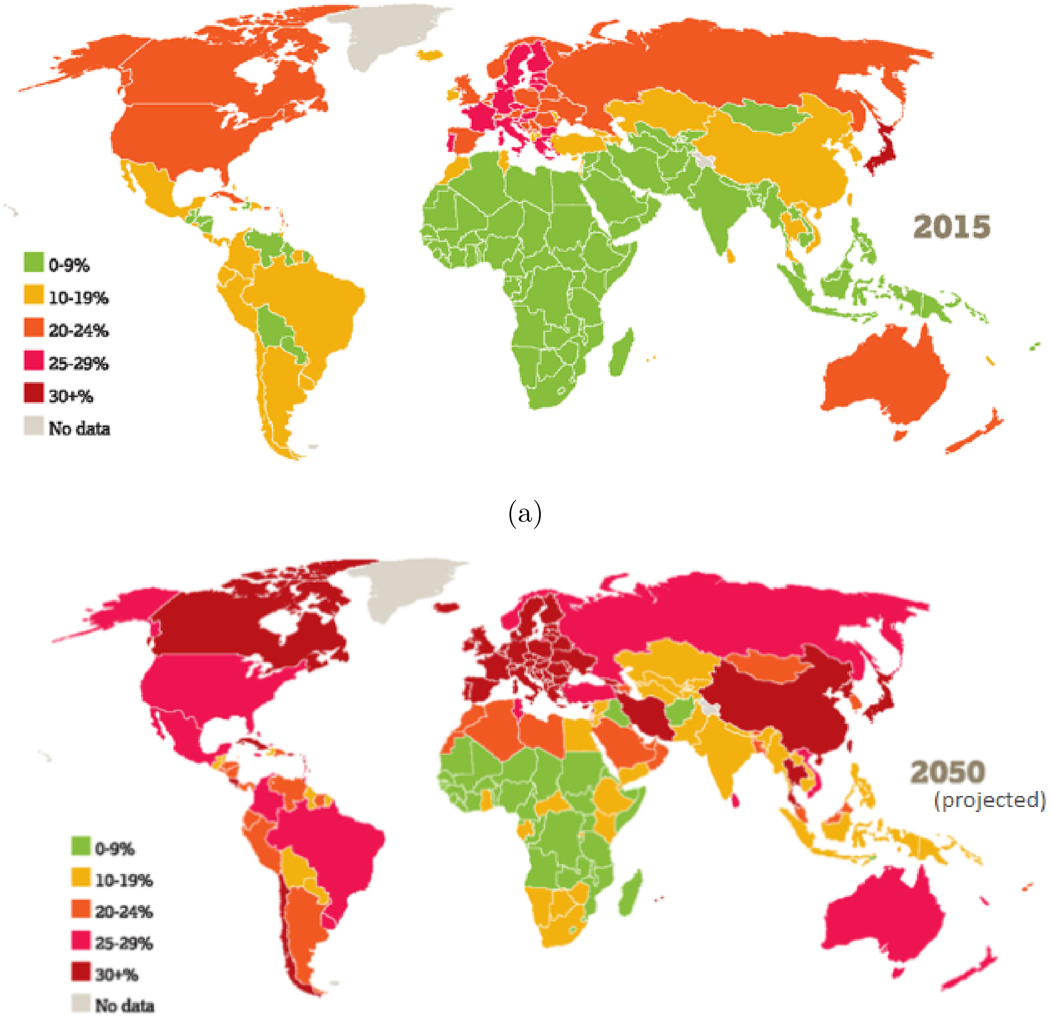

(a)

(b)

Figure 1.1: Proportion of population aged 60 years or older, by country, in (a) 2015 and (b) 2050. Source: Global AgeWatch Index (www.globalagewatch.org) - Adapted from World Health Organization.

variety of molecular and cellular damage over time. Which leads to a gradual decrease in physical and mental capacity, a growing risk of disease and ultimately death. Beyond the social and economic altering the life quality for elderly people, many health-related problems are associated with aging. These health-related problems, defined as chronic pathologies, include hearing loss, cataracts and refractive errors, back and neck pain and osteoarthritis, chronic obstructive pulmonary disease, diabetes, depression and dementia, and musculoskeletal disorders. Moreover, elderly people are more likely to experience several health-related problems at the same time with an emergency state and risks of total or partial disability.

The main challenge for scientists and researchers is to evaluate and predict these disability risks at an early stage and propose therapies and recommendations for long-time healthy aging.

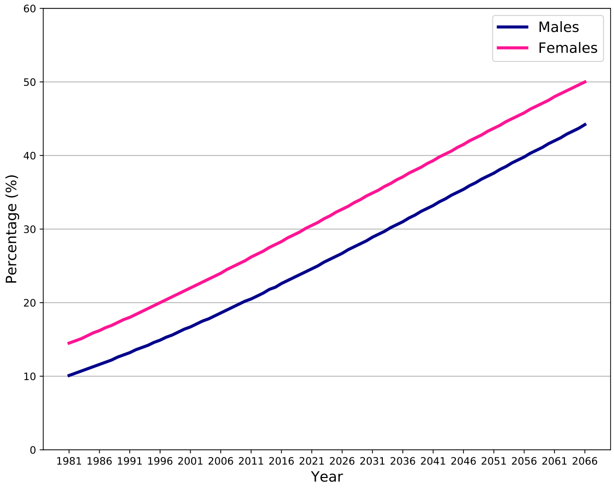

Figure 1.2: Percentage of people expected to survive to age 100 by year of birth, males and females. Source: plotted using data of UK Office for National Statistics(www.ons.gov.uk)

1.2.2 Aging Metrics

Prevention of frailty and evaluation of the disability risks are ascending research themes as the aging population increases. Disability can be defined as a failure in exerting activities in any domain of life due to a health or physical problem [12]. The aging chronic pathologies, cited in section 1.2.1, can evolve into impairments and functional limitations and eventually leads to the inability to perform activities of daily life independently, known as disability (Fig. 1.3) [4]. In the Fig. 1.3, authors of [4] define three aging patterns: healthy, normal and accelerating aging. Many factors are impacting these patterns, such as the biological and physiological changes of the organs, the environmental conditions, and the daily life routine of the person (e.g., nutrition, physical activity. smoking, etc.)[13, 14, 15, 16].

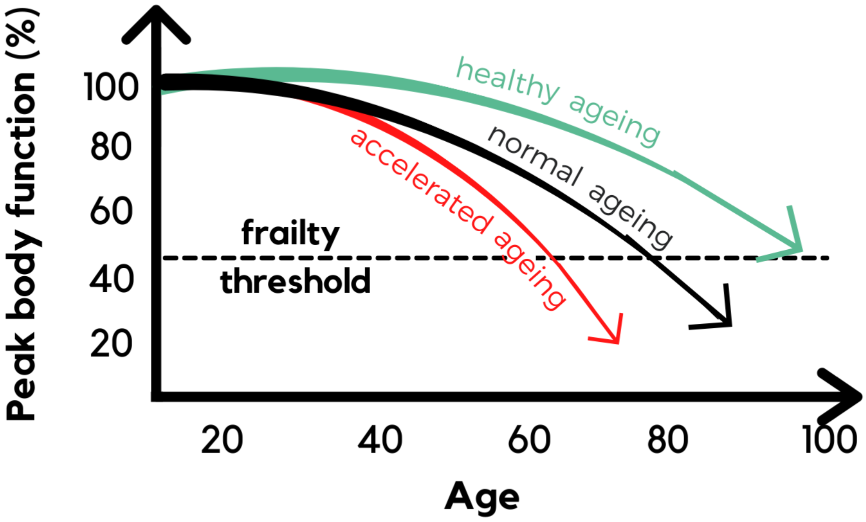

Figure 1.3: Schematic representation of aging trajectories. The curved lines represent (red) accelerated aging, (black) normal aging and (green) healthy aging. Adapted from [4]

However, there is no typical older person beyond the studies cited in the previous paragraph. Indeed of factors cited in [13, 14, 15, 16], some 80-year-old have physical and mental capacities similar to many 30-year-olds while other people experience significant declines in capacities at much younger ages. This unpredictable aging pattern for some people can be due to other factors, unknown instead of advances in medicine and sciences. A comprehensive public health response should address this wide range of older people's experiences. Recent research themes are focusing on genetic factors and their impacts on lifespan among individuals [17, 18, 19, 20]. These studies have tried to identify genes and variants playing some role in longevity, known as Genome-Wide Association Studies (GWAS). Results of GWAS for many phenotypes relevant to aging have started to emerge, and valuable information rises to the surface from these studies. This information correlated between chronic diseases and aging genes/traits as shown in Fig.1.4(e.g., obesity, cancer, etc.). It estimates the faculty of each cited chronic aging pathologies to damage the parental lifespan gene and, as consequence, accelerates the biological aging pattern.

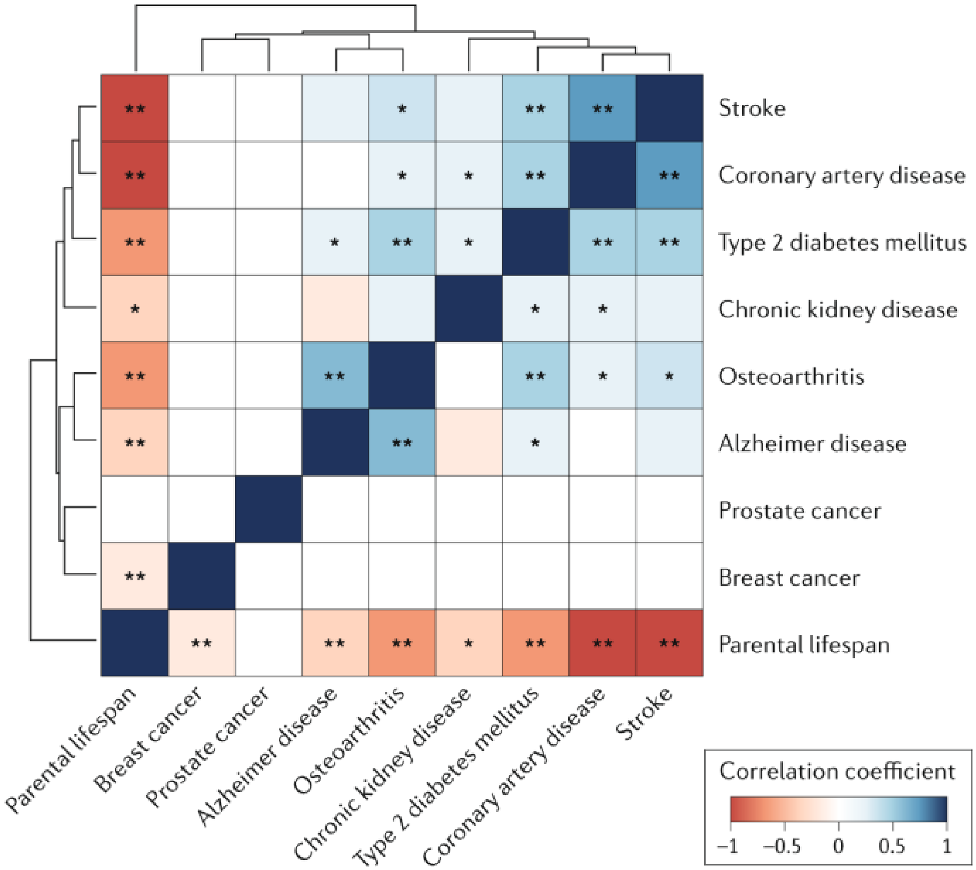

Figure 1.4: Correlated variants with aging as depicted in [18]. Genetic overlap between age-related chronic diseases and parental longevity, based on correlations between whole-genome association results (GWAS: Genome Wide Association).

The biological aging is the first stage in the metrics of aging. Many diagrams of the major influences and mechanisms of human aging and many metrics for aging are proposed in the literature [6, 18]. The most recent and reliable ones, based on animal models, are proposed by [6]. Authors in [6] elucidated the connections between longitudinal changes at the molecular, cellular, and functional levels. As shown in Fig.1.5, the aging metric is composed of three main stages: 1) Biological aging: first released and featured mainly by molecular damage and defective repair of cells; 2) Phenotypic aging: featured by changes in the body composition and alteration of energetic mechanisms; 3) Functional aging:

the last released aging, mainly featured by a decline in cognitive and physical functions. This thesis will mainly focus on impairments in the neuro-musculoskeletal system. It will simulate and study some features of phenotypic and functional aging: mainly the changes in muscle quality and the decline in muscle neural control and force.

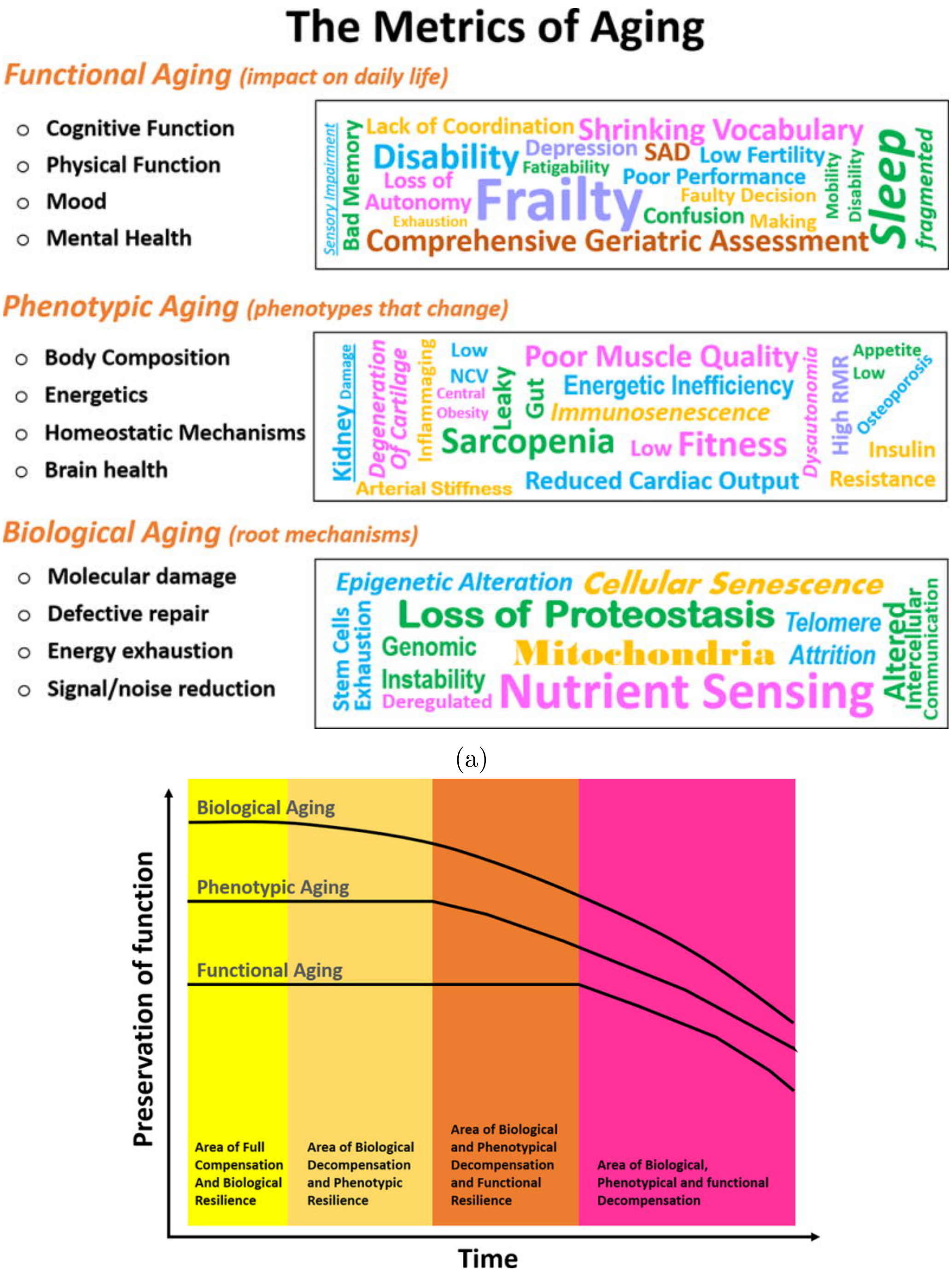

(a)

(b)

Figure 1.5: Correlated variants with aging as depicted in [18]. (a) The metrics of aging. (b) Trajectories of biological, phenotypic and functional aging and their interaction over the life span. Of note, functional aging occurs only when all resilience mechanisms of the biological and phenotypic aging domains are exhausted.

1.2.3 Aging and disability risks: the neuromusculoskeletal disorder

The National Council of Aging[3] (NCA) indicates that about 80% of older people have at least one chronic pathology of those cited in section 1.2. Next to functionality and independency loss during aging, the risk of falling is one of the most important causes of mortality for older adults [21]. About 24-40% of community-dwelling people, aged 65 or older, fall at least once a year, whereas this number increases to 50% for residents in care facilities [22]. Moreover, the NCA declares that every 19 minutes, an older person dies because of a fall. Including all aspects, aging is accompanied by a loss of functional performance capacity and a higher risk of falling, leading to a loss of autonomy. Due to this loss of autonomy, the rising medical costs, and the higher need for primary health care, a relevant economic burden for society exists. In an attempt to counteract this problem, a better understanding of the risk factors and underlying mechanisms is warranted. Therefore, many research areas focus on changes during the aging process. A combination of neural, hormonal, immunological, physiological, and external factors such as nutrition, physical activity, and the environment seems to play a role in the loss of functional performance capacity and the higher risk of falling during aging [23]. This thesis will focus on simulating neural, morphological, and structural changes in muscle quality and control during aging. Before underlying researches elucidating these changes, we will introduce a description of the neuromusculoskeletal anatomy.

1.3 The neuromuscular system: anatomy and mechanisms

Skeletal muscle is the body actuator. In terms of mass, it is the heaviest organ in the body. It comprises approximately 40% of total body weight and contains 50–75% of all body proteins [24]. It is essential for respiration, locomotion, posture, and whole-body energy homeostasis [25]. These actions allow human functional independence, maintain and enhance health, and contribute to social and economic life [24]. The neuromusculoskeletal system displays a higher structural and hierarchical organization to achieve maximal performance and efficiency for these roles. Three human body systems coordinate and work together: the skeletal system, the muscular system, and the nervous system. Decades of research in these body subsystems' physiology have provided multi-scale insights into these essential anatomical tissues' structural and functional complexity.

This section will review the skeletal muscle anatomy, the peripheral neural system, and the electrical and mechanical mechanisms contributing to muscle contraction. These descriptions are required to elucidate and simulate mechanisms involved during muscle aging.

1.3.1 Anatomy of musculo-skeletal system

The human body incorporates more than 600 muscles attached to the skeleton. They provide a pulling force that allows movement. Each muscle extremity is attached to bones by the tendons and has a contractile fleshy portion called the muscular body. In the human body, the skeletal muscles have a variety of shapes depending on their fiber

---

[3] www.ncoa.org

orientation, and the tendon junction is aligned with the tendon (fusiform muscle) or is at an angle (pennated muscle). In the case of pennated muscles, the muscle fibers are connected to the muscle's aponeurosis. Thus, we can classify the skeletal muscles according to their forms, as illustrated in Fig. 1.6.

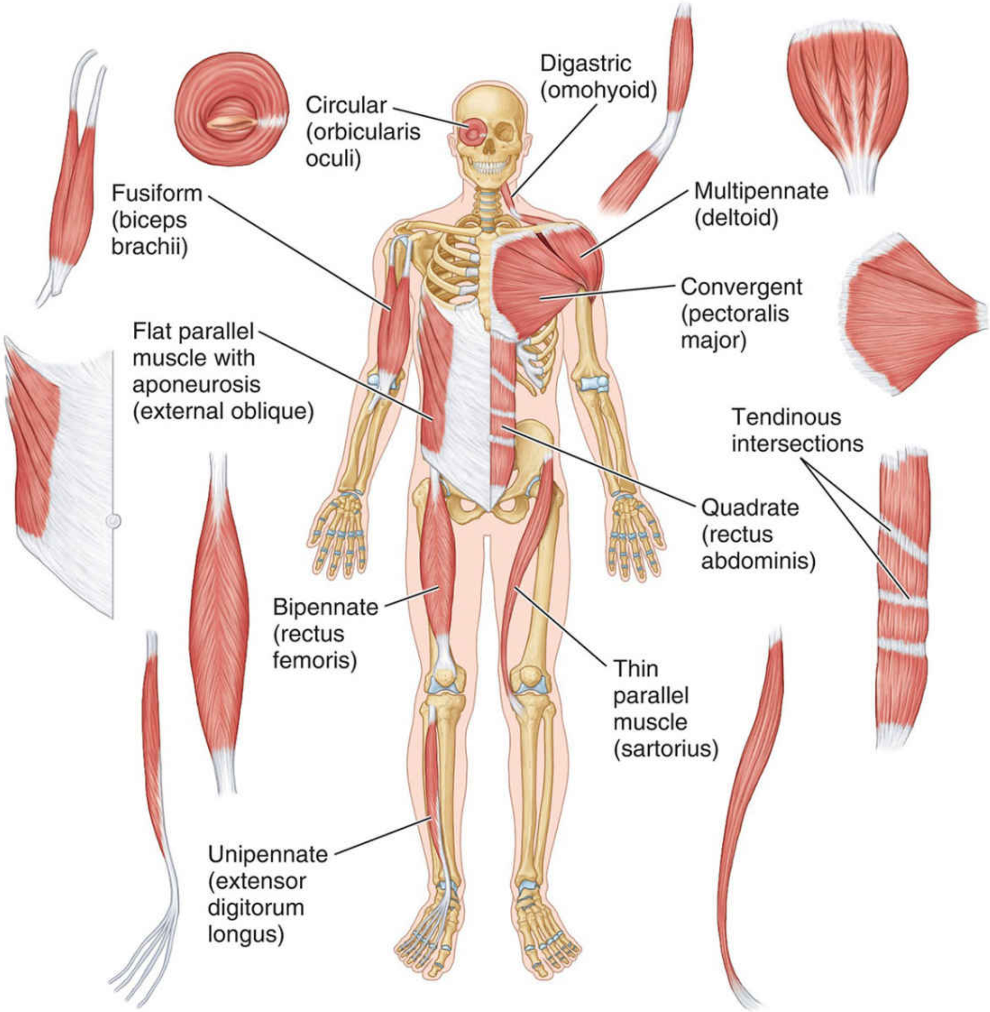

Figure 1.6: Architecture and shapes of skeletal muscles. The architecture and shape of a skeletal muscle depend on the arrangement of its fibers. Source: www.anatomynote.com

1.3.1.1 Macroscopic anatomy

Skeletal muscle is made up of several interconnected components. These tissues encompass skeletal muscle fibers, vasculature, peripheral nerves, and connective tissue. Three layers of connective tissue envelop each skeletal muscle, providing it structure and compartmentalizing the muscle fibers within it (Fig. 1.7). The first layer is a dense and irregular connective tissue called the **epimysium**. This enables a muscle to contract and move forcefully while maintaining structural integrity. The epimysium also separates muscle from surrounding tissues and organs, allowing it to move independently. Muscle fibers are organized into **fascicles**, which are bordered by a middle layer of connective tissue termed the **perimysium**, inside each skeletal muscle. This fascicular organization is typical in muscles of the limbs (e.g., the Biceps Brachii muscle). It permits the nervous system to activate a subset of muscle fibers inside a muscle fascicle to cause a specific muscle action. Each muscle fiber is coated in a thin connective tissue layer of collagen and reticular fibers termed the **endomysium** inside each fascicle. The endomysium surrounds the cells' extracellular matrix and helps to carry the force generated by muscle fibers to the tendons. The hypodermis is the outermost of these connective tissues, located just below the skin. It protects muscles, regulates the heat loss generated by muscles, and stores the triglyceride surplus of the human body. The innermost of these connective tissues are aponeurosis, also known as fascia, located between skin and bones. In skeletal muscles that work with tendons to pull on bones, e.g., the Biceps Brachii muscle, these fasciae continuously surround the muscle and some sub-parts. The fasciae connective tissues are present in all the muscles up to the tendon to form what is defined as the myotendinous junction. The tendon then extends to the bone to form the osteo-tendinous junction.

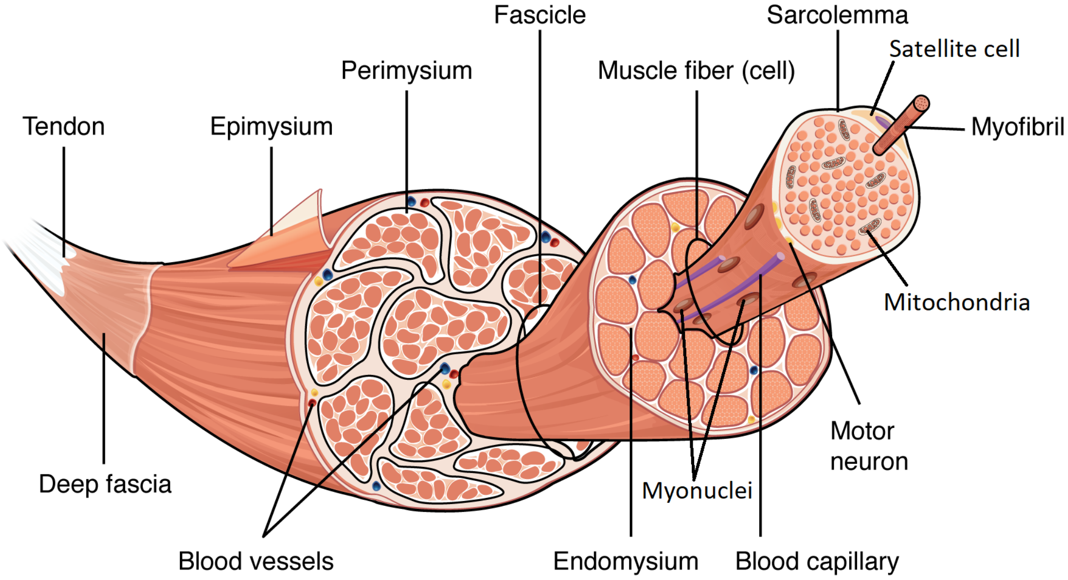

Figure 1.7: Macroscopic architecture and structure of skeletal muscles. The perimysium covers three connective tissue layers: bundles of muscle fibers called fascicles. Muscle fibers are surrounded by the endomysium (Source: http://open.oregonstate.education).

1.3.1.2 Muscle fiber: macroscopic anatomy

Muscle fibers (or myofibers) are the commonly used name for skeletal muscle cells since they are long and tubular. Moreover, skeletal muscle fibers can be quite large compared to other cells. In fact, the muscle fiber diameter varies from 10 μm to 100 μm according to the considered muscle. Similarly, its length differs depending on the muscle. It varies between 10 and 30 cm in a healthy adult human body (e.g., the diameter of the Sartorius is up to 100 µm, and its length is up to 30 cm). The high number of fiber nuclei produces the vast amounts of proteins and enzymes required to keep these large protein-dense cells functioning normally. In addition, skeletal muscle fibers contain nuclei as well as cell components standard in other cells, such as mitochondria. Some of these components, however, are specific to muscle fibers. The plasma membrane that covers muscle fibers is known as the sarcolemma (Fig. 1.7). Inside the sarcolemma is the sarcoplasm, corresponding to the cytoplasm of the fiber. Similar to the cytoplasm, the sarcoplasm mainly holds glycogen, used for the synthesis of Adenosine TriPhosphate (ATP) which acts as an energetic supply for the fiber. In addition, myoglobin protein is also found in the sarcoplasm. This protein only exists in the muscles of vertebrates. It stores oxygen molecules for the formation of ATP by the mitochondria when needed. Proteins are structured within muscle fibers into myofibrils, which are cylindrical components that run the length of the cell and contain sarcomeres joined in series (Fig. 1.8). Because myofibrils are only about 1.2 µm in diameter, one muscle fiber can have hundreds to thousands of them. These myofibrils are the minor contractile units in the muscle. They are enclosed in a specialized smooth endoplasmic reticulum, called the Sarcoplasmic Reticulum (SR), which stores, releases, and retrieves calcium ions (Ca^{2+}). When the muscle is at rest, the SR stores a certain amount of calcium ions (Ca^{2+}). Then, during muscle contraction following a neural command from the Central Nervous System (CNS), the SR will release the Ca^{2+} stored in the fiber in order to realize the muscle contraction (see section 1.3.3.2).

1.3.1.3 Muscle fiber: Sarcomere

The striated structure of skeletal muscle fibers is owing to the arrangement of the thick and thin myofilaments within each sarcomere, which is defined as the portion of a myofibril contained between two cytoskeletal structures termed Z-discs (also called Z-lines) (Fig. 1.8). Striated dark A band comprises myosin thick filaments that span the sarcomere's core and extend toward the Z-discs. A protein called myomesin anchors the thick filaments in the center of the sarcomere (the M-line). Thin actin filaments are tethered at the Z-discs by a protein called alpha-actinin in the lighter I band regions. The thin filaments expand into the A band and overlap with portions of the thick filament as they go toward the M-line. The A band is darker because myosin filaments are thicker and overlap with actin filaments. Because the thin filaments do not reach into this region, the H zone in the middle of the A band is slightly lighter in color. A single sarcomere has one dark A band with half of the lighter I band on each end, as defined by Z-discs (Fig. 1.8). Myofilaments

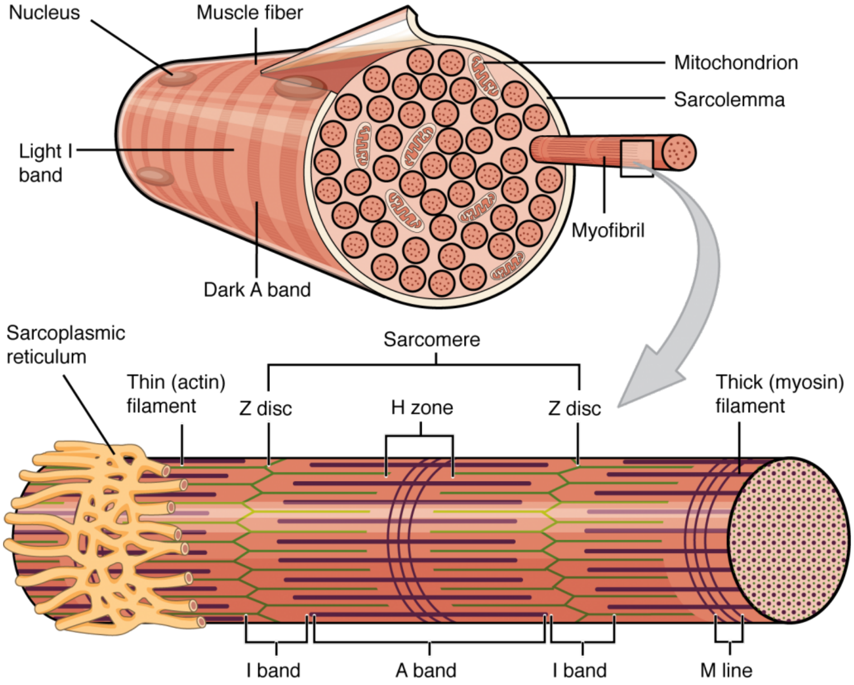

Figure 1.8: Anatomic structure of a muscle myofibril. A muscle fiber is structured by numerous myofibrils, which contain striated sarcomeres with bright and dark areas (Source: http://open.oregonstate.education).

do not change length during contraction; instead, they glide across each other, shortening the space between the Z-discs. The length of the A band remains constant (because of the thick myosin filament), while the H zone and I band areas diminish. These are locations where the filaments do not overlap, and when filament overlap rises during contraction, these no overlap regions shrink.

1.3.1.4 Muscle fiber: myofilament components

Two filamentous actin chains (F-actin) composed of individual actin proteins form the thin filaments (Fig. 1.9). The Z-disc anchors these thin filaments, which expand to the sarcomere's center. Each globular actin monomer (G-actin) within the filament contains a myosin binding site linked to the regulatory proteins troponin and tropomyosin. There are three polypeptides in the troponin protein complex. Troponin I (called TnI) binds to actin, troponin T (called TnT) to tropomyosin, and troponin C (called TnC) to calcium ions. Troponin and tropomyosin are proteins that run along actin filaments and regulate when actin-binding sites are accessible for myosin binding. Thick myofilaments are formed up of myosin protein complexes, consisting of six proteins: two heavy chains and four light chains. The heavy chains are made up of a tail region, a flexible gate/pivot region, and a globular head with an Actin-binding site and a binding site for the high-energy molecule ATP. The light chains control the hinge region, but the heavy chain head interacting with actin is the most important force generator. Hundreds of myosin proteins are found in each thick filament, with tails pointing to the M-line and heads pointing to the Z-discs.

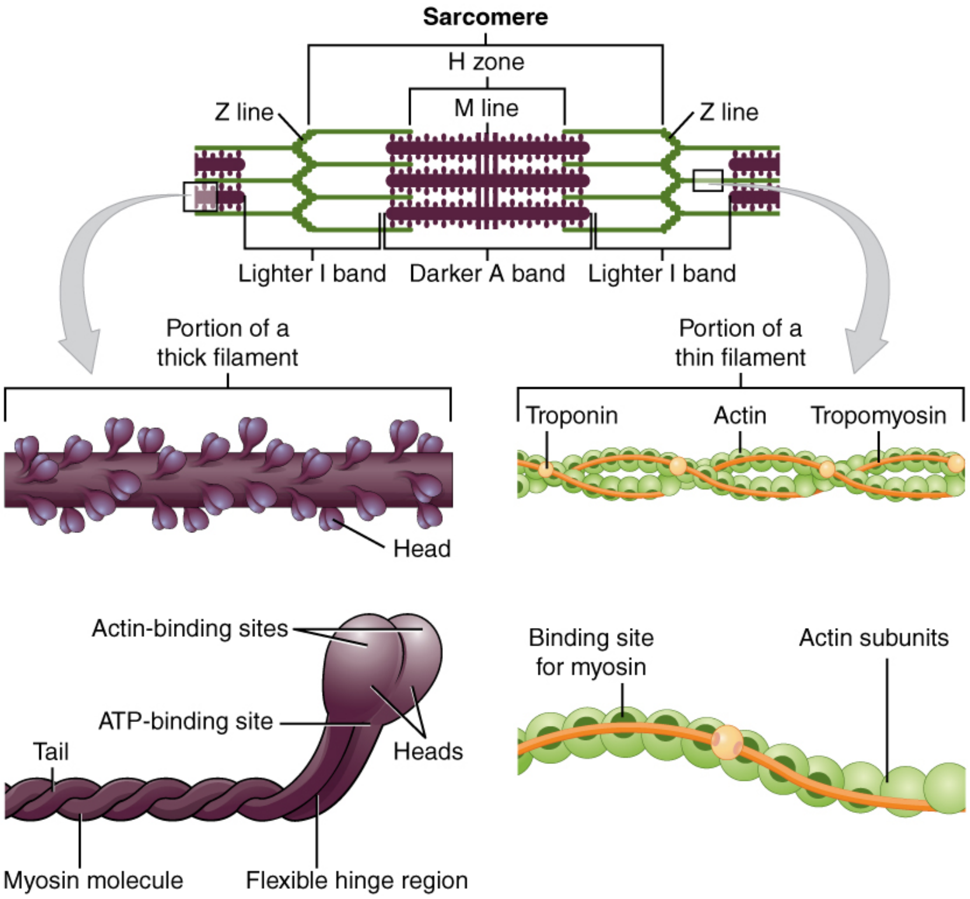

Figure 1.9: The sarcomere, the region from one Z-line to the next Z-line. The sarcomere is the functional unit of a skeletal muscle fiber (Source: http://open.oregonstate.education).

Other structural proteins are found in the sarcomere but do not contribute to active force generation. Titin, the world's biggest protein, aids in the alignment of the thick filament and gives the sarcomere its elasticity. Titin starts from the M-Line and stretches to the Z-disc. The thin filaments feature a protein called nebulin that crosses the length of the thick filaments and helps to keep them stable.

1.3.1.5 Muscle fiber: types and characteristics

Skeletal muscles are composed mainly of two fiber types: slow-twitch fibers (type I) and fast-twitch fibers (type II), identified by specific Myosin Heavy Chain (MyHC) isoforms. This classification is based on the functional metabolism of these fiber cells, where the slow fibers use aerobic metabolism (oxidative phosphorylation) with abundant oxidative enzyme and myoglobin complement and lower levels of glycolytic enzymes. In contrast, at the other extreme, the fast fibers use anaerobic metabolism with higher levels of glycolytic enzymes [26]. Actually, three essential classification techniques are commonly applied to type fibers: histochemical staining for myosin ATPase, myosin heavy chain isoform identification, and biochemical identification of metabolic enzymes [27]. However, beyond the research effort, identifying the type of fibers through their physiological properties is still a challenge today. In fact, since the introduction of enzyme histochemical methods into the study of muscle fiber properties in the 1950s, a significant number of histochemical methods were developed for muscle fiber typing based on the calcium method for myosin ATPase staining (ATP: Adenosine TriPhosphate).

First appeared methods (e.g., [28]) have identified two fiber types: slow-twitch fibers (type I) and fast-twitch fibers (type II), based on the stability of fiber cells at different pH-concentration which allows or inhibits the myosin ATPase reaction. Later, more advanced techniques have demonstrated that more ATPase activities could be distinguished by their stability to acidic or basic preincubation solutions. Thus, the fibers of type II were labeled into two subgroups: IIa (or Fast Resistant (FR) fiber) and IIb (or Fast Fatigable (FF) fibers). More recent methods have shown the existence of intermediate fiber types (from slowest to fastest): Ic, IIc, IIac, and IIab [29, 27]. These types have intermediate myosin ATPase staining characteristics (e.g., IIab intermediate characteristics between IIa and IIb). In summary, the human muscle fiber types, as identified by myosin ATPase histochemical staining, are (from slowest to fastest): types I, Ic, IIc, IIac, IIa, IIb, and IIab.

Because of the different ATPase protocols, studies vary on how many fiber types each muscle holds (see reviews in [27, 30]). Some have delineated only two muscle fiber types (type I and all type II). Others have delineated up to six fiber types (I, Ic, IIc, IIa, IIab, and IIb) based on histochemical staining patterns. Therefore, delineating the type 2 subfibers using immunohistochemistry is challenging and consequently varied between studies. In Biceps Brachii (BB) muscle, for example, it was found four main fiber types and subtypes (I, IIb, IIa, and IIc) with different repartition ratios between superficial and deep muscle layers.

The Fig. 1.10 shows a histochemical appearance of different fiber types within the BB muscle. Based on their metabolic and physiologic characteristics cited above, human muscle fibers can generate force at the point of contraction and during a time relevant to its characteristics, where:

- Type I fibers (or Slow (S) fibers) are the fibers with the smallest diameter and generating the least force. They appear dark red in the histochemical study (see

Fig. 1.10) because they contain a large amount of myoglobin and blood capillaries. These fibers synthesize ATP mainly by the aerobic respiration of cells because they are also composed of large mitochondria. These fibers are considered slow because hydrolysis by the ATPase enzymes is slower than in type II fibers. Type I fibers slowly produce low force but are highly resistant to muscle fatigue and capable of providing prolonged activity and maintaining it for several hours. These fibers are mainly present in the muscles responsible for maintaining the posture;

- Type II fibers (or fast fibers) have a larger diameter than type I but have less myoglobin. Therefore, they have a clearer appearance in the histochemical study (see Fig. 1.10). In addition, the release of calcium by the SR takes place more rapidly as well as the hydrolysis of the ATPase enzymes. Within fast fibers, we can also differentiate two main types:
    1. Type IIa fibers (or FR fiber). They are similar in their composition to slow fibers and are more resistant to fatigue than other fast fibers;
    2. Type IIb fibers (or FF fibers). These fibers are the closest to the definition of fast fibers. They produce a lot of force very quickly but are very sensitive to muscle fatigue;
- The Fast Intermediate (FI) fibers: These fibers are called intermediate fibers because they are in their composition and characteristics in between the fibers. For example, IIc is between IIb and I, IIab is between IIa and IIb.

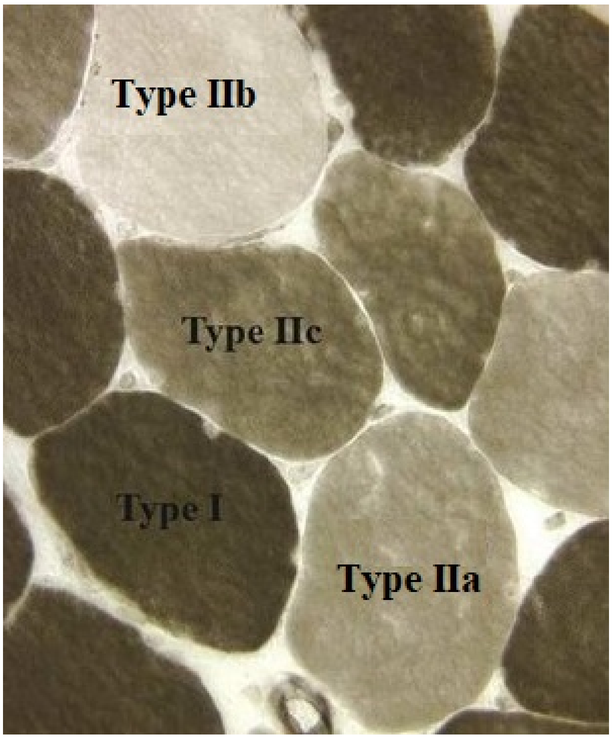

Figure 1.10: Histochemical appearance of different types of fiber in the skeletal muscle [31].

Differences in physiological, biochemical, histochemical, and force-generating characteristics of fibers are provided in Table 1.1 as a valuable base to distinguish between them.

The aging process affects these two-type fibers' functional, structural, and morphological behaviors. These age-related changes will be detailed in section 1.4.

Table 1.1: The main different types of fibers in skeletal muscle and their characteristics.

Characteristic	Type I	Type IIA	Type IIB
Alternative name	Slow oxidative Slow-twitch	Fast oxidative-glycolytic Fast-twitch A	Fast glycolytic Fast-twitch B
Metabolism	Oxidative (aerobic)	Oxidative and Glycolytic (combined)	Glycolytic (anaerobic)
Color	red	pink	white
Time to maximal contraction (ms)	100–200	50–80	50–80
Frequency to reach tetanic contraction (Hz/s)	16	60	60
Force-generating capacity	+	++	+++
Contraction velocity	+	++	+++
Diameter	+	++	+++
Myoglobin content	+++	++	+
Mitochondria density	+++	++	+
Fatigue resistance	+++	++	+
Generated force	+	++	+++
ATPase capacity	+	++	+++
Recruitment order	1st	2nd	3rd

1.3.2 Anatomy of the peripheral neural system

The skeletal muscles are non-functional without innervation. They are the effectors of the neural system and are muscles that are controlled voluntarily. In this thesis, we will focus on the control by the Peripheral Nervous System (PNS) of skeletal muscles. The PNS are made up of all neurons outside of the brain and spinal cord including long nerve fibers and ganglia formed of neural cell bodies. The PNS connects the CNS to various parts of the body. The functional classification of the PNS provides three subsystems/categories:

- Sensory nervous system: is carrying signals from the viscera, sense organs, muscles, bones and joints towards the CNS. Nerve fibers that carry this information are part of the afferent division. Sensory receptors can transduce a physical stimulus such as pressure, sound waves, electromagnetic radiation, or chemical composition into an electrochemical signal.

- Somatic nervous system: It controls the voluntary activation of skeletal muscles in the limbs, back, shoulders, neck, and face.

- Autonomic nervous system: is related to all the involuntary visceral activity of the body. It consists of the sympathetic and parasympathetic nervous systems, and their effector organs include cardiac muscle, smooth muscle, and various glands.

The first step in the contractile process is transmitting a signal to contract from a motor nerve of the somatic nervous system to a skeletal muscle fiber. This occurs at the Neuromuscular Junction (NMJ), a type of synapse between the terminal branch of a motor nerve fiber and a specialized region near the midpoint of a muscle fiber. Transmission of the neural signal in the PNS is realized through a neural action potential produced by an α-motoneuron (or somatic motor neuron) placed in the spinal cord and propagates along its axon surrounded by a thick myelin sheath. Each α-motoneuron innervates several fibers composing the targeting muscle. A muscle fiber can only be innervated by one α-motoneuron. This set of fibers innervated by the same α-motoneuron is called a Motor Unit (MU).

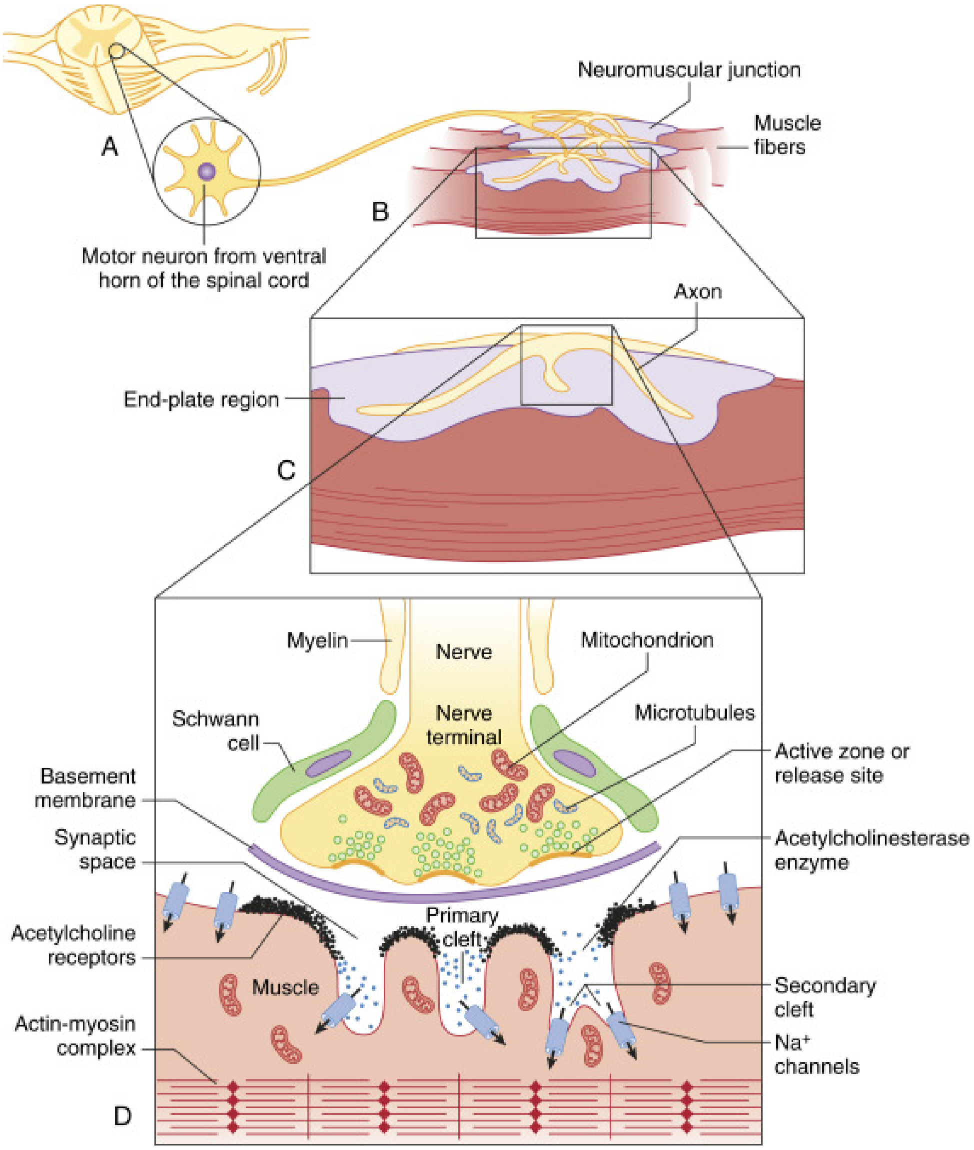

Figure 1.11: Description of the PNS and its communication with the muscular system. (A) Cell body of an α-motoneuron. (B) and (C) The synaptic description with its vesicles and ACh. Source: https://aneskey.com/neuromuscular-physiology-and-pharmacology

The NMJ is located around the middle of the muscle fibers. This position allows a quasi-simultaneous contraction of the whole muscular fiber. There is no direct contact between the synapse and the muscle fiber. The communication between these two cells is made through chemical processes. At the end of the axon, there are synaptic vesicles containing thousands of Acetylcholine (ACh) molecules. These ACh molecules are neurotransmitters that communicate with the fiber. The region of the fiber facing the axonal termination is called the motor end-plate. Each motor end-plate consists of several millions of ACh receivers. When a nerve firing arrives at the axonal termination, it causes a fiber contraction following several chemical phenomena. If a new nerve firing arrives at the NMJ, this chemical processing chain is repeated.

1.3.2.1 Motor unit: types and characteristics

Although we have been discussing fiber types, the true functional unit of the neuromuscular system is the motor unit. Because control of muscle is realized at the level of the MU, it seems important to consider the physiological properties of motor units (MUs) when attempting to understand and model muscle function decline during aging. The motor unit (MU) consists of a single α-motoneuron and all of the muscle fibers it innervates. It is the smallest functional component of the neuromuscular system. In mammals, most skeletal muscle fibers are innervated by α-motoneurons to generate movements. These α-motoneurons are clustered in columnar (spinal nuclei) called motor neuron pools (or motor nuclei), placed in the spinal (the ventral horn). Each motor neuron pool innervates one skeletal muscle. The α-motoneuron cells of each pool extend an axons that branch to form a NMJ at the site of innervation. Each fiber is innervated by one α-motoneuron. On the contrary, an α-motoneuron innervates many fibers.

All the muscle fibers within a MU have the same phenotypic characteristics (i.e., slow or fast, type I or type II) and are activated together in an all-or-none manner. Thus, as fiber types, motor units can be divided into groups based on the contractile and fatigue characteristics of the muscle fibers. Based on contractile speed, motor units are classified as either slow-twitch (MUS or MU-type I) or fast-twitch (MUF or MU-type II). The MUFs are further subdivided into fast-twitch fatigue-resistant (MUFR or MU-type IIa) and fast-twitch fatigable (MUFF or MU-type IIb), with an intermediate type: fast-twitch fatigue-intermediate (MUFI or MU-type IIc).

To not, there are no universal criteria distinguishing α-motoneuron subtypes. However, some trends are observed in terms of size, excitability, and firing pattern. Small α-motoneurons tend to have a smaller cell body diameter and thus a higher input resistance making them responsive to a lower Excitation Threshold (ETh). As a result, fibers of type S are recruited first during muscle contraction. Larger α-motoneurons are firing after the initial recruitment of small ones with a higher ETh, giving extra strength to the activated muscle [32]. The manner in which intact or denervated fiber induces motoneurons of the same type to connect or sprout is not well-known, although several factors are Highlighted. It is generally assumed that motoneuron axons can respond to neurotrophic factors and other chemicals by directional growth [33, 34, 35]. Nonetheless, it is not well-known if sprouts are actually stimulated by denervated muscle fibers to grow toward them [35, 36].

This thesis will employ two terms: the innervation ratio and the MU territory. The MU territory can be defined as "the subset area of the total muscle cross sectional area that encloses all the fibers belonging to a single motor unit" [37, 38] (see Fig. 1.12). A direct measure of the MU territory is not possible *in vivo* (expect one recent study [39], see section 1.5.1.1) and indirect approaches are used (e.g., in [37] based on sEMG technique).

For biceps brachii muscle, the MU territory has an estimated cross sectional area of 5-10 mm (ie, diameter) [40, 41]. The innervation ratio is the number of fibers per MU. It has an estimated value of 500-2000 fibers per one MU for large limb muscles [40]. Therefore, fibers of the same MU are rarely ever located immediately adjacent to one another (a few numbers compared to the MU territory). This ensures the distribution of forces across relatively large areas of muscle, and repetitive extracellular depolarization is less likely to be intense in any one area upon activation [42]. The MU territories and the innervation ratio for the BB muscle will be reviewed in chapter 3 with revealing the aging impact and reported modeling approaches.

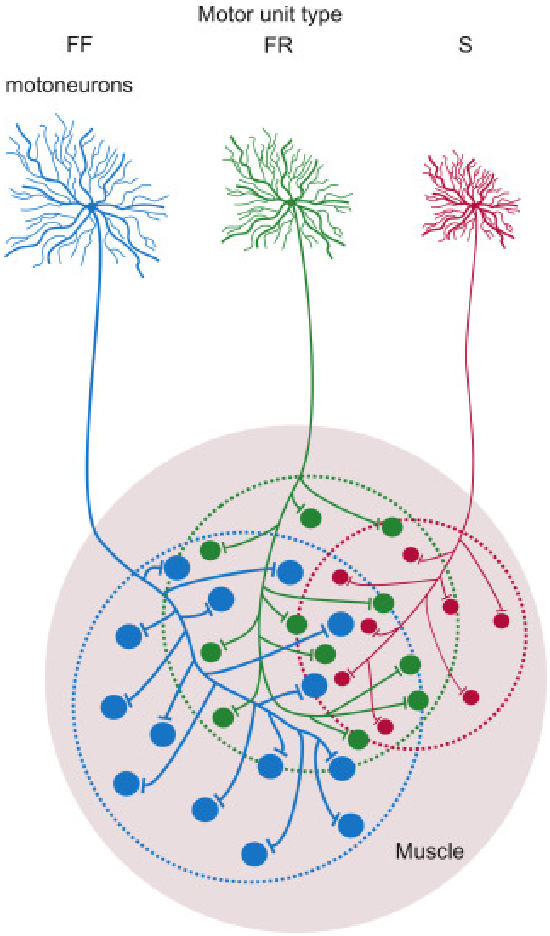

Figure 1.12: Territories of the three types of motor units. The scheme reflects the differences in the size of α-motoneuron cells, the MUs innervation ratios, The MUs territories, and the diameter of innervated muscle fibers. Recruitment order: from small (S) to larger (FF) MU/α-motoneurons.

1.3.2.2 Motor unit: Recruitment order

The force and electrical activity intensity increase according to the rise of the number of recruited MUs and the increase of their corresponding firing rate. The spatial recruitment of the MUs is modulated by the intensity of contraction and follow a rule called the "size principle" defined in [43]. The "size principle" assessed that during isometric contraction the recruitment of MUs is done through increasing the motoneuron size and thus, the MU size. Thus, MUs are recruited from the MU innervated by the smallest diameter motoneuron to the MU innervated by the highest diameter. Each MU is excited according to the goal of the contraction level, if the goal is below its intensity threshold, the MU is not recruited for this contraction. It has been assessed that the MU recruitment law describing the evolution of the MUs threshold according to contraction level is exponential [44]. Depending on the muscle characteristics, all the MUs are recruited for a contraction level varying between 60 and 90% of the Maximal Voluntary Contraction (MVC) [44]. Beyond this threshold, only increasing the MU firing rate can increase the generated force.

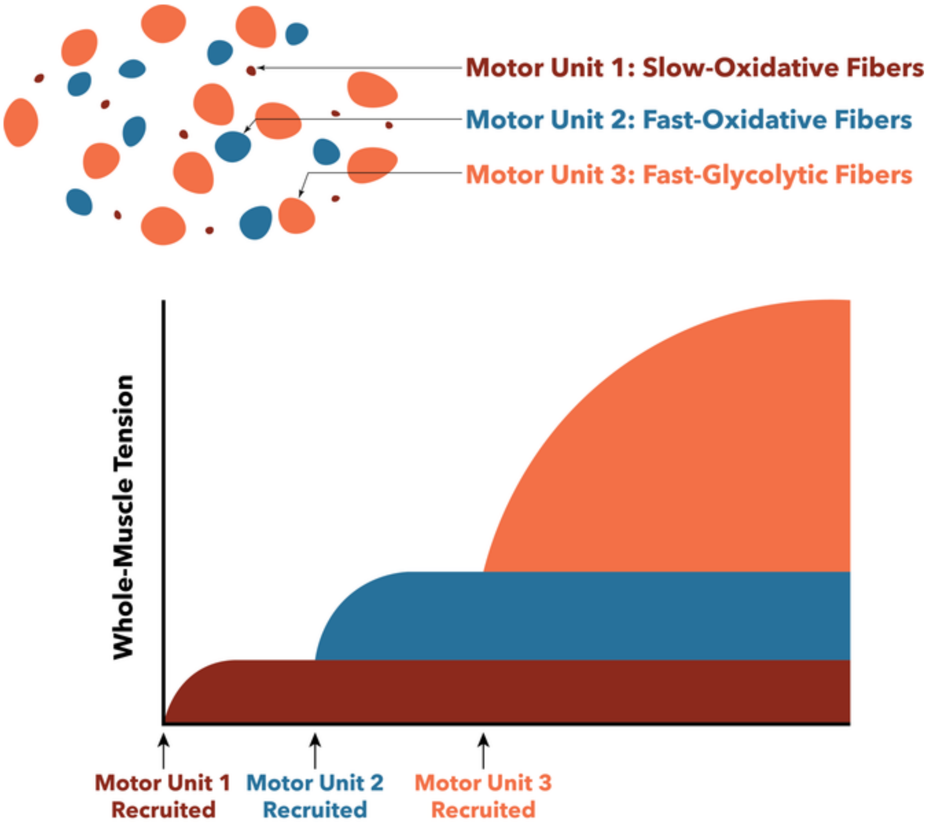

Figure 1.13: Illustrative scheme of motor unit recruitment. Source: www.stackprinter.com

1.3.3 Mechanisms of muscle contraction

Muscle cells are made to move and generate force. Mainly, four skeletal muscle characteristics lead to motion production: i) Excitability: is the capability of the muscle tissue to contract when stimulated by a voluntary or involuntary neural command; ii) Contractility: is the ability of the muscle tissue to respond to a stimulus by developing a tension; iii) Extensibility: refers to the ability of the muscle tissue to be stretched or increased in length; iv) Elasticity: refers to the ability of the muscle tissue to return to its resting state after being stretched.

There are two modalities of muscle contraction [45]: dynamic (isotonic, isokinetic, auxotonic, and plyometric) and static (isometric). It can be separated into concentric (positive phase: the muscle shortens, creating tension) and eccentric (negative phase: the muscle stretches, developing tension) contractions when a muscle changes its length by moving a constant load shortening phase. Isokinetic contraction occurs when the muscle exerts maximum effort across the whole range of motion while contracting consistently. With muscular shortening, the amount of auxiliary contraction rises. An explosive concentric contraction preceded by an eccentric contraction is referred to as a plyometric contraction. When a muscle contracts isometrically, it does so without changing its length and hence without moving the burden.

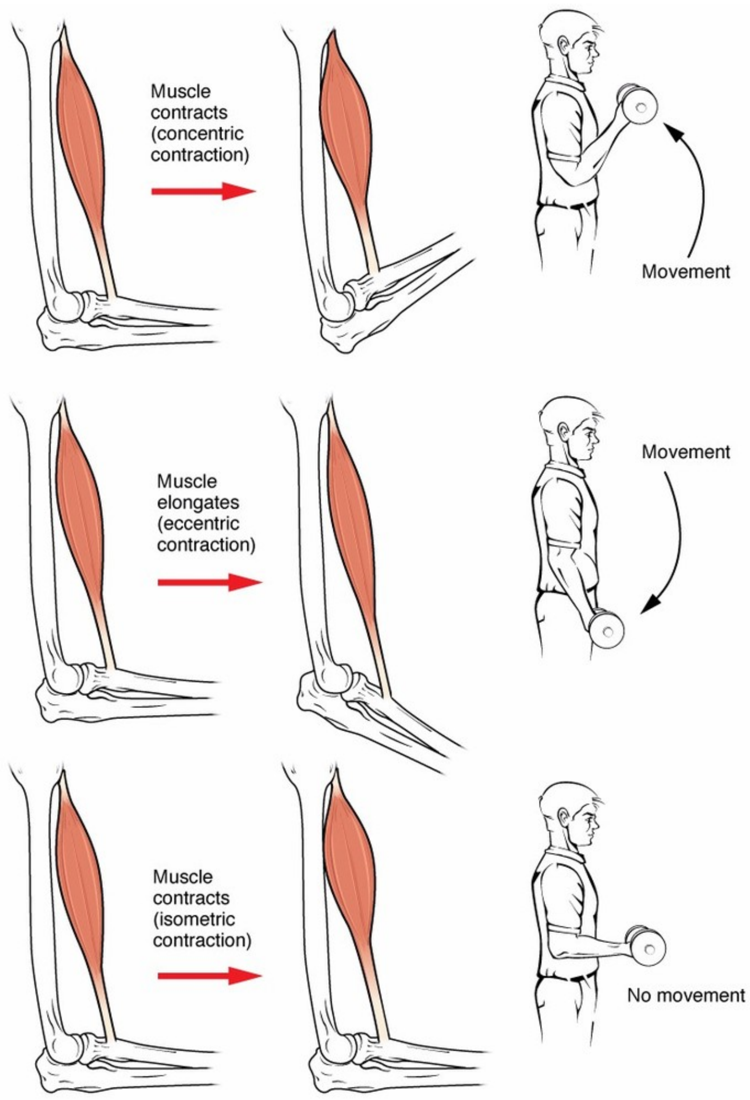

Figure 1.14: An isotonic concentric contraction results in the muscle shortening, an isotonic eccentric contraction results in the muscle lengthening. During an isometric contraction the muscle is under tension but neither shortens nor lengthens. Source: Structure and Function of the Body. 14th ed. St. Louis, MO: Elsevier; 2012

Considering the complexity of the muscle contraction nature and the specified underlying processes interacting for each contraction, we decided to focus on modeling the skeletal muscle during voluntary, isometric, and non-fatiguing contractions.

1.3.3.1 Electrical mechanism

The action potential is an 'all-or-nothing' event: it does not occur if the triggering input is less than a threshold value. The action potential, once triggered, has a well-defined amplitude and duration. Action Potential (AP) propagation allows rapid signaling within excitable cells over relatively long distances. In most respects, the electrogenesis of the APs in nerve axons and skeletal muscle fibers is quite similar, from the fact that both are long fibers and have very brief, and fast-rising APs [46]. However, skeletal muscle fibers have an extensive internal transverse tubular system formed by periodic tubules of the surface cell membrane (Fig. 1.11 (D)) that propagate excitation from the cell surface into the deep interior of the fiber for purposes of electrical-mechanical coupling. The muscle fiber excitation can be explained by the model of a semi-permeable membrane describing the electrical properties of the sarcolemma. The ionic balance between the inside and outside of a fiber cell produces a resting action potential potential (approximately -70 to -80 mV). This potential difference, which is maintained by physiological processes (ion pump), leads to a negative intracellular charge compared to the external medium. The activation of an α-motoneuron causes conduction of excitation along the motoneuron axon. A motor end-plate potential is produced on the muscle fiber membrane innervated by this *alpha*-motoneuron after acetylcholine is released into the synaptic cleft. The diffusion characteristics of the muscle fiber membrane are briefly changed, and Na^+ ions enter. If a threshold level is exceeded, depolarization of the membrane causes an action potential (AP), and the potential difference changes rapidly from - 70 mV to +40 mV (Fig. 1.15). A monopolar electrical burst is immediately followed by a repolarization phase, at which Na^+ channels close and those of K^+ open. Then a period of hyperpolarization of the membrane occurs: AP becomes more negative than the resting action potential. The hyperpolarization phase is the consequence of the slow gradual closure of the voltage-gated K^+ channels, which results in the membrane being briefly more permeable to K^+ than at the resting action potential.

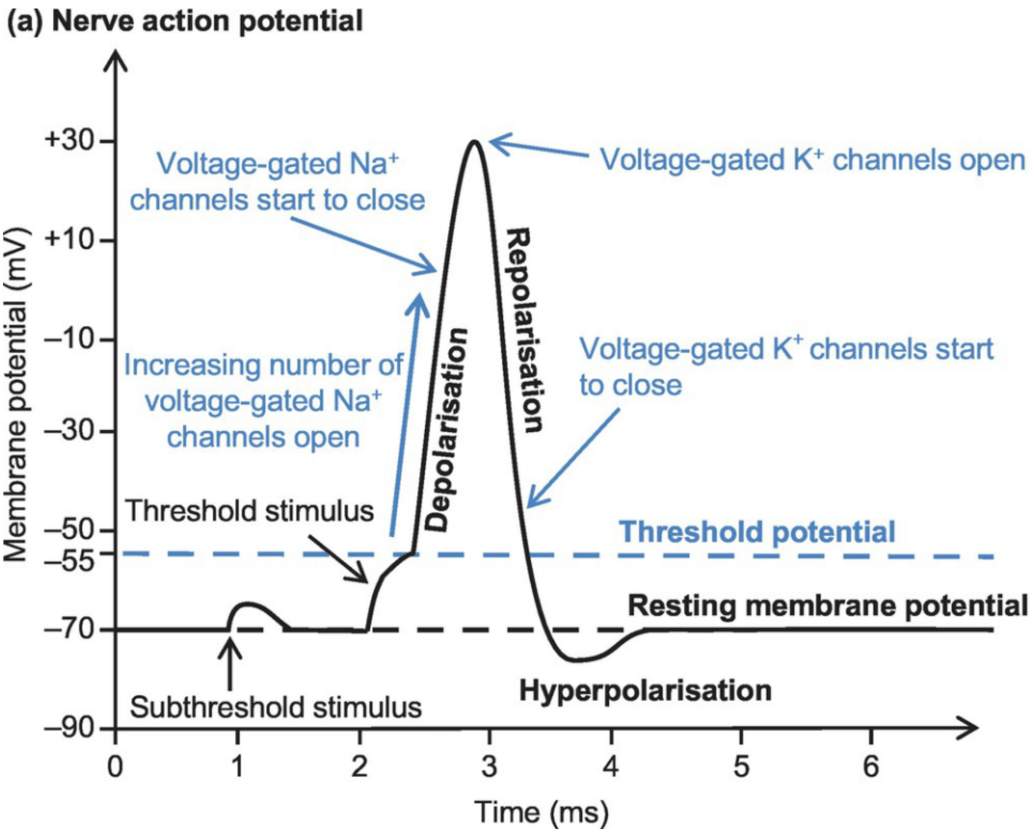

Figure 1.15: Typical membrane action potential. Source: www.aneskey.com/

As mentioned above, an α-motoneuron innervates several fibers forming a MU. When a neural firing reaches the NMJ of the fiber, it generates Single Fiber Action Potential (SFAP). The SFAP is propagated down the muscle fiber in both directions from the end-plate with a constant velocity of about 5 $m.s^-1$ over the surface sarcolemma. The electromyogram (EMG) can be recorded from the skin covering an active skeletal muscle because external longitudinal currents can use the full fiber interstitial fluid space (because current follows the path of least resistance) [46]. Thus, the amplitude of the EMG potentials becomes larger when more fibers within the muscle are activated (fiber summation) because of the summation of SFAP of all activated fibers. The frequency of EMG potentials represents the muscle's activation frequency and asynchrony. Moreover, because fiber recruitment depends upon the α-motoneuron recruitment, we can define a Motor Unit Action Potential (MUAP) corresponding to the sum of the SFAP generated by its corresponding fibers. This MUAP is correlated with the phenotypic characteristics of fibers and MUs (see sections 1.3.2.1 and 1.3.1.5). In addition, the morphological, structural, and electrical properties of media through the MUAP is propagating (muscle, blood vessel, adipose, and skin tissues), known as the conductor volume, have an (age-related) effect on the electrical signal recorded at the skin. These effects, and the manner of modeling sEMG, will be detailed in the section.

1.3.3.2 Mechanical mechanism

The study [47] has established the concept of interaction between actin and myosin from microscopy of single frog muscle fibers and proposed the most prevalent theory regarding muscle contraction in 1957. Since this theory was enhanced, other mechanisms/theories were added to explain the muscle contraction (see review in [48]). The mechanism of muscle contraction is based on the theory of the sliding filament [47] and the cross-bridge cycle. To understand this theory, we will follow the path of the electrical signal emitted by the α-motoneuron as a Action Potential (AP), and its transformation to a chemical signal in the NMJ synapse before coming forward as the mechanical response at the muscle fibers. The arrival of α-motoneuron AP at the axon's terminal initiates a calcium ion $Ca2+$ influx in the presynaptic terminal, resulting in the release of the neurotransmitter acetylcholine (ACh). Then, the ACh binds to the sarcolemma receptors, which induces the opening of ion channels. Thus, Sodium (Na^{2+}) ions enter, and Potassium (K^{+}) ions exit the muscle fiber. This variation in the ion concentrations changes the membrane potential (endplate potential), which causes the depolarization of the membrane and the propagation of the AP at the sarcolemma. The action potential from sarcolemma spreads to the interior of the muscle fiber through T tubules where the voltage-sensitive proteins lead to the opening of Ca^{2+} channels and the releasing of Ca^{2+} in the sarcoplasmic reticulum. Thus, the Ca^{2+} ions concentration in the sarcoplasmic reticulum increases, and the Ca^{2+} ions start to bind to the troponin C of the actin filaments. The troponin then removes the tropomyosin present at the actin-binding sites. Once these sites are free, the contraction cycle begins and is repeated until tropomyosin returns to attach to these sites. This phenomenon of pairing an electrical event with a mechanical event is called Excitation Contraction Coupling (ETC). A cross-bridge cycle is the sequence of events that occur during the interaction between myosin cross-bridges and actin molecules. During each cycle, the cross-bridge (myosin head) attaches to a thin filament causing displacement of thick filament over thin filament followed by detachment of myosin head in a repetitive fashion. ATP is required during the cycle; for the movement of the cross bridge as well as for its detachment. However, all the cross-bridges do not go through the same phase at any instant during a cycle. This helps in a smooth and sustained contraction.

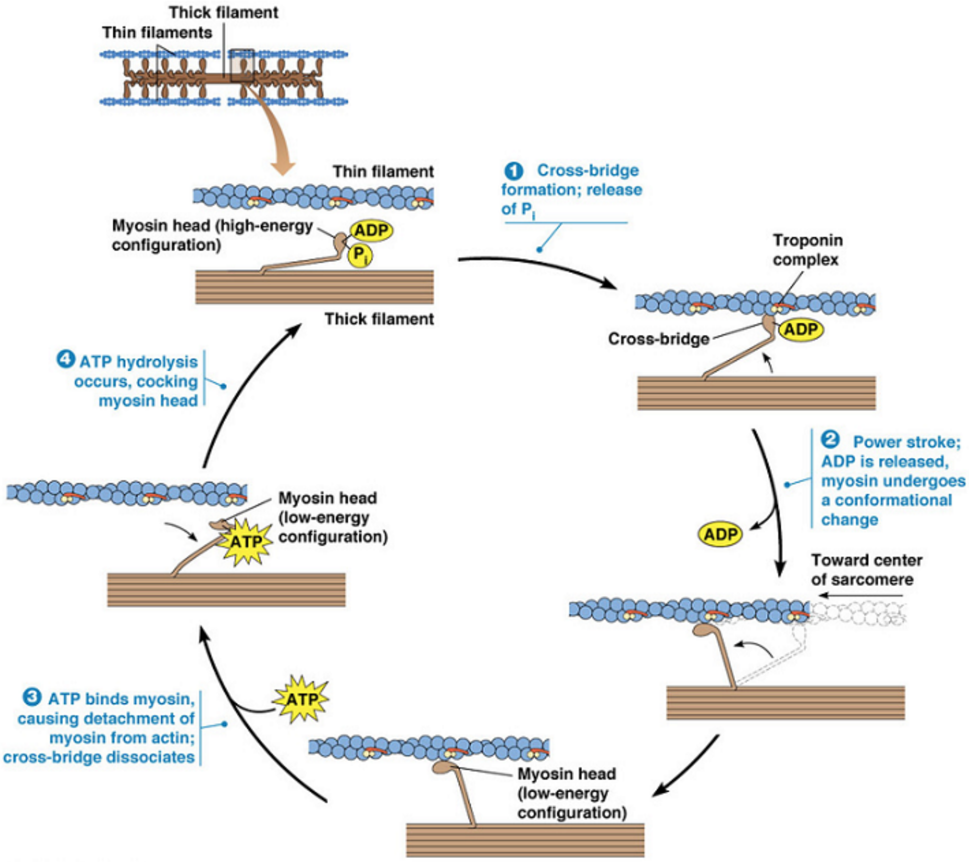

Figure 1.16: The cross-bridge muscle contraction cycle, which is triggered by Ca^2+ binding to the actin active site. With each contraction cycle, actin moves relative to myosin (image from Pearson education, Inc 2005).

1.4 The neuromuscular system: age-related changes

The aging-related decline of muscle functions involves quantitative and qualitative changes in skeletal muscle structure and function. This process is typically slow, and the functional loss varies significantly among individuals but is observed in all humans (i.e., also in healthy, well-nourished, and physically active individuals)[49].

1.4.1 Effects of aging on muscle morphology and physiology

1.4.1.1 Muscle mass changes

Aging is a process where the balance between damaging and repairing body cells becomes defective and slow. The skeletal muscle mass is regulated by the dynamic balance between muscle protein synthesis and muscle protein breakdown [50]. Aging impacts this protein synthesis balance and leads to progressive loss of muscle mass. Age-related muscle mass loss is observed in all humans. Only the rate of this loss varies among individuals. Factors such as healthy nutrition or physical activity can flatten the aging muscle mass loss curve. Many studies have qualified and quantified the impact of these lifestyle factors on muscle mass during aging [51, 52, 53, 54, 55, 56]. Beyond these environmental factors, this thesis will focus only on reporting the "standard" behavior and rate of muscle mass loss during aging for healthy subjects. In fact, muscle mass loss is an insightful parameter. It is correlated to Cross-Sectional Area (CSA), which is essential for the definition of muscle structure and morphology when modeling. Indeed, it is necessary to define the amount and sizes of fibers, MU territories, fat tissue distribution, and other muscle characteristics, which are helpful for reliable muscle models. Moreover, many age-related diseases, such as Sarcopenia, use this parameter as a criterion in diagnosis [57]. Several studies have attempted to assess the rate of skeletal muscle deterioration [58, 59, 60, 61]. These quantifications are made mathematically by qualifying the mass muscle decline as a uniform process that starts at the completion of growth [62]. Hence, all studies cited above recall data models to estimate muscle mass loss without considering the structure and the process of the system's functioning. For this reason, these studies deliver limited information on how the tissue compartment develops across the lifespan. This thesis will recall these aging data models with a distinctive feature: they will be incorporated into system models for more informative results (more details in section and chapter). These studies estimate that the loss of muscle mass by age 18–80 years ranges from 8 to 49%. Moreover, several studies share the mutual aspect of these declines:

- Aspect 1: Declines were detectable after the age of 40 years approximately;
- Aspect 2: Declines are accentuated for men than for women;
- Aspect 3: Declines are greater in the lower limbs compared to the upper limbs;
- Aspect 4: Declines rate increases and becomes much higher for very elderly people;

The table 1.2 shows an illustration of these aspects with reported data of mass muscle decline during aging. For more detailed data, see [63]. The study [63] enumerated the reasons contributing to the differences between studies and reported data, such as the techniques of measurement, the characteristics of the sample studied, and the data model assumptions.

Table 1.2: Illustration of reported muscle mass decline during aging. (*) BSMM: Body Skeletal Muscle Mass

Study	Technique	Measured variable	Gender	Younger age	Elder age	Decline (%)	Decline/yr (%)
[61]	Magnetic resonance imaging	BSMM* BSMM* Lower BSMM* Upper BSMM*	M F	18–29 18–29	>70 >70	-18 -17 -25 -5,6	NC
[64]	Cadaveric dissection	Vastus lateralis CSA	M	19 ± 3	73 ± 2	-26	−0.48
[64]	Cadaveric dissection	Vastus lateralis CSA	M	73 ± 3	82 ± 1	−23	−2.6

We will not discuss these reasons or the discrepancies in mass muscle decline ranges reported in the literature in this thesis. The valuable information for our study is the behavior of this decline (the four aspects cited above) and the correlation between these aspects and the decline in muscle functions. In fact, the findings of these studies are correlated with results of other studies reporting a decline in muscle force/strength since the same approximate age [65, 66, 67]. The Fig. 1.17 shows similarities between curves (behavior and rate) of muscle mass loss and strength loss. This correlation agrees with several studies reporting that the loss in muscle mass is the primary determinant of the age-related decline in muscle strength [68, 69, 70], e.g, the correlation between arm muscle mass and biceps muscle strength was 0.60 ($r^2 = 36\%$, $p < .001$) in men and 0.48 ($r^2 = 23\%$, $p < .001$) in women in [70].

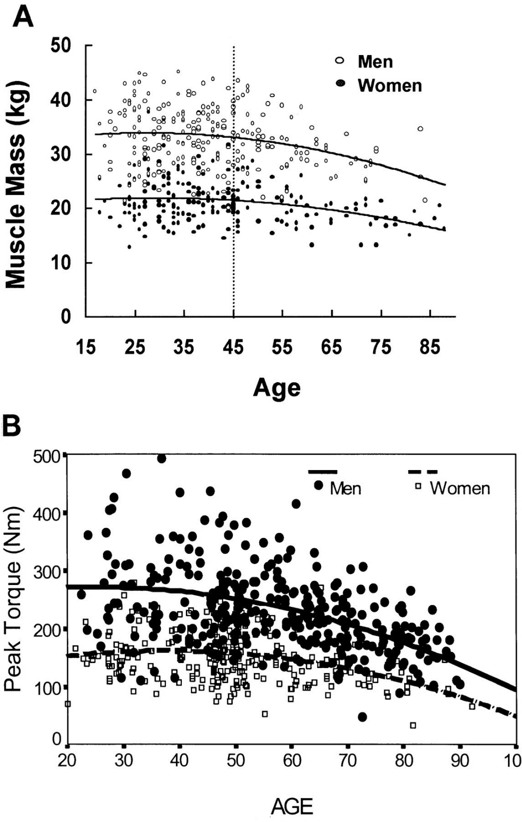

Figure 1.17: (A) The age-related muscle mass loss for men and women as depicted in ([61]; Data of 468 men and women aged between 18 and 88 years old are figured in white and black marks respectively. (B) The age-related differences in peak torque of knee extensors at slow velocity as depicted in [67]; Data of 346 men and 308 women aged between 20 and 93 years old are figured in black and white marks respectively.

In addition to its correlation with muscle strength, the loss of muscle mass can be useful, with mathematical models, in elucidating other morphological and structural changes of muscle with aging at the fiber and motor unit scale.

1.4.1.2 Fiber scale changes

As mentioned in the previous paragraph, aging triggers a general decline in muscle mass in approximately the third or fourth decade. This decline accelerates in the sixth decade [64]. This has been attributed to two leading causes: a reduction in muscle fiber size (atrophy) and/or a reduction in their number (hypoplasia). However, numerous studies have found that type I and type II fibers are lost in almost similar numbers [71, 72]. Other studies [73], have reported an accentuated loss of type II between 25 years and the end of the seventh decade, whereas loss of type I is mainly apparent from the eighth decade onwards.

On the contrary to the discrepancy in fiber number decrease between fiber types, studies have the same agreement that the reduction of size is mostly of type II fibers in all studies [64, 74]. Given the large gap between powers generated by type I (slow, oxidative), type IIa (fast, oxidative), and type IIb (fast, glycolytic) fibers [52], the type II atrophy is the most important contributor to muscle weakness during aging [74, 33, 73]. This leads to dependence, fall risks (first cause of mortality in the aged population), and reduced quality of life for elderly people [75]. To note, the effect of aging seems to be different in different muscle groups [76, 77]. This thesis aims to study the BB muscle. We observe that the gap between the number of fibers for young and elderly people is between 7% and 10% [78] for BB muscle. The studies [79, 80] have reported a decrease of 15% to 30% in the number of fibers type IIb for the same muscle. This loss can reach 55% of the number of the total fibers for other muscles [78, 50]. This decline could be attributed to type II fibers being more susceptible to apoptosis (denaturation of mitochondria or stem cells) or "the fast-to-slow" fiber type transformation (accentuated during aging). For the fiber sizes, which are more impacted by the aging process, the attenuation of the type II fiber area for BB muscle is equal to -24% between aged and young men [78]. This attenuation of fiber area can reach around -30% for ages >74 to 88 [81]. Moreover, we observe in the literature that this decrease of the fiber sizes is most accented in lower limbs than upper limbs. It was reported a decrease of 42% of type II fiber sizes in lower limbs [82]. To note, few studies in the literature have reported the number and size of fibers for BB muscle, and much more rarely for different subject categories (young, elder, male, and female). We will try, in chapter 3, to collect all available data for this muscle to build an aging model for atrophy and hypoplasia at a fiber scale. Next to atrophy and reduction of numbers, we would simulate fiber grouping during aging and changes in fiber type distribution. These two aspects modify the structure and quality of muscle in the aging process. Although a preferential loss of type II fibers may not be accurate, a transition of fast-twitch muscle fibers to take on slow-twitch characteristics appears to be pertinent during aging and can lead to fiber grouping [83].

Fiber type grouping with aging is an age-related characteristic early reported is [72, 82]. A fiber-type group is a collection of fibers that includes at least one enclosed fiber [84]. However, the leading causes of this phenomenon are yet unclear. The two main causes are reported:

- The fast-to-slow fiber type transformation: Muscle fibers are dynamic structures capable of altering their phenotype (MyHC) in sequential and reversible transitions from slow-to-fast types or fast-to-slow types, under various conditions, e.g., increased or decreased neuromuscular activity, mechanical loading or unloading, altered hormonal profiles (especially of the thyroid hormones). However, during aging, All these conditions are present and more featured, which leads to accentuating the fiber type transformation in non-reversible transition: mostly from slow-to-fast types [83, 85].

- The denervation–reinnervation cycles of fibers in muscle increases the fiber type clustering and, as consequence, to type grouping seen in aging muscle [72, 86]. The alterations of denervation–reinnervation cycles during aging will be discussed with more details in the section 1.4.1.3.

The Fig. 1.18 outlines the estimated fibers age-related changes (loss of fibers, atrophy, fiber-type grouping) of the Vastus Laterlis (VL) muscle. Medical imaging techniques are an important tool to reveal these fiber transitions and changes in proportions (Fig. 1.18). However, it is also interesting to quantify these changes by measuring the rate of expression of MyHC isoforms, the major contractile protein in skeletal muscle.
In addition, the rate of this expression can be correlated to the reduction in excitation-contraction coupling [73]. To note, the reduction in excitation-contraction coupling may also be the result of a decline in the function of dihydropyridine receptors leading to reduced Ca^{2+} release by the sarcoplasmic reticulum. In fact, the changes in function and volume of the sarcoplasmic reticulum can lead to a decrease in the shortening velocity of type II fibers [33]. However, for type I fibers, this decrease appears to be mainly the result of changes in the properties of the myosin protein [87].
In addition, the loss of specific tension may be due to a reduction in single fiber force per cross-sectional area [88]. The loss of power and force development during fast and explosive actions might be explained by an additional decrease in the maximal contraction velocity of the muscle fibers, next to the decreased force potential [89]. Because the muscle fibers take on the characteristics of the nerves that innervate them, we can assume that changes in MyHC composition result from changes in neural drive [90], which will be described in the following section.

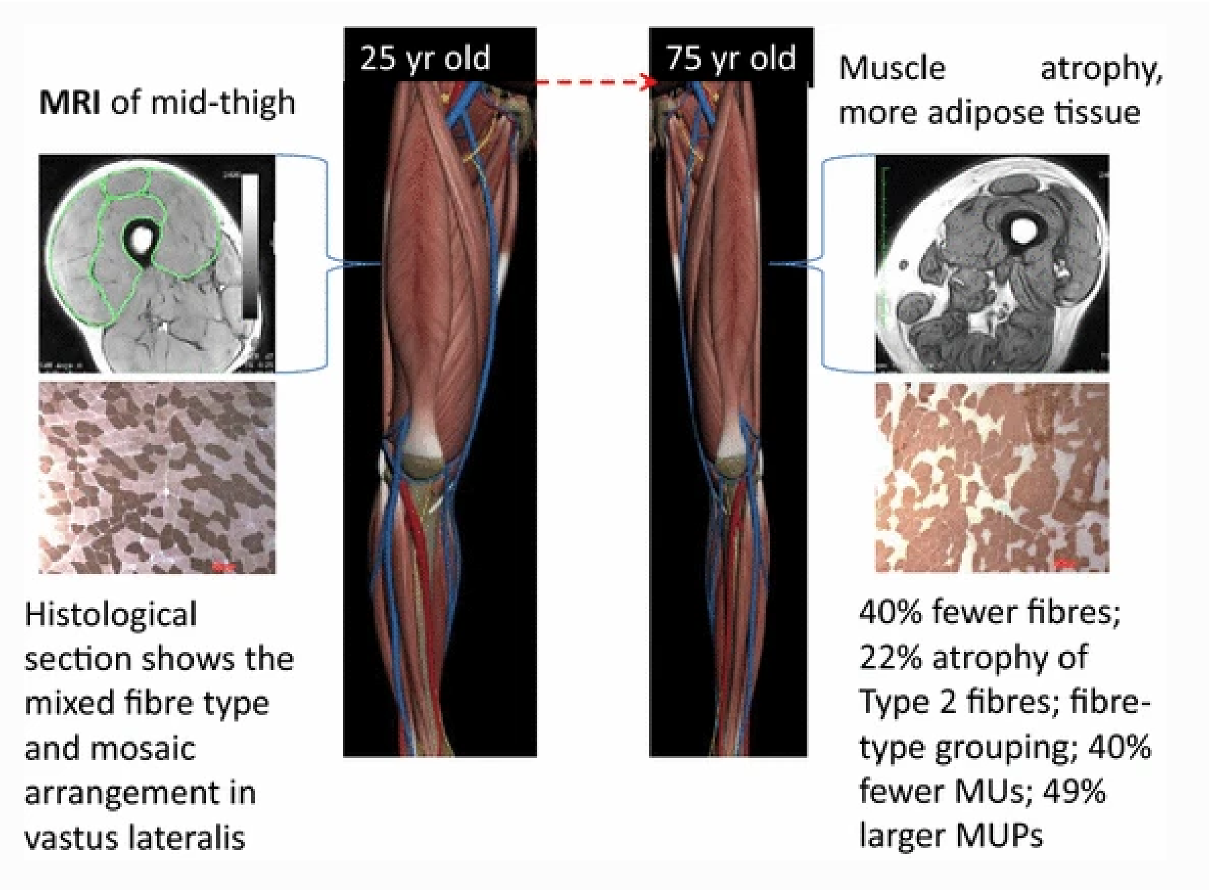

Figure 1.18: Healthy lower muscles for young and old man. A 75-year-old man with normal appendicular lean mass has a 15% lower appendicular lean mass [91]; 30% smaller knee extensor muscles [92]; 35% lower knee extension strength [91] and 35% lower leg power [93]; The VL has 20–40% fewer muscular fibers, fiber-type clustering, and tiny, angular fibers [64, 72].

1.4.1.3 Motor unit scale changes

The α-motoneuron is the musculoskeletal system's final common pathway for translating all synaptic inputs into the motor function. Aging is escorted by a significant loss of motor units [94, 95], a neuromuscular junction (NMJ) deterioration [96], and a changes of the morphology and properties of existing motor units [86, 97]. In order to know how the MUs change with aging, it is necessary to have methodologies to assess their numbers, characteristics, and functions.

There are no techniques currently available to directly count MUs in healthy humans, so efforts have been restricted to post-mortem anatomical estimates (rare studies, e.g., [95]) or Electromyography (EMG). EMG enables detailed investigations of MU function and recruitment patterns as well as estimation of their numbers in individual muscles. The range of techniques available to estimate MU numbers using EMG in humans has been reviewed [98, 99]. However, these methods should be viewed as an index rather than an accurate anatomical count.

We observe, through these studies, that the number of motor units has been found to remain almost constant till the age of 60 years but rapidly declines after that with variable reported rates [97]. As a representative example, we report a decline of around 30% to 50% in the lumber spine muscle of older (>60 years) was reported in [95] (anatomical count) compared with younger adults; A decline from 150 MUs (estimated with sEMG technique) for young adults (∼25 years), to 91 MUs for old adult (∼65 years), to 59 MUs for very old adult (>80 years)[100]; People aged over 75 years had fewer than 50% of the MUs compared with young, and some of the very oldest subjects apparently had fewer than 10% of their MUs remaining [97].

In the chapter 3, we will review the loss of MUs for the BB muscle in order to model this age-related mechanism. Of note, these mentioned studies have been conducted in healthy older adults, which demonstrates that neuromuscular remodeling is, to some degree, an unavoidable physiological consequence of aging. In fact, The loss of MUs leaves the muscle fibers within the MU denervated, but some are "rescued" by sprouting of nearby neuron branches. The reinnervation process increases fiber density (or innervation ratio) and territories of rescued MUs (see Fig.1.19). Which leads to enlarge MU action potential (MUAP) area [101, 102] (see Fig. 1.20).

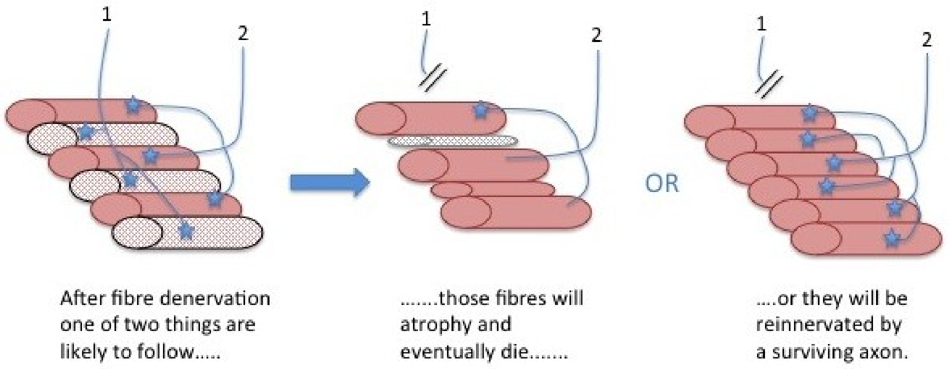

Figure 1.19: Motor unit remodeling during the normal aging process includes loss of α-motoneurons and enlargement of the surviving motor units. The denervated muscle fibers may atrophy and die (middle image) or be reinnervated by nearby motor nerve axon branches. They adopt the same phenotypic traits as the motor unit's existing fibers (right image). Source: www.motorimpairment.neura.edu.au

This enlargement of MUAP area is around of 26 to 41% for healthy older men [102] (see Fig.1.20). In addition, MU loss was stated as a cause of muscle weakness. The Maximal Voluntary Contraction (MVC) force reported in the same study [102], shows a decline of 34 to 39% for these older subjects.

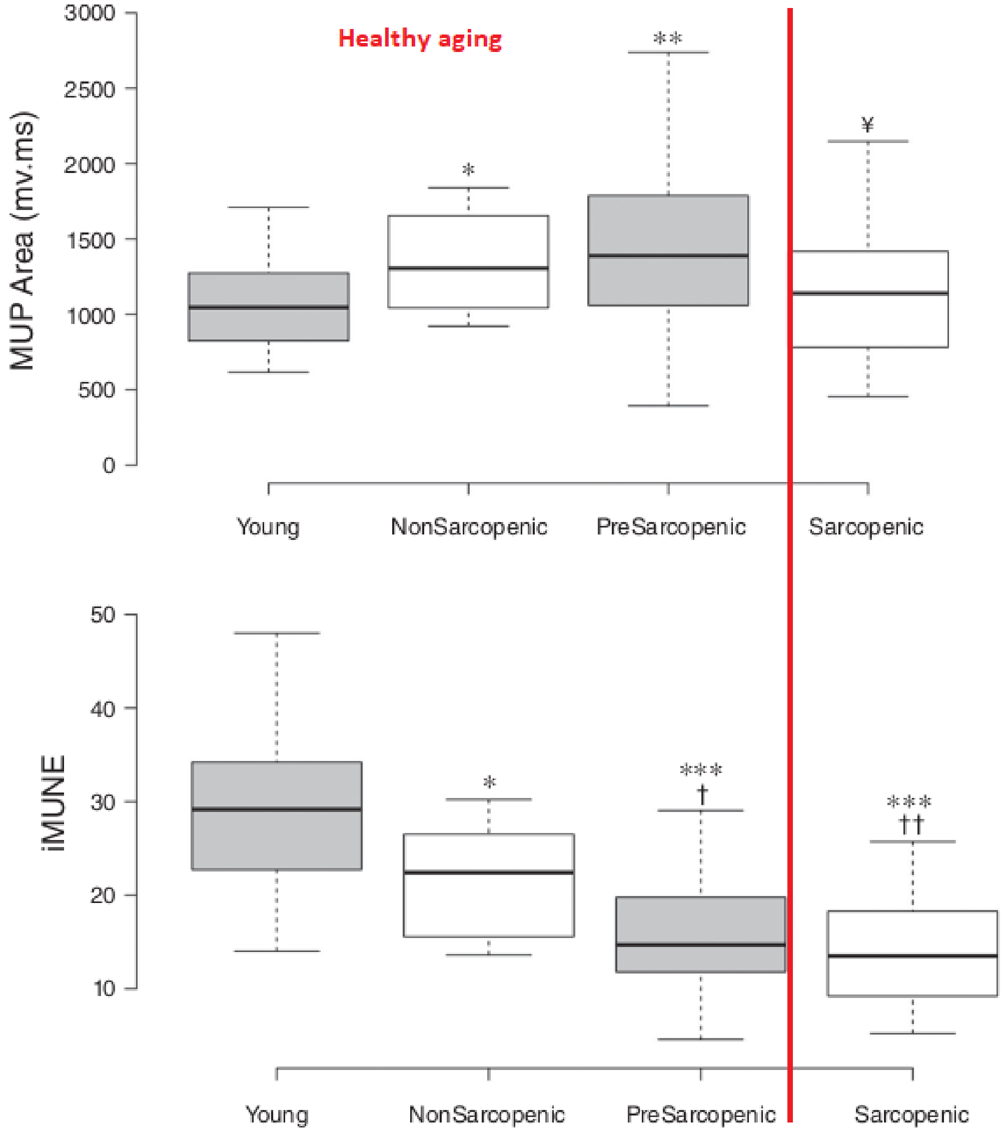

Figure 1.20: (Upper) Muscle motor unit action potential size (MUP Area, named MUAP in this study), and (Lower) iMUNE values (MUs number) in different stages of aging (vastus lateralis muscle). Image adapted from [102].

However, MU remodeling remains unclear whether any particular MUs, small or large, are preferentially lost or which are enlarged during normal aging. The fiber grouping described in paragraph 1.4.1.2 appears as a consequence of MU remodeling during aging. This leads to the estimate that fast MUs are more impacted by the failure of the denervation–reinnervation cycle during aging (Loss of number and expansion of areas).
In this thesis, when modeling the age-related changes at the MU scale, we will focus on the death rate of MUs and the changes in their sizes (innervation ratio and territory areas) within the muscle.

1.4.1.4 Neural drive changes

The nervous system is affected by age at multiple levels [103]. To start, aging is accompanied by decreased supraspinal drive generated from the cortex [104]. Further, a decline in the number of α-motoneurons with a preferential loss of α-motoneuron that supply fast motor units are apparent in the spinal cord together with losses and changes in the properties of peripheral nerves [83, 105]. Reduced spinal α-motoneuron excitability and increased pre- and post-synaptic spinal inhibition can lead to a reduction in peripheral nerve conduction speed with aging [106]. At the neuromuscular junction, the number of axon terminals [107], and synaptic vesicles are reduced with aging [108]. On the other hand, age-related increases in the number of axon terminals through sprouting and branching and increases in the number of neurotransmitters have been reported [109]. The latter may explain the adaptive mechanism of motor units that re-innervate de-innervated muscle fibers (see section 1.4.1.2). As a result of changes in the nervous system, fine motor control is impaired with aging. The magnitude of neural activation depends on the number of motor units that are activated (i.e., MU recruitment) and the rates at which the α-motoneurons discharge the action potentials (i.e., MU discharge rate or MU firing frequency) [110]. To evaluate these neural deficits, previous research has been using needle electromyography by investigating the additional force when delivering a supramaximal electrical stimulus to a nerve or muscle during a maximal voluntary contraction (e.g., in [94]).

In this way, the reduced neural drive in the older adults was presented by the reduced ability to voluntarily activate their quadriceps muscles compared to younger adults [111, 112] (i.e., reduced recruitment threshold, see Fig. 1.21(a)). In addition, a reduction in MU doublets [113], which can be described as two consecutive motor unit discharges that occur with short interspike intervals, and maximal MU discharge rate [114] have been shown to be reduced at an older age (see Fig. 1.21(b)). As an alternative to needle electromyography techniques, surface electromyography (sEMG), which is a non-invasive method, has been used to monitor changes in overall neural activation. Using the sEMG technique, the reduction of the recruitment threshold and firing rate with aging was confirmed by many studies (e.g., in [115, 116]). Moreover, it was observed that MU recruitment is compressed towards lower forces [117, 115]. This shift may be observed due to a selective loss of high threshold motor units (faster MUs). This concept supported the hypothesis that the decrease in the number of fast MUs with aging is more significant than the decrease of slow MUs (see the previous paragraph). This reduced recruitment suggests that a more significant proportion of the force capacity of the muscle arises from changes in discharge rate. However, maximal discharge rates are also reduced (see Fig. 1.21(b)). This fact suggested that a change in the contractile properties of old adult muscle fibers enhances the ability of force generation at lower discharge rates [118]. However, it has been suggested that sEMG signals may be biased towards high threshold motor units [115]. In reality, studies have shown that rapid muscle fibers (innervated by large, high threshold motor neurons) are likely to be found near the skin's surface (e.g., the location of BB muscle fibers in [119]). Thus, if surface fibers previously innervated by high threshold motor neurons become reinnervated by low threshold motor neurons, this might suggest that the sEMG signal in older adults reflects a more outstanding balance of motor unit types. Potential age-related and experimental differences between groups may have also affected these results (e.g., subcutaneous and intramuscular fat, electrode positioning, etc.).

To not, the discharge rate of MUs during isometric contractions exhibits a degree of variability. At low discharge rates (long interspike intervals), the standard deviation of discharge rate is high and declines as the discharge rate increases. When discharge variability is normalized to the mean interspike interval (coefficient of variation), discharge variability is highest at recruitment. Subsequently, it drops off as force increases above recruitment [120] (the shape of the interspike interval histogram can be used to characterize MU discharge variability). Some studies have reported greater discharge variability in old adults (e.g., in [121]). Changes in the amount of discharge variability have implications for altering the performance of the motor system in regards to maintaining a constant force [121, 120].

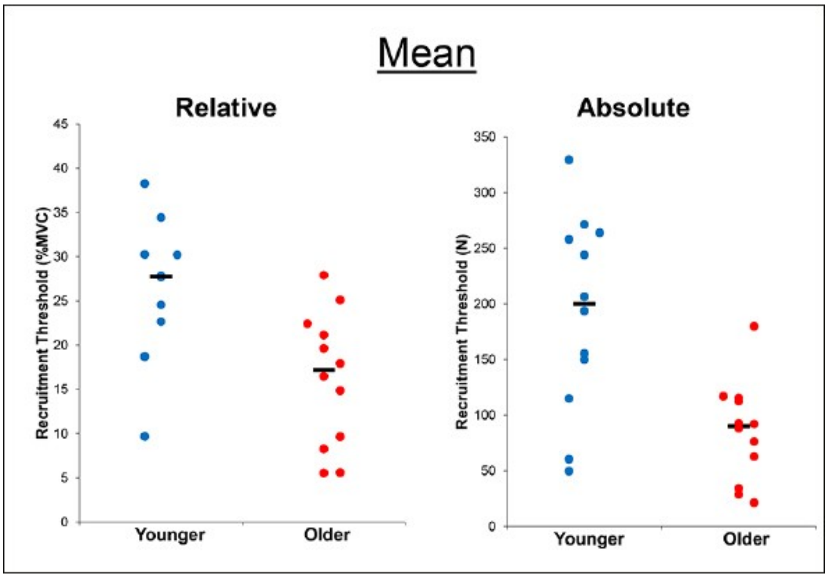

(a)

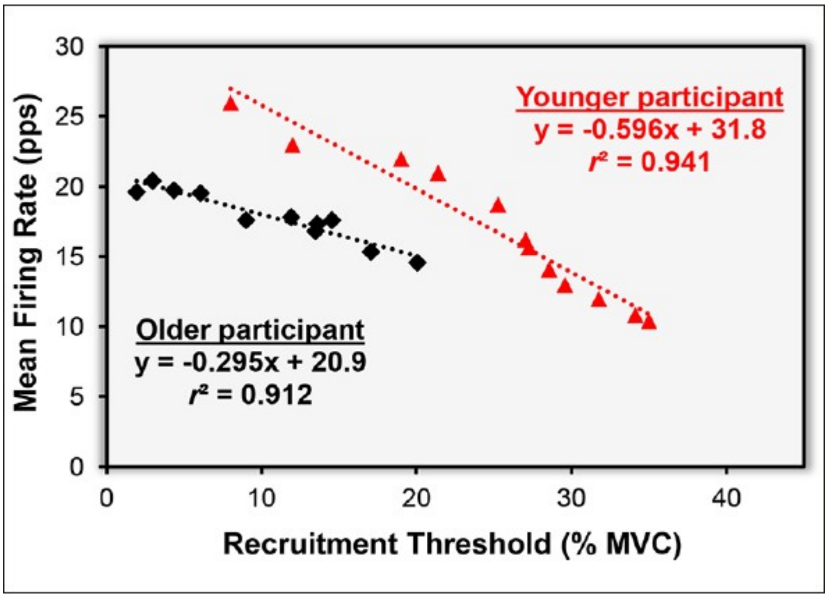

(b)

Figure 1.21: (a) The mean recruitment threshold expressed in relative and absolute terms for both younger and older men (estimated from EMG decomposition) [115]. (b) The mean firing rate versus the recruitment threshold relationship in one younger and one older man [115].

1.4.1.5 Inter and Intramuscular fat changes

Our understanding of the role of adipose tissue organs has quickly expanded during the last two decades. Fat tissue is no longer an inactive calorie storage area. Adipose cells have been shown to express and secrete a variety of hormones and proinflammatory cytokines, which operate in an autocrine, paracrine, and endocrine manner to signal the heart, musculoskeletal, central neurological, and metabolic systems [122]. It was observed that the increase of adipose tissue ratio is associated with the decrease in strength and mobility in older adults [123, 124]. The study [125] indicates that the change in echo intensity of BB muscle starts from middle age and that this change occurs prior to the change in muscle thickness. This study indicates that the increase of adipose and connective tissue within this muscle is associated with the decrease of contractile tissue and muscle strength in middle age. Therefore, we decided to incorporate the adipose tissue infiltration efficiently through the muscle into our personalized aging model.

Two kinds of fat tissues are identified: 1) Inter/intramuscular fat (Intra Muscular Adipose Tissue (IMAT)), which is generally considered to be any adipocyte deposition located between muscle fibers or between muscle groups; 2) Subcutaneous Fat (SF) is the fat between muscle and skin.

As people become older, their fat distribution changes, with IMAT increasing compared to subcutaneous fat declines increasing. Experimental measures of muscle fat have been achieved with various imaging (Magnetic Resonance Imaging (MRI), Computer Tomography (CTO)) and biochemical techniques. However, measures for BB muscle are rarely reported compared to lower arm muscles (Vastus Lateralis (VL), Biceps Femoris (BF), etc.). Generally, the loss in lean body mass is thought to be mainly the result of increased fat mass relative to total body mass [73], increase of intramuscular fat and connective tissue known as "myosteatosis" [126] and atrophy of the muscle fibers due to denervation. Specifically for the thigh muscles, increments of 59-127% intramuscular fat have been reported for older men compared to younger men, as well as annual increases of 18% in longitudinal designs [90]. Despite these increases in fat mass with aging, a decrease in food intake across the life span is observed [127]. In addition, the intake of high-quality proteins has been demonstrated to be less than 1 g/kg/day for more than 50% of older adults aged above 60 years and less than 0.8 g/kg/day, which is recommended for healthy adults, for 30% of a sample of older subjects [128]. However, the existing evidence of enhanced benefits of exercise training when combined with protein supplementation is inconsistent [129].

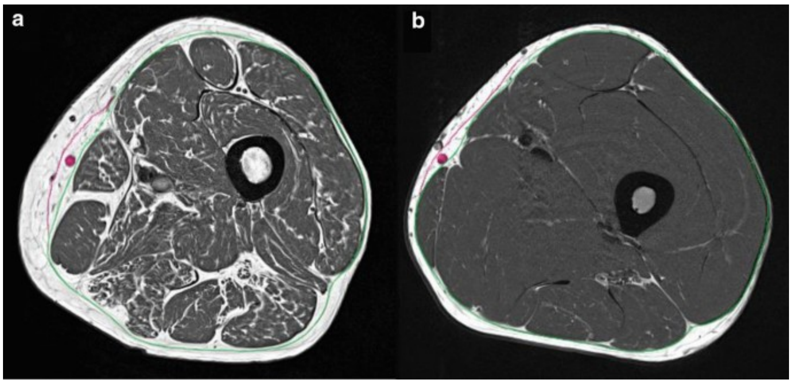

Figure 1.22: Intramuscular fat distribution for: (a) Elderly sarcopenic subject; (b) a healthy young subject. Image from [130].

1.4.1.6 Aging as a disease entity: Sarcopenia and Dynapenia

The main question arising from the age-related muscle changes reviewed in previous paragraphs is: When are these age-related changes normal or express a disease?

Sarcopenia In 1988 (published in 1997), Irwin Rosenberg in [131] was the first to define the age-related loss of muscle mass as a disease that proposed a Greek composite name: sarcopenia (sarx in Greek is flesh and penia is loss). Over time, the original definition of sarcopenia as purely a loss of muscle mass [131] was evolved, and many cross-sectional studies supported a link between muscle mass and strength [132].
Therefore, in 2010, the European Working Group on Sarcopenia in Older People (EWG-SOP1) defined sarcopenia as low muscle mass together with low muscle function (strength or performance)[132]. The EWGSOP1 has also defined a pre-state and advanced state of sarcopenia termed respectively "pre-sarcopenia" and "severe sarcopenia". The pre-sarcopenia is characterized by low muscle mass with no impact on muscle strength or physical performance. Severe sarcopenia is defined when the three criteria: low muscle mass, low muscle strength, and low physical performance, are present.
Rapidly, between 2011 and 2014, other working groups have proposed a similar consensus definition for sarcopenia: the International Working Group on Sarcopenia (IWGS) [133]; The Foundation for the National Institutes of Health (FNIH) [134]; The Asian Working Group for Sarcopenia (AWGS) [135], And the Society for Sarcopenia Cachexia and Wasting Disorders (SCWD). The definitions of sarcopenia proposed by these working groups are shown in Table 1.3.

Table 1.3: Definitions and criteria of five major research group working on sarcopenia.

Research group	Definition
EWGSOP	Sarcopenia is a state defined by a gradual and widespread loss of skeletal muscle mass and strength, as well as an elevated risk of negative outcomes such as disability, poor quality of life, and death [. . .]
IWGS	Sarcopenia is a muscle and function loss that occurs with age. Is a complex syndrome that is linked to localized muscle loss or increased fat mass [...]
SCWD	Sarcopenia is a syndrome characterized by a loss of muscle mass and difficulty walking that is not caused by a specific pathologic illness or cachexia [...]
FNIH	Sarcopenia is a functional constraint characterized by diminished strength (weakness) as a result of decreased muscle mass [...]
AWGS	Sarcopenia is a relatively new geriatric illness defined by age-related skeletal muscle deterioration as well as decreased muscle strength and/or athletic performance [...]

The World Health Organization (WHO) initiated, in 2016, the International Classification of Disease (ICD) code for sarcopenia as a disease entity with the awarding code: ICD-10-CM (M62.84) [7]. In 2018, the EWGSOP2 published a revised consensus of sarcopenia, with a new working definition, based on low muscle strength as the primary parameter of sarcopenia (contrary to low muscle mass for EWGSOP1), with a new sequence of diagnostic criteria [8]. These collective efforts have led to many research studies in the last decade to: 1) Assess the sarcopenic portion in the aging population; 2) And to correlate sarcopenia with other chronic diseases (as a trigger factor or as a result) and mortality. In fact, depending on the definition used, sarcopenia is prevalent in 1-29% of community-dwelling healthy older adults [136], and some estimates are as high as 60% [137]. These percentage raise more over for very old population and for hospitalized patients: 53.2% of community-dwelling healthy very older adult($>$ 80 years) [138]; Up o 76% of acutely hospitalized older patients ($>$ 65 years) [139]. Moreover, statistics confirm the prevalence of sarcopenia with chronic diseases, e,g. 31.4% of individuals with cardiovascular diseases (CVD) are sarcopenic [140]. Next, it was proved that sarcopenia significantly increases in the presence of several co-morbidities, such as osteoporosis, type 2 diabetes, advanced organ failure, and chronic inflammatory states [132, 8].

This statement can be valid in the opposite way, e,g,. osteoporosis increases in the presence of sarcopenia [141]. However, despite these collective efforts, the lack of a unique consensus defining sarcopenia and the use of different cut-off points prevent formal diagnosis in clinical settings and reliable comparison of research studies. The cut-off points are the criteria/variable values from which the subject is assessed as sarcopenic (e,g,. body mass index (BMI), body fat, muscle index, handgrip). These cut-off points are essential for clinicians to differentiate between healthy and sarcopenic aging people. Moreover, they can be helpful in age-related modeling. However, the challenge is to correlate these cut-off pints with the age-related change at the different scales aforementioned. The Table 1.4 shows some cut-off points form EWGSOP2 and IWGS consensus. Most of the studies cited above use these cut-off points to evaluate sarcopenia.

Table 1.4: Original cut-off points according to consensus. SPPB: Short Physical Performance Battery protocol [142]. SMI: Index Skeletal Muscle Mass.

Consensus	Variable	Men	Women
EWGSOP2	Grip strength SMI/m2 Index SPPB	$< 27\ kg$ $< 7\ kg/m^2$ ≤ 8	$< 16\ kg$ $< 5.5\ kg/m^2$ ≤ 8
IWGS	Gait speed SMI/m2 Index	$1\ m/s$ $< 7.23\ kg/m^2$	$1\ m/s$ $< 5.68\ kg/m^2$

The biceps brachii muscle is the subject of this thesis (BB). As a result, we attempted to describe variables reflecting morphological and structural changes in this muscle as it ages, using clinically agreed-upon cut-off points. Rare studies give the sarcopenic and non-sarcopenic aged population this kind of information. In particular, one recent study [143] has reported the BB muscle thickness, the muscle CSA, and the fat thickness (subcutaneous) for these two populations. Values of these variable are depicted in Table 1.5

Table 1.5: Morphology of the biceps brachii muscle of sarcopenia group and non-sarcopenia group. Sarcopenia was identified by EWGSOP2 [143]. Abbreviations: BMI, body mass index; FT, fat thickness; MT, muscle thickness; CSA, cross-sectional area; SMI, index skeletal muscle mass. The data were shown as Median(first quartile 25%, third quartile 75%).

Variable	Gender	Non-sarcopenia group	sarcopenia group
BMI (kg/m^2)	M	25.1(23.1, 27.4)	21.8(19.5, 23.7)
	F	23.4(22.0, 25.5)	22.5(20.1, 24.6)
SMI (kg/m^2)	M	6.5(5.8, 7.7)	5.5(4.8, 5.8)
	F	5.4(4.7, 6.5)	4.5(4.1, 5.0)
CSA (cm2)	M	9.24(7.37, 10.67)	7.06(6.40, 9.00)
	F	5.50(4.60, 6.12)	4.40(3.34, 5.49)
FT (cm)	M	0.26(0.18, 0.33)	0.20(0.14, 0.25)
	F	0.35(0.26, 0.42)	0.23(0.19, 0.31)
MT (cm)	M	2.20(2.03, 2.63)	2.08(1.97, 2.11)
	F	1.71(1.47, 1.92)	1.61(1.33, 1.74)

Dynapenia The first study has argued that the loss of muscle mass and strength need to be defined independently is [144]. Authors of this study have proposed the term "dynapenia" to describe the age-related loss of muscle strength (The Greek term dynapenia translates to "poverty of strength"). The authors proposing this dissociation argued that dynapenia is characterized by deficiencies in neural activation and motor recruitment patterns, the loss of α-motoneurons, the replacement of type II fibers with type I fibers, as well as changes in muscle mass and architecture [144]. They are based on several studies boosting this hypothesis (see [144]). One study, in particular, demonstrated that, in a sample of 120 adults initially aged 46 to 78 years who were followed over ten years, less than 5% of the change in strength was attributable to the corresponding change in muscle size [145]. Next to the reduction of the intrinsic force-generating capability and excitation-contraction coupling, the increase of intramuscular and body fat with aging is one of the leading causes of dynapenia [146]. However, the new definition of sarcopenia EWGSOP2 based on low strength as primary criteria in sarcopenia diagnosis may be redundant [147] and more referable to sarco-dynapenia disease. As in the sarcopenia paragraph, we have tried to report variables reflecting the morphological and structural changes during dynapenia aging for BB muscle considering the cut-off points fixed by EWGSOP2 (considering low strength criteria).

Rare studies give this kind of information for dynapenia and non-dynapenia aged groups. In particular, one recent study [146] has reported that BB muscle thickness and Echogenicity can be correlated with intramuscular fat for these two populations. Values of these variable are depicted in Table 1.6.

Sarcopenia and dynapenia, in addition to the consensus definitions and diagnosis recommendations, are among the fundamental causes of functional decline in older persons, owing to the loss of voluntary strength contraction.

The different consensus has proposed many diagnosis recommendations and tools to evaluate muscle mass, strength, and performance. However, these tools were not satisfactory. The linkage between the measurable variables that give these tools (e,g. BMI, SMI, gait speed) and the inner scales of the aforementioned muscle age-related changes are missed. The following paragraph will describe the muscle age-related diagnosis tools, as recommended by the sarcopenia consensus for clinicians and deployed by researchers assessing muscle functions.

Table 1.6: Morphology of the biceps brachii muscle of dynapenia group and non-dynapenia group. Dynapenia was identified by EWGSOP2 [146]. Abbreviations: BMI, body mass index; MT, muscle thickness; SMI, index skeletal muscle mass. The data were shown as Mean(Standard deviation).

Variable	Non-dynapenia group	dynapenia group
BMI (kg/m^2)	24.38 (3.11)	23.63 (3.11)
SMI (kg/m^2)	6.23 (0.90)	6.54 (0.81)
Waist (cm)	82.55 (8.20)	78.51 (8.59)
MT (cm)	2.03 (0.30)	1.86 (0.73)
Echogenicity (pixel)	88.06 (14.68)	89.51 (19.15)

1.5 Muscle aging: Diagnosis tools

Diagnosis is crucial when treating a disease. A reliable and precise diagnosis, after its role in finding the appropriate treatment methods, enhances our understanding of disease causes, issues, and prevention directives.

Muscle aging, as a disease entity, was referred to as sarcopenia or/and dynapenia. As cited in the previous paragraph, the groups working on sarcopenia have suggested many diagnosis tools to evaluate the three criteria: low muscle mass, low muscle strength, and low performance. The philosophy of recommending the evaluation of these three criteria is based on the fact that only measuring the muscle composition, size, and architecture does not consider the neural input into the muscle fibers that dictate contraction potential and force production. The collective research effort, as aforementioned, has associated muscle weakness with alterations in muscle composition, contractile muscle quality, and neural activation [144].

Therefore, strength measures represent an essential measure of muscle performance. The common feature of the metric is the expression of muscle force production relative to muscle or body size. We will expose, in this section, the principal diagnosis tools of sarcopenia (as the aging disease), recommended with consensus, to measure these three criteria: low muscle mass, low muscle strength, and low performance. However, with the same exposure, we will report the capacity of these tools to measure other inner-scale age-related changes. In particular, at the fiber and MU scale (morphology, structure, and neural drive).

1.5.1 Muscle mass and fat infiltration

1.5.1.1 MRI and CT scanning

The gold standards for evaluating body composition are Magnetic Resonance Imaging (MRI) and Computed Tomography (CT) scanning (muscle morphology and adipose tissues) [148]. MRI and CT scanning both measure intra- and intermuscular adipose tissue, which is an indicator of muscle quality [122]. There is currently no consensus on sarcopenia diagnosis criteria or cut-off values or even which indices should be employed to quantify skeletal muscle mass using these techniques. However, some studies have proposed gender-related cut-off points. For example, in [149], authors have proposed that subjects with a total abdominal muscle area inner than 52.4 cm2/m2 for men and 38.5 cm2/m2 for women are sarcopenic. For this reason, the diagnostic cut-off values must be standardized, which requires further work at large scale studies [150].

Next, the usefulness of these tools in sarcopenia consensus diagnosis, MRI, and CT scanning have increasingly approved its usefulness in assessing muscle aging in general for many research fields. A latest reviewed study, for the first time, has assessed a human motor unit's morphology (territory) and firing rate with MRI technique [39]. In fact, authors in [39] have applied an in-scanner electrical stimulation of the tibial nerve with specific increased current steps (extremely small steps). Then, they delineated the regions of interest within the stimulated muscle, creating a current profile against signal intensity. The stimulation current at which activity was first visible is defined from this profile. Using a second scan and decreased steps starting from the defined activity-related current, the authors have succeeded in identifying regions of MUs regions (see Fig.1.23). This study has revealed large territories of MUs for aged participating volunteers (> 40 years). Such MRI or CT scanning applications can be valuable in the MU modeling (either for the recruitment pattern or for positioning and territories). However, these techniques are expensive, and CT emits higher radiation.

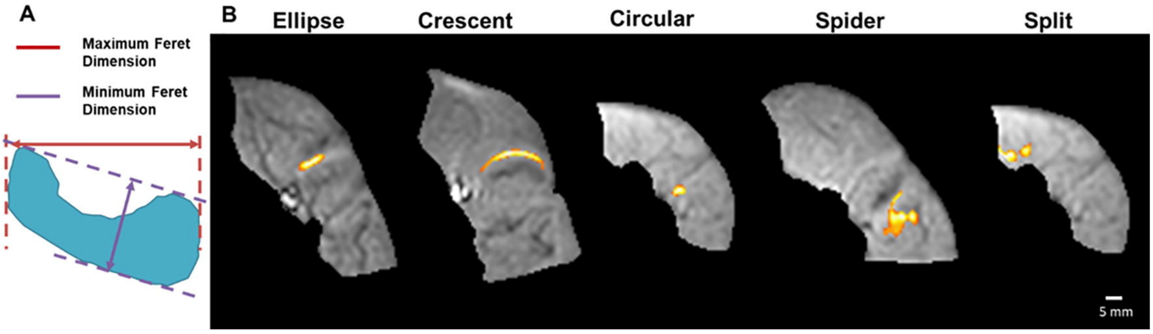

Figure 1.23: MRI technique is used in combination with in-scanner electrical stimulation to quantify the shape and cross-sectional area of MUs [39]. (A) Example motor unit shape. (B) Typical examples of the five detected motor unit shapes.

1.5.1.2 Ultrasound

Ultrasound can measure muscle size (thickness and cross-sectional area), muscle quality (including IMAT through echogenicity), angle of pennation (for pennate muscles), the velocity of muscle tissue, and fascicle length [151, 152]. It is a technique easy to use, with a lack of radiation, low cost, portability, and a real-time visualization [153]. Ultrasound is not yet endorsed for diagnosis of sarcopenia, and reference data are lacking, despite its approval in tracking sarcopenia progression [153] and in studying skeletal muscle [151]. Beyond the fact that ultrasound cannot achieve inner scales of age-related muscle changes, it can be helpful in rapid and efficient measurement of morphological parameters from arm and leg muscles, such as the subcutaneous fat and/or muscle thickness/mass.

Recently, non-invasive high frame rate (>2000 images per sec) high-resolution ultrasound imaging has been introduced [154]. In skeletal muscle applications, accompanied by surface EMG, ultrasound has mainly been used for visualization of structural features and detection of contraction onset (e,g,. in [155]). Other applications of this technique rise in modeling and evaluating muscle functions, e,g,. imaging of MUs during externally controlled electro-stimulations [156], identifying of single MU under low force isometric voluntary contractions [157] (Fig. 1.24), and modeling functional movements [158]. However, the use of this technique calls always the use of sEMG , MMG, and/or mathematical model, e,g,. in [157, 158, 156, 152].

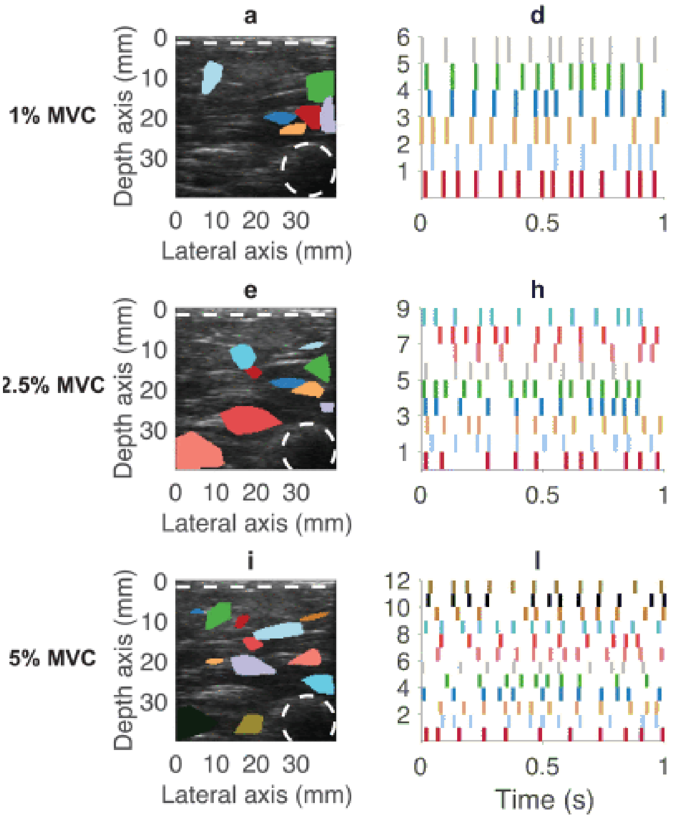

Figure 1.24: The use of ultrasound in the identification of mechanical response of Motor MUs in the BB muscle [157]. The territories and firing patterns of MUs are identified using modeling approach and sEMG (column (d,h,i) and (a,e,i)).

1.5.1.3 DXA

Dual-energy X-ray Absorptiometry (DXA) is the most widespread technique for measuring body composition due to its low cost, rapidity, and safety of use [159]. However, despite its positive endorsement by EWGSOP, it cannot quantify fatty infiltration of muscle, which is a bias in the diagnosis of sarcopenia obesity [159]. In addition, DXA measures appendicular lean mass (ALM), which is not a true reflection of actual muscle mass [160]. In comparison to appendicular muscle mass, a recent study found that calculating the percentage of skeletal muscle mass (total muscle mass/weight x 100) provides a higher estimate of sarcopenia prevalence and is more linked with obesity status [150].
It is important to note that DXA cannot assess functional aspects of the neuromuscular system.

1.5.1.4 Bioelectrical impedance analysis (BIA)

BIA involves a weak electric current flowing through the body, with the resultant electrical impedance to the current flow measured [161]. This impedance is then converted into an estimate of fat and fat-free mass using conversion equations. BIA is popular due to its simplicity, portability, and low cost. The disadvantages of using BIA are: overestimation of muscle mass; a lack of standardization on how to measure muscle mass; and cut-off points vary depending on the model used [162].

1.5.2 Muscle strength

Muscle strength is expressed as the maximal force or tension exerted by a group of muscles or a single muscle in a maximum voluntary contraction (MVC) within certain conditions (type of contraction and joint angle) [163]. There are few reliable techniques to measure muscle strength [164]. Different assessments have been proposed and recommended by sarcopenia working groups to measure muscle strength in the aging population: arm strength and leg strength. The review-study [165] has reported and evaluated the reliability of all the tools and tests used by clinicians to evaluate arm and leg strengths. However, we have observed that sarcopenia diagnosis tools tend to use handgrip strength rather than leg strength measurements.

The rising application of the handgrip strength dynamometry method is because of its simplicity, time-efficiency, affordability, and reliability [166]. This method has been shown to reflect the overall strength status of an old subject and to be a good predictor of morbidity, hospitalization, and mortality [166]. Standardized conditions for the test include [166]: seating the subject in a standard chair with their forearms resting flat on the armchairs; six measures should be taken, three with each arm; the highest reading of the six measurements is reported as the final result. The cut-off points for handgrip strength, according to EWGSOP, are: < 30 kg in men and < 20 kg in women. To note, the handgrip strength is measured by a dynamometer (e,g,. hydraulic, mechanic, pneumatic). Differences appear between measures of these dynamometers, in particular for older adults [167], and between genders [168]. It depends if the instruments were properly and regularly calibrated for the measurements [167]. Moreover, the design of each dynamometer may cause this difference. In fact, the ability to exert handgrip strength is influenced by pain or discomfort, so the design and mechanism may affect the measurement [168]. More research in this area is needed.

However, force evaluations performed with the devices described above are non-selective, as measuring the force or torque of a single muscle is nearly impossible. Moreover, these tools disallow the force evaluation at the cellular muscle scale (fibers). In fact, as aforementioned in previous sections, the maximum force produced by a muscle is related to many factors [169]: (1) the physiological cross-sectional area of the muscle; (2) neuromuscular performance; (3) Fiber type composition; (4) anatomical factors; (5) length of the muscle Fiber; (6) Electrical properties of fibers; and (7) mental factors. Thus, many of the issues associated with studying mechanisms behind strength loss in whole muscles are overcome using single muscle fibers. Although the relationships between the above factors and the maximum forces have already been well studied, there are still unknown factors.

In this thesis, we aim to more understand and assess age-related muscle changes by using aided-modeling approaches. Thus, in this section, we present different tools used to evaluate: (1) a specific muscle force; And (2) a specific fiber force ("specific" here average force per size as normally named in literature). These tools and procedures can be useful for future validation of the age-related modeling approaches.

1.5.2.1 Specific muscle force evaluation

Beyond the sEMG technique (will be described in section 1.5.4), MRI and ultrasound methods (described in sections 1.5.1.1 and 1.5.1.2), other recent techniques exist to evaluate specific muscle force. Recently, mechanomyography (MMG) has been introduced. This non-invasive technique records and quantifies the low-frequency lateral oscillations produced by the active skeletal muscle fibers [170]. In reality, pressure waves can be sensed on the skin surface due to the vibration of muscle fibers and their dimensional changes during activation. As a skin displacement measured by a piezoelectric contact sensor, laser distance sensor, or condenser microphone, or as an acceleration measured by sensors such as an accelerometer [171] (see Fig. 1.25). The recorded signal at the skin surface has been demonstrated to possess valuable information on the neuromuscular parameters leading to contraction and thus reliable in muscle function assessments [171]. Inference from various scientific research verified that the MMG signal could be used for the following: (i) muscle fiber typing; (ii) assessment of fiber force; (iii) assessment of muscle force; (iv) MU activities and properties; (v) muscle fatigue; and (vi) indication of the resonance frequency of muscle (see the reviews [171, 172, 173] for more details).

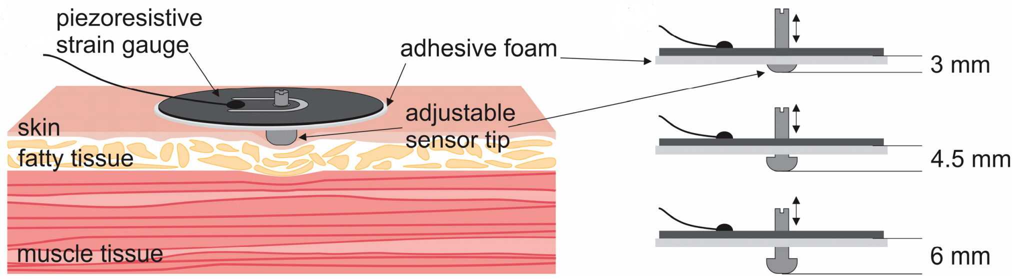

Figure 1.25: Piezo-resistive muscle contraction sensor used to detect MMG signal evoked by muscle stimulation [174].

1.5.2.2 Specific fiber force evaluation

The application of the single fiber technique to the intrinsic contractile dysfunction in muscle fibers from aged subjects was first published by [175]. Since then, this technique has significantly contributed to improving our understanding of the cellular mechanisms of sarcopenia [176, 177]. This technique in the evaluation of primary fiber function and its relation to muscle quality can be performed using measurements of morphological, biochemical, physiological, and mechanical properties at the muscle cell level using the isolated permeabilized (skinned) single muscle fiber preparation (this technique was detailed in [178]; The measurement tool is depicted in Fig. 1.26). In general, for human muscles evaluation, the technique is based on two successive stages: (1) Measuring the whole muscle force/strength using a dynamometer tool, for example; (2) Measuring the fiber specific force after isolating of single human muscle fibers obtained for example with the percutaneous muscle biopsy needle.

Fibers are made permeable during the second stage, and then segments are activated maximally with high calcium concentrations. Due to fiber permeability, there is no (or very little) sarcolemma or sarcoplasmic reticulum to obstruct calcium ion transit. As a result, the activation level (or voluntary drive) is no longer a confounding factor. Finally, the lack of a tendon and mechanical leverage system allows force generation to be measured directly from the fiber, and its myofilament structure, rather than at a distance [177]. Several fiber variables can be measured and/or calculated using the single muscle fiber approach, as shown below:

- Morphological and physiological variables: sarcomere length; fiber length, depth, and diameter.
- Physiological and mechanical variables: fiber force and specific force (force/size); shortening velocity; elasticity and stiffness.
- Biochemical variables: MyHc expression; regulatory and structural proteins (e.g., tropomysosin).

Rare are the studies using this technique to evaluate human muscle aging. The Table 1.7 shows some cross-sectional studies using single muscle fibers obtained from aged human beings. We can observe in this table the reduction in muscle fiber-specific force in both slow-twitch type I and fast-twitch type II fibers. For the case of fiber prepared in vivo before measuring force, we cannot extract this related-type information.

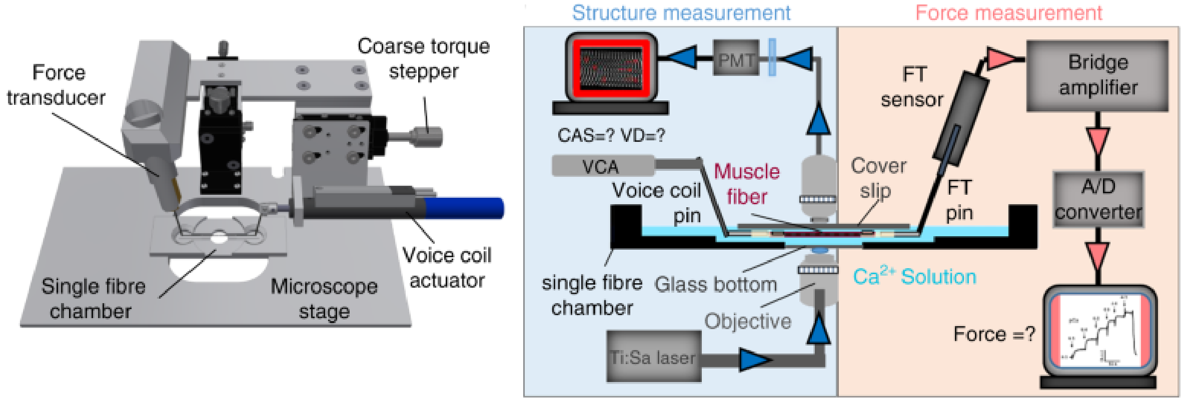

Figure 1.26: Apparatus are preparing a skinned fiber and assessing its specific force and its morphological, physiological, and biochemical characteristics [179]. Abbreviations: FT, Force Transducer.

Table 1.7: Quantification of specific fiber force in healthy/active aged human muscle.

Study	Gender	Young age	Old age	Muscle	Preparation	Fiber type	specific force change (%)
[180]	Male	25-36	60-74	VL	skinned fiber	I IIa	-25% -33%
[181]	Male	28±0.1	68 ± 0.5	BB	in vivo	NC	-14%
[88]	Male	30.2±2.2	72.7±2.3	VL	skinned fiber	I IIa	-22% -16%
[182]	Female	22±3	72±4	knee extensor	in vivo	NC	-17%
[183]	Male	23.0±2.2	70.9±4.1	VL	skinned fiber	I IIa	-10% -26%

1.5.3 Physical performances evaluation

For the first time, the idea of physical performance was created to objectively and clinically assess how an individual performed various activities of daily life or physical tasks, rather than scales based on asking questions about the ability to accomplish these tasks [184].
However, the concept of physical performance has developed since then, and it is now mostly associated with ambulation and transfers. It is included in the most recent definitions of sarcopenia. The usual gain speed (UGS), the time up and go test (TUG), and the short physical performance battery (SPPB) are the most widely used tools for the assessment of functional performance. Their cut-off points recommended by the EWG-SOP2 to diagnosis sarcopenia are depicted in Table 1.8.

Table 1.8: Physical performance tests and cut points recommended by the EWGSOP.

Physical performance test	Cut-off points
Usual gain speed test (UGS)	$\leq$ 0.8 m/s
Short physical performance battery (SPPB)	$\leq$ 8 points
Up-and-go test (TUG)	$\geq$20 seconds

They can be assessed as individual items, but in clinical practice, they are more commonly assessed as part of a brief physical performance battery (SPPB). Which is a test developed by the national institute on aging for use in the Established Population for the Epidemiologic Studies of the Elderly (EPESE). It includes three tests: 1) balance tests, 2) walking speed test, and 3) repeated Sit To Stand (STS) test. More details about theses test are available in many references [8, 185, 162]. However, a recent study has revealed that the statistics of sarcopenia prevalence are similar to using performance tests and without their application during diagnosis [185] (see Fig. 1.27).

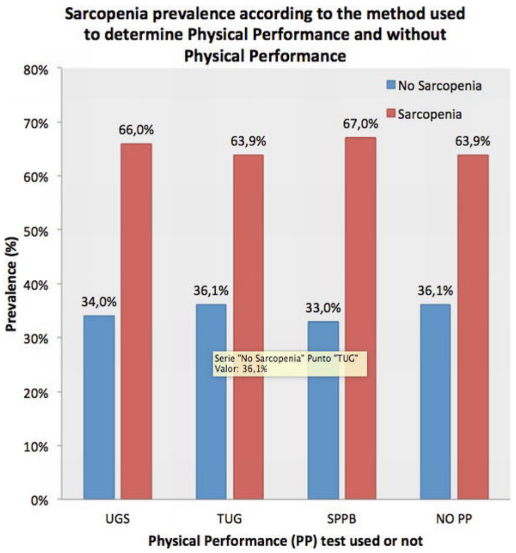

Figure 1.27: Prevalence of sarcopenia using three different methods: Usual gait speed (UGS); get-up-go test (TUG); short physical performance battery (SPPB) and without physical performance evaluation[185].

This finding is consistent with our objective in this thesis which aims to evaluate age-related (sarcopenia) using more reliable approaches.
Therefore, in the next paragraph, we will come forth the surface electromyography technique as a more precise and reliable technique in the assessment of functional muscle abilities and in the evaluation of several phenomena related to the quality and performance of skeletal muscle.

1.5.4 Surface electromyography

The surface Electromyography (sEMG) is, at this time, a limited diagnostic tool/power but is a powerful tool for prevention, assessment, and evaluation of the effectiveness of treatments and interventions [186].
We will start this section with a paragraph describing the history of dealing with sEMG signals. Then, we will describe the sEMG generation process. In the last paragraph, we will discuss the application of the sEMG technique in aging assessment.

1.5.4.1 History

The development of electromyography was possible thanks to the collective contribution of many scientists and professionals from different fields, both clinical and engineering. The first experimentation dealing with EMG was in 1666 by Francesco Redi. He discovered that the highly specialized muscle of the electric ray fish generates electricity. In 1792, Luigi Galvani, through his concept of "animal electricity", demonstrated that the electrical stimulation of a nerve could initiate muscle contraction (using an apparatus known later as a galvanometer). Between 1840 and 1845, Carlo Matteucci proved that the muscles generate the electric current described by Galvani. His work in bioelectricity influenced directly the research developed by Emil du Bois-Reymond (1818–1896), who tried to duplicate Matteucci's experiments and ended up discovering and recording the nerve's action potential in 1849. The evolution of electromyography has been possible due to the evolution of acquisition equipment and processing techniques. In 1922, Gasser and Erlanger used an oscilloscope instead of a galvanometer to display the EMG signal from muscles. Edgar Douglas Adrian (1889–1977), the Nobel Prize winner in Medicine (1932), collaborated with Detlef Bronk to quantify the action generated by a single nerve fiber in 1929 [187]. They recorded the electrical activity of muscle fibers generated by a single nerve fiber using a needle electrode and a speaker, which became known as the Motor Unit Action Potential (MUAP). In 1934, Fritz Buchthal developed a microelectrode to record the potential of isolated muscle fibers. Edward H. Lambert has established the first clinical electromyography laboratory in the United States in 1943 (a Mayo Clinic laboratory).
Afterward, through the 50's and 70's, major contributions of EMG were achieved, including the quantitative analysis of the Motor Unit AP (MUAP), EMG decomposition techniques and EMG amplitude analysis. Researchers began to use improved electrodes more widely to study muscles during the same period. The sEMG was introduced as a non-invasive technique that can detect the MUAP activity in a large volume. In fact, an EMG signal is the electrical activity of a muscle's motor units, which consist of two types: surface EMG (sEMG) and intramuscular EMG. Non-invasive and invasive electrodes record surface EMG and intramuscular EMG signals. Hardyck and his researchers were the first (1966) practitioners to use sEMG. Then, the sEMG technique was spread

across the scientific community in the following years. These days, surface-detected signals are preferably used to obtain information about the time or intensity of superficial muscle activation.

The non-invasive aspect, the real-time visualization, and the important information on muscle activation patterns and muscle properties make the sEMG a valuable aging diagnosis tool for clinicians. This is in contrast to the training of cardiologists in electrocardiography (ECG) and neurologists in electroencephalography (EEG), which has taken place for 70 years now. Furthermore, the use of sEMG in terms of real-time feedback can be used to assist patients in becoming more conscious of their muscle activity and during physical exercise.

1.5.4.2 sEMG generation process

The screened "electrical image" evolving in time frames, as a movie, is a 2D analog signal sampled in space (by the electrodes) and in time (by an electronic sampler). The origin source of this 2D signal is the MUAP of the active motor units (MUs), which incorporate thousands of action potentials (SFAP) generated by the individual fibers of such MUs in the muscle. The AP generation mechanism was described in section 1.3.3.1. In fact, all fibers within a single MU are activated together at each discharge of the correspondent α-motoneuron. The algebraic sum of SFAPs generated by the individual fibers of that MU produces a single propagating MUAP. Depending on muscle, a specific number of α-motoneurons are activated at different discharge rates (5-40 pulses/s) to reach the target force level, speed, and duration. The resulting signals are MUAP trains. The interferential monopolar sEMG signal screened at a specific point on the skin (near the muscle), measured with respect to a reference electrode, is the algebraic sum that MUAP trains (see Fig.1.28).

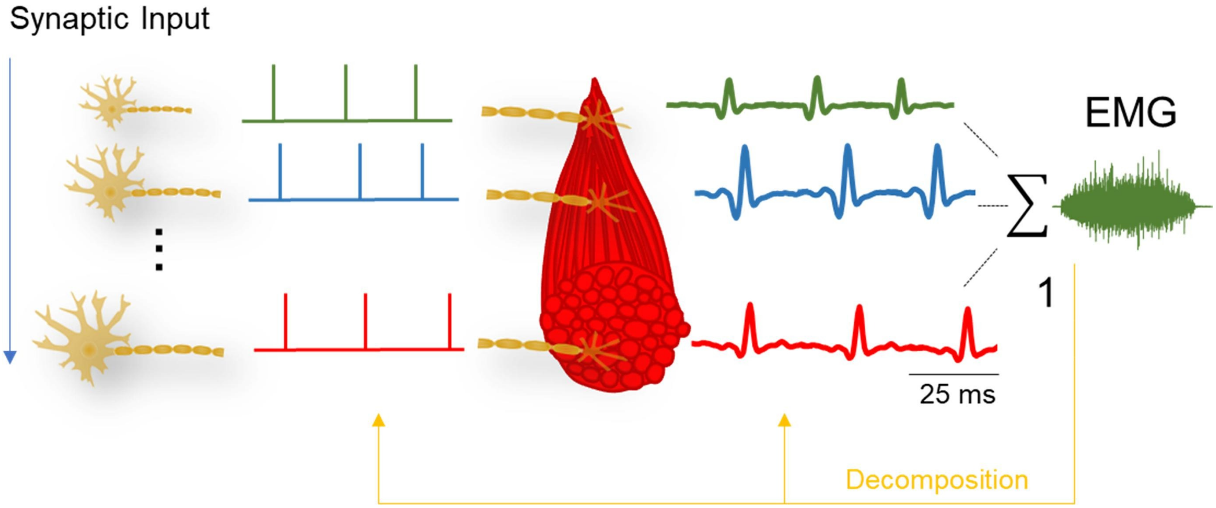

Figure 1.28: sEMG generation during voluntary contraction [188].

However, next to the influence of volume conductor properties on MUAPs [188], the electrodes arrangements and locations play an important role in the qualification and quantification of information measured at the skin surface. We distinguish three types of sEMG detection:

- Monopolar detection: a point electrode is measuring the voltage with respect to a remote reference where the potential is zero. It provides the full information which can be recorded from the detection volume. This arrangement has the most significant detection volume compared to the other electrode arrangements. This technique is not commonly used in biomechanical and neuromuscular investigations. The sensitivity of monopolar sEMG to noise from stray voltage [4], movement artifacts, and possibly cross-talk[5] due to low spatial selectivity [189] may compromise the reliability of a monopolar system. In particular for the evaluation of muscle aging based on MUs characteristics. In fact, it is not evident to find and standardize measure point that minimizes cross-talk activity and the impact of muscle-tendon end effects.

- Spatial filtering: is based on the linear combination of signals detected by a number of electrodes placed over the skin with a defined geometry to attenuate specific spatial frequencies with respect to others (see Fig.1.29). This can partly counteract the low-pass filtering effect of the volume conductor and reduces the number of motor unit coverage [190]. The simplest and most widely used spatial filter is the bipolar or single differential (SD). Enhanced spacial filtering is improved, e.g., the double differential (DD) filter that is constituted by three equally spaced electrodes and the Laplace two-dimensional high-pass spatial filter [191]. To note, the high sensitivity of this filtering mode to the electrode location and orientation regarding the muscle-tendon junctions, the motor end-plate, and the direction of fibers [191, 192] impacts the precision of the latter applications like muscle force estimation. In addition, the use of a few electrodes with this arrangement only gives information about the activity of a group of MUs but not a single MU. Beyond the alteration that this fact can cause on the amplitude and energy of measured signals due to the amplitude cancellation phenomenon [193], this can have a consequent limitation in many domains such as neuromuscular disorder diagnosis and assessment of muscle functions for the aged population. All limitations mentioned above can be avoided using adequate spatial sampling.

- Spatial sampling: The surface EMG signal evolves in time and space, and it can be described as a three-dimensional signal. In fact, If a spatial filter (SD, DD, or the two dimensional) is applied to each detection point, the potential distribution is spatially filtered and also spatially sampled [191]. The spatial sampling grids are, in general, multi-channel grids covering a large part of the muscle. The spatial information is independent of the temporal information, and together they can provide valuable insights into muscle anatomy factors, topographical muscle activity, and the single MU action potential trains (using sEMG decomposition) [191]. In this thesis, we work with this technique using a multichannel detection system: the HD-sEMG [194]. This system has a multi-channel electrode grid with many channels, small electrode sizes, and interelectrode spacing. Most of the limitations of the classical sEMG recordings can be overcome by using the HD-sEMG technique. These recordings are particularly appreciated in clinical applications, including the evaluation of muscle aging (see next paragraph).

---

[4] Potential difference between neutral and monopolar electrode

[5] The EMG from muscles that are neighbors of the one of interest

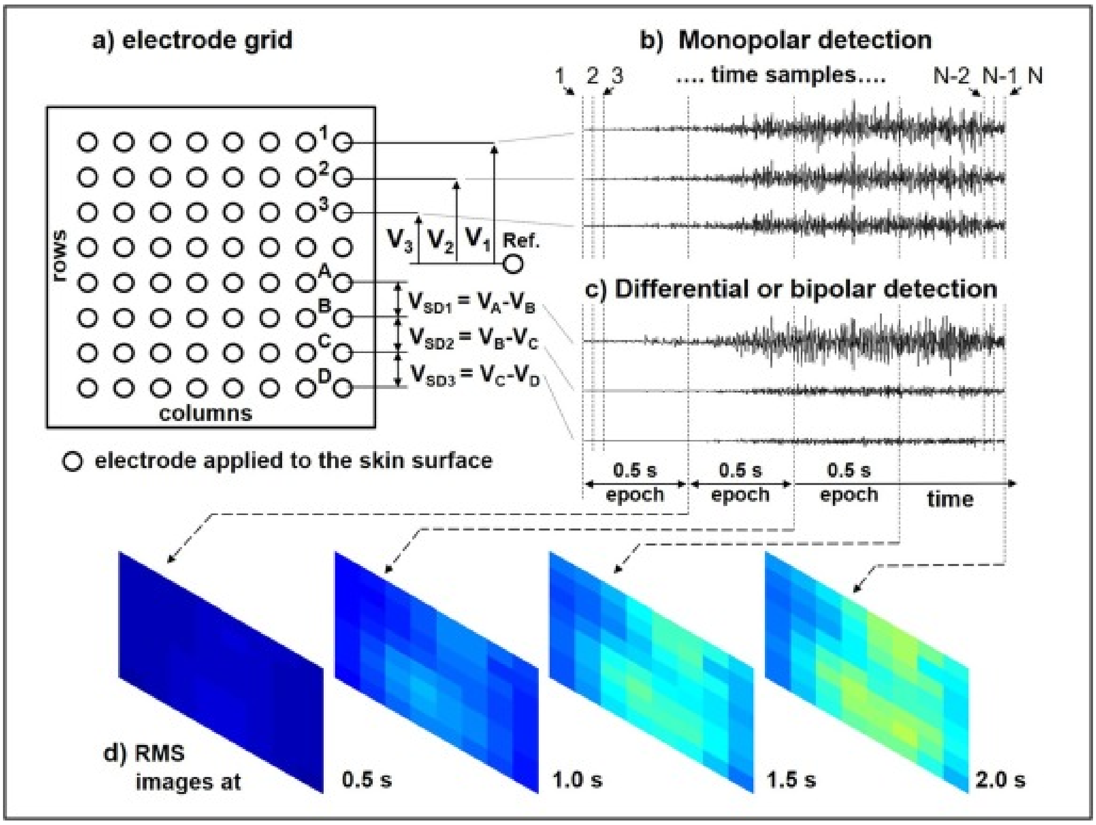

Figure 1.29: sEMG signals in space and time [186].

1.5.4.3 HD-sEMG technique and muscle aging

The sEMG signal is the algebraic sum MUAPs generated by the active MUs and detected over the skin. Like any other signal, it provides quantitative information concerning wave shape, amplitude, and power spectral density. Using such information is a clinical choice or decision. Parameters and features of the spatial and temporal sampling pattern can be examined to understand age-related (and eventually sex-related) differences in skeletal muscle.

- Motor unit characteristics: The number, size, MUAP shape and area, and activation pattern of MUs are reliable indicators of muscle aging (see sections 1.4.1.3 and 1.4.1.4). In sarcopenic individuals, the loss of MUs is accompanied by a rise in the size of the remaining MUs, linked to muscle weakness in the elderly. The MU number index (MUNIX) and size index (MUSIX) techniques can estimate the number and average size of MUs within a muscle using the sEMG technique during electrically elicited contractions. They can be used as biomarkers of muscle aging and/or sarcopenia. MUNIX is already evaluated as biomarker of many patient populations such as the amyotrophic lateral sclerosis (ALS) [195, 196]. For aging patient population, studies evaluation MUNIX and MUSIX are rare [197, 198, 102] and unavailable using HD-sEMG system. Some recent studies (e.g., [196]) have accorded a high reliability to MUNIX using HD-sEMG in neurodegeneration evaluation. However, MUNIX is based on the CMAP [6] assessment during electrical stimulation, rather than the single MUAP measured during voluntary contractions.

---

[6] Compound muscle action potential consists in stimulating a nerve fiber and monitoring the response in the muscle.

Modeling approaches can overcome this limitation.
The MUAP shape and area (an indicator of larger MU) and the activation pattern can be estimated thanks to sEMG decomposition. In fact, the spatial sampling provides usefulness in recognizing the shape and frequency of action potentials of different MUs within the EMG signal. Several methods were proposed in the literature using HD-sEMG system (see review [188]). For the sarcopenic aging patient population, higher variability of MU firing and a lower MU firing rate during sustained contraction are shown [199]. However, performing sEMG decomposition requires high expertise in signal acquisition, interpretation of results, and manual assessment of decomposition quality [188].

- HD-sEMG processing : Requesting a larger muscle force contributes to a greater amplitude of the sEMG signal [199]. Many amplitude descriptors of sEMG are reported, e.g. in [200]. For aged population, it was observed that the maximal muscle strength, power, and rate of force are lower than the young population [199]. The absolute value of sEMG amplitude during MVC shows the same trend, being lower in the elderly compared with young and middle-aged adults. However, the relationship between force exerted and sEMG amplitude is not necessarily linear. Many factors influence the raw sEMG signal recorded over the skin, such as the distribution of active MUs within the muscle, among others [201]. It was observed that the relationship between the Root Mean Square of Amplitude (RMSA)(mV) and muscle force (N) could be modeled using a 3rd degree polynomial equation. Moreover, it appears that the obtained coefficients are patient-specific and dependent on physiological, anatomical and neural parameters [202]. The most widely used frequency spectrum analyses are the mean frequency and the median frequency. They are related to several physiological factors, including the Conduction Velocity (CV) of the MUAP along the fibers [199]. The mean/median frequency-time course during fatiguing contractions should show a steeper decrease if the muscle is characterized by a higher proportion of fast fibers (type II) than slow fibers (type I). The rate of decrease of power spectrum parameters has been observed to be greater in young people than in elderly people during submaximal isometric contractions in many experimental setups [199]. For example, a method based on the surface electromyography (sEMG) processing [9] has demonstrated the great potential of this technique to be used as a biomarker to detect early signs of sarcopenic back muscle. However, some studies indicate that muscle fiber CV (Conduction Velocity) should be preferred to spectral variables [199].

- Muscle fiber CV: The fiber CV, estimated by correlation technique, can relate the modifications in EMG signals with the recruited MU pool and with histochemical characteristics of the muscle. In fact, CV increases gradually when faster and larger MUs are recruited, such as when the intensity of muscle contraction increases, and it is positively related to the fiber diameter. When monitoring CV throughout a wide range of contraction levels (e.g., from 20 to 80% of MVC), the increment of CV is higher in younger subjects and lower in elderly subjects. This agrees with bioptic studies reporting a decrease in muscle fiber size in elderly subjects compared with young people. This reduction in muscle fiber size has been shown to be fiber-type specific, with the size of type II fibers decreasing by 10-40% compared to unchanged type I fiber size.

1.6 Muscle aging: Modeling approaches

The use of models is inevitable in almost all areas of the natural sciences. The model design is the key task in problem-solving. Models are used in two ways. First, they attempt to extract the essentials of reality for the problem at hand, and second, they permit control over variables not easily achieved in reality [203].

However, a living organism has a pecular organization which makes it very different from both a bunch of atoms and a macroscopic material [204]. Living tissues exhibit various self-organization mechanisms and show radically different pictures at different scales. A skeletal muscle, for instance, shows a complicated (but not random) structure at smaller and smaller scales: from fascicles to fibers, to sarcomeres, 77to myosin and actin (see section 1.3). Moreover, living tissue is usually growing (see section 1.4), thus showing a feature that is not shared with ordinary macroscopic materials. Therefore, if one wants to predict a future situation, the type of models that he/she uses may be crucial for the accuracy of the prediction. It is very important to remind that predictions may depend on the model used and some lack of matching with real life is not a matter of wrong basic laws but rather of a wrong or insufficient/imprecise modeling [204].

In order to approach reality, models may have a descriptive character with limited validity. The often-assumed proportionality between sEMG amplitude and muscle force can be considered an example of a descriptive model. Moreover, a model can operate at a phenomenological level, i.e., the model output mimics real-world behavior under a wide range of conditions, but the model is not or only by chance coupled to any underlying 'real world' elements evoking the observed outcomes. Finally, a model can be structure-based, which means that it selectively takes elements of the real system's structure into account in a reductional way in order to represent the system's important elements.

In this thesis, we are dealing with the latter type of model. In fact, the main goal of our research activity is to produce a model capable of quantitatively and/or qualitatively describing the evolution of muscle aging (eventually the sarcopenia disease symptoms). This model will be coupled with another model, generating HD-sEMG signals during isometric contractions. Then, a proportionality relationship between the generated sEMG signals and the neural and anatomical muscle parameters evolving in time will be established. Thus, we can produce quantitative/qualitative information on both muscle tissues and their electrical activity simulated at the skin surface at a selected age. To our knowledge, such a muscle aging model does not exist in the literature.

In order to do this, we need three main ingredients:

- Descriptors of the quality of muscle tissue, that is, some quantity which can summarize the physiological and neural changes due to the aging into a quantitative parameter. For example, the diameter of the fibers, the intramuscular fat area, the muscle/fibers atrophy, and the innervation ratio.

- Phenomenological models (statistic and descriptive models) of the quality degradation of muscle tissue during aging using quality descriptors, which keep into account also the possible loss of muscular mass/strength. For example, the model describing the loss of fibers, the model describing the expansion of MUs and territories with aging.

- A biophysical model including the calculation of each single motor unit action potential (MUAP) and the global HD-sEMG signal as a function of the outputs descriptive models and muscle quality descriptors.

The Fig. 1.30 shows the diagram of the modeling approach adopted in this thesis. The approaches used to build the descriptive models will be detailed in chapter 3. However, the biophysical model used in this thesis will be described in the next paragraph, and improvements will be detailed in chapter 3.

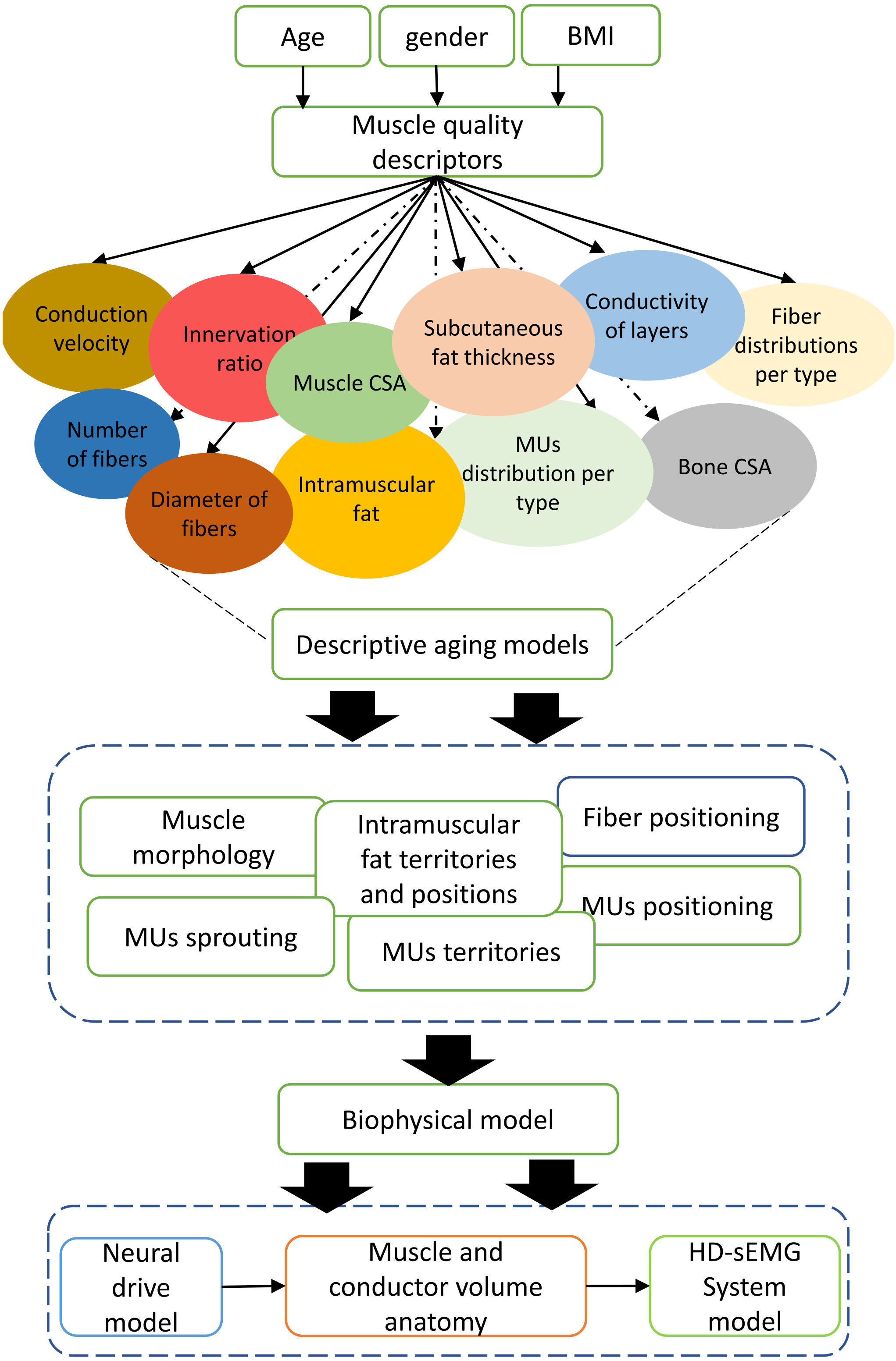

Figure 1.30: Modeling approach of muscle aging: from primitive inputs (age, gender and BMI) to simulated HD-sEMG signal.

1.6.1 Phenomenological models

Muscle age-related changes have been deciphered through several phenomenological experimental models, bringing together the opportunities to conceive a comprehensive analysis of muscle aging. To identify age-related muscle mechanisms, the gold standard of research is the comparison of young subjects with elderly subjects (healthy or sarcopenic). Then, researchers routinely use regression adjustments in order to fit experimental data. In the previous paragraphs, we have shown many figures depicting this kind of regression (e.g., in Fig. 1.21). Phenomenological muscle aging models are based on empirical relationships between age/gender and muscle tissue descriptor (e.g., number of fibers versus age, cross-sectional muscle area versus age, etc.). Researchers routinely use regression adjustments in order to fit experimental data to the "growth" model (e.g., linear, exponential, etc.). The regression analysis is a statistical tool for determining if two variables are related. As a result, we refer to these models as statistical models. In the previous paragraphs, we have shown many figures depicting statistical models of neuromuscular descriptors versus age (e.g., in Fig. 1.21).

In this thesis, we will perform these models as the first step to provide all the neuromuscular parameters needed to simulate sEMG signal by the biophysical model. In fact, the values of these parameters (muscle quality descriptors in Fig. 1.30) will be reported from literature according to the age and the gender of the subjects. The review will be limited to the values measured for the biceps brachii muscle. The definition of the relative statistical models will be made according to the experimental data shapes. This work will be well-reviewed and made in chapter 3. To note, we can not find a study that achieves all these descriptors experimentally together. Such a project is hard to undertake due to the high cost, the difficulty of finding healthy old people to do all that measurement, and the invasive method used (e.g., muscle biopsies) to achieve some age-related changes.

1.6.2 Biophysical model

The action potentials generated by the α-motoneurons trigger the force generation in the skeletal muscle fibers. There exist various different methods to predict skeletal muscle activity due to neural stimulation, that is, motor control, for example, analytical methods, phenomenological Hill-type or continuum-mechanical approaches, biophysical Huxley-type, or multiscale, multiphysics skeletal muscle models. Note, although we distinguish modeling skeletal muscle mechanics into these categories, a clear separation between these models does not exist [203].

1.6.2.1 Motor neuron pool model

Several phenomenological and biophysical models have been proposed for the simulation of the α-motoneuron pool. Phenomenological models are based on the characteristics of α-motoneuron discharges that have been found experimentally. For example, based on the relation between the synaptic input to a α-motoneuron and its output discharge rate, [205] and [44] have proposed powerful phenomenological models for animal and human α-motoneurons, respectively. These models have been used extensively for the testing of neurophysiological hypotheses or for interpreting experimental data [206, 207].

However, one important limitation of phenomenological motor neuron models is the fact that they are not capable of naturally describing the membrane dynamics of the α-motoneurons, where nonlinear behavior of α-motoneurons predominantly originates. To overcome these limitations, several biophysical models have been proposed [208, 209, 210]. These can integrate synaptic and/or common inputs on the α-motoneuron membrane level. This is done by adopting the Hodgkin and Huxley's formalism, derived from their experiments on the giant axon of the squid [47]. Using this formalism, it has been achievable to progressively increase the type and the number of ion channels in multiple compartments of these realistic motor neuron models. Interestingly, the biophysical description of the α-motoneuron behavior inherently accounts for the size principle of α-motoneuron recruitment [43] (small, low-threshold α-motoneurons are recruited before larger α-motoneurons with a higher excitation threshold) and the "onion-skin" property [211](for a certain level of synaptic input to the motor neuron pool, low-threshold α-motoneurons have higher discharge rates than high-threshold α-motoneurons). Additionally, these complex α-motoneuron descriptions were able to reproduce and help to interpret important results from human experiments [212]. In favor of the increased computational power and the flexibility of the simulator environments, it has been possible to create models based on the three-dimensional reconstructed morphology of experimentally recorded α-motoneurons. These models provide the unique possibility to investigate the neural alterations arising from pathologies of the neuromuscular system.

More recently, biophysical neuromuscular models have been proposed to describe the link between neural activity and force generation [213, 214, 207]. These models are a progression from the *alpha*-motoneuron models that were previously proposed. They also commonly comprise simple models of supraspinal pathways (e.g., motor cortex, brain stem), full spinal cord networks (e.g., excitatory and inhibitory interneurons, gamma motor neurons, afferent projections), and musculotendon unit simulations (proprioception,e.g., joint dynamics). Recent applications of these biophysical neuromuscular models include the analysis of the force variability during steady isometric contractions, postural sway, and nonlinear control of force oscillations [215].

1.6.2.2 Multi-scales and multi-physics HD-sEMG model

In this thesis, we will use the modeling approach depicted in [1][11]. It simulates the electrical activity of BB muscle during isometric contractions. The main axes of this neuromuscular system are: (1) the modeling of the MU recruitment and firing behavior, (2) the modeling of motor-unit action potential (MUAP), and (3) the modeling of the conductor volume and the recording system. In fact, the model describes the generation and the propagation of the electrical activity through a three-layered conductor volume composed of muscle, adipose tissues, and the skin. The recording channels are simulated to mimic a high-density electrode system. All steps for the generation and dissemination of the electrical activity are considered in the model, from the motor neuron pool model, the sources of action potential generated by muscle motor units MUs, the filtering of these sources by the conductor volume, and the recording system at the skin surface (Fig. 1.31). The model has 50 inputs: anatomical, neural, and electrical muscle and volume conductor parameters (see Fig. 1.31). The main output of the model is the 64 HD-sEMG signals according to the number of simulated channels (see Fig. 1.31). In order to correlate these signals to the physiological and anatomical muscle properties, many features are extracted from raw signals. These features are considered as the model outputs to be studied. This thesis will propose a new personalized neural drive model for muscle aging. The detailed description of the Hd-sEMG model personalized to aging and thereby, the new neural drive model will be presented in chapter 3.

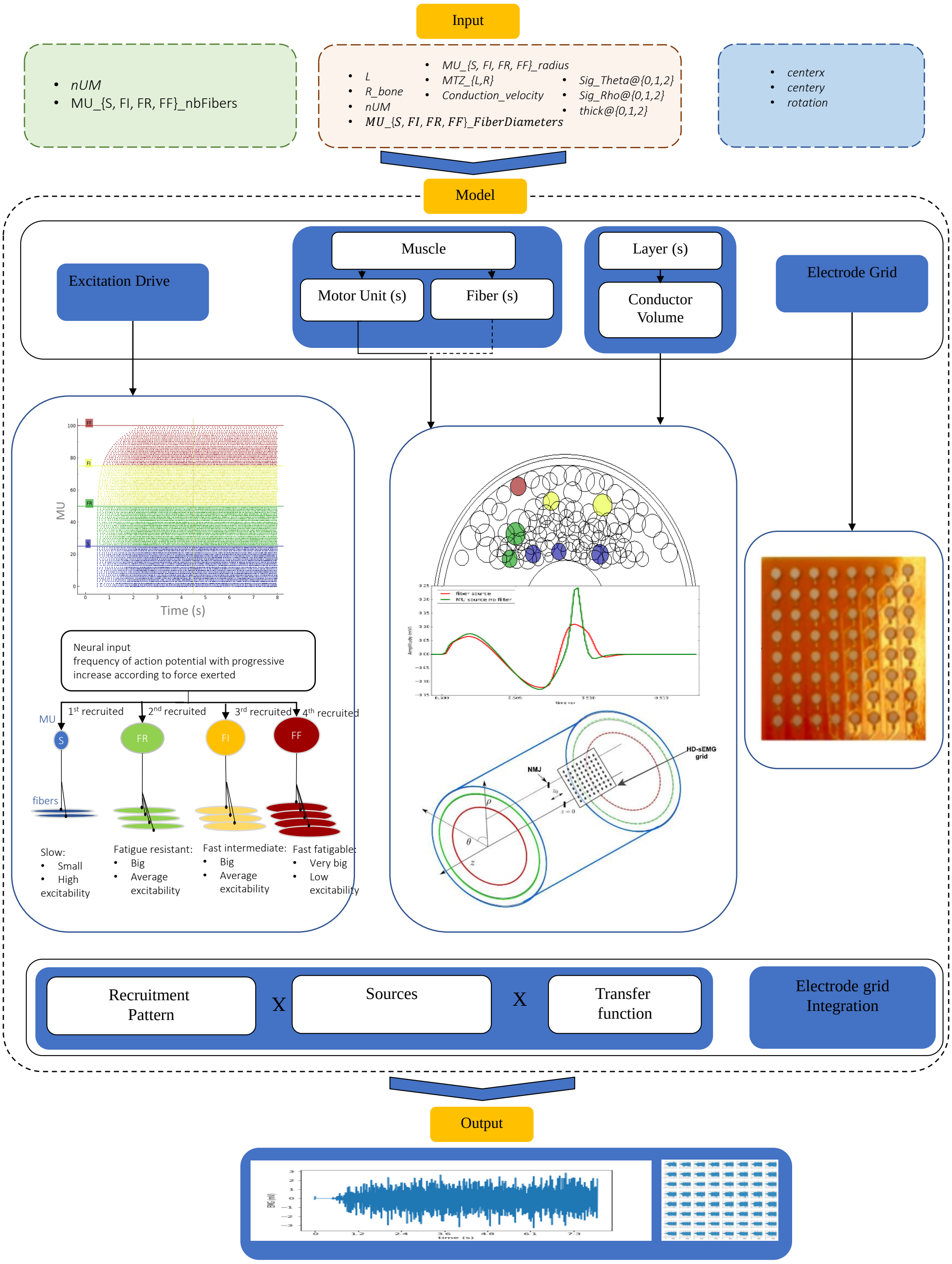

Figure 1.31: Modeling approach as depicted in [1, 11].

1.7 Objectives of the thesis

A better understanding of age-related muscle alterations leads to a more accurate diagnosis and the prevention of rapid functional deterioration.

However, indeed of the well-known of many muscle age-related mechanisms, the diagnosis of muscle aging as a disease entity suffers from a lack of accuracy and reliability. From this perspective, this thesis proposes the high-density surface electromyography technique

(HD-sEMG) coupled with muscle aging personalized models as a reliable device able to assess motor decline and to identify indicator(s) of muscle aging using inverse methods. To reach this objective, we should ensure that:

1. The biophysical model simulating HD-sEMG signal can help in the parameter identification process. For this purpose, in chapter 2, we propose an Improved Morris Sensitivity Analysis (IMSA) with new screening indices. These indices are less affected by outliers of distributions of elementary effects. Thus, they enhance the stability and the reliability of the parameter rankings. Then, using this method, we draw a global inputs/outputs sensitivity matrix, correlating the variation ranges/uncertainties of the neuromuscular parameters to the simulated HD-sEMG signals.
2. This biophysical model can simulate muscle aging with accuracy and reliability. For this purpose, in chapter 3, we decide to enhance the biophysical model simulating HD-sEMG muscle signal by phenomenological models describing the muscle quality degradation during aging. In particular, the morphological, structural, and neural changes (e.g., the modeling of the intramuscular fat infiltration). The muscle quality descriptors are extracted from the literature to accomplish this task. Furthermore, the coupling of the biophysical model and muscle aging descriptive models makes an important cross-simplification of the global model since the sEMG signal is related to age, gender, and body mass index. Which makes the new approach more accessible for clinicians and easy to use in muscle aging diagnosis.

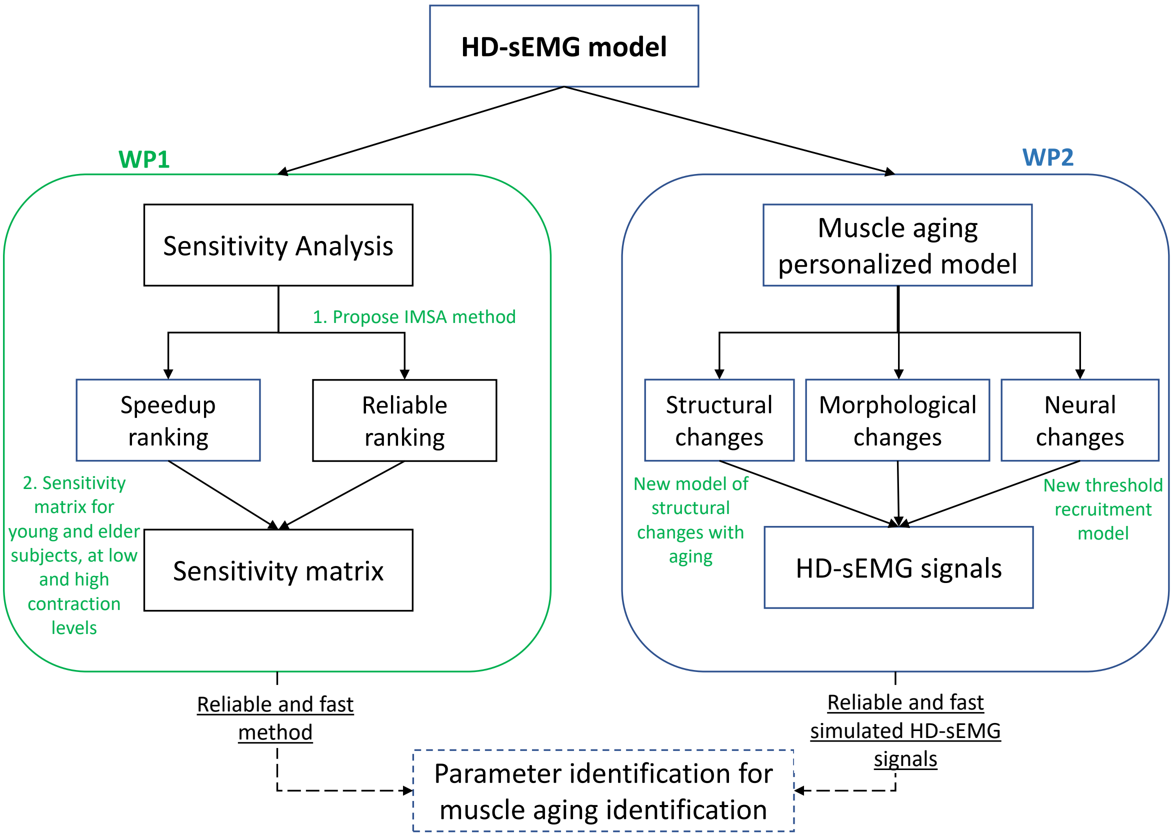

Figure 1.32: Thesis outlines.

1.8 Conclusion

Sarcopenia is a serious aging syndrome that is one of the primary causes of senior frailty and disability. It shows up as a gradual loss of skeletal muscle mass and functionality. Far from finding a medical therapy, even the disease diagnosis is problematic due to the scarcity of quantitative parameters (besides the total muscle mass and strength) and the difficulty of measuring them. In order to help the active aging and healthy living, we aim, in this thesis, to produce a mathematical model of the behavior of the human skeletal muscle capable of describing the quality/quantity of the muscular tissue/function. Such a model would be valuable in the feedback of muscle aging biomarker(s), coupled to a Model Aided Diagnosis (MAD) architecture that will allow access to underlying properties by analyzing noninvasive HD-sEMG signals.

Chapter 2

Sensitivity analysis

Contents

Problematic The neuromuscular model depicted in [1, 11] and described in the previous chapter, is a multi-scales and multi-physics model simulating the electrical activity at the skin surface during isometric contractions. All the steps of the electrical activity generation and dissemination are described in this model, from the motoneuron model pool, the sources of action potential generated by muscle motor units (MUs), the filtering of these sources by a three-layered conductor volume (muscle, adipose tissues, and skin), and the recording system at the skin surface. The recording channels are simulated to mimic a High-density electrodes system [202].
This model have a complex design with a large number of inputs, more than 50 parameters, and marked by switching between behaviors according to threshold concepts. In addition, many of these parameters are associated to large uncertainties due to the lack of knowledge and/or the measurement errors. Little data of these parameters is available in the literature. The exact values of many parameters and the effect on the outputs of their potential variation are not well defined. A better understanding of the relationships between model inputs (neuromuscular parameters) and outputs would allow the identification of the most influential parameters as well as those with a negligible impact. The definition of a groups of parameters with a strong and small influence on the model outputs would allow us to know which ones are important to determine precisely or, on the contrary, which ones can be fixed at an average value. Moreover, the input-output relationships built are useful for the subsequent identification of those parameters. In fact, in addition of reducing the number of parameters to identify and thus the identification computation time, it will figure out the convenient output(s) for each parameter to accomplish the identification process. This identification will be performed to evaluate muscle aging effects using the presented personalized model. The Sensitivity Analysis (SA) is a precious tool to define the influential group of parameters and to build a reliable relationships between these parameters and the different model outputs. However, the selection of an adequate sensitivity analysis method providing reliable and robust results is a complex task. Furthermore, the definition of a simulation plan/methodology to figure out the input-outputs relationships is not evident. In this chapter, we will address these several issues.

2.1 Introduction

Many sensitivity analysis methods are reported and classified in literature [216, 217, 218, 219] according to the model complexity and its computation time. The two main classes reported are : local methods and global methods [216, 218]. Local approaches investigate the impact of a small variation around a fixed point of input uncertainty range on the model output(s). These approaches are commonly applied when output have a linear behavior near a specific nominal value of model inputs, and are not able to assess interactions between parameters. Global approaches can explore all the input space and interactions between parameters. These methods are commonly grouped into derivative-based methods, regression-based methods, qualitative screening methods, and variance-based methods [216, 218]. The results of these methods can be illustrated by: ranking, screening, or mapping. Each representation has a defined utility: Ranking methods are valuables for parameter identification; Screening methods can be useful for reducing model complexity; Mapping methods are adapted for studying and understanding model output behavior and at where input space area this output is stable or optimal.
To facilitate the selection of an adequate sensitivity analysis method, a decision tree is

proposed by [216] (Fig. 2.1). It suggests the minimum number of model evaluations needed for each method based on the complexity and regularity of the studied system. Most of global sensitivity analysis methods are requiring a large number of model evaluations [216, 218]. Thus, performing these sensitivity analysis methods with complex and high computation time models can be a very long time process.

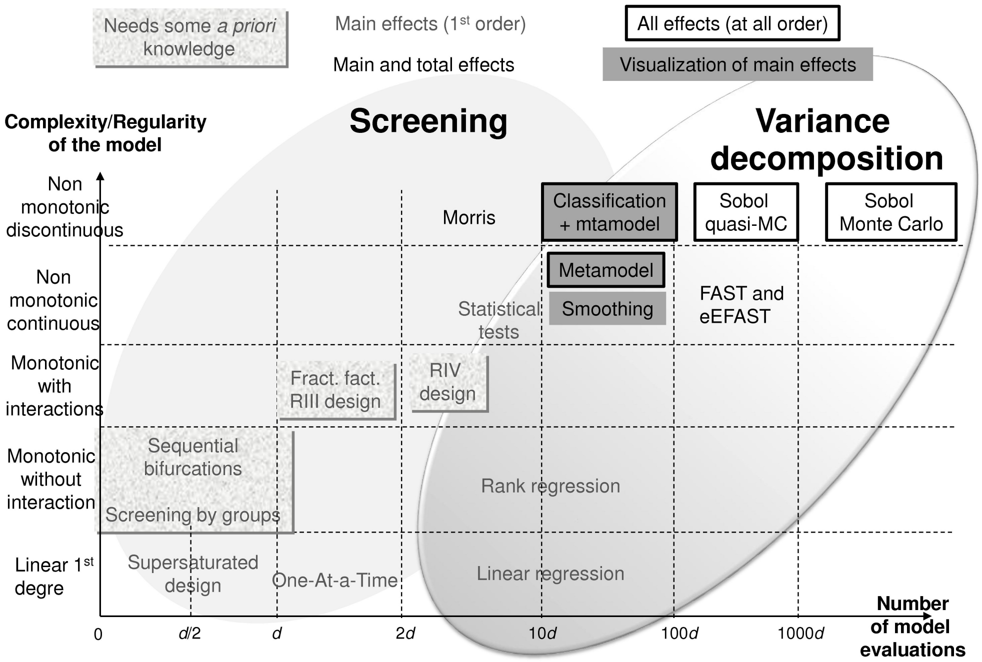

Figure 2.1: SA methods synthesis as depicted in [216]. d is the number of parameters.

However, based on this decision tree, the MSA [220] come forth as the method needing the minimum number of model evaluations for complex, non-regular and/or non-linear ones. It is widely adopted by model makers in many fields [221, 222, 223, 224]. It screens the most and least sensitive parameters with the fewer number of model simulations and can be considered as semi-quantitative method regarding the information that gives for interactions between parameters. In fact, the MSA varies one input at a time and computes the elementary effect of this variation on the system output. This computation is repeated several times for each input by following different trajectories in the input space. The mean and the standard deviation of Elementary Effect (EE) for each input are considered as the MSA indices. The input impact is assessed according to values and rankings of these indices. The stability and reliability of MSA indices are rarely investigated [225, 226, 227, 228]. MSA users refer in the most of cases to a reference book in this field [218] to fix MSA variables when performing sensitivity analysis. In fact, the mean and standard deviation are not suitable for non-normal data distributions. This condition, with the reproducibility of MSA results, is not usually verified and investigated by MSA users.

In this chapter, we will first introduce the HD-sEMG model [1, 11] in the section 2.2. Second, we will propose in section 2.3 an IMSA approach and an effective methodology to deliver reliable, stable and reproducible ranking results at a minimum computation time. Then, we will apply the new IMSA on the presented model to define parameters with small and large impacts on the HD-sEMG signals generated by a recent neuromuscular model. For this purpose, the HD-sEMG signals will be described by 23 features (e.g., amplitude, energy, frequency). Four subject categories are studied: Young Men (YM), Old Men (OM), Young Women (YW), and Old Women (OW) for evaluating both gender and aging effect on the input/output relationships. Two contraction levels are investigated to assess the sensitivity to muscle activation: Low Contraction (LC) (LC = 20% of MVC) and High Contraction (HC) (HC = 60% of MVC). The Fig. 2.2 resume the chapter workflow: describing briefly the model, proposing IMSA, comparing IMSA and MSA, and the employment of IMSA method on the HD-sEMG model. The IMSA allow us to determine the most influential parameters for each feature which can offer a useful guide-map for subsequent parameter identification. Furthermore, the IMSA will explore, evaluate and validate the modeling approach used in [1, 11]. It will assess the impact of measurement uncertainties of parameter values and evaluate the impact of muscle anatomy factors on subjects sharing the same age and health conditions. This aspect can steer the experimental effort toward a precise objectives and a development of personalized instrumental protocols.

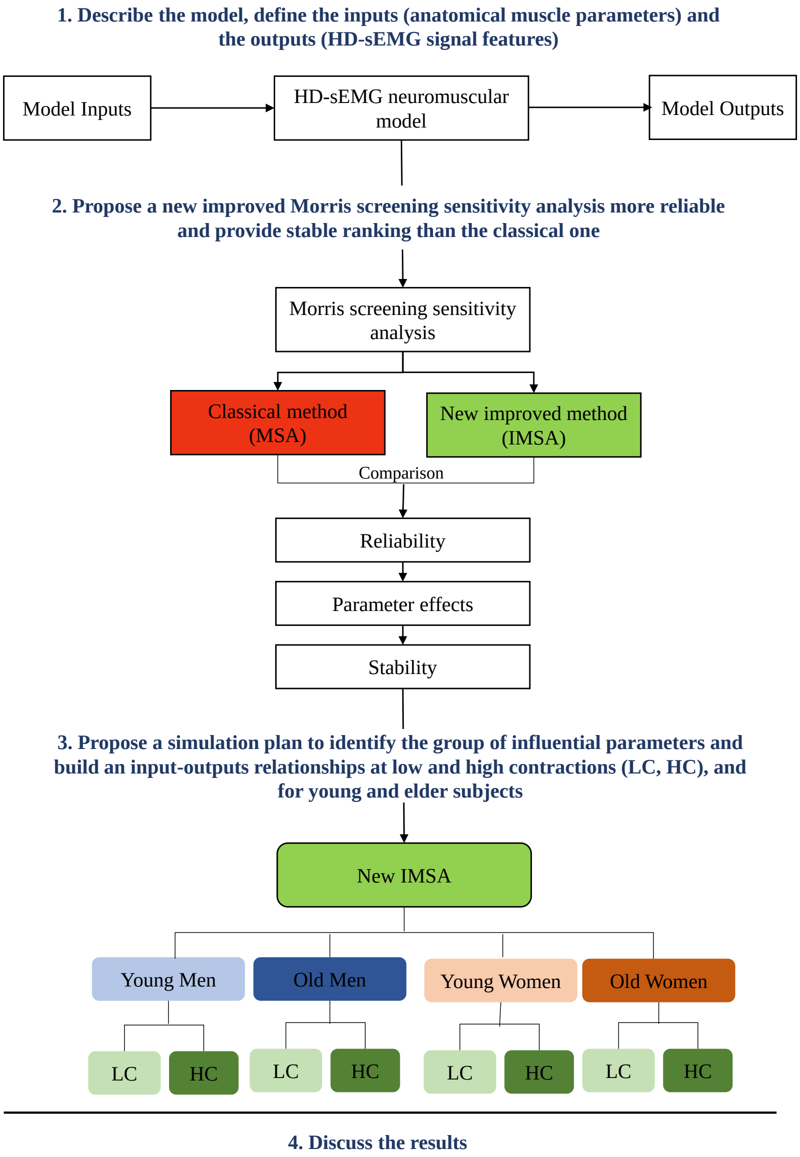

Figure 2.2: Chapter outlines.

2.2 The neuromuscular model

The neuromuscular model [1, 11] simulates the electrical activity recorded at skin surface during isometric contractions of a striated muscle (see chapter1, section 1.6.2.2). This simulation describes the generation and the propagation of muscle electrical activity through a three-layered conductor volume composed of muscle, adipose tissues, and skin. The recording channels are simulated as a high-density electrode system [202]. This model contains sub-models simulating current source (motor units: motoneuron and fibers) recruitment, its firing rate, and the force generated by the striated muscle during isometric contractions. The motor unit action potential simulated at the skin surface is computed at different levels of muscle contractions.

To perform the sensitivity analysis on this model and build a sensitivity matrix between model inputs and outputs (see Fig. 2.3), we need to: (i) well report the variation ranges of the several parameters involved in this model, and (ii) select the appropriate features describing the HD-sEMG signals (model output). In fact, we will compute the effects of input variations not on the HD-sEMG signals themselves but on features extracted from these signals. The feature extraction is the transformation of the raw signal data into a relevant data structure highlighting the important data of HD-sEMG signals [229].

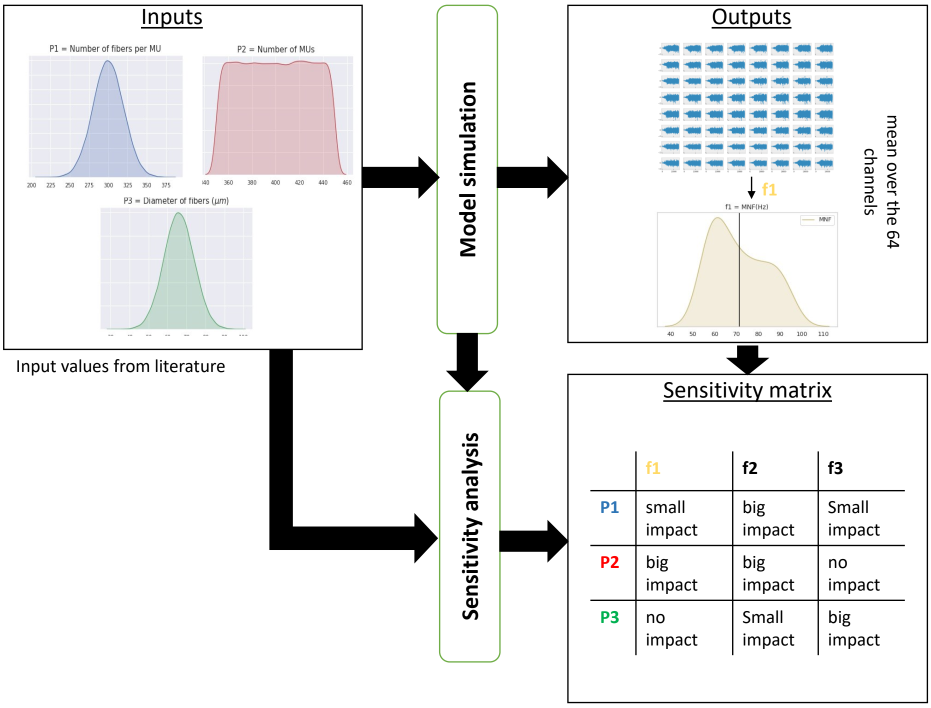

	f1	f2	f3
P1	small impact	big impact	Small impact
P2	big impact	big impact	no impact
P3	no impact	Small impact	big impact

Figure 2.3: A schematic representation of performing the sensitivity analysis method on the HD-sEMG model.

2.2.1 Model inputs

The neuromuscular model expresses the theoretical relationship of the generated HD-sEMG signals according to a specific set of parameters: neural, anatomical and physiological. It involves more than 50 parameters. To perform the sensitivity analysis, we decide to limit the analysis on 35 parameters (Table 2.1) covering the neural, anatomical and physiological muscle factors. In addition, we decide to fix 12 parameters (Table 2.2 and Table 2.3) for a reliable assessment of sensitivity analysis results. The fixed parameters describe the configuration of the electrode grid (ex: number of electrode, size of electrodes), and the source recruitment pattern (e.g., contraction level and time).

Table 2.1: List of neural, anatomical and physiological parameters involved in the sensitivity analysis. $\mathcal{U}$ uniform distribution. S: Slow, FI: Fast Intermediate, FR: Fast Resistant, FF: Fast Fatiguable. (-) No measurement unit.

Name	Description	Unit
nMU	Number Motoneuron Unit	-
MU_{dist}	Distribution of MU according to their type	(%)
MU^r_S	Radius of MU type S	mm
MU^r_{FI}	Radius of MU type FI	mm
MU^r_{FR}	Radius of MU type FR	mm
MU^r_{FF}	Radius of MU type FF	mm
n^f_{SMU}	Number of fibers per MU type S	mm
n^f_{FIMU}	Number of fibers per MU type FI	-
n^f_{FRMU}	Number of fibers per MU type FR	-
n^f_{FFMU}	Number of fibers per MU type FF	-
L	Muscle length	mm
$bone_r$	Bone radius	mm
S_{fD}	S fiber diameter	μm
FI_{fD}	FI fiber diameter	μm
FR_{fD}	FI fiber diameter	μm
FF_{fD}	FF fiber diameter	μm
$C_{velocity}$	Conduction velocity	m.s^{-1}
NMJ_{pos}	Neuromuscular junction center	-
MTZ_L	Left myotendinous length	mm
MTZ_R	Right myotendinous length	mm
ρ^c_{muscle}	Radial muscle conductivity	S.m^{-1}
θ^c_{muscle}	Angular muscle conductivity	S.m^{-1}
Z^c_{muscle}	Longitudinal muscle conductivity	S.m^{-1}
$thick_{muscle}$	Muscle thickness	mm
ρ^c_{Fat}	Radial fat conductivity	S.m^{-1}
θ^c_{Fat}	Angular fat conductivity	S.m^{-1}
Z^c_{Fat}	Longitudinal fat conductivity	S.m^{-1}
$thick_{Fat}$	Fat thickness	mm
ρ^c_{skin}	Radial skin conductivity	S.m^{-1}
θ^c_{skin}	Angular skin conductivity	S.m^{-1}
Z^c_{skin}	Longitudinal skin conductivity	S.m^{-1}
$thick_{skin}$	Skin thickness	mm
$Grid_\theta$	Angular grid center	°
$Grid_Z$	Longitudinal grid center	mm
$Grid_{rot}$	Electrode grid rotation	°

Table 2.2: Recruitment parameters needed to define the MUs recruitment

Parameter	Description	Unit
RR	Recruitment range	%MVC
a	Recruitment threshold slope	
lvl	Contraction level	%MVC
T_r	Resting time	s
T_h	Holding time	s
c_s	Contraction speed	$\%\text{MVC.s}^{-1}$
f_s	Sampling frequency	Hz

Table 2.3: Electrode grid parameters needed to define an electrode grid

Parameter	Description	Unit
n_θ	Number of electrode in θ direction	
n_z	Number of electrode in z direction	
d_θ	Inter-electrode distance in θ direction	mm
d_z	Inter-electrode distance in z direction	mm
r_e	Electrode radius	mm

Collecting input data from literature The uncertainty ranges of the 35 parameters will is defined according to literature values. Information concerning exact values for almost of these parameters is uncertain due to the complexity of muscle anatomy, the large variability of muscle configuration between subjects, and the experimental difficulty to measure an exact value or a reduced uncertain range.
We have performed electronic database searches in Pubmed and ScienceDirect. The search terms are composed usually of the biceps brachii term, the name of the parameter we search, and subject category (e.g., aged, women, young, old). The results of search are sorted by the most recent. The focus was on investigation of parameters related to the Biceps Brachii muscle. In some studies, it is designed as the Long Head Biceps (LHB) or elbow flexors and also some authors design the BB as the upper limb. In that respect, we take into account the corresponding values. Our priority was also on values reported for young and elderly people and for both women and men to explore gender and age effect. The data is selected based on the methods and technics involved in the measurement, and the clarity of information related to the age and gender of subjects. Moreover, priority was assigned to values extracted by autopsy or biopsy for some parameters like the fiber number and length. On other cases, the priority is given to recent methods of measurement like Magnetic Resonance Imaging (MRI) and imaging technics especially for defining parameters like bone radius or muscle thickness, etc. For parameters measured with surface EMG (e.g., MU number, Conduction velocity), the selection is based on the reliability of three essential factors: the performance of the recording system, the fitting of the experimental protocol used with our criteria (e.g., isometric contraction), and the reliability of the algorithms applied to extract data from recorded signals.
The table lists parameters with their potential variation ranges extracted from literature. 4 subject categories are considered according to the age and gender: young men (YM), old men (OM), young women (YW), and old women (OW).

Table 2.4: List of parameters with variation ranges extracted from literature. Values for young men (YM), old men (OM), young women (YW), and old women (OW). $\mathcal{N}$ normal distribution. $\mathcal{U}$ uniform distribution. S: Slow, FI: Fast Intermediate, FR: Fast Resistant, FF: Fast Fatigable.

Name	YM value	OM value	YW value	OW value	References
nMU	$\mathcal{U}[350, 450]$	$\mathcal{U}[250, 350]$	$\mathcal{U}[300, 400]$	$\mathcal{U}[200, 300]$	[230]
MU_{dist}	$\mathcal{N}_S(47,8)$ $\mathcal{N}_{FI}(10,11)$ $\mathcal{N}_{FR}(20,6)$ $\mathcal{N}_{FF}(29,11)$	$\mathcal{N}_S(52,8)$ $\mathcal{N}_{FI}(18,2)$ $\mathcal{N}_{FR}(15,6)$ $\mathcal{N}_{FF}(12,9)$	$\mathcal{N}_S(50,3)$ $\mathcal{N}_{FI}(10,11)$ $\mathcal{N}_{FR}(20,6)$ $\mathcal{N}_{FF}(24,7)$	$\mathcal{N}_S(56,6)$ $\mathcal{N}_{FI}(18,2)$ $\mathcal{N}_{FR}(15,6)$ $\mathcal{N}_{FF}(10,6)$	[231]
MU_S^r	$\mathcal{N}(2.5, 0.5)$	$\mathcal{N}(2.75, 0.5)$	$\mathcal{N}(2.3, 0.5)$	$\mathcal{N}(2.6, 0.5)$	[41]
MU_{FI}^r	$\mathcal{N}(2.75, 0.5)$	$\mathcal{N}(3.0, 0.5)$	$\mathcal{N}(2.6, 0.5)$	$\mathcal{N}(3.2, 0.5)$	[41]
MU_{FR}^r	$\mathcal{N}(3, 0.5)$	$\mathcal{N}(3.25, 0.5)$	$\mathcal{N}(2.8, 0.5)$	$\mathcal{N}(3.45, 0.5)$	[41]
MU_{FF}^r	$\mathcal{N}(3.25, 0.5)$	$\mathcal{N}(3.5, 0.5)$	$\mathcal{N}(3.25, 0.5)$	$\mathcal{N}(3.5, 0.5)$	[41]
n_{SMU}^f	$\mathcal{N}(240, 310)$	$\mathcal{U}(160, 210)$	$\mathcal{N}(200, 280)$	$\mathcal{U}(120, 180)$	[78, 230]
n_{FIMU}^f	$\mathcal{N}(80, 100)$	$\mathcal{U}(80, 90)$	$\mathcal{N}(70, 90)$	$\mathcal{U}(60, 80)$	[78, 230]
n_{FRMU}^f	$\mathcal{N}(100, 150)$	$\mathcal{U}(100, 140)$	$\mathcal{N}(100, 150)$	$\mathcal{U}(90, 120)$	[78, 230]
n_{FFMU}^f	$\mathcal{N}(170, 260)$	$\mathcal{U}(120, 200)$	$\mathcal{N}(150, 230)$	$\mathcal{U}(100, 180)$	[78, 230]
L	$\mathcal{U}(115, 130)$	$\mathcal{U}(95, 115)$	$\mathcal{U}(110, 120)$	$\mathcal{U}(90, 110)$	[202]
$bone_r$	$\mathcal{U}(11.7,13.2)$	$\mathcal{U}(9.5,13)$	$\mathcal{U}(10,11.4)$	$\mathcal{U}(10.5,11.9)$	[232]
S_{fD}	$\mathcal{N}(66, 9)$	$\mathcal{N}(51, 6)$	$\mathcal{N}(45, 0.4)$	$\mathcal{N}(43, 2)$	[233]
FI_{fD}	$\mathcal{N}(73,15)$	$\mathcal{N}(56,13)$	$\mathcal{N}(37,2)$	$\mathcal{N}(35,0.8)$	[233]
FR_{fD}	$\mathcal{N}(76, 15)$	$\mathcal{N}(60, 11)$	$\mathcal{N}(37,2)$	$\mathcal{N}(35,0.8)$	[233]
FF_{fD}	$\mathcal{N}(74, 15)$	$\mathcal{N}(51, 15)$	$\mathcal{N}(37,2)$	$\mathcal{N}(35,0.8)$	[233]
$C_{velocity}$	$\mathcal{U}[3.5, 5.9]$	$\mathcal{U}[2.5, 4.2]$	$\mathcal{U}[3.1, 5.5]$	$\mathcal{U}[2.3, 4.1]$	[234]
NMJ_{pos}	$\mathcal{U}[-15, 15]$	$\mathcal{U}[-15, 15]$	$\mathcal{U}[-15, 15]$	$\mathcal{U}[-15, 15]$	[1]
MTZ_L	$\mathcal{N}(15,2)$	$\mathcal{N}(15,2)$	$\mathcal{N}(15,2)$	$\mathcal{N}(15,2)$	[1]
MTZ_R	$\mathcal{N}(15,2)$	$\mathcal{N}(15,2)$	$\mathcal{N}(15,2)$	$\mathcal{N}(15,2)$	[1]
ρ_{muscle}^c	$\mathcal{U}[0.4, 0.6]$	$\mathcal{U}[0.3, 0.56]$	$\mathcal{U}[0.3,0.45]$	$\mathcal{U}[0.3, 0.56]$	[235]
θ_{muscle}^c	$\mathcal{U}[0.4, 0.6]$	$\mathcal{U}[0.3, 0.5]$	$\mathcal{U}[0.3, 0.45]$	$\mathcal{U}[0.3, 0.5]$	[235]
Z_{muscle}^c	$\mathcal{U}[0.81, 0.99]$	$\mathcal{U}[0.73, 0.96]$	$\mathcal{U}[0.53, 0.69]$	$\mathcal{U}[0.50, 0.66]$	[235]
$thick_{muscle}$	$\mathcal{N}(44, 2)$	$\mathcal{N}(40, 2)$	$\mathcal{N}(35, 4)$	$\mathcal{N}(31, 3)$	[232]
ρ_{Fat}^c	$\mathcal{U}[0.04, 0.07]$	$\mathcal{U}[0.04, 0.07]$	$\mathcal{U}[0.04, 0.07]$	$\mathcal{U}[0.04, 0.07]$	[236]
θ_{Fat}^c	$\mathcal{U}[0.04, 0.07]$	$\mathcal{U}[0.04, 0.07]$	$\mathcal{U}[0.04, 0.07]$	$\mathcal{U}[0.04, 0.07]$	[236]
Z_{Fat}^c	$\mathcal{U}[0.04, 0.07]$	$\mathcal{U}[0.04, 0.07]$	$\mathcal{U}[0.04, 0.07]$	$\mathcal{U}[0.04, 0.07]$	[236]
$thick_{Fat}$	$\mathcal{U}[4,6]$	$\mathcal{U}[4,8]$	$\mathcal{U}[4,6]$	$\mathcal{U}[4,9]$	[237]
ρ_{skin}^c	$\mathcal{U}[0.9, 1.2]$	$\mathcal{U}[0.9, 1.2]$	$\mathcal{U}[0.9, 1.2]$	$\mathcal{U}[0.9, 1.2]$	[236]
θ_{skin}^c	$\mathcal{U}[0.9, 1.2]$	$\mathcal{U}[0.9, 1.2]$	$\mathcal{U}[0.9, 1.2]$	$\mathcal{U}[0.9, 1.2]$	[236]
Z_{skin}^c	$\mathcal{U}[0.9, 1.2]$	$\mathcal{U}[0.9, 1.2]$	$\mathcal{U}[0.9, 1.2]$	$\mathcal{U}[0.9, 1.2]$	[236]
$thick_{skin}$	$\mathcal{U}[0.9,1.2]$	$\mathcal{U}[0.9,1.2]$	$\mathcal{U}[0.9,1.2]$	$\mathcal{U}[0.9,1.2]$	[235]
$Grid_\theta$	$\mathcal{U}[0,5]$	$\mathcal{U}[0,5]$	$\mathcal{U}[0,5]$	$\mathcal{U}[0,5]$	[1]
$Grid_Z$	$\mathcal{U}[22,26]$	$\mathcal{U}[22,26]$	$\mathcal{U}[22,26]$	$\mathcal{U}[22,26]$	[1]
$Grid_{rot}$	$\mathcal{U}[0,10]$	$\mathcal{U}[0,10]$	$\mathcal{U}[0,10]$	$\mathcal{U}[0,10]$	[1]

2.2.2 Model output

The main output of the model is the 64 HD-sEMG signals. In order to correlate these signals to the physiological and anatomical muscle properties, many features are extracted from raw signals. These features are considered as the model outputs. Table 2.5 summarize all the features extracted from the HD-sEMG signals and considered as the model outputs for this study. Features depicted in Table 2.5 are classified according to their computation algorithm techniques (Fig. 2.4). We have classified features into monovariate and bivariate subgroups, according to the fact of using one electrode channel or two. Then, the monovariate features are classified either as time, frequency domain or non-linear based algorithms.

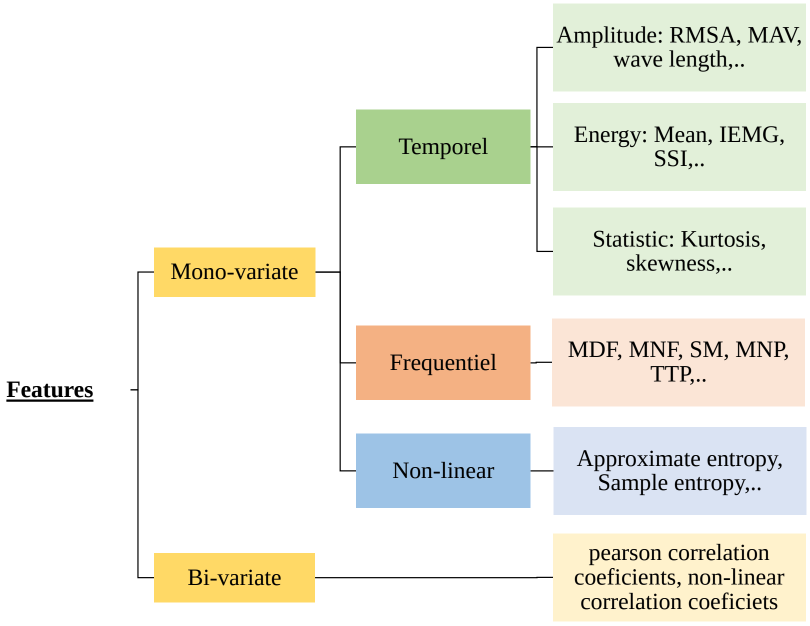

Figure 2.4: Classification of HD-sEMG features.

Table 2.5: List of Features extracted from the HD-sEMG and considered as the model outputs.

Feature classes	Feature name	Abbreviation
Time domain	1.Root Mean Square of Amplitude	RMSA
	2.Integrated EMG	IEMG
	3.Mean Absolute Value	MAV
	4.Modified Mean Absolute Value 1	MAV1
	5.Modified Mean Absolute Value 2	MAV2
	6.Wilson Amplitude	wilson_amp
	7.Kurtosis	Kurt
	8.Skewness	Skew
	9.Variance of EMG	Var
Non-linear	10.Approximate entropy	ap_ent
	11.Sample entropy	sp_ent
Frequency domain	12.Median frequency	MDF
	13.Mean frequency	MNF
	15.Mean power	MNP
	16.Peak frequency	Peak_f
	17.Frequency ratio	Freq_r
	18.Spectral moment 0 (Total power)	SM_0 (TTP)
	19.Spectral moment 1	SM_1
	20.Spectral moment 2	SM_2
	21.Spectral moment 2n (Variance of central frequency)	SM_{2n}(VCF)
	22.Spectral moment 3	SM_3
Bivariate	23.Pearson correlation coefficient	R_2
	24.Non-linear correlation coefficient	H_2

2.2.2.1 Monovariate approach

Time domain features

Root mean square of amplitude (RMSA) The RMSA is a popular amplitude/time domain feature in the EMG signal analysis, known also as "EMG amplitude detector". This popularity is due to his capacity to assess the main force generated by the muscle through the estimating of the level of the isometric voluntary contraction. In this study, the RMSA is defined as the square root of the signal mean over time, and in addition, over the all electrode signals. Thus, the RMSA is defined as:

$$RMSA = \frac{1}{N_e}\sum_{j=1}^{N_e}(\sqrt{\frac{1}{n}\sum_{i=1}^{n}(Y_j(i)^2)} \tag{2.1}$$

Where N_e is the number of the grid-electrodes, n is the length of electrode EMG signal, and Y_j is the EMG signal of electrode j.

Integrated Electromyography signal (IEMG) The IEMG gives the total amount of muscle activity during a given duration of the signal gives integration value. More amplitude, duration and frequency of action potentials lead to the large value of integration. The IEMG feature is defined as:

$$IEMG = \frac{1}{N_e}\sum_{j=1}^{N_e}(\frac{1}{n}\sum_{i=1}^{n}Y_j(i)) \tag{2.2}$$

Where N_e is the number of the grid-electrodes, n is the length of electrode EMG signal, and Y_j is the EMG signal of electrode j.

Mean and modified absolute value (MAV, MAV1, MAV2) The mean absolute value MAV represents the area under the EMG signal once it has been rectified (all of the negative voltage values have been made positive). The modified absolute value MAV1 and MAV2 are an extension of MAV, using weighting window function to improve the robustness of MAV. These three features provide a best indicator of the total muscle effort.

$$MAV = \frac{1}{N_e}\sum_{j=1}^{N_e}(\sqrt{\frac{1}{n}\sum_{i=1}^{n}|Y_j(i)|}) \tag{2.3}$$

$$MAV1 = \frac{1}{N_e}\sum_{j=1}^{N_e}(\sqrt{\frac{1}{n}\sum_{i=1}^{n}w_i|Y_j(i)|}), \quad \text{with} \quad w_i = \begin{cases} 1, \ \texttt{if} \ \ 0.25n \leq i \leq 0.75n \\ 0.5, \ \texttt{otherwise} \end{cases} \tag{2.4}$$

$$MAV2 = \frac{1}{N_e}\sum_{j=1}^{N_e}(\sqrt{\frac{1}{n}\sum_{i=1}^{n}w_i|Y_j(i)|}), \quad \text{with} \quad w_i = \begin{cases} 1, \ \texttt{if} \ \ 0.25n \leq i \leq 0.75n \\ \frac{4i}{n}, \ \texttt{if} \ \ i < 0.25n \\ 0.5, \ \texttt{otherwise} \end{cases} \tag{2.5}$$

Where N_e is the number of the grid-electrodes, n is the length of electrode EMG signal, Y_j is the EMG signal of electrode j, and w_i is weighting function.

Willson amplitude (wilson_amp) The wilson_amp computes the number of time resulting from the difference between EMG signal amplitude of two adjoining segments that exceeds a predefined threshold. This measure can quantify the firing of motor unit action potentials and muscle contraction level.

$$wilson\_amp = \frac{1}{N_e}\sum_{j=1}^{N_e}(\frac{1}{n}\sum_{i=1}^{n} f_j(|Y_j(i+1) - Y_j(i)|)) \quad with \quad \begin{cases} 1 \texttt{ if } Y \geq threshold \\ 0 \texttt{ otherwise} \end{cases} \tag{2.6}$$

Where N_e is the number of the grid-electrodes, n is the length of electrode EMG signal, and Y_j is the EMG signal of electrode j.

Kurtosis (Kurt) The Kurtosis is a measure of whether the a sample distribution (histogram) is are peaked or flat relative to a normal distribution. For healthy patients, The Kurtosis values decreases when the muscle contraction levels increases. Moreover, it was observed that the probability density function of EMG signal at isometric, non-fatiguing, low contraction levels is super-Gaussian (have more spiky peak and a longer tail than a Gaussian distribution) [238].

$$Kurt = \frac{1}{N_e}\sum_{j=1}^{N_e}(\frac{E(Y_j - \mu_{Y_j})^4}{\sigma_{Y_j}^4}) \tag{2.7}$$

Where N_e is the number of the grid-electrodes, and Y_j is the EMG signal of electrode j, $E(.)$ the expectation operator, and μ_{Y_j} and σ_{Y_j} are the expected values and standard deviation of the signal Y_j.

Skewness (Skew) The Skewness assesses the asymmetry of a distribution. It is defined as the third standardized moment.

$$Skew = \frac{1}{N_e}\sum_{j=1}^{M}(\frac{E(Y_j - \mu_{Y_j})^3}{\sigma_{Y_j}^3}) \tag{2.8}$$

Where N_e is the number of the grid-electrodes, and Y_j is the EMG signal of electrode j, $E(.)$ the expectation operator, and μ_{Y_j} and σ_{Y_j} are the expected values and standard deviation of the signal Y_j.

Variance (Var) The Var is the mean of square of signal deviation. It can give a clear cut difference between healthy subjects and person with muscular diseases

$$Var = \frac{1}{N_e}\sum_{j=1}^{N_e}(\frac{1}{n-1}\sum_{i=1}^{n}(Y_j(i)^2) \tag{2.9}$$

Where N_e is the number of the grid-electrodes, n is the length of electrode EMG signal, and Y_j is the EMG signal of electrode j.

Approximate and sample entropy (ap_ent, sp_ent) Approximate entropy (ap_ent) was introduced by [239] to quantify the irregularity and complexity of a time series. Time series data that are more irregular or entropic over time are considered more complex than those that show irregular behavior at only a single time scale [3]. The more deterministic time series present a high degree of regularity. Therefore, higher is the regularity, lower is ap_ent. To calculate ap_ent of one electrode EMS signal $Y(i)$ of n values, one should first set an embedding dimension m and a distance threshold r and then:

1. Form a series of $n-m+1$ vectors of m components $G(i) = [Y(i), Y(i+1), \ldots, Y(i+m)]^T$;
2. Compute the distance between any couple of vectors $G(i)$ and $G(k)$ as the largest absolute difference between the corresponding scalar components (if the difference is less than the distance r the two vectors are similar);
3. Count $nG_i^m(r)$, number of the $n-m+1$ vectors $G(k)$ similar to $G(i)$ and the probability to find a vector similar to $G(i)$ as:
$$C_i^m(r) = \frac{nG_i^m(r)}{n-m+1} \tag{2.10}$$
4. Calculate $C^m(r)$ as the average of $C_i^m(r)$ for all the vectors $G(i)$;
5. Repeat the steps from 1 to 4 for the embedding dimension $m+1$.

Then the ap_ent of $Y(i)$ is calculated as:

$$ap\_ent = -\ln\left(\frac{C^{m+1}(r)}{C^m(r)}\right) \tag{2.11}$$

The sample entropy (sp_ent) is originally proposed by [240] as a refinement of the approximate entropy (ap_ent) introduced by [239]. The sp_ent is computed in the same way as the ap_ent and is given by the same equation (eq. 2.11). However, to reduce the bias avoiding self-comparison between vectors, it calculates $nG_i^m(r)$ (the number of vectors similar to $G(i)$) for all the vectors $G(k)$ excluding $k = i$.
It is recommended [241] to use $r \cong (0.15-0.25)*sd$, where the sd is the standard deviation $Y(i)$.

Frequency domain features The frequency domain or spectral domain features are useful in the analyzing of MUs recruitment [200, 242, 243]. To transform the EMG signal in the time-domain to the frequency-domain, a Fourier transform of the autocorrelation function of the EMG signal is employed to provide the Power Spectral Density (PSD). The PSD describes how power of a signal is distributed over frequencies. To estimate the PSD, there are parametric and non-parametric methods [244]. The parametric methods assume that the data follows a certain model, and the non-parametric methods do not make any assumption on the data structure [244]. From the non-parametric methods, the most commonly used PSD estimator in the EMG signal analysis is the periodogram: the Bartlett method (1948), the Blackman and Tukey method (1958), and the Welch method (1967). In this study, we employ the Welch method to estimate the PSD [245].

Power spectral density (PSD): Welch method There are several steps to compute PSD with the Welch method (see [245]). Briefly, this method involves: 1) Partitioning the signal into M segments; 2) For each segment ($k = 1$ to M), computing a windowed discrete Fourier transform (DFT) at some frequency f; 3) For each segment, forming a modified periodogram value $P_k(f)$ from the DFT. Finally, the calculated periodogram values from different windows are averaged and the PSD estimate is obtained:

$$P(f) = \frac{1}{K}\sum_{k=1}^{K} P_k(f) \tag{2.12}$$

In this study, to compute the PSD of the HD-sEMG signals, we will use a Hanning window function and a sampling rate equal to 2048 Hz. As consequence, from an electrode signal $Y(t)$ of length n , we will obtain a representation of the PSD $P(Hz)$ of size M.
We can then extract several descriptors from this PSD. Those that we have used for the sensitivity analysis are:

Median Frequency (MDF) and Mean Frequency (MNF) MDF is the frequency at which the spectrum is divided into two regions with equal amplitudes. It is defined as :

$$MDF = \sum_{j=1}^{MDF} P_j/M = \sum_{j=MDF}^{M} P_j/M = \frac{1}{2}\sum_{j=1}^{M} P_j/M \tag{2.13}$$

MNF is the frequency average. It is defined as:

$$MNF = \sum_{j=1}^{M} f_j P_j / \sum_{j=1}^{M} P_j \tag{2.14}$$

Where f_j is the frequency value of EMG power spectrum at the frequency bin j, P_j is the EMG power spectrum at the frequency bin j, and M is the length of frequency bin. The variation of mean frequency power may assess the frequency work of slow and fast MUs knowing what kind of MUs are recruited for each level of isometric contractions. The MDF and the MNF shifted to lower frequencies at the isometric contractions which is an indice of muscle fatigue [246]. The authors in [247] reveal that the increase of isometric contraction level cause the increase of the MDF slope which is an indicator of fiber strategies recruitment.

Mean power (MNP) MNP is an average power of EMG power spectrum.

$$MNP = \sum_{j=1}^{M} P_j/M \tag{2.15}$$

Peak frequency (Peak_f) Peak_f is a frequency at which the maximum EMG power spectrum occurs.

$$Peak\_f = Max(P_j), \qquad j = 1, ..., M \tag{2.16}$$

Frequency ratio (Freq_r) The Freq_r is used to discriminate between relaxation and contraction of the muscle using a ratio between low- and high-frequency components of EMG signal

$$Freq\_r = \frac{P_0}{P} = \sum_{j=LLC}^{ULC} P_j / \sum_{j=LHC}^{UHC} P_j \tag{2.17}$$

Where ULC and LLC are respectively the upper- and the lower-cutoff frequency of low-frequency band, and UHC and LHC are respectively the upper- and the lower-cutoff frequency of high-frequency band.

Spectral moments (SM) SM is an alternative statistical analysis way to extract feature from the power spectrum of EMG signal [248, 200, 242]. Their equations can be defined as:

$$SM_0 = \sum_{j=1}^{M} P_j \tag{2.18}$$

$$SM_1 = \sum_{j=1}^{M} P_j f_j \tag{2.19}$$

$$SM_2 = \sum_{j=1}^{M} P_j f_j^2 \tag{2.20}$$

$$SM_{2n} = \frac{1}{SM_0} \sum_{j=1}^{M} P_j (f_j - MNF)^2 = \frac{SM_2}{SM_0} - (\frac{SM_1}{SM_0})^2 \tag{2.21}$$

$$SM_3 = \sum_{j=1}^{M} P_j f_j^3 \tag{2.22}$$

We will name SM_0 as TTP (Total power) and SM_{2n} as VCF (variance of the central frequency) in the next paragraphs.

2.2.2.2 Bivariate approach

This approach evaluates the similarity between between two signals of length n. The two signals Y_1 and Y_2 are selected from the 64 signals of the HD-sEMG electrode grid described previously.

Linear correlation coefficient (R_2) The linear correlation, also called Pearson correlation efficiency, measures the dependence between the two signals Y_1 and Y_2.

$$R_2 = \frac{\sum_{k=1}^{n} (Y_1(k) - \mu_{Y_1})(Y_2(k) - \mu_{Y_2})}{\sqrt{\sum_{k=1}^{n} (Y_1(k) - \mu_{Y_1})^2 \sum_{k=1}^{n} (Y_2(k) - \mu_{Y_2})^2}} \tag{2.23}$$

Where μ_{Y_1} and μ_{Y_2} are, respectively, the average of Y_1 and Y_2. The coefficient R_2 ranges from -1 to +1. A -1 means there is a strong negative correlation and +1 means that there is a strong positive correlation. A 0 means that there is no correlation.

Non-linear correlation coefficient (H_2) The main idea of the H_2 coefficient is that if the value of Y_1 is considered as a function of the value of Y_2, the value of Y_2 given Y_1 can be predicted according to a nonlinear regression curve [249]. The nonlinear correlation coefficient between Y_1 and Y_2 is then computed using the following equation:

$$H_2 = \frac{\sum_{k=1}^{n} Y_2(k)^2 - \sum_{k=1}^{n} (Y_2(k) - f(Y_1(k)))^2}{\sum_{k=1}^{n} Y_2(k)^2} \tag{2.24}$$

where $f(Y_1)$ is the linear piecewise approximation of the nonlinear regression curve (for more details see [249]). The estimator H_2 ranges from 0 (independent signals) to 1 (correlated signals).

2.2.3 Computation time

The sensitivity analysis are achieved by running the model for many different samples of the parameter space to determine their impact on the model outputs. If the model has a high computational time, the employment of sensitivity analysis methods will be not possible, limited or computationally highly expensive [216]. Which is the case of the most of models simulating the electrical activity of striated muscles. However, the author of this HD-sEMG model [1, 11] have proposed a fast generation model of muscle electrical

activity computed at the motor unit (MU) scale (summation of hundred of sources) rather than at fiber scale (summation of many hundreds of thousand sources). The implementation and the computation workflow of this model well be detailed in the next chapter 3. Next to the MU scale computing, the model computation time can significantly decrease by optimal programming/implementing strategies. The Table 2.6 shows the computation time of the neuromuscular model for the same simulations (high an low muscle contractions) in two different computing configurations (serial and parallel) [1]. According to this Table, parallel computation time of the HD-sEMG signals using the electrical macro source model corresponds approximately to 1% of serial computation time. The use of 10 threads (Table 2.6) increases significantly the model speedup. As consequence, the development in computer sciences can resolve one crucial feature about modeling which is the computation time. This model speedup promotes high costly processes relevant in medical applications and diagnostic of muscle diseases (e.g., sensitivity analysis and parameter identification).
Taking advantage of this model speedup, we will assess the Morris sensitivity analysis method at high number of samples in the parameter space in the next section.

Table 2.6: Computation time of the neuromuscular model (MUs sources) to simulate HD-sEMG during 5 seconds of isometric contractions at three force levels: 20, 40, and 60% of the MVC (Maximal Voluntary Contraction). Comparison between computation time using signals serial computing (1 thread) and parallel computing (10 threads). Workstation: 2×8 cores Intel Xeon 2.40 GHz with hyperthreading (32 threads), 128 Go RAM, Ubuntu 14.04 64bits

Number of used process	**Level of force contractions**		
	20% of MVC	**40% of MVC**	**60% of MVC**
Serial (1 thread)	20min03s	27min50s	38min10s
Parallel (10 threads)	1min56s	3min03s	4min10s

2.3 Morris screening sensitivity analysis

2.3.1 Classical Morris Sensitivity Analysis (MSA)

The MSA method is based on the discretization of variation ranges of inputs n into l levels at where each input is varied while fixing the rest. This process is known as One At a Time design (OAT). The n-dimensional space is thus transformed in n-dimensional l-level grid. Variation ranges of inputs are defined for each of the parameters and then sized to obtain a dimensionless interval for all parameters (between 0 and 1). The Fig. 2.5 shows an illustration case of creating an input space with $n = 3$ and $l = 4$.

The algorithm of trajectory construction starts at a randomly chosen point in the n-dimensional space (Fig. 2.5) and creates a trajectory through all the n-dimensional variable space. The trajectory is built with $n + 1$ points. Two adjacent points differ by standardized step Δ only in one dimension of the n-dimensional variable space. The coordinates of every point of the single trajectory are used as input values to the computational algorithm. Step-by-step construction of the single trajectory for $n = 3$ parameters is presented in Fig. 2.6. In the construction of the single trajectory, it is assumed that each input factor is varied with a discrete number of values, called levels l.

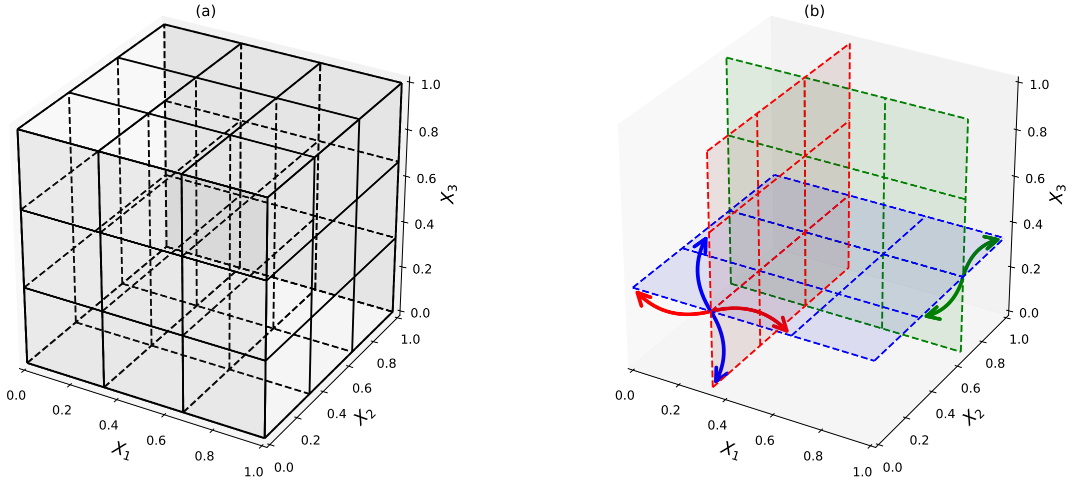

Figure 2.5: (a) Illustration of creating an input space of three parameters ($n = 3$). All parameters are subdivided into $l = 4$ levels. (b) Each parameter can changes value with a Δ step.

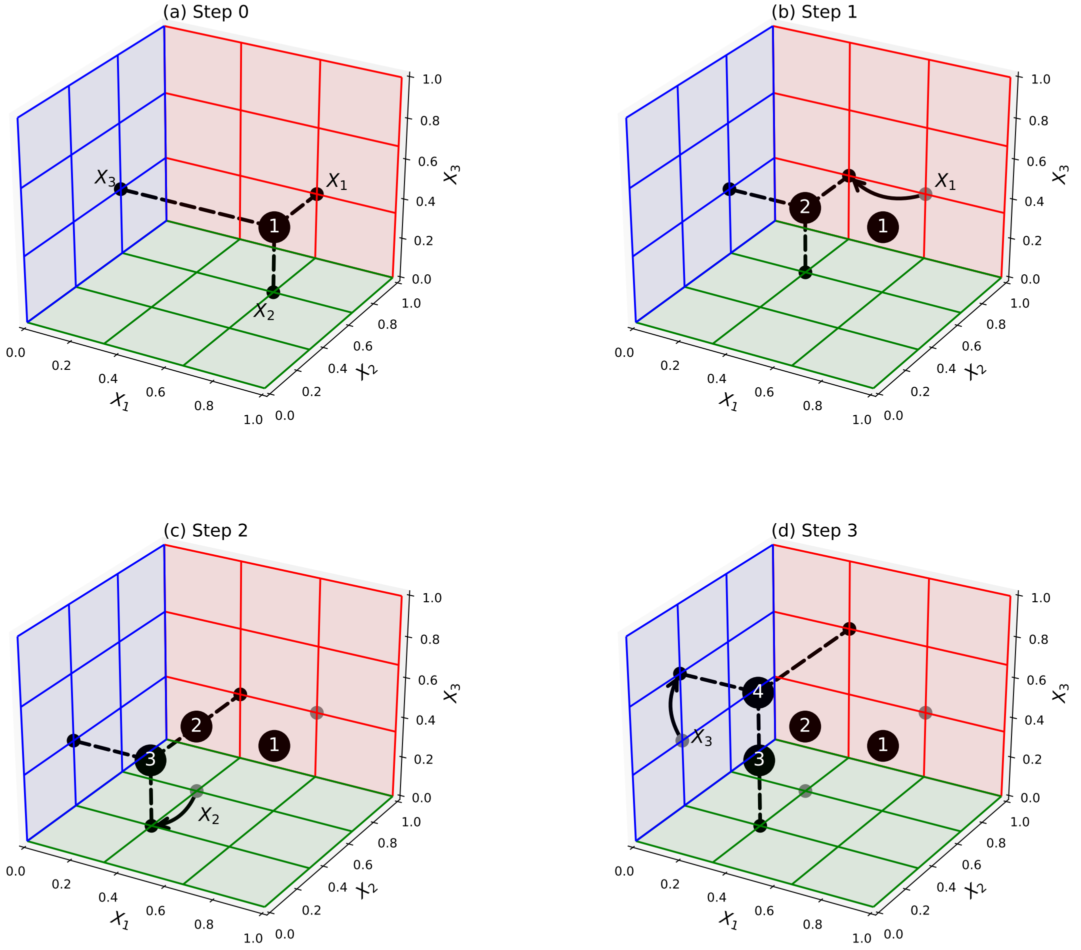

Figure 2.6: An example of a single trajectory T constructed of three-dimensional input space ($n = 3$, inputs $= \{X_1, X_2, X_3\}$). The trajectory is built with 4 points ($n + 1$). (a) Step 0: the first point is randomly chosen; (b) Step 1: Only X_1 can change value by Δ step; (c) Step 2: Only X_2 can change value by Δ step; (d) Step 3: Only X_3 can change value by Δ step.

The elementary effect of this variation on the model output is computed by the following equation:

$$EE_{jk} = \frac{y_k(X_1, ..., X_j + \Delta, ..., X_n) - y_k(X_1, ..., X_j, ..., X_n)}{\Delta} \tag{2.25}$$

Where, EE_{jk} is the elementary effect of input j on the k^{th} model output, Δ is a predetermined perturbation factor of X_j, $y_k(X_1, X_2, ..., X_j, ..., X_n)$ is the scalar model output evaluated at inputs $(X_1, X_2, ..., X_j, ..., X_n)$, while $y_k(X_1, X_2, ..., X_j + \Delta, ..., X_n)$ is the scalar output corresponding to a Δ changes in X_j, and n is the total number of inputs.

To obtain a reliable impact of inputs, Morris in [220] suggests to repeat computation of EE_{jk} for each input several times. At each time, the input changes its value in a new configuration inside the input space. A number, T, of different trajectories through variable space have to be constructed. Trajectories respect the one at a time design: only one input can change its value through levels l by jumping only by one step Δ at each time. The step Δ depends of l (Fig. 2.6). The total number of points for each trajectory is equal to $n+1$ (the total number of model evaluation to deliver Morris sensitivity analysis result for all parameters is equal to $T * (n + 1)$). The mean (μ, equation 3.11) and the standard deviation (σ, equation 3.12) of all elementary effects (EE) for each input over its T trajectories are proposed as MSA indices by Morris in [220].

$$\mu_{jk} = \frac{1}{T}\sum_{i=1}^{T} EE_{jk} \tag{2.26}$$

$$\sigma_{jk} = \sqrt{\frac{1}{T}\sum_{i=1}^{T} (EE_{jk} - \mu_{jk})^2} \tag{2.27}$$

The mean μ assesses the input influence on the model output. The σ estimates possible non-linear effect and/or interactions between inputs. However, for non monotonic and non-linear models, the distribution of elementary effects can contains positive and negative elements. In this case, the μ cannot give an exact impact of inputs due to the sign effect of EE. The study [250] suggests the use of EE absolute values (μ^*, equation (3.13)) as a reliable and complement MSA indicator.

$$\mu^*_{jk} = \frac{1}{T}\sum_{i=1}^{T} |EE_{jk}| \tag{2.28}$$

Many variables are involved in the MSA method: the number of levels (l), the sampling strategy, the number of trajectories (T), the distributions of the EE, and their averaging mode. However, it does not exist in the literature a completed and reliable study or guide to adjust these variables for complex models. Studies and users, in the literature, deliver MSA results without justifying the adjustment of the method variables, and in most of times without giving values of these variables.

Moreover, an investigation of the MSA indices adequacy related to its statistical significances was not reviewed properly. The mean and the standard deviation are adapted to normal distributions or large samples of elementary effects. Recently, few studies have evaluated the stability of MSA results. The Table 2.7 lists all studies evaluating MSA method variables in different fields. This evaluations are limited to only stability criteria in a restricted domains and low order model (small computation time).

Table 2.7: List of studies assessing the MSA method variables to obtain stable ranking with MSA method. (∗) missed information in the study

Study	field	T	levels l	Parameter number n
[251]	oceanology	500	*	20
[222]	Thermo-chemical	50	6	30
[221]	Hydrology	20	*	30
[223]	Energy	*	*	50
[252]	Hydrology	50	8,4	20
[253]	Environment	200	*	20
[228]	Materials	100<>600	*	*
[226]	Building	>=100	>=4	*
[254]	Agriculture	50	8	*
[224]	Energy	500	2, 4, 6, 8, 10, 12	24

2.3.2 Improved Morris Sensitivity Analysis (IMSA)

The philosophy of MSA is to give two approximate indicators quantifying and qualifying a set of elementary effects (EE). Mathematically, the two indicators are the expectation of EE ($\mu = \mathbb{E}(EE)$) and its dispersion ($\sigma^2 = var(EE)$). The original MSA performs the mean as estimator of μ and the root mean square deviation as estimator of σ^2 (equations (3.11) and (3.12)). Statistically, these two indices/estimators gives a reliable characterization of a Laplace-Gaussian distribution. Where the mean (μ) is an unbiased estimator of the expectation, and (σ^2) is asymptotically unbiased estimator of dispersion/variance (biased for small set of data).

However, the symmetry and Gaussianity of EE distributions are not evident for complex models. In addition, with MSA method, it is common to compute indices from small samples (small T). As consequence, the credibility of μ and σ^2 cannot be established. In this study, we propose new indices more adapted to asymmetric and non Gaussian sample distribution: the absolute median (χ^*, equation (2.29)) and the median absolute deviation (ρ, equation (2.30)). These two indices are more robust to extremely high and low outliers values and more efficient for non-normal shapes of EE distributions.

$$\chi^*_{jk} = |EE_{jk}|_{(T+1)/2} \tag{2.29}$$

$$\rho_{jk} = (|EE_{jk}| - \chi_{jk})_{(T+1)/2} \tag{2.30}$$

Reproducibility of IMSA indices ranking The IMSA requires $T * (n+1)$ model evaluations, where n is the number of inputs. The variable T have an important impact on the computation cost: high value of T increases the computation time, when a very small value can gives wrong input impacts. In this study, we keep the original MSA design (sampling strategy), and we investigate the stability of IMSA indices through eight scales of T: from 10 to 100. The purpose is to define at which value of T the stability and reproducibility are guaranteed. In particular, the minimum value of T needed for reliable and convergent indices. Table 2.8 summarizes the total number of model simulations needed for each trajectory T and the correspondent computing time. We should note that MSA and IMSA run in the same computation time since they use the same sampling strategy of the input space and the same calculator. Method indices

are computed afterwards.
The stability is assessed with: 1) an individual ranking of parameters using MSA and IMSA indices, and 2) a ranking by group of parameters sharing the same influence/effect.

1. For individual ranking, the stability is evaluated with a numerical position factor as proposed in [255]:
$$PF^{\{\mu^*,\chi^*\}}_{T_i \to T_j} = \sum_{p=1}^{p} \frac{|R^{\{\mu^*,\chi^*\}}_{r,i} - R^{\{\mu^*,\chi^*\}}_{r,j}|}{\{\mu^*,\chi^*\}_{R_{p,i}R_{p,j}}} \tag{2.31}$$
   Where $R_{r,i}$ and $R_{r,j}$ are the position/ranking of parameter p at T_i and T_j respectively, and $\{\mu^*,\chi^*\}_{R_{p,i}R_{p,j}}$ is the ranking average of parameter p obtained by T_i and T_j with MSA or IMSA method. The position factor $PF^{\{\mu^*,\chi^*\}}_{T_i \to T_j}$ evaluates the ranking changes of all parameters between two different trajectories for MSA or IMSA indices (μ^* and χ^* respectively). In fact, low value of $PF^{\{\mu^*,\chi^*\}}_{T_i \to T_j}$ indicates a small ranking variation between T_i and T_j. Furthermore, the average position obtained by T_i and T_j: $\{\mu^*,\chi^*\}_{R_{p,i}R_{p,j}}$ reduces the position changes of negligible parameters. As consequence, the smallest obtained $PF_{T_i \to T_j}$ with a posterior stable values, indicates that T_j is the minimum trajectory needed for convergent and reliable indices.

2. To evaluate the stability of ranking by group of parameters sharing the same impact on the model output, we decide to perform the ranking task according to the influence threshold concept. Thresholds are fixed to define from which value of MSA and IMSA indices the impact of each input is considered important or not. To define this concept, we have fixed the following thresholds : (i) The input is considered in influential group if its EE average varies more than 20% of the model output($\chi^* > 20\%$, $\mu^* > 20\%$), or the dispersion of its EE is bigger than this value ($\rho > 20\%$, $\sigma > 20\%$), or both. (ii) If χ^* or ρ and respectively μ^* or σ have values causing less than 5% of output variation: the input is considered with negligible effect (non-influential group), (iii) parameters situated between these values (5% and 20%) are classified in the intermediate impact group. Then, we test the stability of indices by increasing T values. We should note that thresholds are fixed at 20% and 5% of the model output as illustrative example to perform parameter rankings with this concept. In fact, threshold values depend of the studied model.

Reliability of IMSA indices Classically, MSA users apply the ratio σ/μ^* to define linearity and monotonicity of input impacts. This ratio appears firstly in [256]. Since, it was performed by the majority of studies applying MSA. In this study, we evaluate the reliability of this ratio with new IMSA indices. Based on normal distribution statistics, authors in [256] estimate that σ/μ^* is an indicator of almost linear effects (if < 0.1) or monotonic effects (if < 0.5). To define linearity and monotonicity of parameter effects with IMSA indices, we propose to perform the following steps:

1. Test the normality of EE distributions around χ^* and ρ. For this purpose, we have performed a Kolmogorov-Sminov non parametric goodness-of-fit test in the present study [257, 258].

2. Given that EE distributions are normal, we use the statical property: 95% of EE are within a range $\chi^*_r \pm 1.96\rho_r$, to define (non)linearity and (non)monotonicity of EE as justified below:

Table 2.8: Computation time and number of model evaluations needed for each T. The computation time was obtained using 32 parallel threads (workstation: 2×24 cores, Intel Xeon Platinum 8160 X7542, 2.1 Ghz, 1 To RAM).

Number of trajectories (T)	Number of model evaluations	Computation time (32 parallel processes)
10	360	03h25min
20	720	06h02min
30	1080	10h49min
40	1440	15h40min
50	1800	20h28min
60	2160	25h54min
80	2880	37h39min
100	3600	42h35min

- If $\rho_r/\chi_r^* < 0.1$: most EE are in a range ±20% around χ^* (Fig. 2.7 : 95% of EE values are within $\chi_r^* \pm 1.96 * 0.1\chi_r^* \approx \chi_r^* \pm 0.2\chi_r^*$). As consequence, most EE can be considered as constant and the input r has an almost linear and monotonic effect (linear effect when $\rho_r/\chi_r^* = 0$).

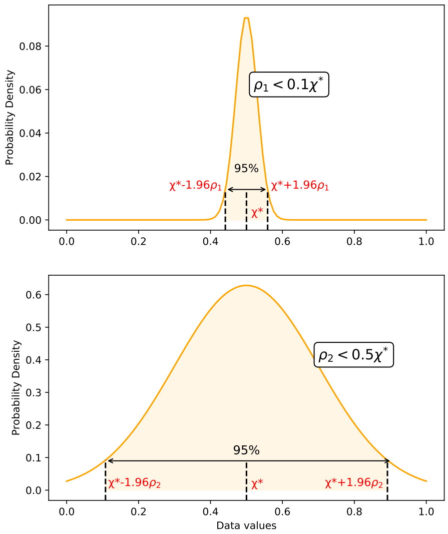

Figure 2.7: The shape of EE probability density function according to the ratio ρ_r/χ_r^*.

- If $\rho_r/\chi_r^* < 0.5$: 95% of EE are within $\chi_r^* \pm 2 * 0.5\chi_r^* = \chi_r^* \pm \chi_r^*$ which is always positive. As consequence, most EE have the same sign (monotonic effect of input r).

By applying these assumptions, we can use the ratio ρ_r/χ_r^* as graphic indicator of (non)linearity and (non)monotonicity of EE in the input screening with the IMSA method.

2.3.3 Assessment of the IMSA approach

2.3.3.1 Results

To evaluate the reliability of sensitivity analysis using classical MSA and the new IMSA methods, we will: (1) test the normality of elementary effect distributions according to MSA and IMSA indices, (2) test the stability and reproducibility of indices when changing/increasing T values, and (3) compare between MSA and IMSA results according to these two previous criteria.

Evaluation of EE distributions To investigate the reliability of parameter ranking with MSA and IMSA indices, we analyze the elementary effects (EE) distributions. The Fig. 2.8 shows the EE distributions of the 35 parameters involved in the neuromuscular model. The EE are computed on the mean RMSA output at $T = 30$ (Trajectory needed for stable raking (Fig. 2.10). This figure shows that many input histograms are marked by a skewed and localized EE distributions (e.g., diameter of fast intermediate fibers (FI_{fD}), the neuromuscular junction position (NMJ_{pos})). However, visually, we cannot claim if EE are normally distributed around MSA indices (μ^* and σ) or not just by observing the Fig.2.8.

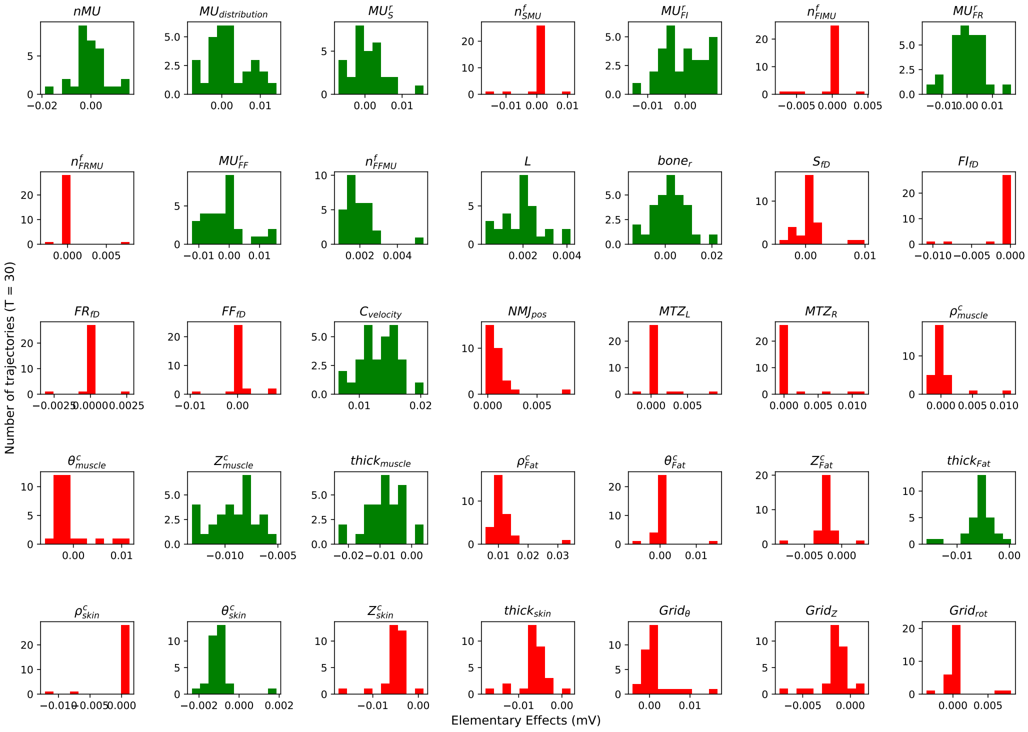

Figure 2.8: The EE distributions of 35 parameters featured in the neuromuscular model. $T = 30$, output = RMSA. Green color: significantly normal EE distributions around (μ^*,σ). Red color: non-normal EE distributions around (μ^*,σ). Normality test is preformed by Kolmogorov-Smirinov test (Table 2.9).

To perform a reliable investigation of EE distributions, we apply a statistical normality test: the Kolmogorov-Smirnov test in this case. The test compares between EE distribution of each input and a theoretical fitted normal distribution generated using the average and dispersion estimators of these input elementary effects. A distribution is considered normal or significantly normal: $N(\mu^*, \sigma)$ or $N(\chi^*, \rho)$, if p-value > 0.05 (default value of the level of significance).

The Table 2.9 shows the results of performing the Kolmogorov-Simirinov normality test on EE distributions for MSA and IMSA methods at $T = 30$. We observe that EE are not normally distributed around μ^* and σ for many inputs (red color). In contrast, all inputs have a normal distribution around χ^* and ρ using the same test (green color). As consequence, the (non)linearity and (non)monotonicity of parameter effects according to MSA indices are not reliable in agreement with the results of Kolmogorov-Smirnov test.

For IMSA indices, as aforementioned in the section 2.3.2, we can define these aspects according to ρ/χ^* ratio.
The new IMSA screening is proposed in this study with three impact zones: (1) linear effects for parameters with $\rho/\chi^* < 0.1$, (2) monotonic effects for parameters with $\rho/\chi^* < 0.5$, (3) non-linear and/or non-monotonic effects with possible interactions between parameters ($\rho/\chi^* > 0.5$).

Table 2.9: The results of Kolmogorov-Smirnov normality test applied on elementary effects data of each parameter, and according to MSA and IMSA indices at $T = 30$. The *p values* > 0.05 indicate that EE distribution is significantly normal (green color).

Parameters	p value (MSA,T=30)	p value (IMSA,T=30)
nMU	0.48	0.954
$MU_{distribution}$	0.8118	0.656
MU^r_S	0.9945	1
n^f_{SMU}	7.43e-06	0.811
MU^r_{FI}	0.9107	0.925
n^f_{FIMU}	1.27e-05	0.632
MU^r_{FR} m	0.5864	0.736
n^f_{FRMU}	1.05e-06	0.448
MU^r_{FF}	0.4159	0.762
n^f_{FFMU}	0.5493	0.949
L	0.6869	0.448
$bone_r$	0.9908	0.892
S_{fD}	3.59e-02	0.432
FI_{fD}	5.01e-07	0.632
FR_{fD}	1.28e-05	0.996
FF_{fD} m	6.20e-04	0.384
$C_{velocity}$	0.8885	0.627
NMJ_{pos}	1.36e-02	0.441
MTZ_L	4.08e-05	0.866
MTZ_R	3.44e-06	0.632
ρ^c_{muscle}	4.96e-03	0.07
θ^c_{muscle}	4.02e-03	0.402
Z^c_{muscle}	0.6422	0.937
$thick_{muscle}$	0.976	0.869
$\rho^c_{Fat}m$	4.69e-02	0.436
θ^c_{Fat}	8.54e-07	0.728
Z^c_{Fat}	3.19e-02	0.901
$thick_{Fat}$	0.2454	0.774
ρ^c_{skin}	5.22e-08	0.108
θ^c_{skin}	0.0948	0.564
Z^c_{skin}	4.42e-02	0.335
$thick_{skin}$	4.39e-02	0.548
$Grid_\theta$m	8.13e-03	0.528
$Grid_Z$	3.06e-02	0.759
$Grid_{rot}$	2.44e-05	0.91

Evaluation of ranking stability The ranking stability is investigated with eight scaled trajectories (from $T = 10$ to $T = 100$) to identify the minimum T needed for a stable ranking for both MSA and IMSA methods. The model output studied is the RMSA averaged on the 64 electrodes. For individual ranking, parameters are sorted in ascending order from 1 to 35 (total number of parameters) according to μ^* for MSA method and χ^* for IMSA method. Parameter with highest μ^* or χ^* (highest effect on the model output) is ranked number one for MSA/IMSA method. Conversely, parameter with the most negligible effect on the model output (lower value of μ^* or χ^*) is ranked number 35. The parameter ranking is evaluated at each trajectory T:{10,20,30,40,50,60,80,100}.
The Fig. 2.9 depicts the stability of individual parameter ranking through the eight-scaled preselected T values. The inputs are ranked according to μ^* (MSA, Fig. 2.9(a)) and χ^* (IMSA, Fig. 2.9(b)).

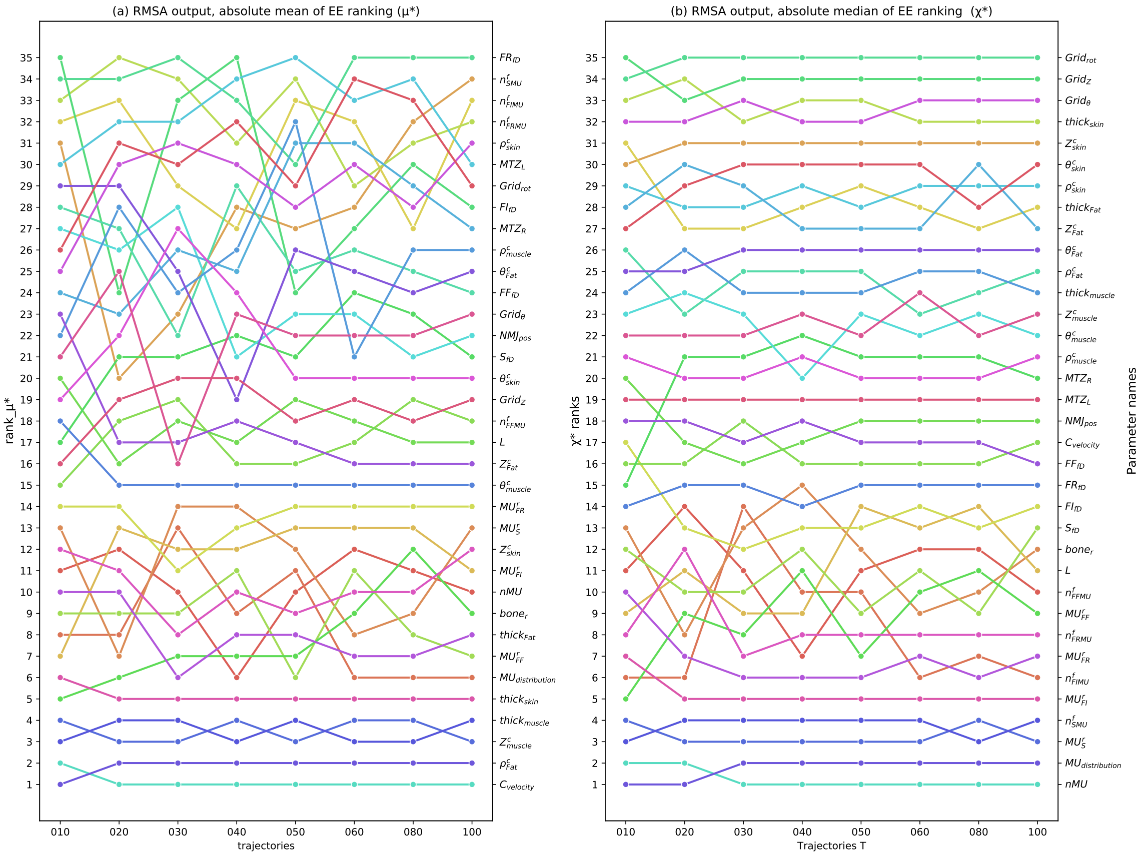

Figure 2.9: Comparison between ranking stability of neuromuscular system inputs using μ^*(a) and χ^*(b). Output = Mean RMSA value.

In this figure, the ranks starts from 1 (most influential with respectively high μ^* , χ^*) to 35 (least impact with respectively negligible μ^* , χ^*). The model output is the mean RMSA feature. For each column of ranking points/parameters according to the given T. We observe a large impact of the averaging mode on the stability of individual parameters ranking. This impact is more accentuated for parameters with low μ^* (negligible effects). This observation is consistent with observations of the study [225]. In addition, this figure demonstrates that applying χ^*, as indicator of EE, reduces the minimum T needed for reliable results (T = 20 or 30 for RMSA output).
To evaluate efficiently the changes between individual rankings when increasing T, the position factors are computed for each pair of trajectories using the equation (2.31).

The table 2.10 and Fig. 2.10 show the resulting position factor ($PF_{T_i \to T_j}$) values and behavior obtained for each pair of trajectories with: (a) MSA indices, and (b) IMSA indices. We observe that from low number of trajectories with IMSA method (from $T = 30$), the $PF^{\chi^*}_{T_i \to T_j}$ values remain stable and lower than with MSA method ($PF^{\mu^*}_{T_{80} \to T_{100}}$ $> PF^{\chi^*}_{T_{30} \to T_{40}}$). In fact, low values of PF indicate that most of the parameters remain in the same or nearly the same position in the ranking between two successive trajectories. Therefore, according to table 2.10 and Fig. 2.10, values of T above 30 provide a suitable estimation of sensitivity measures with IMSA indices.

Table 2.10: Computed position factors $PF_{T_i \to T_j}$ according to μ^* rankings (MSA); χ^* ranking (IMSA). Position factors are computed according to the RMSA model output feature.

$PF_{T_i \to T_j}$	$T_{10} \to T_{20}$	$T_{20} \to T_{30}$	$T_{30} \to T_{40}$	$T_{40} \to T_{50}$	$T_{50} \to T_{60}$	$T_{60} \to T_{80}$	$T_{80} \to T_{100}$
$PF^{\mu^*}_{T_i \to T_j}$	6.9	4.9	4.7	4.8	5.1	4.1	4.4
$PF^{\chi^*}_{T_i \to T_j}$	4.9	4.6	2.4	2.4	2.8	2.6	2.4

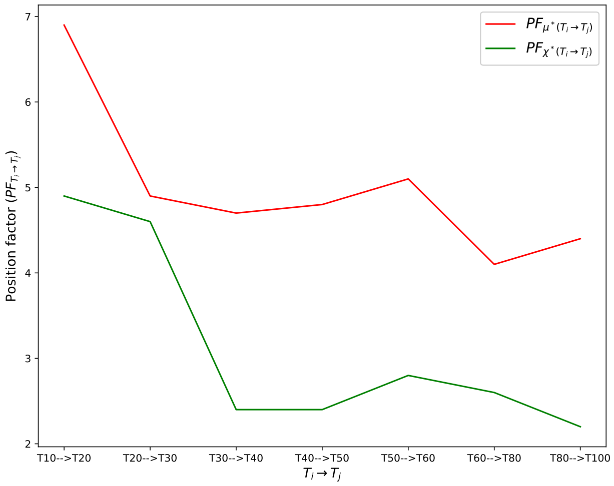

Figure 2.10: The position factors $PF_{T_i \to T_j}$ values and behavior obtained for each pair of trajectories with MSA indices (red color), and IMSA indices (green color). Position factors are computed with RMSA output.

However, it is more reliable and intuitive to assess stability according to the ranking by a group of parameters sharing the same impact on the model output. Thus, we have fixed the effect thresholds based on MSA and IMSA indices as outlined in 2.3.2: (1) influential group including parameters with EE average and/or dispersion causing more than 20% of the model output($(\chi^*, \rho) > 20\%$, $(\mu^*, \sigma) > 20\%$), (2) non-influential group with parameters causing less than 5% of output variation ($(\chi^*, \rho) < 5\%$, $(\mu^*, \sigma) < 5\%$), and (3) intermediate group of parameters located between the two previous groups.

The Fig.2.11(a) illustrates a screening sensitivity analysis of the neuromuscular model with the MSA method at $T = 30$ and using classical μ^* and σ indices. The model output is the RMSA of HD-sEMG signals measured at the skin surface by the 64 electrodes. The sensitivity analysis space is divided into four zones according to the ratio σ/μ^*_r classification suggested in [256]. Each group of inputs is marked by a defined color and marker according to its influence level. Thresholds separating influential zones are marked by continuous lines. Elementary effects have the same unit as the model output: mV.

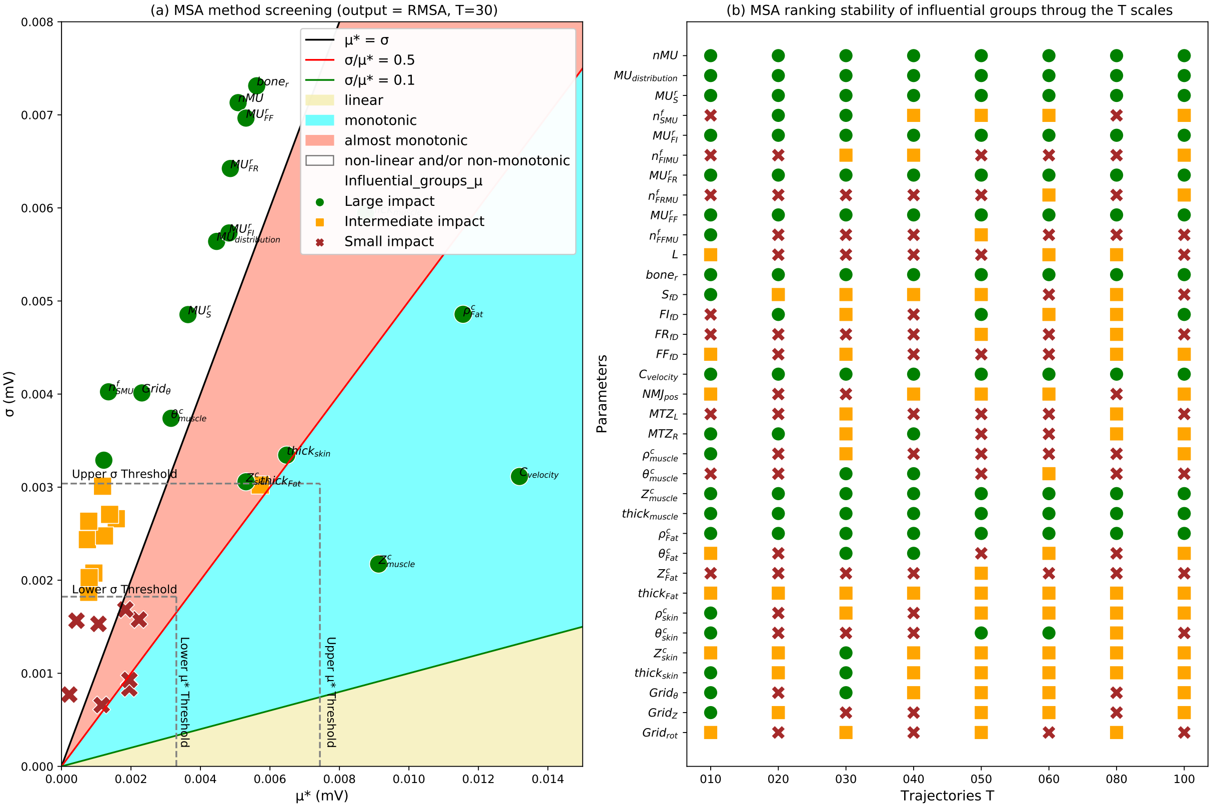

Figure 2.11: (a) Sensitivity analysis screening with MSA method. Output = Mean RMSA value of HD-sEMG signals (mV). T = 30. Three influential groups: low impact (dark red cross), Medium impact (orange square). High impact (green circle). (b) Ranking stability of MSA method at different T.

The stability of this approach is observed in Fig.2.11(b) at different trajectories T. The Fig.2.12(a) illustrates a screening sensitivity analysis with the IMSA method at $T = 30$ with the same model output and with the same colors and markers for influential groups. The stability of the IMSA indices is observed in Fig.2.12(b) at different trajectories T. We observe that the IMSA guarantees the stability and reproducibility of parameter ranking from $T = 20$ (Fig. 2.12(b)). A small T value reduces significantly the computation time of the sensitivity analysis. The minimum number of model evaluations needed to perform a sensitivity analysis at $T = 20$ is 720 which is performed during $6h02min$ of computing time(Table 2.8). In contrast, the Fig. 2.11(b) shows that parameter ranking remains unstable until $T = 100$ with MSA method (the computation time is equal to $42h35min$). In this figure, we observe many disruptions in the ranking for many inputs, e.g., the parameter θ^c_{skin} (angular skin conductivity) varies its ranking from large impact group at $T = 60$, to intermediate impact group at $T = 80$, to small impact group at $T = 100$. This instability distorts the evaluation of parameter impacts when delivering sensitivity analysis results. Furthermore, the (non)linearity and (non)monotonicity of input impacts are attributed for only few parameters with significantly normal EE according to MSA indices (Table 2.9). Thus, a common attributions/screening of (non)linear and (non)monotonic effects for all parameters as in Fig.2.11(a) is inconsistent. However, the IMSA indices give a conjoint representation of (non)linear and (non)monotonic zones for all parameters (Fig. 2.12(a)). Moreover, the Table 2.11 shows the value of T needed to obtain a stable parameter rankings with IMSA method for each output feature depicted in Table 2.5. The estimated values of T depicted in this table are obtained using the same workflow/methodology of this section.

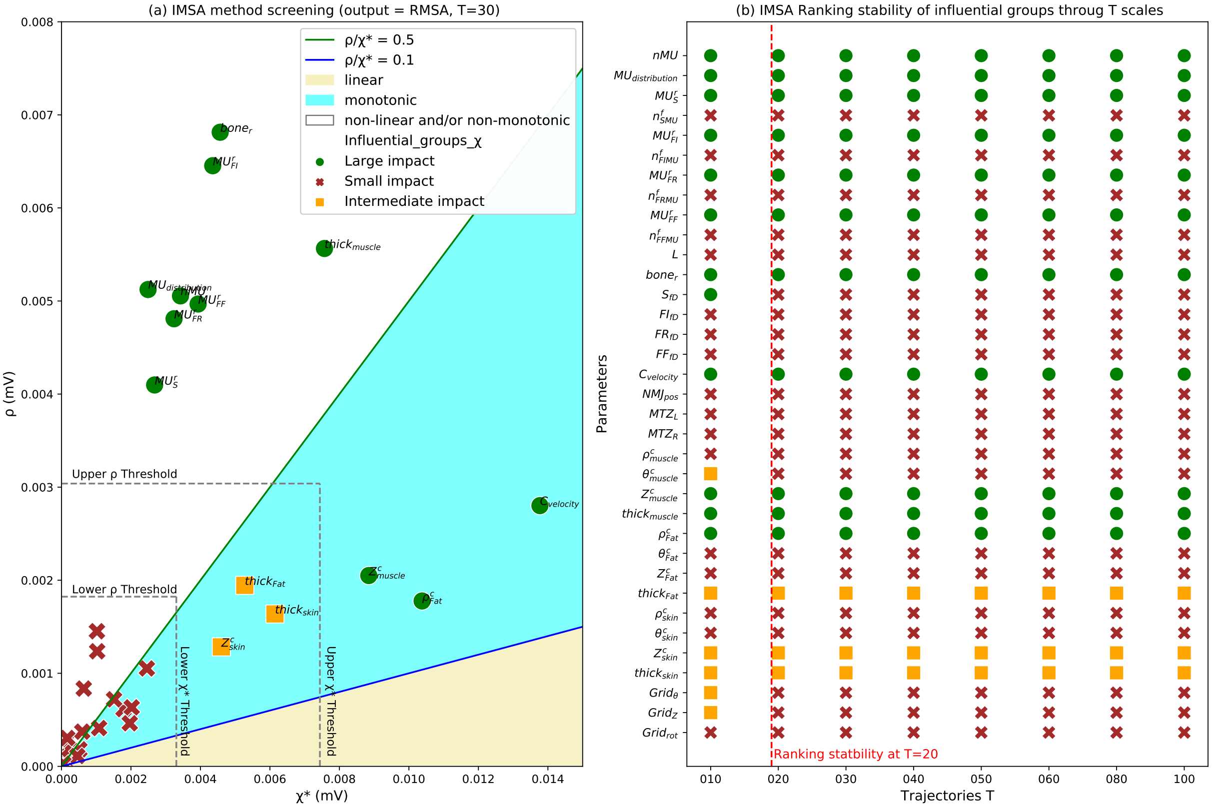

Figure 2.12: (a) Sensitivity analysis screening with IMSA method. Output = Mean RMSA value of HD-sEMG signals (mV). T = 30. Three influential groups: low impact (dark red cross), Medium impact (orange square). High impact (green circle). (b) Ranking stability of IMSA method at different trajectories T. The IMSA ranking stability is established from $T = 20$.

Table 2.11: List of features and the corespondent estimated T.

Output feature	Stable ranking at T
1. RMSA	20∼30
2. IEMG	20∼30
3. MAV	20∼30
4. MAV1	20∼30
5. MAV2	20∼30
6. wilson_amp	50
7. Kurt	20∼30
8. Skew	20∼30
9. Var	30
10. ap_ent	30
11. sp_ent	30
12. MDF	30
13. MNF	30
14. MNP	30
15. Peak_f	30∼40
16. ap_ent	30∼40
17. Freq_r	30∼40
18. SM_0	30
19. SM_1	30
20. SM_2	30
21. SM_2 (VCF)	30
22. SM_3	30
23. R_2	30∼40
24. $H2$	30∼40

2.3.3.2 Discussions

The MSA method is one of the rare tools to perform sensitivity analysis for high computing cost and complex models at the smallest computation time as depicted in the selection decision tree proposed in [216]. However, the approach bears on strong normality hypothesis of the EE distributions and presents unstable results. The present study is motivated by proposing a fast, reliable and stable Morris screening sensitivity analysis for high computation cost and complex models. The model depicted in [1] satisfies these criteria. The methodology and the results of comparison between the two methods: MSA and IMSA, are summarized in the Fig. 2.13.

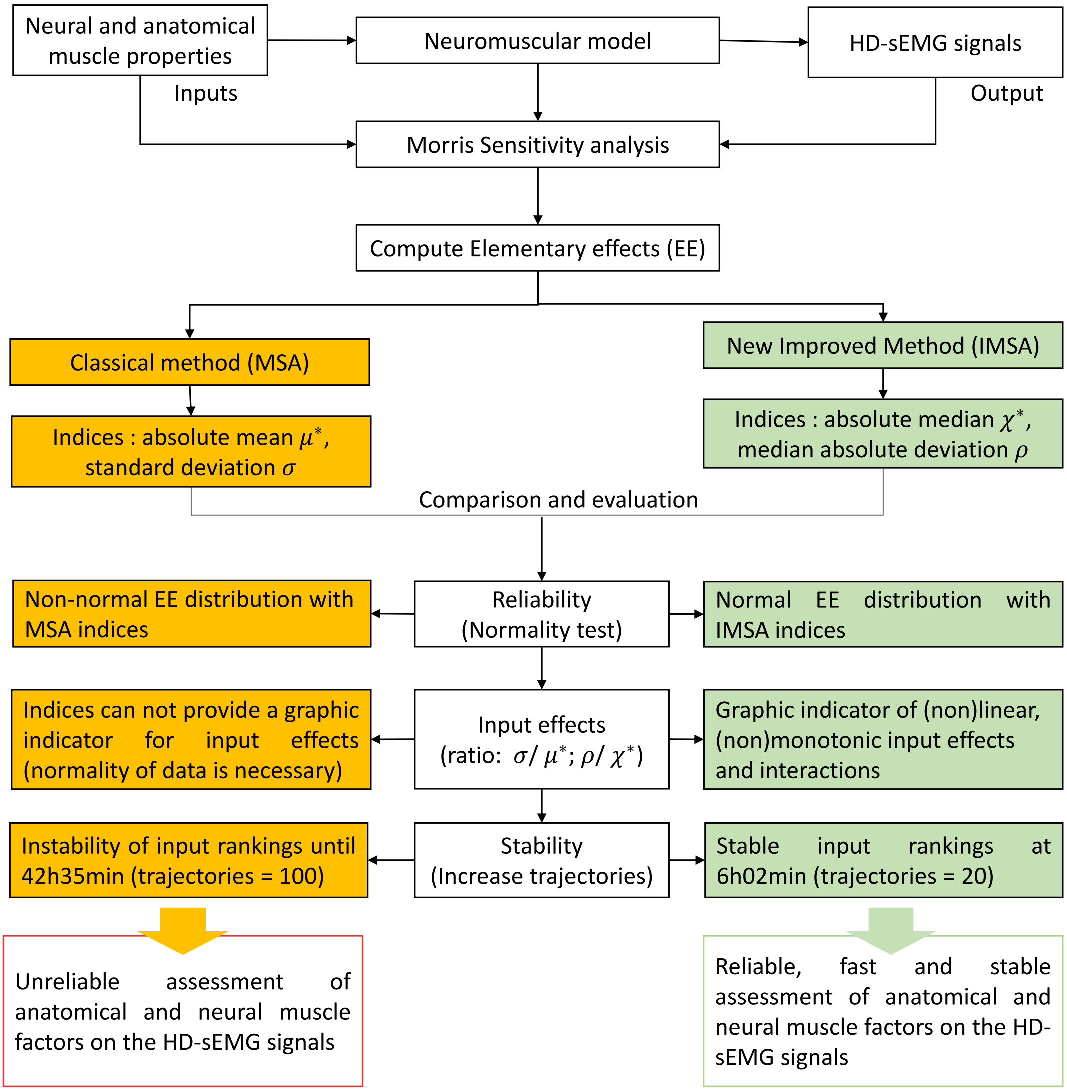

Figure 2.13: Methodology and results of comparing between MSA and IMSA methods.

Selection of appropriate indices: χ^* and ρ Few studies have investigated the robustness of MSA indices (μ^* and σ), efficient only for normal or significantly normal data [259]. The study [250] have underlined that more robust indicators should be investigated, and have suggested to apply, without demonstration, a new ones based on EE distribution shapes introduced by[260]. A more recent study [225] have proposed and applied χ^* in the computation of EE average. Authors of [225] have demonstrated the

robustness of χ^* against μ^* to reproduce a stable ranking. However, they have not proposed a new indicator for EE dispersion. For that reason, authors of [225] have conserved the original screening analysis proposed by [220].
The new IMSA proposes the application of χ^* and ρ as sensitivity indicators: the absolute median and the median absolute deviation respectively. The selection of these indices is based on several studies e.g., [260, 261] for its relevance to non-normal data distributions and its robustness to eliminate outliers causing a wrong estimation of data average and dispersion. The Kolmogorv-Simirinov normality shows that EE distributions are significantly normal around IMSA indices for all parameters, but such was not the case for MSA indices (Table 2.9). We should note that other alternatives for ρ exist in the literature and can be applied instead of ρ if the normality of EE distributions is not achieved [262].

Performing the (non)linearity and the (non)monotonicity of parameter effects using the ρ/χ^* ratio The study[256], using the ratio σ/μ^*, has defined the zone of linear effects, monotonic effects, and non linear effects and/or with interactions between inputs. The hypothesis depicted in [256] is based on: 1) statistical properties of normal EE distributions, 2) equality between the two ratios σ/μ^* and $\sigma/|\mu|$ to define the three zones mentioned above for non-normal data. However, This equality cannot deliver the same conclusions with the new IMSA indices. In fact, the equality between ρ/χ^* and $\rho/|\chi|$ means that χ^* is equal to $|\chi|$ but does not mean necessarily that EE have the same sign (eq. 2.29). To identify the (non)monotonicity and (non)linearity of parameter effects, this study have proposed to use the ρ/χ^* ratio. Statistical properties of normal or significantly normal EE distributions (normality test is required), indicate that most EE (95%) have the same sign (monotonic effect) if ρ/χ^* is smaller than 0.5, and 95% of EE are constant (linear effect) if ρ/χ^* is smaller than 0.1. Such conclusions give the monotonic and linear effects zones as depicted in the Fig.2.12(a) and presented partially in [256].

Stability of IMSA indices against MSA indices The present study demonstrates the stability of IMSA indices ranking from $T = 30$ with individual ranking. For ranking by group of parameters sharing the same influence on the model output (thresholds concept), the IMSA method reduces the minimum T needed for stable ranking from ($T = 20 < T = 30$ with individual ranking). In contrast, MSA indices remain unstable until $T = 100$ (Fig. 2.11 and 2.12). The computation time needed to perform Morris screening analysis, without computing indices, at $T = 20$ and $T = 100$ are respectively $6h02min$ and $42h35min$ (Table 2.8). Yet, 20 trajectories are sufficient to get a stable and robust ranking with IMSA indices for the studied neuromuscular model.

2.4 Aging sensitivity matrix using IMSA method

The new proposed IMSA method is applied on the neuromuscular model [1, 11]. The variable of IMSA will be adjusted using results of previous section. The number of trajectories is fixed at $T = 30$ and an optimal sampling strategy is adopted [250]. Two subject categories are studied: Young Men (YM) and Old Men (OM). The evaluation of input impacts is performed at two contraction levels: LC = 20% of MVC and HC = 60% of MVC. The impact of each input variation is assessed on all output features of Table 2.5 (expect for wilson_amp, which need $T = 50$ for stable parameter rankings). Each mean output feature is computed from the 64 HD-sEMG simulated signals. We have performed a parallel computation using a 32 CPUs intel Xeon calculator.

Simulations plan Two categories of subjects are studied: Young Men (YM), Old Men (OM). Two contraction levels are considered: Low Contractions (20% of MVC) and High Contractions (60% of MVC). The total number of sensitivity analysis performed is four (Fig. 2.14).

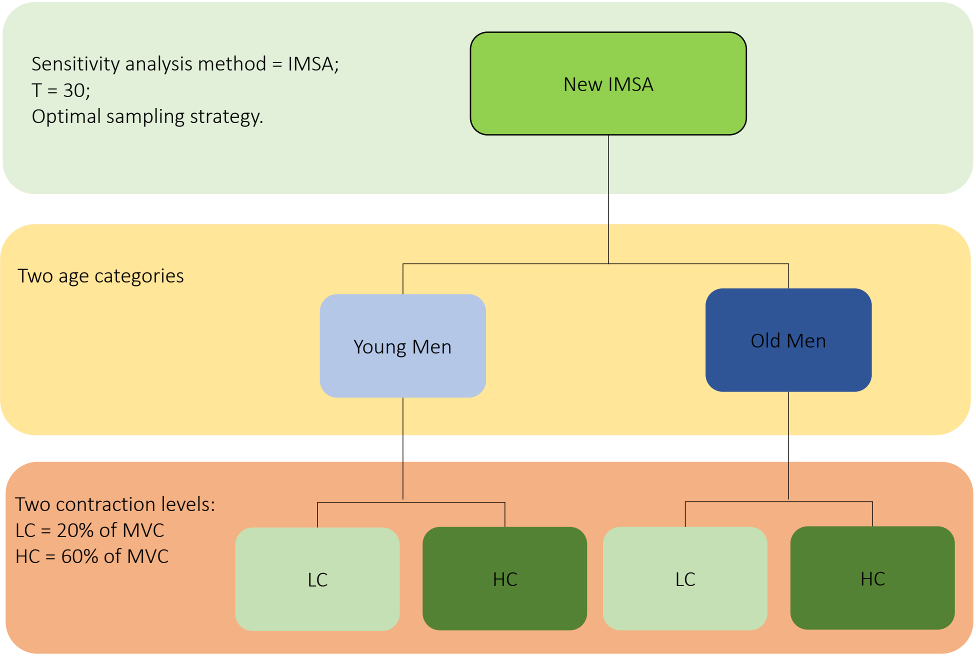

Figure 2.14: Simulation plan. Four sensitivity analysis: YM at LC; YM at HC; OM at LC; OM at HC

Presentation of results Results are presented mainly as cluster maps with min/max normalized IMSA indices (between 0 and 1). For each subgroup of outputs, each age category, and for each contractions level, a cluster map gives a relationship map between inputs and outputs.

Clustering of influential parameters We will evaluate the impact of 35 parameters on 22 HD-sEMG features for 2 age categories, and at 2 contraction levels. Regarding the huge amount of the result data ($35 * 22 * 2 * 2$), we will proceed by automatically selecting the most important parameters for each feature using an unsupervised learning of IMSA results (two groups of parameters: influential group and non-influential group). A clustering process divides the entire data into groups (also known as clusters) based on the patterns and similarities in the data. Many clustering techniques exists in literature (DBSCAN, Birch,etc.). However, we select a simple and frequently used partitioning unsupervised learning algorithms : K-mean algorithm.
Its goal is to form groups of data points based on the number of clusters, represented by the variable k (predefined before the execution). K-means uses an iterative refinement method to produce its final clustering based on the number of clusters defined by the user and the data set. Initially, k-means randomly chooses k as the mean values of k clusters, called centroids, and find the nearest data points of the chosen centroids to form k clusters. Then, it iteratively recalculates the new centroids for each cluster until the

algorithm converges to one optimum value.

2.4.1 Results

2.4.1.1 Mono-variate features

Time domain (TD) and non-linear features Eleven features from Table 2.5 are selected: five amplitude features (RMSA, MAV, MAV1, MAV2, wilson_amp), three energy features (IEMG, SSI, Variance), two statistical features (Kurtosis, Skewness), and two non-linear features (ap_entropy, samp_entropy).

Amplitude and energy features Features of this class are easy to implement with the capacity to assess the main electrical activity generated by muscle. They can estimate efficiently the amount of muscle activation. Correlating anatomical muscle properties to muscle force and fatigue is useful for clinical and research fields. We observe, in Fig. 2.15, that all categories (YM, OM) and contraction levels (LC, HC) share approximately the same influential and non-influential muscle parameters. However, few changes are noted between Fig. 2.15(a), (b), (c), and (d). For YM (a & b), the number of fast fibers per MU (n^f_{FFMU}) has an important impact at HC. Which is not the case at LC, where the number of slow fibers n^f_{SMU} have more effects. Moreover, electrode grid properties (position and rotation: $Grid_Z$, $Gridrot$), total MU number (n_{MU}), and radial conductivity of fat tissues (ρ^c_{Fat}) have more impact at HC. Its influences at LC is not negligible but not important. For OM, we note the same observation for the number of slow and fast fibers between HC and LC. In addition, we observe that the ratio of MU ($MU_{distribution}$) have a strong effect on amplitude and energy features at HC and a negligible one at LC. Comparing changes between young and old categories, we cannot find differences at LC, expect a slight increase of bone radius ($bone_r$) and muscle length (L) effects for OM. At HC, we observe same trends as LC, with the fact that ($MU_{distribution}$) has large effect for OM.

Statistical features Kurtosis and Skewness measure the peakedness and the symmetry/asymmetry of HD-sEMG signal respectively. The Fig. 2.15 shows a different behaviors of these features for each category. We cannot identify clearly a reduced and common number of influential inputs. The IMSA screening depicted in Fig. 2.16, 2.17, 2.18, 2.19 show that all parameters have a close positions and situated at the non linear and/or with interactions effects zone, in contrast of amplitude and energy features (e.g., the RMSA feature in the same figures. The stability of ranking is not assumed for these features due to the very close values of IMSA indices ($\chi^* \approx \rho$). For that reason, we cannot find common trends between categories.

Non linear features The conduction velocity along fibers ($C_{velocity}$) is the most influential parameter for entropy features: approximate entropy (ap_ent) and sample entropy ($samp\_ent$) for both YM and OM at LC and HC. Entropy features are used to identify regularity and predictability of the signals. The conduction velocity has a large and monotonic effect on these features. The rest of of inputs have a negligible effects (Fig. 2.15 and Fig. 2.16, 2.17, 2.18, 2.19.

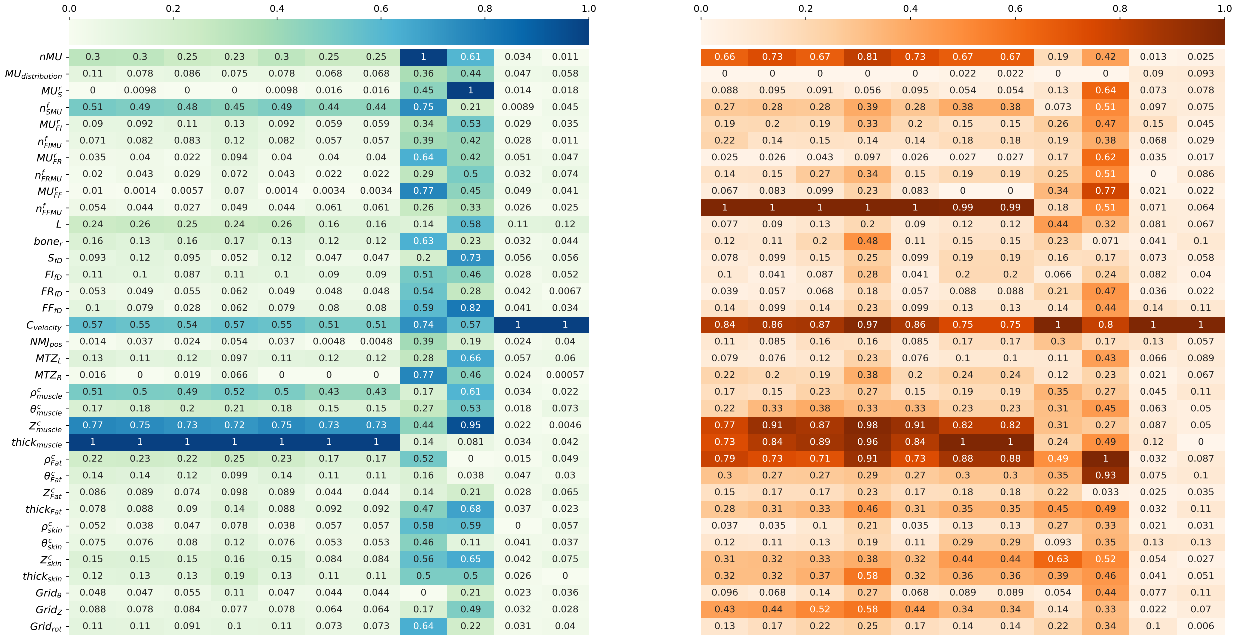

(a) Young men, 20% of MVC (b) Young men, 60% of MVC

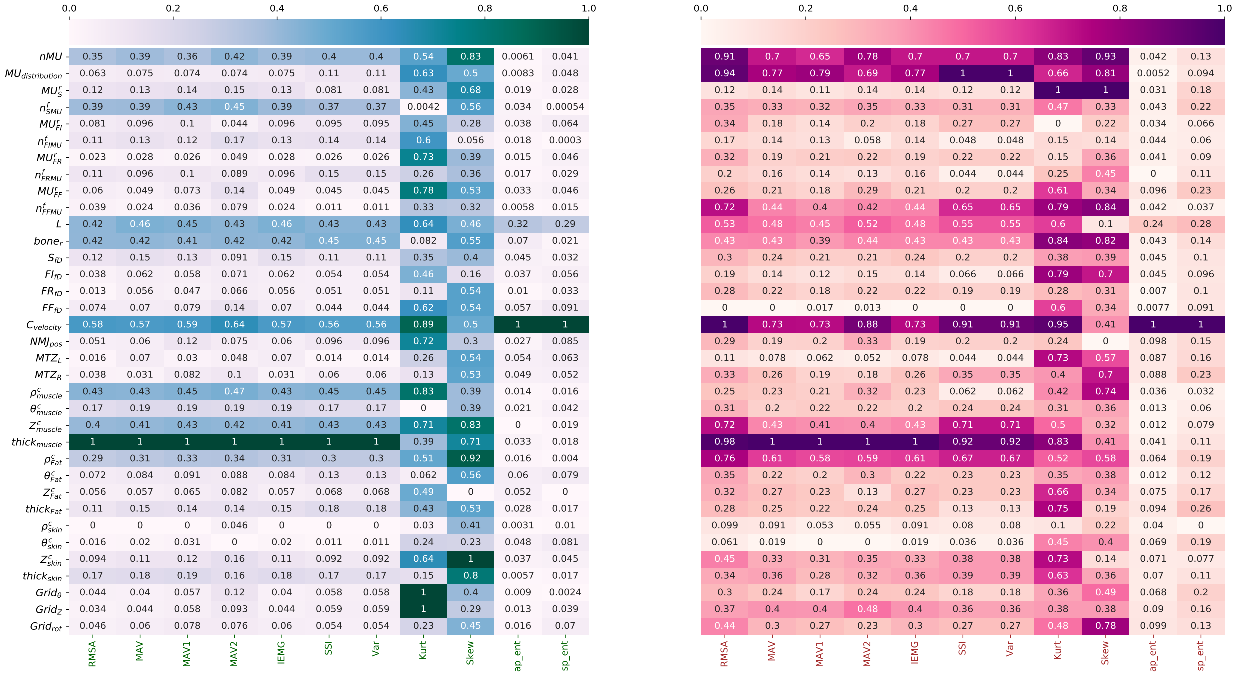

(c) Old men, 20% of MVC (d) Old men, 60% of MVC

Figure 2.15: Impacts of model inputs on extracted TD features (IMSA results). IMSA impact indice = Normalized SI (from 0 (light color) to 1 (dark color)). Ranking of neuromuscular inputs according to age (young (a,b) and old men (c,d)), and level of force contractions (low (a,c) and high(b,d)).

K-mean algorithm results for time domain features The application of K-mean algorithm on the data of IMSA results provides the most influential group of parameters for each feature. The Tables 2.16 2.17 2.18 2.19 show the result of k-means algorithm. We observe in Fig. 2.16, 2.17, 2.18, 2.19 the screening of parameters using IMSA method. In these figures, cluster of parameters with strong impact on the studied feature is marked by green color (red color for parameters with negligible effects). The results of the unsupervised learning of sensitivity analysis data are similar to visual observations of Fig. 2.15.

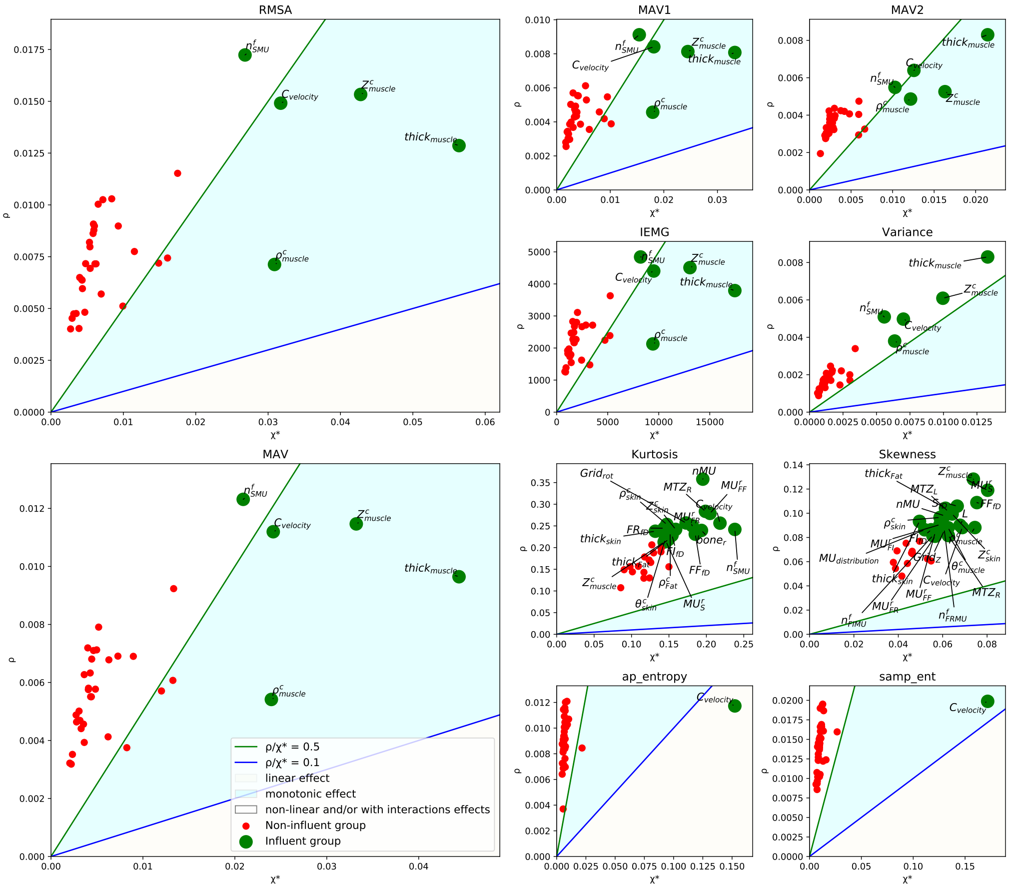

Figure 2.16: IMSA screening of influential parameters. Categories: YM, LC. Clustering method = K-means

Table 2.12: Group of influent parameters for young men (YM) at low contractions (LC = 20% of MVC). Time domain features.

Feature	Number of Influent parameters	List of influent parameters
RMSA MAV MAV1 MAV2 IEMG Variance	5	$thick_{muscle}$, $C_{velocity}$, n^r_{SMU}, Z^c_{muscle}, ρ^c_{muscle}
Kurtosis	19	nMU, MU^r_S, n^f_{SMU}, MU^r_{FR}, MU^r_{FF}, $bone_r$, FI_{fD}, FR_{fD}, FF_{fD}, $C_{velocity}$, MTZ_R, Z^c_{muscle}, ρ^c_{Fat}, $thick_{Fat}$, ρ^c_{skin}, θ^c_{skin}, Z^c_{skin}, $thick_{skin}$, $Grid_{rot}$
Skeweness	23	nMU, $MU_{distribution}$, MU^r_S, MU^r_{FI}, n^f_{FIMU}, MU^r_{FR}, n^f_{FRMU}, MU^r_{FF}, L, S_{fD}, FI_{fD}, FF_{fD}, $C_{velocity}$, MTZ_R, MTZ_L, Z^c_{muscle}, ρ^c_{muscle}, θ^c_{muscle}, $thick_{Fat}$, ρ^c_{skin}, Z^c_{skin}, $thick_{skin}$, $Grid_Z$
ap_entropy samp_ent	1	$C_{velocity}$

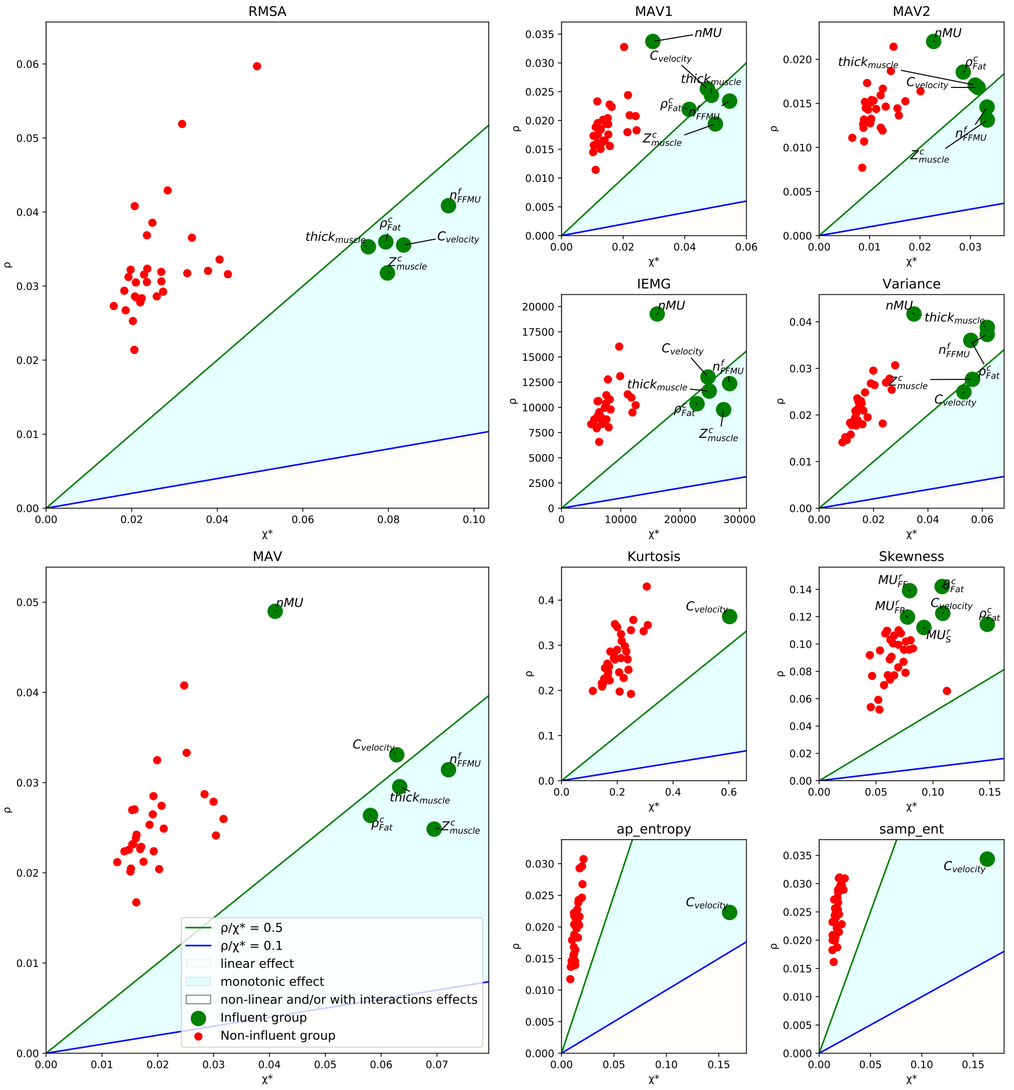

Figure 2.17: IMSA screening of influential parameters. Categories: YM, HC. Clustering method = K-means

Table 2.13: Group of influent parameters for young men (YM) at high contractions (HC = 60% of MVC). Time domain features.

Feature	Number of Influent parameters	List of influent parameters
RMSA	5	$thick_{muscle}$, $C_{velocity}$, n^r_{FFMU}, Z^c_{muscle}, ρ^c_{fat}, L
MAV MAV1 MAV2 IEMG Variance	6	$thick_{muscle}$, $C_{velocity}$, n_{MU}, n^r_{FFMU}, Z^c_{muscle}, ρ^c_{fat}
Skewness	5	$C_{velocity}$, MU^r_s, MU^r_{FR}, MU^r_{FF}, ρ^c_{fat}, θ^c_{fat}
ap_entropy samp_ent Kurtosis	1	$C_{velocity}$

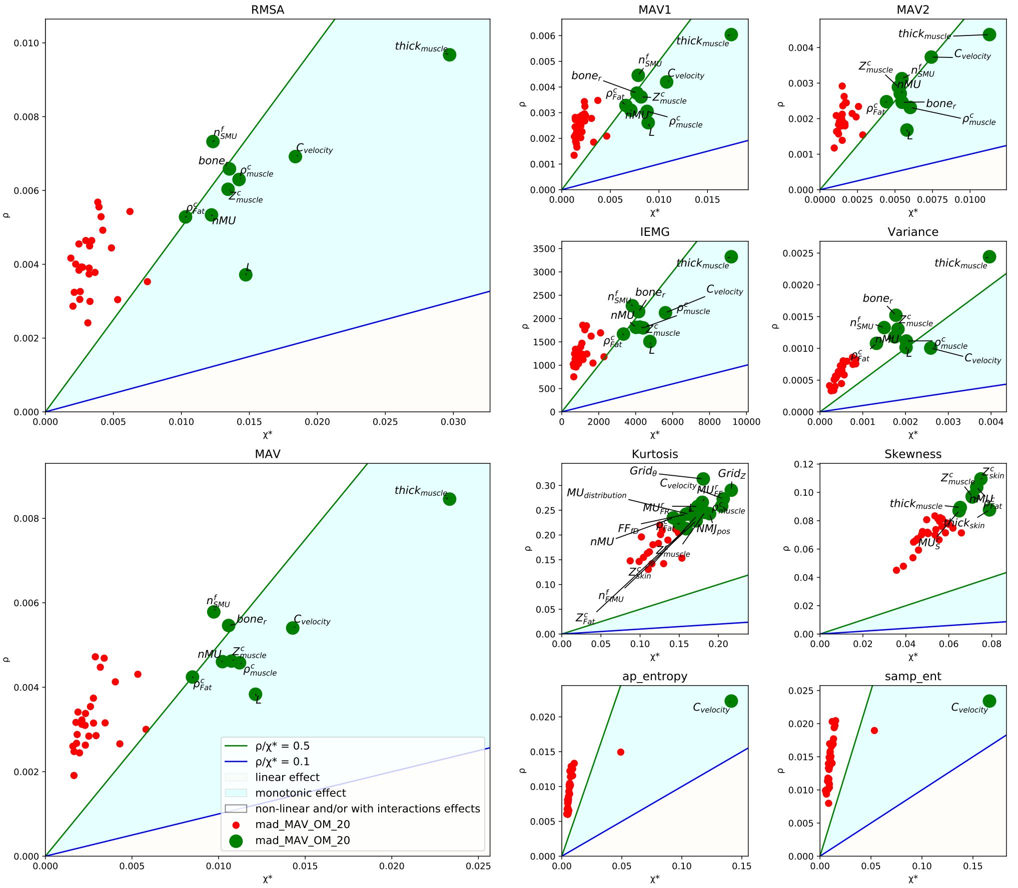

Figure 2.18: IMSA screening of influent parameters. Categories: OM, LC. Clustering method = K-means

Table 2.14: Group of influent parameters for ol men (OM) at low contractions (LC = 20% of MVC). Time domain features.

Feature	Number of Influent parameters	List of influent parameters
RMSA MAV MAV1 MAV2 IEMG Variance	9	nMU, n^f_{SMU}, L, $bone_r$, $C_{velocity}$, ρ^c_{muscle}, Z^c_{muscle}, $thick_{muscle}$, ρ^c_{Fat}
Skewness	7	nMU, MU^r_S, Z^c_{muscle}, $thick_{muscle}$, ρ^c_{Fat}, Z^c_{skin}, $thick_{skin}$
Kurtosis	19	MU^r_S, n^f_{SMU}, MU^r_{FI}, n^f_{FRMU}, n^f_{FFMU}, $bone_r$, S_{fD}, FI_{fD}, FR_{fD}, MTZ_L, MTZ_R, θ^c_{muscle}, $thick_{muscle}$, θ^c_{Fat}, $thick_{Fat}$, ρ^c_{skin}, θ^c_{skin}, $thick_{skin}$, $Grid_{rot}$
ap_entropy samp_ent Kurtosis	1	$C_{velocity}$

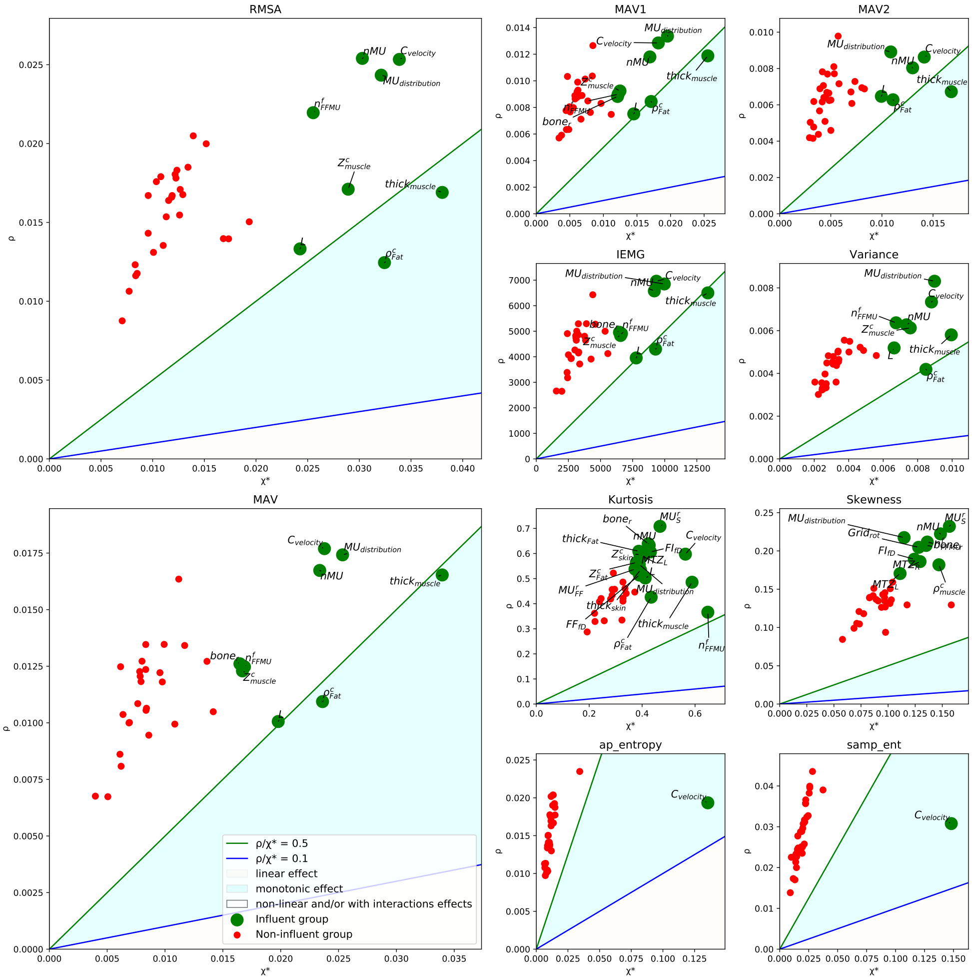

Figure 2.19: IMSA screening of influent parameters. Categories: OM, HC. Clustering method = K-means

Table 2.15: Group of influent parameters for old men (OM) at high contractions (HC = 60% of MVC). Time domain features.

Feature	Number of Influent parameters	List of influent parameters
RMSA Variance	8	$thick_{muscle}$, $C_{velocity}$, $MU_{distribution}$, n_{MU}, n^{r}_{FFMU}, Z^{c}_{muscle}, ρ^{c}_{fat}, L
MAV MAV1	8	$thick_{muscle}$, $C_{velocity}$, $MU_{distribution}$, n_{MU}, $bone_{r}$, Z^{c}_{muscle}, ρ^{c}_{fat}, L
MAV2	6	$thick_{muscle}$, $C_{velocity}$, $MU_{distribution}$, n_{MU}, ρ^{c}_{fat}, L
Kurtosis	17	nMU, $MU_{distribution}$, MU^{r}_{S}, MU^{r}_{FF}, n^{f}_{FFMU}, L, $bone_{r}$, FI_{fD}, FF_{fD}, $C_{velocity}$, MTZ_{L}, $thick_{muscle}$, ρ^{c}_{Fat}, Z^{c}_{Fat}, $thick_{Fat}$, Z^{c}_{skin}, $thick_{skin}$
Skewness	10	nMU, $MU_{distribution}$, MU^{r}_{S}, n^{f}_{FFMU}, $bone_{r}$, FI_{fD}, MTZ_{L}, MTZ_{R}, ρ^{c}_{muscle}, $Grid_{rot}$
ap_entropy samp_ent Kurtosis	1	$C_{velocity}$

Frequency domain (FD)features The Frequency Domain (FD) features are computed from Power Spectral Density (PSD). These features required more Computational Time (CT) compared to Time Domain (TD) features, and are useful in the detection of muscle fatigue. Ten FD features are computed (Fig. 2.20): MDF, MNF, SM1, SM2, SM3, TTP, MNP, Peak_f, Freq_r, and VDF.

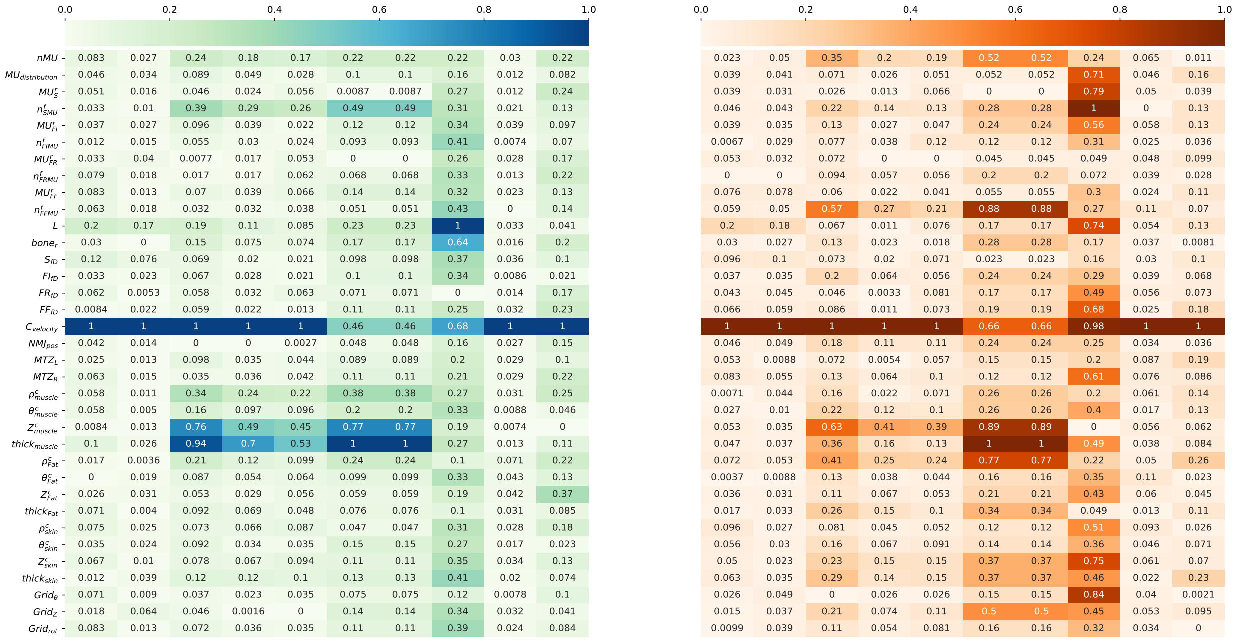

(a) Young men, 20% of MVC

	MDF	MNF	SM1	SM2	SM3	TTP	MNP	Peak_f	Freq_r	VDF
nMU	0.083	0.027	0.24	0.18	0.17	0.22	0.22	0.22	0.03	0.22
$MU_{distribution}$	0.046	0.034	0.089	0.049	0.028	0.1	0.1	0.16	0.012	0.082
MU^r_S	0.051	0.016	0.046	0.024	0.056	0.0087	0.0087	0.27	0.012	0.24
n^f_{SMU}	0.033	0.01	0.39	0.29	0.26	0.49	0.49	0.31	0.021	0.13
MU^r_{FI}	0.037	0.027	0.096	0.039	0.022	0.12	0.12	0.34	0.039	0.097
n^f_{FIMU}	0.012	0.015	0.055	0.03	0.024	0.093	0.093	0.41	0.0074	0.07
MU^r_{FR}	0.033	0.04	0.0077	0.017	0.053	0	0	0.26	0.028	0.17
n^f_{FRMU}	0.079	0.018	0.017	0.017	0.062	0.068	0.068	0.33	0.013	0.22
MU^r_{FF}	0.083	0.013	0.07	0.039	0.066	0.14	0.14	0.32	0.023	0.13
n^f_{FFMU}	0.063	0.018	0.032	0.032	0.038	0.051	0.051	0.43	0	0.14
L	0.2	0.17	0.19	0.11	0.085	0.23	0.23	1	0.033	0.041
$bone_r$	0.03	0	0.15	0.075	0.074	0.17	0.17	0.64	0.016	0.2
S_{fD}	0.12	0.076	0.069	0.02	0.021	0.098	0.098	0.37	0.036	0.1
FI_{fD}	0.033	0.023	0.067	0.028	0.021	0.1	0.1	0.34	0.0086	0.021
FR_{fD}	0.062	0.0053	0.058	0.032	0.063	0.071	0.071	0	0.014	0.17
FF_{fD}	0.0084	0.022	0.059	0.022	0.013	0.11	0.11	0.25	0.032	0.23
$C_{velocity}$	1	1	1	1	1	0.46	0.46	0.68	1	1
NMJ_{pos}	0.042	0.014	0	0	0.0027	0.048	0.048	0.16	0.027	0.15
MTZ_L	0.025	0.013	0.098	0.035	0.044	0.089	0.089	0.2	0.029	0.1
MTZ_R	0.063	0.015	0.035	0.036	0.042	0.11	0.11	0.21	0.029	0.22
ρ^c_{muscle}	0.058	0.011	0.34	0.24	0.22	0.38	0.38	0.27	0.031	0.25
θ^c_{muscle}	0.058	0.005	0.16	0.097	0.096	0.2	0.2	0.33	0.0088	0.046
Z^c_{muscle}	0.0084	0.013	0.76	0.49	0.45	0.77	0.77	0.19	0.0074	0
$thick_{muscle}$	0.1	0.026	0.94	0.7	0.53	1	1	0.27	0.013	0.11
ρ^c_{Fat}	0.017	0.0036	0.21	0.12	0.099	0.24	0.24	0.1	0.071	0.22
θ^c_{Fat}	0	0.019	0.087	0.054	0.064	0.099	0.099	0.33	0.043	0.13
Z^c_{Fat}	0.026	0.031	0.053	0.029	0.056	0.059	0.059	0.19	0.042	0.37
$thick_{Fat}$	0.071	0.004	0.092	0.069	0.048	0.076	0.076	0.1	0.031	0.085
ρ^c_{skin}	0.075	0.025	0.073	0.066	0.087	0.047	0.047	0.31	0.028	0.18
θ^c_{skin}	0.035	0.024	0.092	0.034	0.035	0.15	0.15	0.27	0.017	0.023
Z^c_{skin}	0.067	0.01	0.078	0.067	0.094	0.11	0.11	0.35	0.034	0.13
$thick_{skin}$	0.012	0.039	0.12	0.12	0.1	0.13	0.13	0.41	0.02	0.074
$Grid_\theta$	0.071	0.009	0.037	0.023	0.035	0.075	0.075	0.12	0.0078	0.1
$Grid_Z$	0.018	0.064	0.046	0.0016	0	0.14	0.14	0.34	0.032	0.041
$Grid_{rot}$	0.083	0.013	0.072	0.036	0.035	0.11	0.11	0.39	0.024	0.084

(b) Young men, 60% of MVC

	MDF	MNF	SM1	SM2	SM3	TTP	MNP	Peak_f	Freq_r	VDF
nMU	0.023	0.05	0.35	0.2	0.19	0.52	0.52	0.24	0.065	0.011
$MU_{distribution}$	0.039	0.041	0.071	0.026	0.051	0.052	0.052	0.71	0.046	0.16
MU^r_S	0.039	0.031	0.026	0.013	0.066	0	0	0.79	0.05	0.039
n^f_{SMU}	0.046	0.043	0.22	0.14	0.13	0.28	0.28	1	0	0.13
MU^r_{FI}	0.039	0.035	0.13	0.027	0.047	0.24	0.24	0.56	0.058	0.13
n^f_{FIMU}	0.0067	0.029	0.077	0.038	0.12	0.12	0.12	0.31	0.025	0.036
MU^r_{FR}	0.053	0.032	0.072	0	0	0.045	0.045	0.049	0.048	0.099
n^f_{FRMU}	0	0	0.094	0.057	0.056	0.2	0.2	0.072	0.039	0.028
MU^r_{FF}	0.076	0.078	0.06	0.022	0.041	0.055	0.055	0.3	0.024	0.11
n^f_{FFMU}	0.059	0.05	0.57	0.27	0.21	0.88	0.88	0.27	0.11	0.07
L	0.2	0.18	0.067	0.011	0.076	0.17	0.17	0.74	0.054	0.13
$bone_r$	0.03	0.027	0.13	0.023	0.018	0.28	0.28	0.17	0.037	0.0081
S_{fD}	0.096	0.1	0.073	0.02	0.071	0.023	0.023	0.16	0.03	0.1
FI_{fD}	0.037	0.035	0.2	0.064	0.056	0.24	0.24	0.29	0.039	0.068
FR_{fD}	0.043	0.045	0.046	0.0033	0.081	0.17	0.17	0.49	0.056	0.073
FF_{fD}	0.066	0.059	0.086	0.011	0.073	0.19	0.19	0.68	0.025	0.18
$C_{velocity}$	1	1	1	1	1	0.66	0.66	0.98	1	1
NMJ_{pos}	0.046	0.049	0.18	0.11	0.11	0.24	0.24	0.25	0.034	0.036
MTZ_L	0.053	0.0088	0.072	0.0054	0.057	0.15	0.15	0.2	0.087	0.19
MTZ_R	0.083	0.055	0.13	0.064	0.1	0.12	0.12	0.61	0.076	0.086
ρ^c_{muscle}	0.0071	0.044	0.16	0.022	0.071	0.26	0.26	0.2	0.061	0.14
θ^c_{muscle}	0.027	0.01	0.22	0.12	0.1	0.26	0.26	0.4	0.017	0.13
Z^c_{muscle}	0.053	0.035	0.63	0.41	0.39	0.89	0.89	0	0.056	0.062
$thick_{muscle}$	0.047	0.037	0.36	0.16	0.13	1	1	0.49	0.038	0.084
ρ^c_{Fat}	0.072	0.053	0.41	0.25	0.24	0.77	0.77	0.22	0.05	0.26
θ^c_{Fat}	0.0037	0.0088	0.13	0.038	0.044	0.16	0.16	0.35	0.11	0.023
Z^c_{Fat}	0.036	0.031	0.11	0.067	0.053	0.21	0.21	0.43	0.06	0.045
$thick_{Fat}$	0.017	0.033	0.26	0.15	0.1	0.34	0.34	0.049	0.013	0.11
ρ^c_{skin}	0.096	0.027	0.081	0.045	0.052	0.12	0.12	0.51	0.093	0.026
θ^c_{skin}	0.056	0.03	0.16	0.067	0.091	0.14	0.14	0.36	0.046	0.071
Z^c_{skin}	0.05	0.023	0.23	0.15	0.15	0.37	0.37	0.75	0.061	0.07
$thick_{skin}$	0.063	0.035	0.29	0.14	0.15	0.37	0.37	0.46	0.022	0.23
$Grid_\theta$	0.026	0.049	0	0.026	0.026	0.15	0.15	0.84	0.04	0.0021
$Grid_Z$	0.015	0.037	0.21	0.074	0.11	0.5	0.5	0.45	0.053	0.095
$Grid_{rot}$	0.0099	0.039	0.11	0.054	0.081	0.16	0.16	0.32	0.034	0

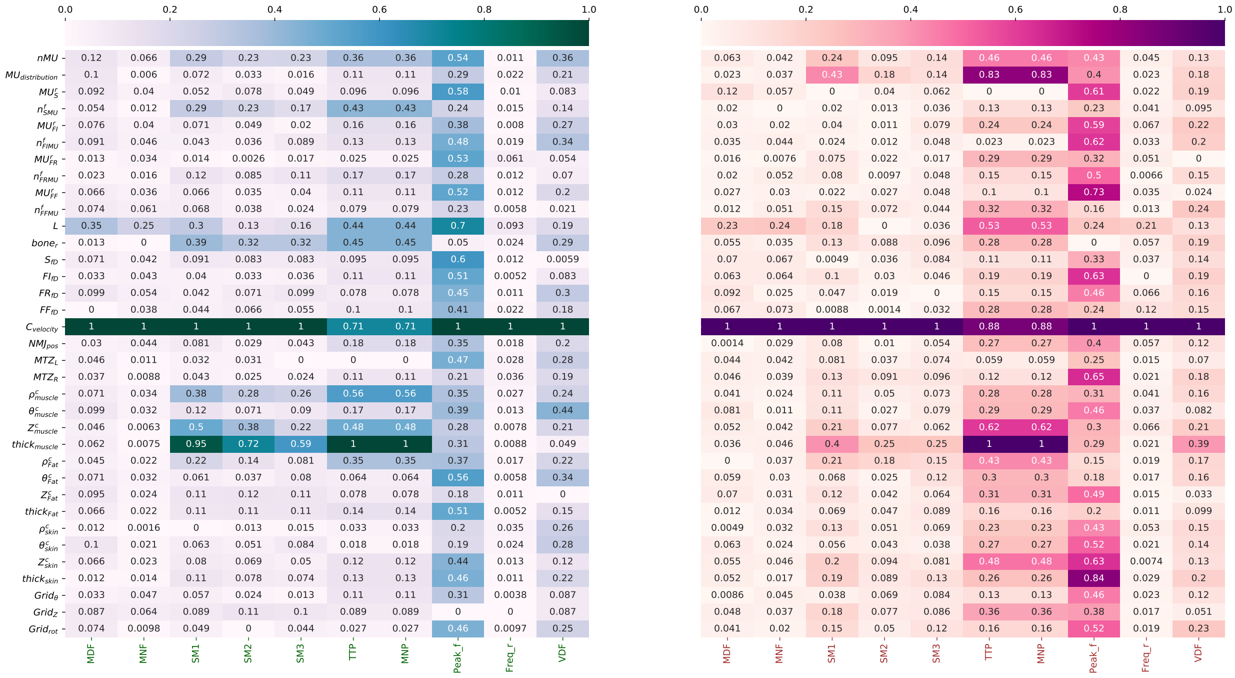

(c) Old men, 20% of MVC

	MDF	MNF	SM1	SM2	SM3	TTP	MNP	Peak_f	Freq_r	VDF
nMU	0.12	0.066	0.29	0.23	0.23	0.36	0.36	0.54	0.011	0.36
$MU_{distribution}$	0.1	0.006	0.072	0.033	0.016	0.11	0.11	0.29	0.022	0.21
MU^r_S	0.092	0.04	0.052	0.078	0.049	0.096	0.096	0.58	0.01	0.083
n^f_{SMU}	0.054	0.012	0.29	0.23	0.17	0.43	0.43	0.24	0.015	0.14
MU^r_{FI}	0.076	0.04	0.071	0.049	0.02	0.16	0.16	0.38	0.008	0.27
n^f_{FIMU}	0.091	0.046	0.043	0.036	0.089	0.13	0.13	0.48	0.019	0.34
MU^r_{FR}	0.013	0.034	0.014	0.0026	0.017	0.025	0.025	0.53	0.061	0.054
n^f_{FRMU}	0.023	0.016	0.12	0.085	0.11	0.17	0.17	0.28	0.012	0.07
MU^r_{FF}	0.066	0.036	0.066	0.035	0.04	0.11	0.11	0.52	0.012	0.2
n^f_{FFMU}	0.074	0.061	0.068	0.038	0.024	0.079	0.079	0.23	0.0058	0.021
L	0.35	0.25	0.3	0.13	0.16	0.44	0.44	0.7	0.093	0.19
$bone_r$	0.013	0	0.39	0.32	0.32	0.45	0.45	0.05	0.024	0.29
S_{fD}	0.071	0.042	0.091	0.083	0.083	0.095	0.095	0.6	0.012	0.0059
FI_{fD}	0.033	0.043	0.04	0.033	0.036	0.11	0.11	0.51	0.0052	0.083
FR_{fD}	0.099	0.054	0.042	0.071	0.099	0.078	0.078	0.45	0.011	0.3
FF_{fD}	0	0.038	0.044	0.066	0.055	0.1	0.1	0.41	0.022	0.18
$C_{velocity}$	1	1	1	1	1	0.71	0.71	1	1	1
NMJ_{pos}	0.03	0.044	0.081	0.029	0.043	0.18	0.18	0.35	0.018	0.2
MTZ_L	0.046	0.011	0.032	0.031	0	0	0	0.47	0.028	0.28
MTZ_R	0.037	0.0088	0.043	0.025	0.024	0.11	0.11	0.21	0.036	0.19
ρ^c_{muscle}	0.071	0.034	0.38	0.28	0.26	0.56	0.56	0.35	0.027	0.24
θ^c_{muscle}	0.099	0.032	0.12	0.071	0.09	0.17	0.17	0.39	0.013	0.44
Z^c_{muscle}	0.046	0.0063	0.5	0.38	0.22	0.48	0.48	0.28	0.0078	0.21
$thick_{muscle}$	0.062	0.0075	0.95	0.72	0.59	1	1	0.31	0.0088	0.049
ρ^c_{Fat}	0.045	0.022	0.22	0.14	0.081	0.35	0.35	0.37	0.017	0.22
θ^c_{Fat}	0.071	0.032	0.061	0.037	0.08	0.064	0.064	0.56	0.0058	0.34
Z^c_{Fat}	0.095	0.024	0.11	0.12	0.11	0.078	0.078	0.18	0.011	0
$thick_{Fat}$	0.066	0.022	0.11	0.11	0.11	0.14	0.14	0.51	0.0052	0.15
ρ^c_{skin}	0.012	0.0016	0	0.013	0.015	0.033	0.033	0.2	0.035	0.26
θ^c_{skin}	0.1	0.021	0.063	0.051	0.084	0.018	0.018	0.19	0.024	0.28
Z^c_{skin}	0.066	0.023	0.08	0.069	0.05	0.12	0.12	0.44	0.013	0.12
$thick_{skin}$	0.012	0.014	0.11	0.078	0.074	0.13	0.13	0.46	0.011	0.22
$Grid_\theta$	0.033	0.047	0.057	0.024	0.013	0.11	0.11	0.31	0.0038	0.087
$Grid_Z$	0.087	0.064	0.089	0.11	0.1	0.089	0.089	0	0	0.087
$Grid_{rot}$	0.074	0.0098	0.049	0	0.044	0.027	0.027	0.46	0.0097	0.25

(d) Old men, 60% of MVC

	MDF	MNF	SM1	SM2	SM3	TTP	MNP	Peak_f	Freq_r	VDF
nMU	0.063	0.042	0.24	0.095	0.14	0.46	0.46	0.43	0.045	0.13
$MU_{distribution}$	0.023	0.037	0.43	0.18	0.14	0.83	0.83	0.4	0.023	0.18
MU^r_S	0.12	0.057	0	0.04	0.062	0	0	0.61	0.022	0.19
n^f_{SMU}	0.02	0	0.02	0.013	0.036	0.13	0.13	0.23	0.041	0.095
MU^r_{FI}	0.03	0.02	0.04	0.011	0.079	0.24	0.24	0.59	0.067	0.22
n^f_{FIMU}	0.035	0.044	0.024	0.012	0.048	0.023	0.023	0.62	0.033	0.2
MU^r_{FR}	0.016	0.0076	0.075	0.022	0.017	0.29	0.29	0.32	0.051	0
n^f_{FRMU}	0.02	0.052	0.08	0.0097	0.048	0.15	0.15	0.5	0.0066	0.15
MU^r_{FF}	0.027	0.03	0.022	0.027	0.048	0.1	0.1	0.73	0.035	0.024
n^f_{FFMU}	0.012	0.051	0.15	0.072	0.044	0.32	0.32	0.16	0.013	0.24
L	0.23	0.24	0.18	0	0.036	0.53	0.53	0.24	0.21	0.13
$bone_r$	0.055	0.035	0.13	0.088	0.096	0.28	0.28	0	0.057	0.19
S_{fD}	0.07	0.067	0.0049	0.036	0.084	0.11	0.11	0.33	0.037	0.14
FI_{fD}	0.063	0.064	0.1	0.03	0.046	0.19	0.19	0.63	0	0.19
FR_{fD}	0.092	0.025	0.047	0.019	0	0.15	0.15	0.46	0.066	0.16
FF_{fD}	0.067	0.073	0.0088	0.0014	0.032	0.28	0.28	0.24	0.12	0.15
$C_{velocity}$	1	1	1	1	1	0.88	0.88	1	1	1
NMJ_{pos}	0.0014	0.029	0.08	0.01	0.054	0.27	0.27	0.4	0.057	0.12
MTZ_L	0.044	0.042	0.081	0.037	0.074	0.059	0.059	0.25	0.015	0.07
MTZ_R	0.046	0.039	0.13	0.091	0.096	0.12	0.12	0.65	0.021	0.18
ρ^c_{muscle}	0.041	0.024	0.11	0.05	0.073	0.28	0.28	0.31	0.041	0.16
θ^c_{muscle}	0.081	0.011	0.11	0.027	0.079	0.29	0.29	0.46	0.037	0.082
Z^c_{muscle}	0.052	0.042	0.21	0.077	0.062	0.62	0.62	0.3	0.066	0.21
$thick_{muscle}$	0.036	0.046	0.4	0.25	0.25	1	1	0.29	0.021	0.39
ρ^c_{Fat}	0	0.037	0.21	0.18	0.15	0.43	0.43	0.15	0.019	0.17
θ^c_{Fat}	0.059	0.03	0.068	0.025	0.12	0.3	0.3	0.18	0.017	0.16
Z^c_{Fat}	0.07	0.031	0.12	0.042	0.064	0.31	0.31	0.49	0.015	0.033
$thick_{Fat}$	0.012	0.034	0.069	0.047	0.089	0.16	0.16	0.2	0.011	0.099
ρ^c_{skin}	0.0049	0.032	0.13	0.051	0.069	0.23	0.23	0.43	0.053	0.15
θ^c_{skin}	0.063	0.024	0.056	0.043	0.038	0.27	0.27	0.52	0.021	0.14
Z^c_{skin}	0.055	0.046	0.2	0.094	0.081	0.48	0.48	0.63	0.0074	0.13
$thick_{skin}$	0.052	0.017	0.19	0.089	0.13	0.26	0.26	0.84	0.029	0.2
$Grid_\theta$	0.0086	0.045	0.038	0.069	0.084	0.13	0.13	0.46	0.023	0.12
$Grid_Z$	0.048	0.037	0.18	0.077	0.086	0.36	0.36	0.38	0.017	0.051
$Grid_{rot}$	0.041	0.02	0.15	0.05	0.12	0.16	0.16	0.52	0.019	0.23

Figure 2.20: Impacts of model inputs on extracted amplitude HD-sEMG FD features (IMSA results). IMSA impact indice = Normalized *SI* (from 0 (light color) to 1 (dark color)). Ranking of neuromuscular inputs according to age (young (a,b) and old men (c,d)), and level of force contractions (low (a,c) and high(b,d)).

- *group 1: MDF and MNF*, these two features are useful as fatigue indicators. Its relation to conduction velocity of fibers was proved as linear impact on HD-sEMG signals at isometric contractions. The length of fibers (L) is in the second position, and the rest of inputs have a negligible effects. These two inputs have a monotonic effect with tendency of $C_{velocity}$ to have an almost linear effect (IMSA screening).
- *group 2: SM1, SM2 and SM3* The $C_{velocity}$ has the most important impact. At low contraction (LC), the muscle thickness and conductivity have the same important impact for YM and OM. This influence decrease for higher order of SM features. Then, a reduced group of parameters have an intermediate influence. This group changes slightly one or more of its members when changing contraction level or age. We observe that this group contains muscle thickness ($thick_{muscle}$) and conductivities (Z^c_{muscle}, ρ^c_{muscle}). For (YM, HC), this group contains, in addition, the number of slow fibers per MU. For (OM, LC), four parameters share the first ranks: conduction velocity, muscle thickness, longitudinal and radial muscle conductivities respectively. We note that, with IMSA screening, these features have an identical distribution of parameters, and that the influential parameters are localized in the "almost-monotonic" zone.
- *group 3: TTP and MNP* The most influential parameters for all categories are: the conduction velocity of fibers ($C_{velocity}$), the longitudinal conductivity of fibers (Z^c_{muscle}), and the muscle thickness ($thick_{muscle}$). For LC categories, the number of slow fibers per MU has a large impact (FF fibers at HC). We observe that the MU repartition have an important impact for OM at HC.
- *group 4: Freq_ratio and VDF* All parameters have a negligible effect, expecting *C_velocity*.
- *group 5: Peak_Freq* Most of parameters have a significant impact.

K-mean algorithm results for frequency domain features The application of K-mean algorithm on the data of IMSA results provides the most influential group of parameters for each feature. The Tables 2.16 2.17 2.18 2.19 show the result of k-means algorithm. We observe in Fig. 2.21, 2.22, 2.23, 2.24 the screening of parameters using IMSA method. In these figures, cluster of parameters with strong impact on the studied feature is marked by green color (red color for parameters with negligible effects). The results of the unsupervised learning of sensitivity analysis data are similar to visual observations of Fig. 2.20.

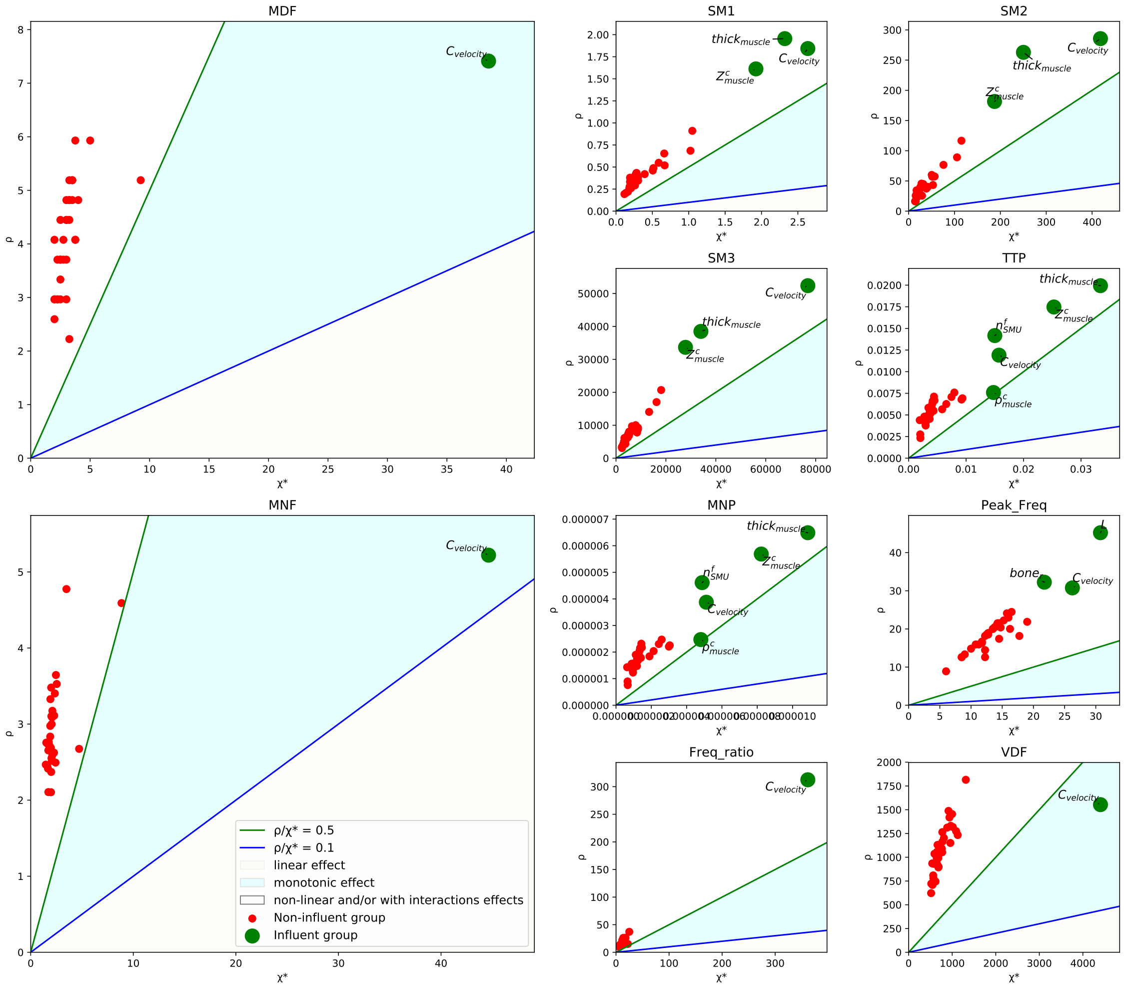

Figure 2.21: IMSA screening of influential parameters for frequency domain features. Categories: YM, LC. Clustering method = K-means

Table 2.16: Group of influent parameters for young men (YM) at high contractions (LC = 20% of MVC). Frequency domain features.

Feature	Number of Influent parameters	List of influent parameters
MDF MNF Freq_ratio VDF	1	$C_{velocity}$
SM1 SM2 SM3	3	$thick_{muscle}$, $C_{velocity}$, Z^c_{muscle}
MNP TTP	5	$thick_{muscle}$, $C_{velocity}$, $MU_{distribution}$, Z^c_{muscle}, n^f_{SMU}, ρ^c_{muscle}
Peak_freq	3	L, $C_{velocity}$, $bone_r$

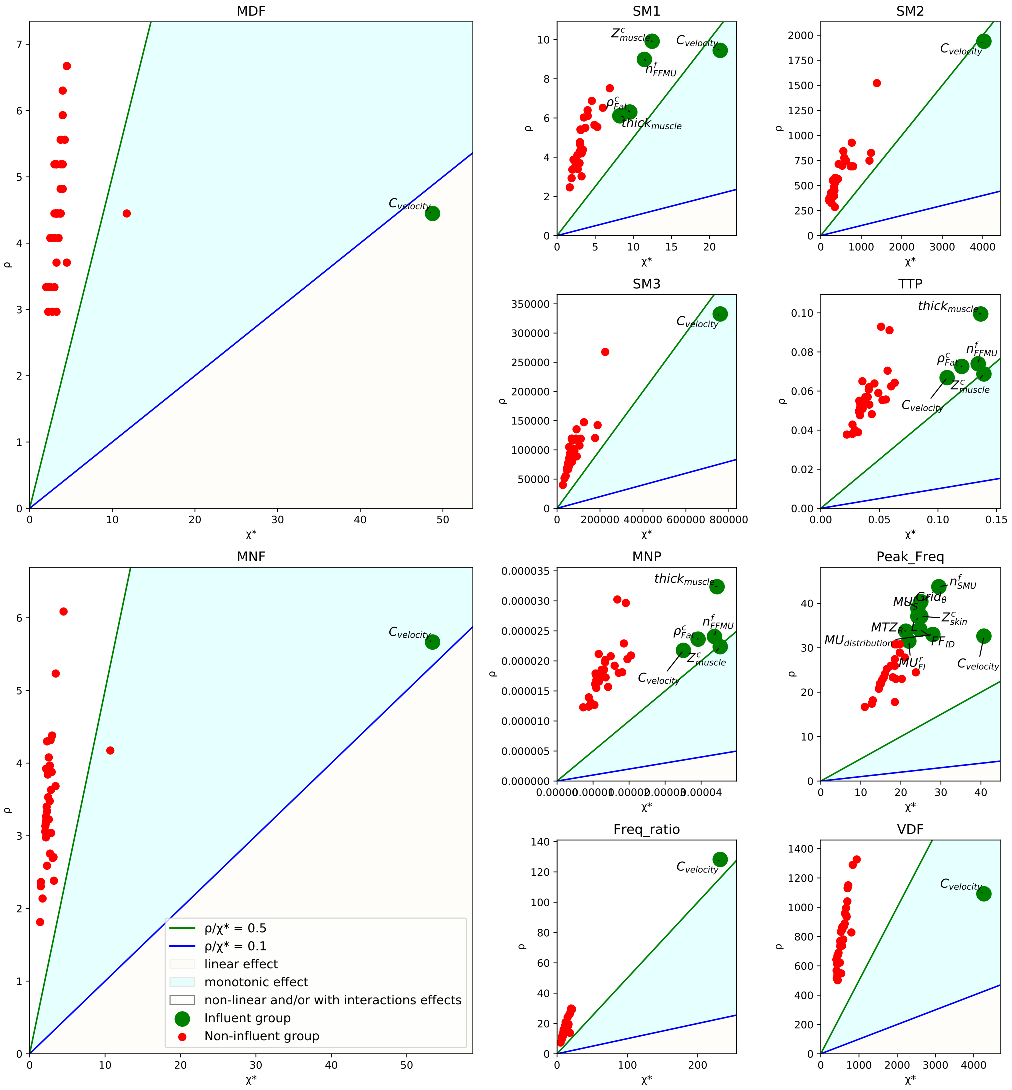

Figure 2.22: IMSA screening of influential parameters for frequency domain features. Categories: YM, HC. Clustering method = K-means

Table 2.17: Group of influent parameters for young men (YM) at high contractions (HC = 60% of MVC). Frequency domain features.

Feature	Number of Influent parameters	List of influent parameters
MDF MNF SM2 SM3 Freq_ratio VDF	1	$C_{velocity}$
SM1 TTP MNP	5	$thick_{muscle}$, $C_{velocity}$, Z^c_{muscle}, n^f_{FFMU}, ρ^c_{Fat}
MNP TTP	5	$thick_{muscle}$, $C_{velocity}$, $MU_{distribution}$, Z^c_{muscle}, n^f_{SMU}, ρ^c_{muscle}
Peak_freq	10	L, $C_{velocity}$, $MU_{distribution}$, n^f_{SMU}, Z^c_{skin}, $Grid_\theta$, MTZ_R, MU^r_S, FF_{fd},MU^r_S

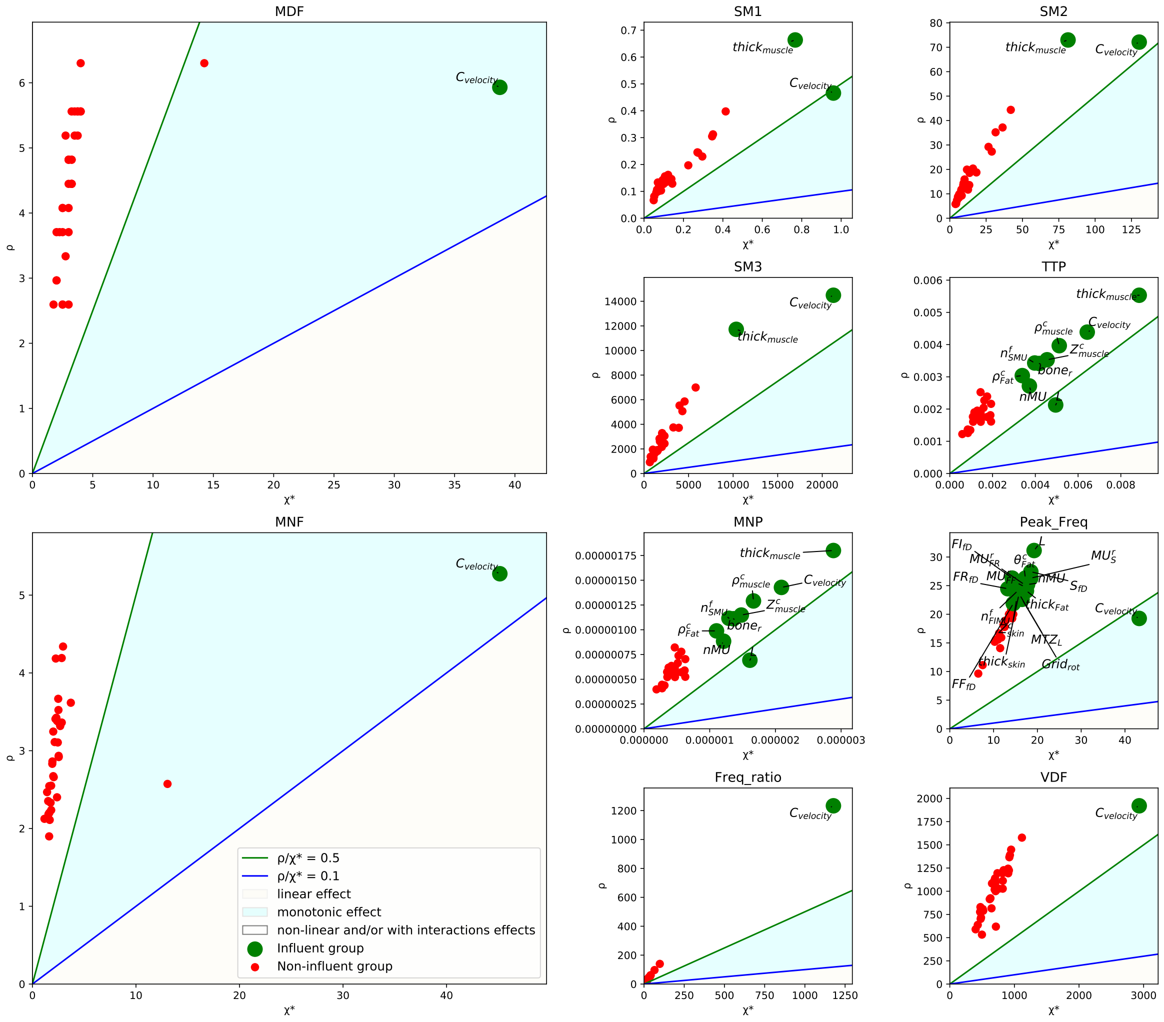

Figure 2.23: IMSA screening of influential parameters for frequency domain features. Categories: OM, LC. Clustering method = K-means

Table 2.18: Group of influent parameters for old men (OM) at high contractions (LC = 20% of MVC). Frequency domain features.

Feature	Number of Influent parameters	List of influent parameters
MDF MNF Freq_ratio VDF	1	$C_{velocity}$
SM1 SM2 SM3	2	$thick_{muscle}$, $C_{velocity}$
MNP TTP	9	$thick_{muscle}$, $C_{velocity}$, $bone_r$, Z^c_{muscle}, n^f_{SMU}, ρ^c_{muscle}, ρ^c_{Fat}, nMU
Peak_freq	17	nMU, MU^r_S, n^f_{FIMU}, MU^r_{FR}, MU^r_{FF}, L, S_{fD}, FI_{fD}, FR_{fD}, FF_{fD}, $C_{velocity}$, MTZ_L, θ^c_{Fat}, $thick_{Fat}$, Z^c_{skin}, $thick_{skin}$, $Grid_{rot}$

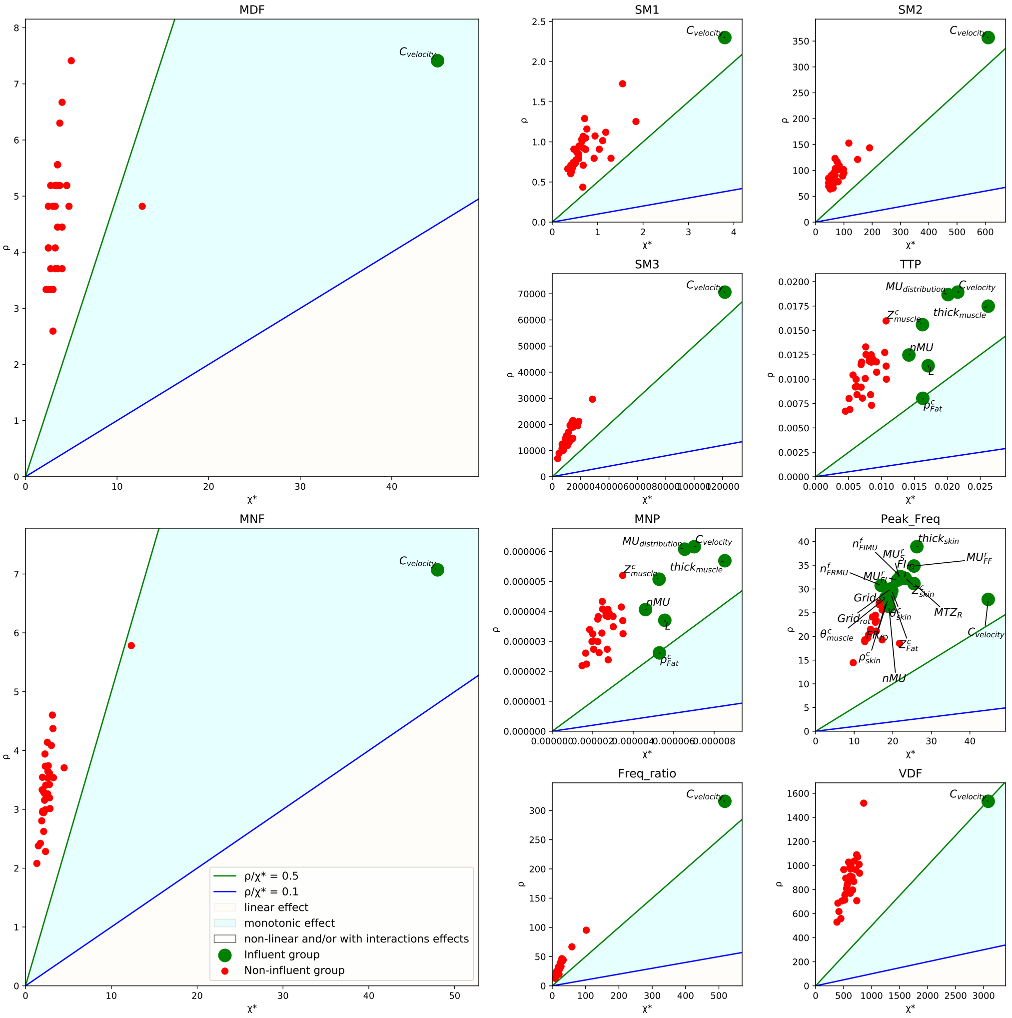

Figure 2.24: IMSA screening of influential parameters for frequency domain features. Categories: OM, HC. Clustering method = K-means

Table 2.19: Group of influent parameters for old men (OM) at high contractions (HC = 60% of MVC). Frequency domain features.

Feature	Number of Influent parameters	List of influent parameters
MDF MNF SM1 SM2 SM3 Freq_ratio VDF	1	$C_{velocity}$
SM1 SM2 SM3	2	$thick_{muscle}$, $C_{velocity}$
MNP TTP	7	nMU, $MU_{distribution}$, L, $C_{velocity}$, Z^c_{muscle}, $thick_{muscle}$, ρ^c_{Fat}
Peak_freq	17	$MU_{distribution}$, n^f_{SMU}, MU^r_{FR}, n^f_{FFMU}, L, $bone_r$, S_{fD}, FF_{fD}, NMJ_{pos}, MTZ_L, ρ^c_{muscle}, Z^c_{muscle}, $thick_{muscle}$, ρ^c_{Fat}, θ^c_{Fat}, $thick_{Fat}$, $Grid_Z$

2.4.1.2 Bivariate features

To assess bivariate relationship between HD-sEMG channels, two features are selected: the linear correlation coefficient: Pearson coefficient R_2, and the nonlinear coefficient: H_2. We cannot observe a significant difference between YM and OM. The changes are observed between LC and HC. For LC, only few parameters (2-3) enhance correlation between recording system channels: L and $C_{velocity}$. For HC, many parameters have a large impact (almost parameters). The results of K-mean algorithm are provided in Fig. 2.26, 2.27, 2.28, 2.29; and Tables 2.20, 2.21, 2.22, 2.23.

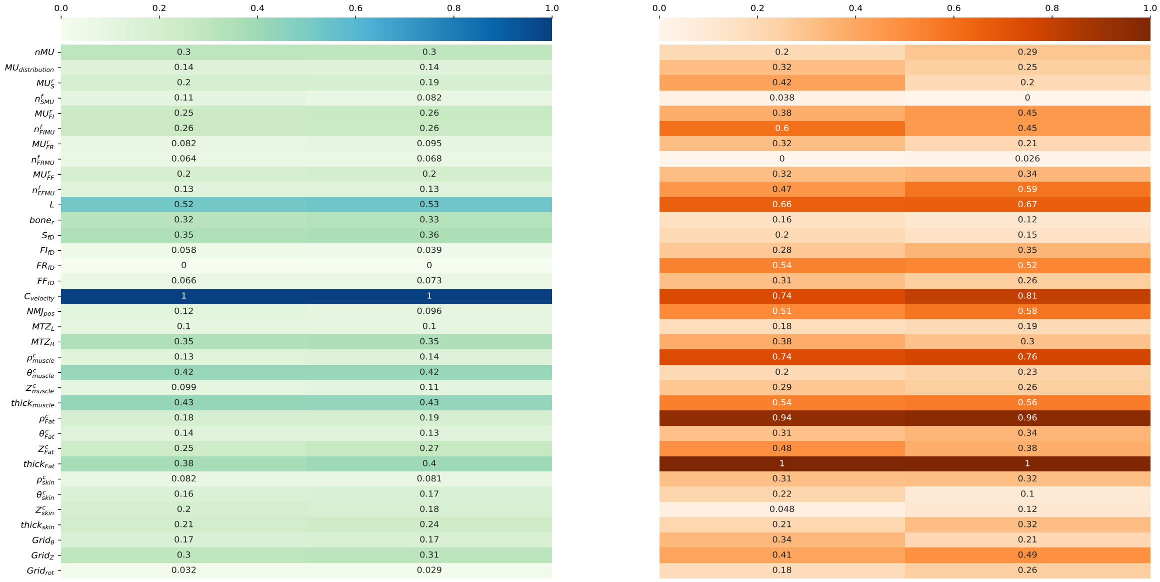

(a) Young men, 20% of MVC (b) Young men, 60% of MVC

(c) Old men, 20% of MVC (d) Old men, 60% of MVC

Figure 2.25: Impacts of model inputs on extracted HD-sEMG Bivariate features (IMSA results). IMSA impact indice = Normalized SI (from 0 (light color) to 1 (dark color)). Ranking of neuromuscular model inputs according to age (young (a,b) and old men (c,d)), and level of force contractions (low (a,c) and high(b,d)).

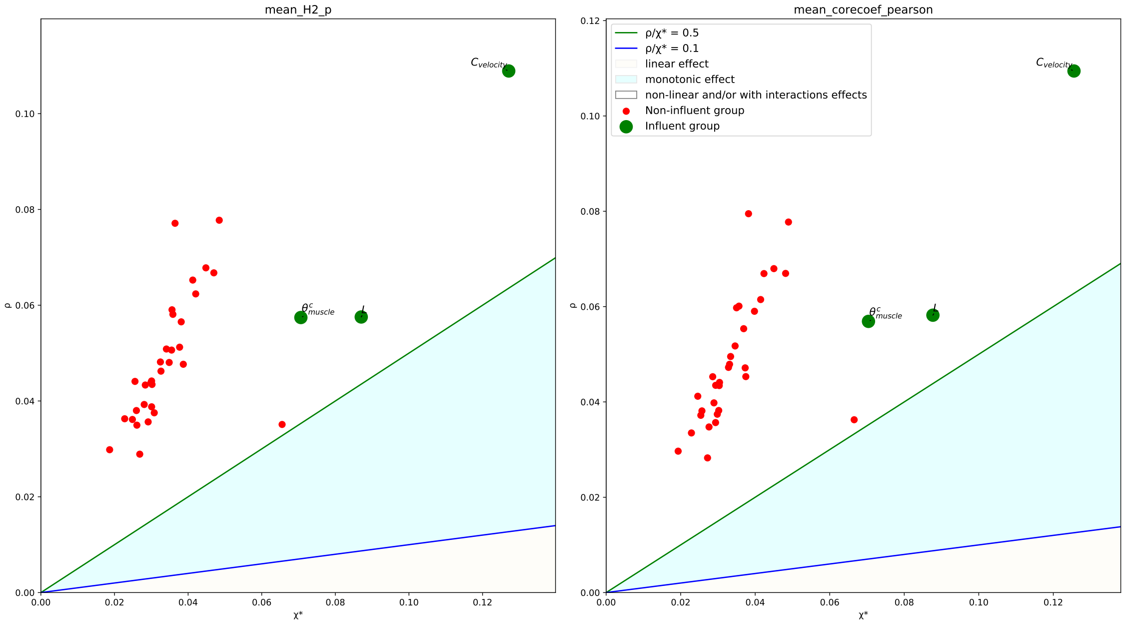

Figure 2.26: IMSA screening of influential parameters for Bi_variate features. Categories: YM, LC. Clustering method = K-means

Table 2.20: Group of influent parameters for young men (YM) at low contractions (LC = 20% of MVC). Frequency domain features.

Feature	Number of Influent parameters	List of influent parameters
H_2^P R_2^P	3	$C_{velocity}$, L, θ^c_{muscle}

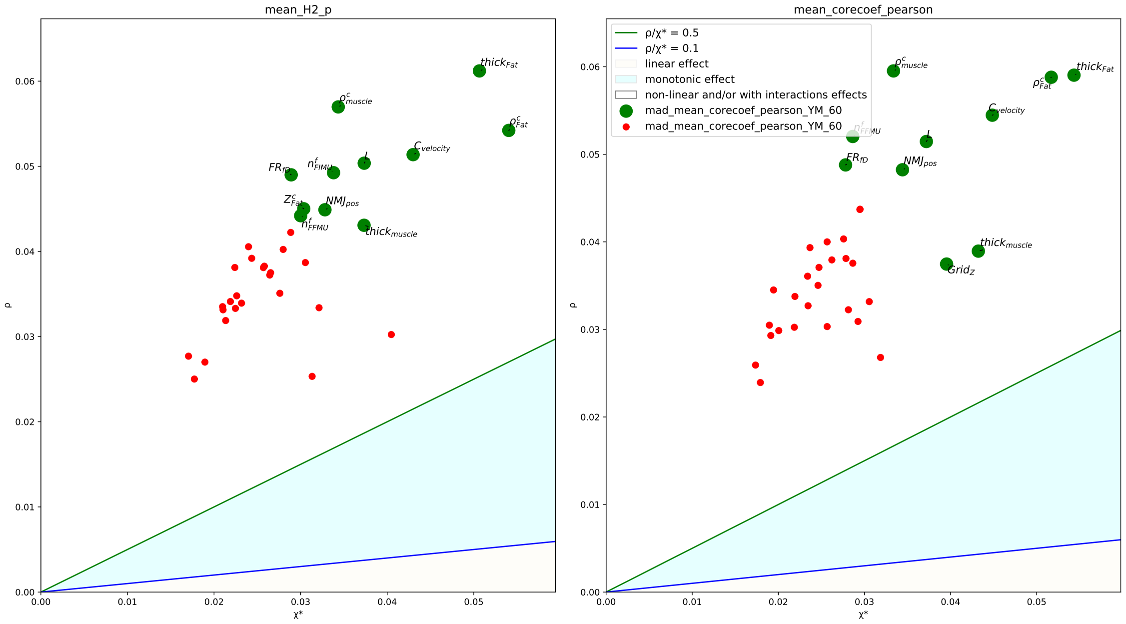

Figure 2.27: IMSA screening of influential parameters for Bi_variate features. Categories: YM, HC. Clustering method = K-means

Table 2.21: Group of influent parameters for young men (YM) at high contractions (HC = 60% of MVC). Frequency domain features.

Feature	Number of Influent parameters	List of influent parameters
H_2^P	24	nMU, $MU_{distribution}$, MU_S^r, n_{SMU}^f, MU_{FI}^r, MU_{FR}^r, n_{FRMU}^f, MU_{FF}^r, $bone_r$, S_{fD}, FI_{fD}, FF_{fD}, MTZ_L, MTZ_R, θ_{muscle}^c, Z_{muscle}^c, θ_{Fat}^c, ρ_{skin}^c, θ_{skin}^c, Z_{skin}^c, $thick_{skin}$, $Grid_\theta$, $Grid_Z$, $Grid_{rot}$
R_2^P	10	n_{FFMU}^f, L, FR_{fD}, $C_{velocity}$, NMJ_{pos}, ρ_{muscle}^c, $thick_{muscle}$, ρ_{Fat}^c, $thick_{Fat}$, $Grid_Z$

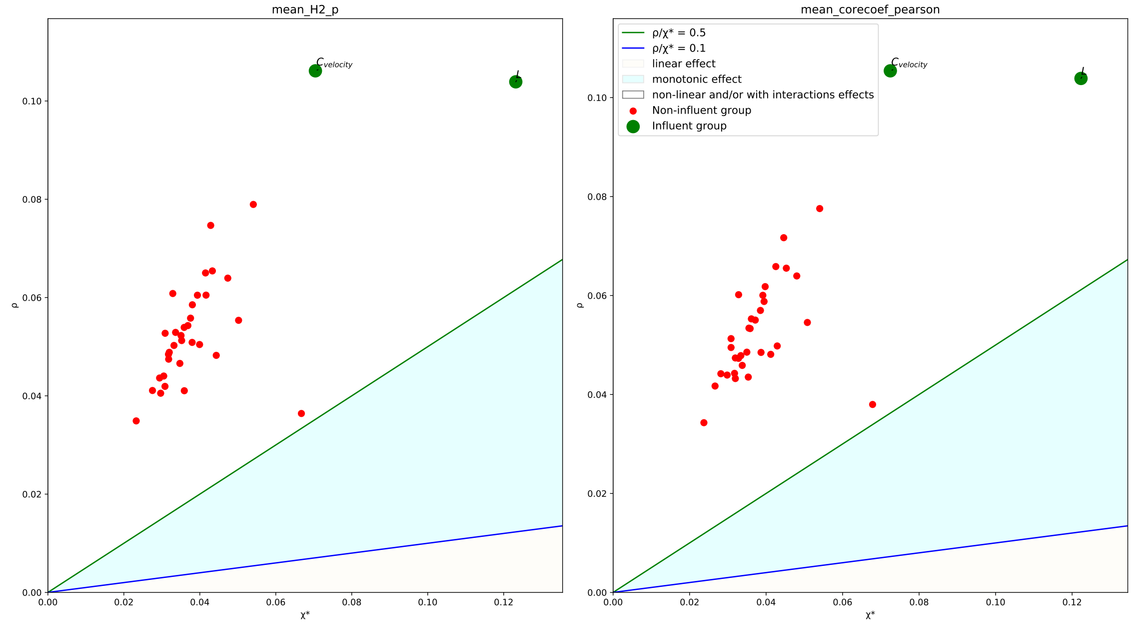

Figure 2.28: IMSA screening of influential parameters for Bi_variate features. Categories: OM, HC. Clustering method = K-means

Table 2.22: Group of influent parameters for old men (OM) at low contractions (LC = 20% of MVC). Bi_variate features.

Feature	Number of Influent parameters	List of influent parameters
H_2^P R_2^P	2	$C_{velocity}$, L

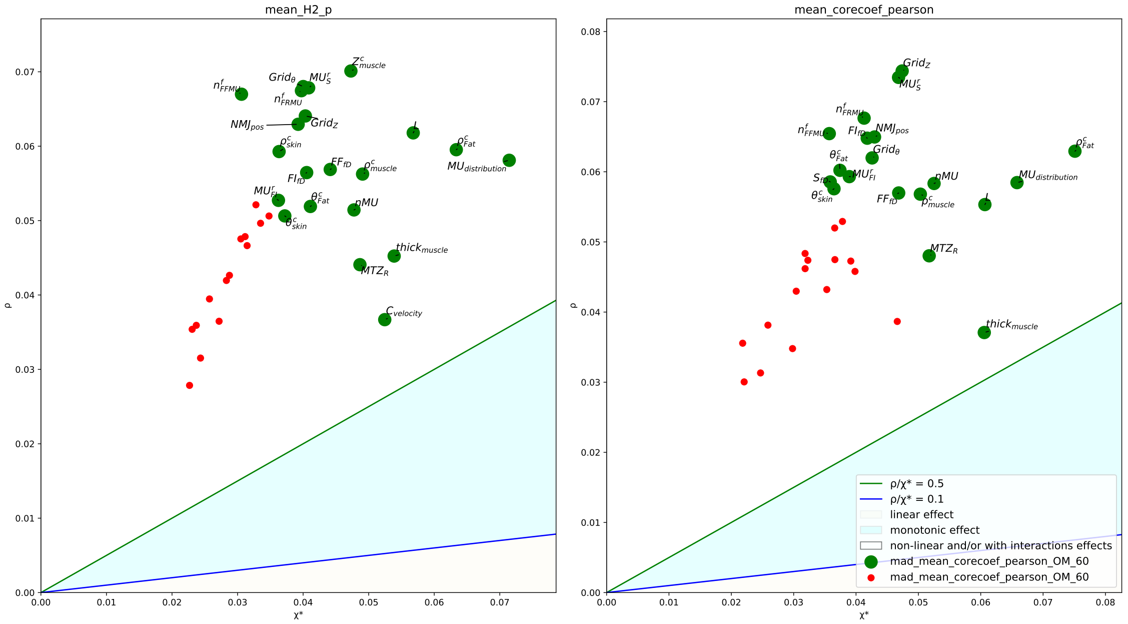

Figure 2.29: IMSA screening of influential parameters for Bi_variate features. Categories: OM, HC. Clustering method = K-means

Table 2.23: Group of influent parameters for old men (OM) at high contractions (HC = 60% of MVC). Frequency domain features.

Feature	Number of Influent parameters	List of influent parameters
H_2^P	20	nMU, $MU_{distribution}$, MU^r_S, MU^r_{FI}, n^f_{FRMU}, n^f_{FFMU}, L, FI_{fD}, FF_{fD}, $C_{velocity}$, NMJ_{pos}, MTZ_R, ρ^c_{muscle}, Z^c_{muscle}, $thick_{muscle}$, ρ^c_{Fat}, θ^c_{Fat}, ρ^c_{skin}, θ^c_{skin}, $Grid_\theta$, $Grid_Z$
R_2^P	19	nMU, $MU_{distribution}$, MU^r_S, MU^r_{FI}, n^f_{FRMU}, n^f_{FFMU}, L, S_{fD}, FI_{fD}, FF_{fD}, NMJ_{pos}, MTZ_R, ρ^c_{muscle}, $thick_{muscle}$, ρ^c_{Fat}, θ^c_{Fat}, θ^c_{skin}, $Grid_\theta$, $Grid_Z$

2.4.2 Discussion

The purpose of this study is the identification of anatomical and neural muscle factors with the largest impact on the HD-sEMG signals simulated with studied model. The application of IMSA method on the Hd-sEMG signals generated by the neuromuscular model allows the identification of parameters with small and large impact for young and old men at low and high contractions. The muscle anatomy for young and old groups is reported from literature, to mimic as much as possible young and aged muscle (e.g. number of fibers, cross sectional area,etc.). The identification of important and negligible parameters is a supporting argument for the validation of modeling approaches and assumptions applied and depicted in [1, 11]. In fact, experimental HD-sEMG signals extracted from striated muscle during isometric contractions confirm many particular aspects observed with IMSA sensitivity analysis results of this study. It was verified in many clinical studies that, for time domain features, parameters related to the structure and morphology of muscle have a large impact on the measured HD-sEMG signals. This study demonstrates that the simulated HD-sEMG signals are sensitive to: muscle thickness, the conduction velocity, and muscle conductivities at LC. In addition, at HC, HD-sEMG signals became sensitive to the number of MU and the electrode grid position. Many studies prove that HD-sEMG amplitude is correlated to the increase of force exerted due to the increase of MU recruited [263, 264, 201]. Likewise, the increase of conduction velocity effect with the increase of contractions level is mentioned in [265] and clearly observed in Fig. 2.15 for YM and OM at HC.

For the electrode placement, many previous studies [266, 267] have evoked its importance. This importance is due to its high dependency to source locations, innervation zone, and the non-homogeneity of the conductor volume. This study shows that the orientation and position of recording system is an important factor at HC with amplitude features, which confirms experimental findings in literature. However, it was not mentioned that this effect increases with increasing contractions level. In fact, in the modeling approach depicted in [1], at HC, fast sources (FF MU) are much more recruited and located at muscle surface layer. This could be an explanation to the large effect of recording system position at HC.

An additional statement was observed in this study: the highest sensitivity of HD-sEMG signals to the number of slow and fast fibers and MU at low and high contractions respectively. It was confirmed in [268, 269, 270] that for LC, only slow fibers/MU are recruited to exert force. Likewise, for HC, the fast fibers are recruited after recruiting all slow ones. Its number is determinant to define the capacity in maintaining muscle contraction amplitude. This study states that fiber diameters have not a direct impact on the HD-sEMG signals compared to number of fibers. The loss of fibers and MU diameters with aging does not have a large impact on the simulated HDsEMG signals. This statement should be viewed cautiously. In fact, it can indicate that apoptosis phenomena have much more impact on the force generated by muscle than other phenomena such as the atrophy for example. From such conclusion, we can confirm that the decline of muscle functions with aging can be related mainly to the neural system (denervation-reinnervation failure) [86]. However, other relevant observation with IMSA results should be mentioned: the muscle thickness have more impact with aged subjects for amplitude features (Fig. 2.15). This parameter is related to muscle cross section area (CSA), and its size reduction is due to both apoptosis and atrophy. From such result, the previous statement is not totally effective. Moreover, the conduction velocity of fibers, which have a large impact in this study, is a function of fiber diameters as depicted in [1]. Therefore, the HD-sEMG signals can be considered as very sensitive to atrophy but indirectly, through muscle thickness and conduction velocity. This is more consistent with many studies correlating the reduction of muscle size to the loss of force with aging.

All these expected results make credible the modeling approaches proposed in this thesis for realistic simulation of muscle electrical activity with aging.

For frequency domain features, it was evident that the conduction velocity of fibers and the muscle conductivity have the most important impacts. This approves experimental results [271, 272] and can validate assumptions and approaches applied in [1]. With IMSA results, we have observed no significant difference between YM and OM at LC and HC. This can be related to two facts: (i) FD features are useful to detect muscle fatigue and this aspect is not considered in [1], and (ii) this model is not incorporating phenomena related to muscle aging (see the following chapter 3 for details).

The previous discussed points lead to enhance the neuromuscular model depicted in [1] with supplement modeling approaches describing structural, morphological, and functional age-related phenomena like: atrophy, apoptosis, MU spatiotemporal recruitment, MU remodeling, and adipose tissue intra/inter muscular infiltration. However, the importance of IMSA results can be extended to cover other important sides. One of the purposes of applying a sensitivity analysis method on HD-sEMG signals is to develop a patient personalized model to evaluate and diagnosis muscle aging and its related pathologies as Sarcopenia. A non accessible model parameter value identification with inverse methods is contemplated to reach a reliable diagnosis. IMSA results offer a map of relationships between inputs and outputs. This will facilitate the decision of which muscle factor should be identified and by which feature and at which condition (age, contractions level).

Other important aspects can be underlined from IMSA results as the homogenization of the most influential muscle parameters for subjects, if possible. In fact, this homogenization can be valuable and crucial for reliable clinical assessment of muscle state and diseases by helping in designing a fitted experimental setup. For a reliable assessment of Neuropathies, for example, it is better to neutralize the effect of muscle thickness on the HD-sEMG signals by selecting subjects with a small variation scale for this parameters. Commonly, clinical test practitioners are not warn against this factor. Usually, studies for clinical EMG measures use essentially the body mass index (BMI) as the main criteria to select subjects/patients. Moreover, this study shows that the position electrodes can be important for many features and at some contractions level (Fig. 2.15). A rotation of the recording grid by few degrees, or a translation by few millimeters can impact greatly the measured HD-sEMG signals. Therefore, this study suggested more care for this kind of aspects when evaluating muscle diseases and health by HD-sEMG techniques.

2.5 Conclusion

In this chapter, we have recalled the usefulness of the MSA method indices and proposed an improved formalism. An assessment of classical MSA in the context of analyzing a bio-reliable HD-sEMG model revealed that parameter rankings, obtained by using the absolute mean value μ^* and the standard deviation σ of the elementary effects as a criterion, are unstable and unreliable. The new proposed IMSA approach guarantees the satisfaction of these criteria without affecting the design of the classical MSA method. It proposes two new robust indices to evaluate elementary effects: the absolute median (χ^*) and the median absolute deviation (ρ). By applying a normality test, we show that elementary effects are normally distributed for all parameters with IMSA indices (χ^*,ρ). In contrast, many parameters have a non-normal distributions around MSA indices (μ^*,σ). As consequence, the screening information about the (non)linearity, (non)monotonicity, and interactions between parameters that provide MSA method are unreliable and distorting the sensitivity analysis results. In fact, this information is based on statistical properties of the ratio σ/μ^* for normal distributions. Thus, the new IMSA ratio ρ/χ^* is more appropriate as a graphic indicator of parameter effect features. Furthermore, by using the new indices, the minimum number of trajectories T needed to obtain a stable

ranking with new IMSA indices is T = 20 (computing time = 06h02min), while MSA indices remains unstable until T = 100 (computing time = 42h35min) using the same computing resources. Such result is useful for high order computational cost models.
Furthermore, we have proved that the modeling approach depicted in [273, 11] can produce a simulated HD-sEMG signal close to the experimental signals. The neuromuscular model is able to deliver signals sensitive to anatomical and neural muscle factors as in real cases. This result makes this model as a valuable candidate to evaluate healthy and diseased muscle state with low cost and in reduced time by also helping in design of optimized experimental setup. However, for a reliable evaluation of muscle aging, modeling approaches should be enhanced to better describe structural, morphological, and functional age-related phenomena. This last point will be the focus of the next chapter.

Chapter 3

Model personalization to muscle aging

Contents

3.1 Introduction

The age-related loss in neuromuscular function comprise loss of MUs and expansion of that remain, reduction in muscle fiber number and size, increase of intramuscular fat infiltration, changes in the neural drive (spatial and temporal recruitment),and force steadiness (see chapter 1). As a consequence, mechanical muscle performance is impaired with concurrent decreases in maximal muscle strength, power, and rate of force development in the elderly.

The monitoring of these age-related alterations in the neuromuscular system from surface Electromyography (sEMG) signals has expanded during the last twenty years [199]. Likewise, the modeling of sEMG signals generation has seen the same expansion [274, 275].

Mathematical models of sEMG are highly useful, on the one hand to advance understanding of the underlying physiological processes, and on the other hand to analyze and investigate the effects of varying physiological parameters on the simulated signal, and to test and validate sEMG signal processing algorithms [203, 274]. In fact, models can provide electromyographic data generated in specific physiological and neural configurations. Those configurations can be controlled in models whereas it is hardly estimated in experimental conditions.

However an accurate and realistic sEMG model is a hard task. In the literature, two sEMG modeling approaches have been proposed. The first one, called phenomenological approach, is based on a statistical analysis of real signals without taking into account their physical and physiological aspect. The second one, called physiological approach, is specified by the simulation of the Action Potential (AP) detected by the electrodes while taking into account the influence of the parameters acting on the collected EMG signals [203, 274]. Physiological approaches can be categorized into analytical (e.g., [1, 276, 277, 278]) and numerical modeling approaches (e.g., [279, 280]). Numerical methods have more accuracy in describing anatomical muscle structure and morphology (e.g, fiber orientation, conductor volume). These models can be derived from imaging techniques to create 3D representations of muscle tissues. Which allow a realistic sEMG signal generation and volume conduction mainly overcoming the muscle electrical anisotropy simplification adopted by analytical modeling approaches. In fact, the space-invariance property (homogeneous conductor volume) in the direction of source propagation, made by a linear, space and time invariant filters to the source with analytical models, can impact considerably the interpreting sEMG signal features. However, this impact can be reduced for fusiform muscles analytical models, like Biceps Brachii, compared to penniform muscles. Nonetheless, the major impediment of numerical modeling approaches is the high computational cost and the complex workflow in the building/solving model process. This factor represents a major obstacle in clinical diagnosis/evaluation of muscle impairment in general, and during aging in particular. In fact, useful applications to identify aging biomarker(s) from sEMG by inverse methods, e.g., sensitivity analysis and parameter identification, can not be performed in reasonable time.

For that reason, in this study, we use a physiological modeling approach analytically solving the sEMG source potential action generation. Analytical models generate sEMG signals by solving the Poisson's equation for the propagation of current sources along the muscle fibers. The computational cost are substantially reduced compared to numerical methods, although the geometry of the volume conductor is usually simpler than in numerical models. However, the selected model [1, 11] have many enhanced advantages compared to other sEMG models, analytically solved, existed in literature:

- It simulates the sEMG of fusiform muscle (Biceps Brachii (BB)) during isometric contractions. The simplification effects, made by analytical models, on muscle architecture have a reduced impact on the simulated sEMG signal using this muscle geometry compared to more complex architectures (pinnate, mutli-pinnate, etc.).
- It expresses the theoretical relationship of the generated signal according to a specific set of parameters (neural, anatomical and physiological) with more biological realism. Around 50 parameters are incorporated in the model, e,g,. anatomical parameters describing the number, size, and placement of MUs and fibers.
- Sources were generated from a three-layer volume conductor in cylindrical coordinates (muscle, subcutaneous fat, and skin). Fibers sources have circular forms and placed in parallel within this volume conductor. MUs sources have circular forms and placed according to Best Candidate (BC) algorithm.
- It proposes an innovative computation scheme for a fast and optimized computation of the muscle electrical activity over the skin surface using 3D matrices in the Fourier domain and parallel computing. Moreover, the electrical source is computed at the MU scale (summation of hundred sources) rather than at fiber scale (summation of many hundreds of thousand sources). This simplification reduced efficiently the computation time without affecting the quality of simulated sEMG.
- It increases the spatial representativeness of the recorded data over the studied muscle by using a high density recording technique that mimic the real HD-sEMG systems. This multidimensional view in the modeling process is proposed in this model without imposing a huge computational time as in other studies.
- It proposes a modular design which allows the modifications or extensions of a specific module easily without having an impact on the other model.

Nonetheless, this model have several limitations to be useful in the purpose of muscle aging evaluation and clinical aided-diagnosis. First, the model incorporates a large number of inputs (50 parameters). To generate young and elderly simulated neuromuscular systems, we need to adjust/calibrate manually the values of most of these neural and anatomical parameters (e.g., the number of MUs, their sizes, their spatial distribution, their innervation ratio, the muscle thickness,etc.). This calibration needs some expertise and a well-known of the variation ranges of all these parameters for young and elder subjects. Moreover, users must have a deep understanding of workflow, building, and solving processes of the model. In fact, based only on the parameter values reported in the literature or determined experimentally, users can introduce contradictory values, e.g., the number and size of fibers per MU must be consistent with the size of correspondent MU. Furthermore, these values were reported from various studies where the age of young and elder population is not the same for each category. However, as mentioned in the chapter 1, some anatomical and neural factors are highly impacted by the various stages of muscle aging within elderly population. For example, the size of fibers/MUs, which are the electrical generator sources of sEMG, changes dramatically between first aging stage ($65 \leq$ age ≤ 80 years) and latter stages (≥ 80 years); or between sarcopenic and sarcopenic subjects. Second, many aged muscle characteristics are not included in this modeling approach, e.g, the fiber atrophy and grouping, the intramuscular fat, and the expansion of MUs territories and fiber density per MU. These morphological and structural age-related changes have an important effect on the produced sEMG signal and force. Moreover, they can contribute to the diagnosis of muscle aging: healthy and accelerated aging inducing possible sarcopenic risk. For example, the increasing of fat mass is used as a sarcopenia feature by IWGS [1], and many studies correlated this increase with the increase of intramuscular fat. Third, the territory and the placement of MUs and fibers with this modeling approach are unrealistic and can impact the simulated sEMG signal for both young and elderly population. In fact, the model [1, 11] have positioned MUs with a best candidate algorithm (BC)[2]. Then, MUs are fulfilled with a number of fibers defined in the model inputs. This approach can cause to an unrealistic number of fibers within muscle (The multiplication of the number of fibers per MU by the total number of MUs can lead to a number of fibers lower than 100000 fibers per muscle which is unrealistic for BB muscle). In addition, the e circular shape of MUs is not realistic. A recent study [39] has proved, using Motor Unit Magnetic Resonance Imaging (MUMRI) technique, that MUs have more complex shapes (e.g., elliptical or spider-shaped forms). Finally, the neural drive model in [1, 11] is the same for young and elder population. However, as reported in chapter 1, the recruitment thresholds is larger for younger subjects [115] (and lower during fatigue [283]), and the motor unit discharge rates became lower in older adults. These findings suggest the reductions in motor unit discharge rates and the increase of recruitment threshold as an important mechanism during aging [284].

Given the above, the aim of the present chapter is to address these limitations and deliver more realistic and user-friendly model to evaluate muscle aging. In a first place, we will describe the modeling approach scheme as depicted in [1, 11], and we will discuss and illustrate its limitations (see section 3.2). Then, to overcome these limitations, we will propose a new user-friendly scheme. In this new scheme, the 50 inputs will be fairly limited to the age, gender, and muscle cross sectional area (if it was available) of the patient. All other parameters will be estimated from descriptive and statistical models built for this purpose. Finally, the impact of these age-related changes will be assessed on the HD-sEMG signals generated by the new model.

3.2 The biophysical HD-sEMG Model

To extract precise information from the HD-sEMG signal, it is necessary to have a firm understanding of how it was generated. This understanding is facilitated by the use of models and simulations. The modeling approach depicted in [1][11] simulates the electrical activity of BB muscle during isometric contractions. The main axis of this neuromuscular system are: (i) the modeling of the MU recruitment and firing behavior, (ii) modeling of MUAP, (iii) modeling of the conductor volume, (iv) and modeling of the recording system. This model mimics a BB muscle. Fast sources (MUs) are placed closer to the muscle surface. Slow and intermediate ones are more deeply immersed. The muscle geometry is considered as a cylinder with three layers: muscle, adipose tissues and skin. The source is simulated as a progressive generation of the intracellular action potential at the end plate and its extinction at the end of the fibers. The electrical activity, generated by these sources and propagated through the cylindrical conductor volume, is detected by an electrode grid at the skin surface (Fig. 3.1).

---

[1] International Working Group on Sarcopenia.

[2] algorithm to maximize the minimal distance between MUs (see [281, 282]).

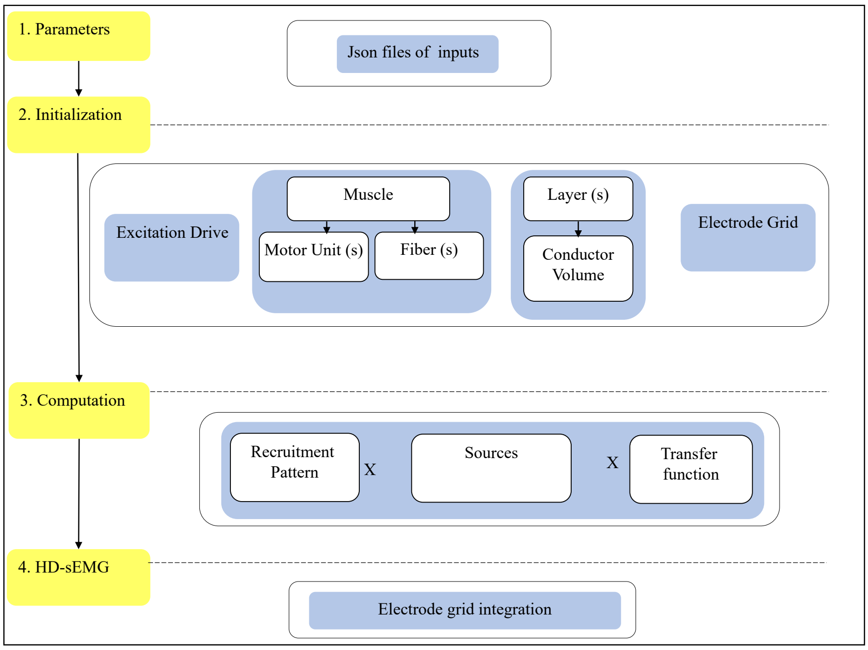

Figure 3.1: Model implementation diagram of the modeling approach in [1] and [11].

3.2.1 Model implementation

The proposed model is implemented through an object-oriented approach and structured with a modular design code. The model is split into independent modules, in a way that each module clearly represents a specific part of the model which allows the modifications or extensions of a specific module easily without having an impact on the other modules (Fig. 3.1). The Fig. 3.2 summarize all the parameters needed to initiate the simulation of HD-sEMG signal for BB muscle during isometric contractions.

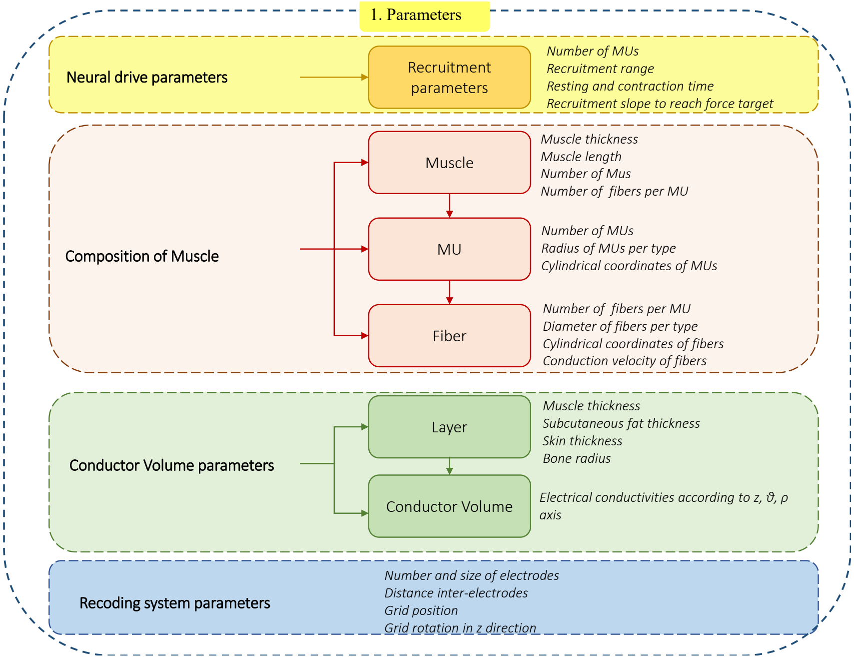

Figure 3.2: Model inputs: All parameters needed to initiate a simulation of HD-sEMG signals during isometric contraction.

The implemented model needs an input file (JSON extension format) to start a simulation. This file contains all the parameters needed to the execution of the model. It indicates the name of the parameter with an associated unit. Around 50 parameters are needed to: initialize the neural drive initiating voluntary contractions, the muscle and conductor volume anatomies, and the grid of electrodes (see Fig. 3.3). Users must provide more parameters like the conduction velocity of the fiber and spatial conductivity of different layer (muscle, subcutaneous fat, and skin).

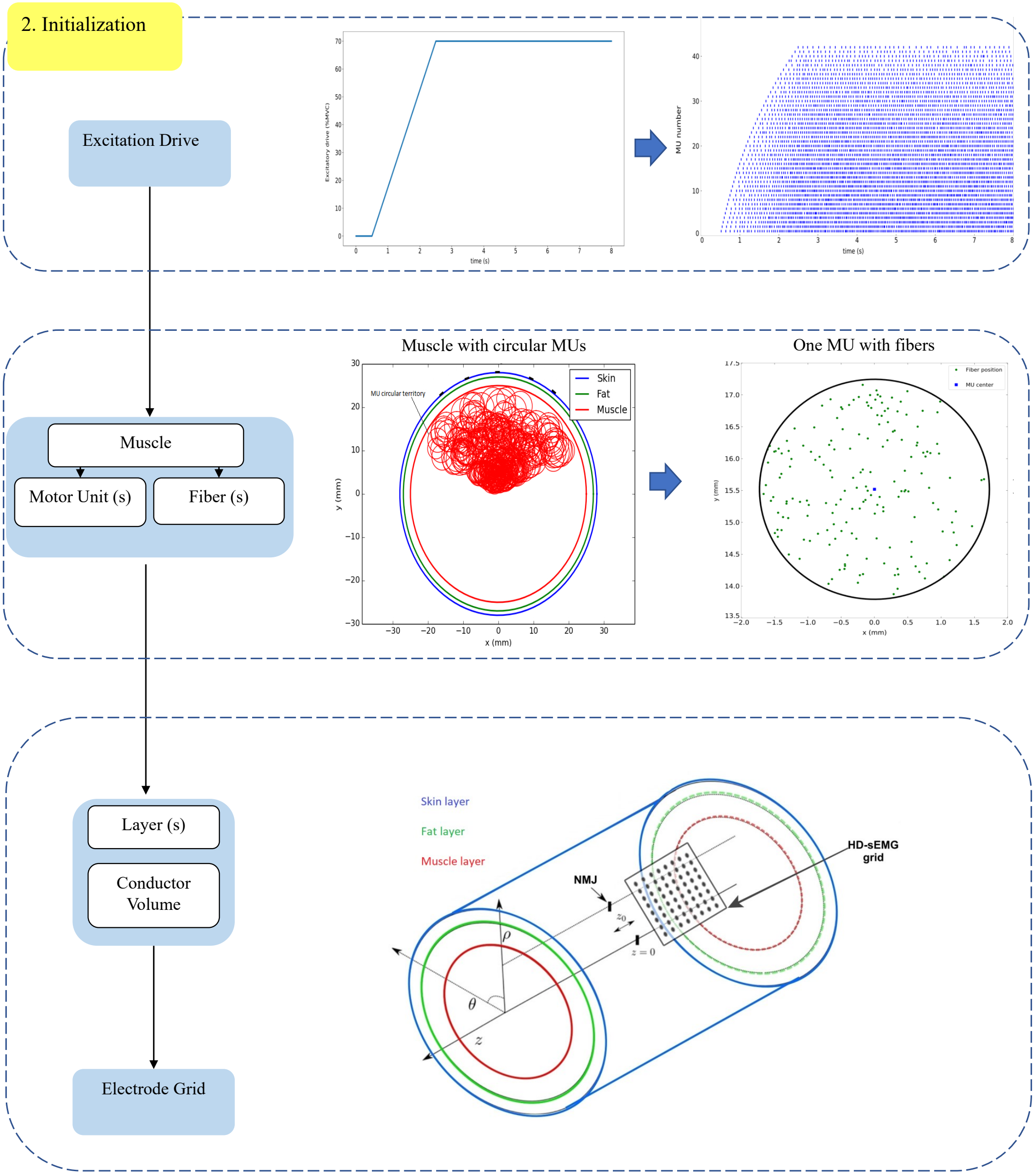

Figure 3.3: Initialization stage: excitation drive, muscle and conductor volume anatomies, and electrode grid.

Once gathered, these parameters will initialize:

- The excitation drive with a specific resting time, holding time, contraction level, goal of the contraction, the contraction slope, recruitment range and the sampling frequency. All these parameters are defined in the input file.

- The muscle anatomy at the fiber and MU scale. In fact, MUs are positioned according to a best candidate algorithm (BC) and regionalized within the muscle according to their types. The territories of MUs were simulated with a circular shapes. Then, each MU was filled with fibers of the same phenotypic. The number of MUs, the number of fibers per MU, and the fibers and MUs diameter's are defined in the input file.

- The conductor volume and the different layers (muscle, subcutaneous fat, and skin). The radius of each layer and its spatial conductivity was gathered from the input file. Likewise, the neuomuscular junction (NMJ) and the myotendinous junction (MTZ) (see Fig. 3.3). Each layer composing the conductor volume is considered as a homogeneous medium. The muscle layer is considered as an anisotropic medium (conductivity is the highest along the longitudinal direction). While, the adipose and the skin tissues are isotropic.

- The electrode grid with the number of electrodes according to θ and z axis, the inter-electrode distances in the two directions, the electrode radius and the position of the grid center.

This model offers the possibility to define sources at the microscopic scale (single fiber intracellular potential generation, propagation and extinction: SFAP), and at the macroscopic scale (motor unit action potential: MUAP, a weighted AP based on the barycenter of fibers within the same MU). Considering the macro sources (MUs) with a computation algorithm fully made in the Fourier frequency domain, the model [1, 11] optimizes significantly the computational time of the surface electrical activity at the skin surface (see Fig. 3.4). In fact, activity is computed from the multiplication between the Fourier transform of the MU discharge times and the 2D Fourier transform of the spatio-temporal signature of the fiber electrical source. Then, the result is multiplied with the volume conductor transfer function expressed in spatial frequency coordinates. The 2D electrical activity over the skin surface is obtained with a 3D inverse Fourier transform.

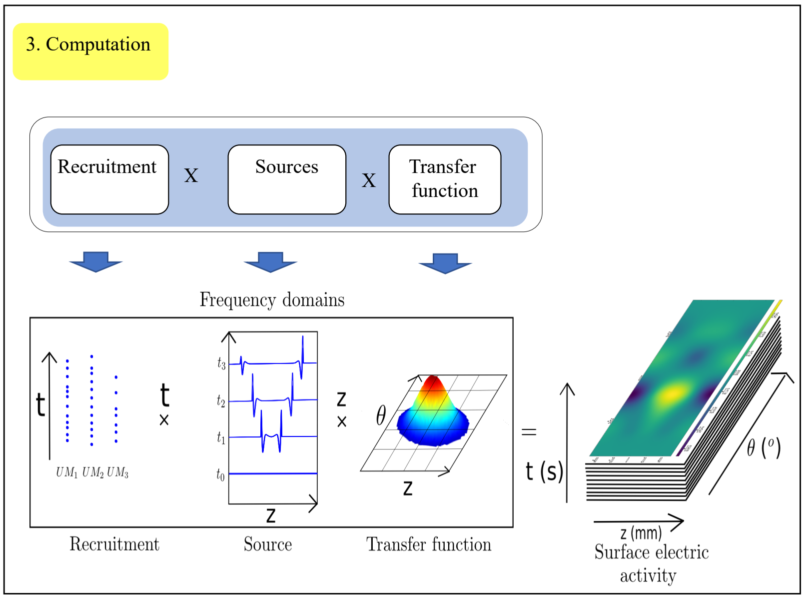

Figure 3.4: Computation scheme of the model [1, 11].

Finally, the HD-sEMG signals are obtained from numerical integration under the electrode area from a high resolution potential map allowing electrode shape diversity and infinite combinations of electrode number and position with no need of re-simulation (see Fig. 3.5).

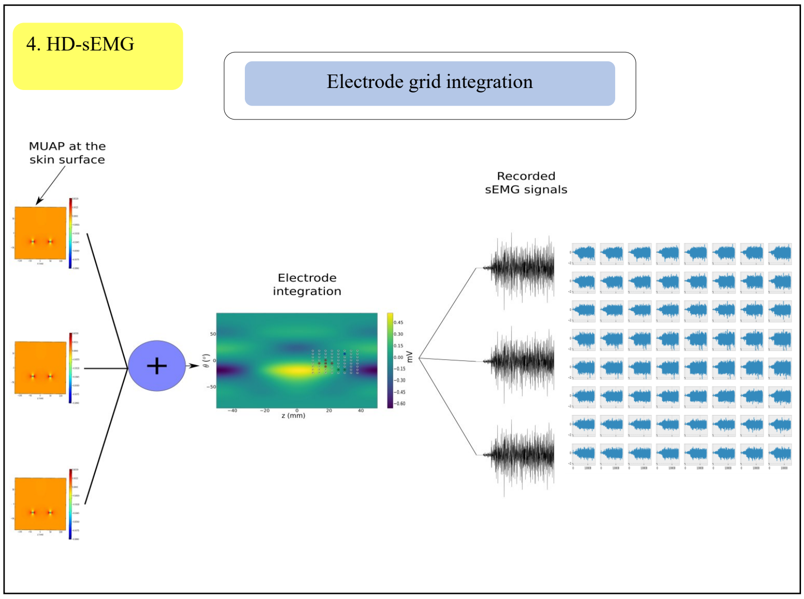

Figure 3.5: The HD-sEMG signals is obtained from numerical integration of the 2D electrical activity computed over the skin surface.

3.2.2 Muscle aging simulated with the previous model

In the purpose of testing accuracy of modeling approach depicted in [1, 11] and illustrated in Fig. (3.2, 3.3, 3.4, and 3.5), we have tried to simulate young and aged muscle. The list of all parameters (inputs) used to generate sEMG signal were depicted in Tables (2.1, 2.2, and 2.3) of chapter 2. The values of these inputs, for young and elderly subjects, were taken based on values reported from literature and depicted in Table 2.4 of chapter 2.
The including of this large amount of parameters, in respect to each age and gender category, requires a meticulous matching work and specific knowledge of this model. Beyond the difficulty of this task for non-expert operators, and assuming that this is done, the Fig. 3.6 shows the muscle morphology and motor units territories generated by this model
A superficial inspection of this figure can lead to a satisfactory outcome: aged muscle is smaller than young one; it contains lower number of MUs and fibers; and MUs are larger for elderly muscle. However, a more in-depth investigation reveals inconsistency and unrealistic structure for both young and old muscles. In fact, the Table 3.1 shows an unrealistic estimated number of fibers per muscle, and the Fig. 3.7 shows inhomogeneous density of fibers.

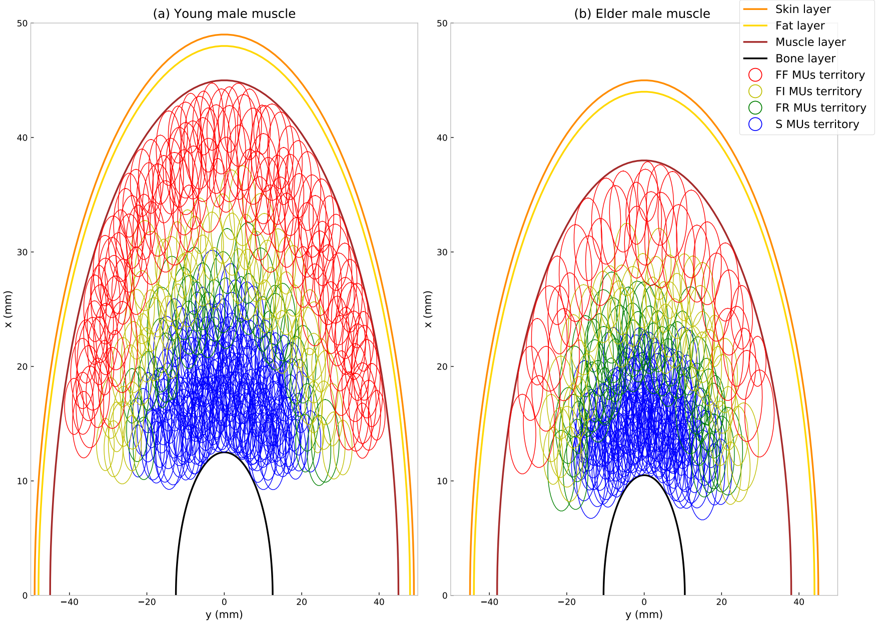

Figure 3.6: Muscle morphology and motor units territories generated with modeling approach of [1, 11]. (left) young muscle, (right) aged muscle.

Table 3.1: The estimated number of fibers per muscle using the modeling approach in [1, 11]. The number of MUs and the number of fibers per MU are given as an average values of model input.

Age	number of MUs	number of fibers per MU	Total number of fibers
Young	450	140	63000
Elder	300	172.5	51750

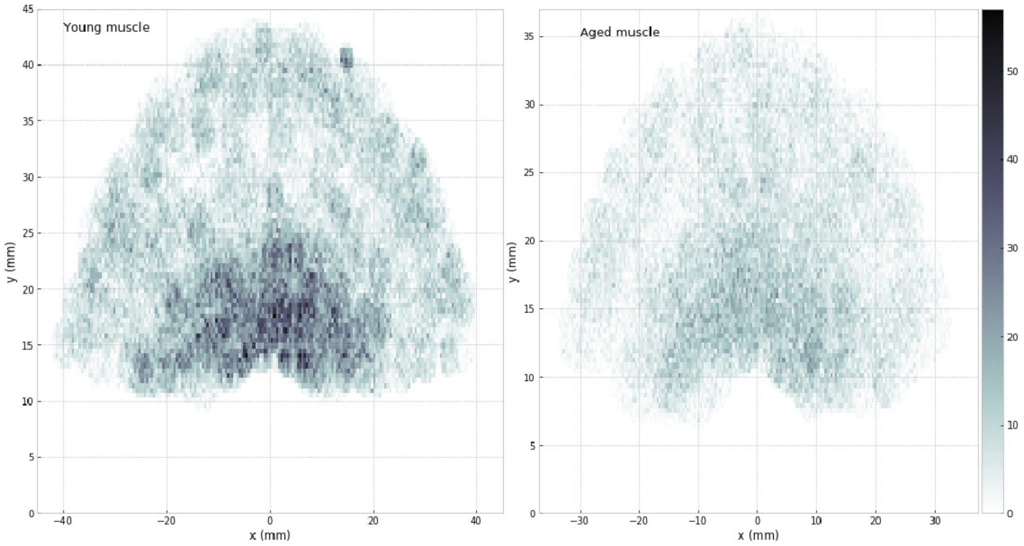

Figure 3.7: Fiber density using the best candidate algorithm with realistic motor units ratio per type. (left) young muscle, (right) aged muscle.

To understand this result, we should understand how the model was designed. In fact, the model build the muscle morphology and structure as follow: muscle was approximated by a cylinder where all MUs are parallel to z-axis and where the xy plane constitutes the muscle cross-section. The input file delivers the number of MUs[3], MUs ratio per type[4], the number of fibers per MU[5], and MU radius[6]; then, MUs are placed, as a circular regions, using a best candidate algorithm (BC) and fulfilled with correspondent number of fibers (see Fig. 3.8(a),(b)). The BC algorithm is governed by the number and radius of MUs. A supplement constraint enforced the positioning of slow MUs at deeper layer of muscle, and fast MUs nearby the muscle surface to mimic histochemical appearance in the biceps brachii muscle [119] ((see Fig. 3.8(a),(d)). As consequence, around 50% of MUs (slow type percentage) are placed in innermost one-third muscle volume (see Fig. 3.6, and see [282] for algorithm details). As result, this design leads to:

1. Inhomogeneous fiber density due to the constraint enforcing type-positioning of MUs. Homogeneous density is guaranteed only if MUs have the same percentage per type, which is unreal for BB muscle (see section 3.7)

2. Unrealistic number of fibers per muscle, estimated when multiplying the number of fibers per one MU by the total number of MUs. The average reported number of fibers for young and elder male is 253600 and 234300 respectively. However, the estimated number using this modeling design is 63000 and 51750 for young and elderly subjects respectively. This difference is due the number of fibers per one MU (innervation ratio) which is not directly available in literature and need efficient based-model estimation.

Moreover, the MUs sizes and innervation ratios, despite considerable details provided on the morphological and electrophysiological characteristics of the motor unit, still unresolved issue [285]. Thus, it was the difficult to report such experimentally data for BB muscle. In fact, the estimation of MU radius per type only was depicted in [41], and innervation ratio of BB muscle was reported in rare studies (e,g,. [286] without related-types information). As consequence, the BC algorithm, driven by inconsistent entries, can lose its efficacy. Which leads to an uneven and physiologically incorrect arrangement of MUs in BB muscle.

Another structural artifact was observed when dealing with this model: the uniform distribution of fibers over motor units (see Fig. 3.8(c)) provides incorrect densities and can lead to overlapped fibers. The fiber diameters were randomly drawn from normal distribution as reported in literature for each type of fiber.

Beyond these above morphological issues, the neural drive performed in this model apply the same MUs recruitment threshold and firing rate for for both young and elderly population. However, recent finding have demonstrated that recruitment threshold range is lower for elderly subjects(e.g., in [115]) with a generally flatter slope of the mean firing rate versus recruitment threshold relationship in older men. Which not the case with this modeling approach.

In the next paragraph, we will try to overcome these artifacts by proposing new modeling schema and approaches. Furthermore, The new proposed model will incorporate missed important age-related changes such as atrophy and intramuscular fat infiltration.

---

[3] nMU in Table 2.4

[4] MU_{dist} in Table 2.4

[5] n^f_{SMU}, n^f_{SMU}, n^f_{SMU} , n^f_{SMU} in Table 2.4

[6] MU^r_S, MU^r_{FI}, MU^r_{FR}, MU^r_{FF} in Table 2.4

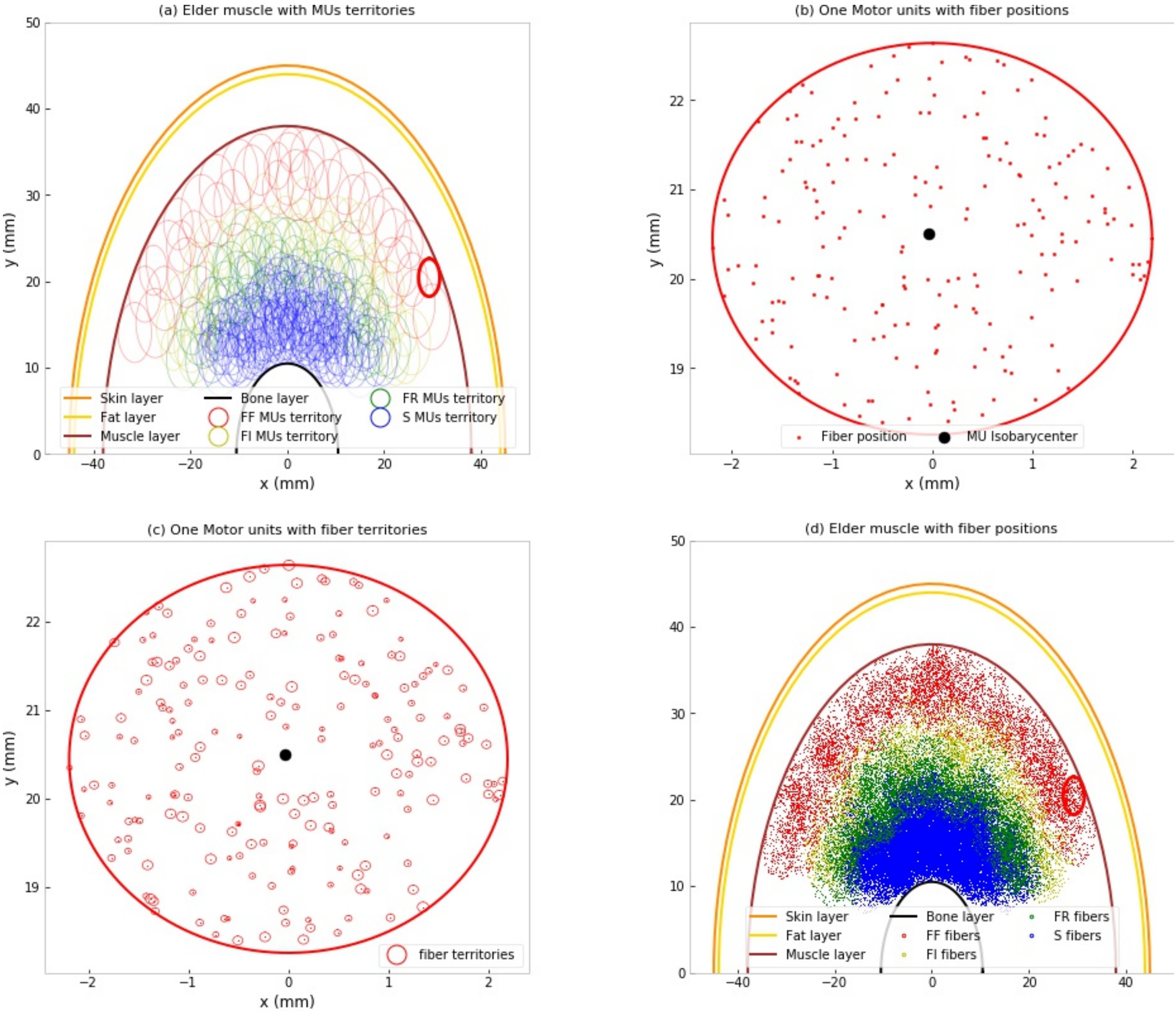

Figure 3.8: Fiber distribution within circular MU territory. Aged muscle anatomy generated with modeling approach of [1] and [11].

3.3 New modeling scheme personalized for muscle aging

The new modeling approach is based on the age and gender factors as model entries. The model users should give, as model inputs, only age and gender. Optional parameters, easily measured/monitored, like muscle length and cross sectional area can be added to the model inputs for more accuracy. Then, all needed parameters to define BB muscle morphology will be estimated through specific age-related statistical models. In fact, a mini review will be realized to report experimental values of these parameters according to the age/gender of biceps brachii muscle. Then, using statistical models (e.g., growth equation models), a fitted relationship between age and experimental data will be established for each parameter.

Once the parameters of muscle morphology are computed from these fitted relationships, The muscle structure can be defined according to the descriptive age-related model (see Fig. 3.9).

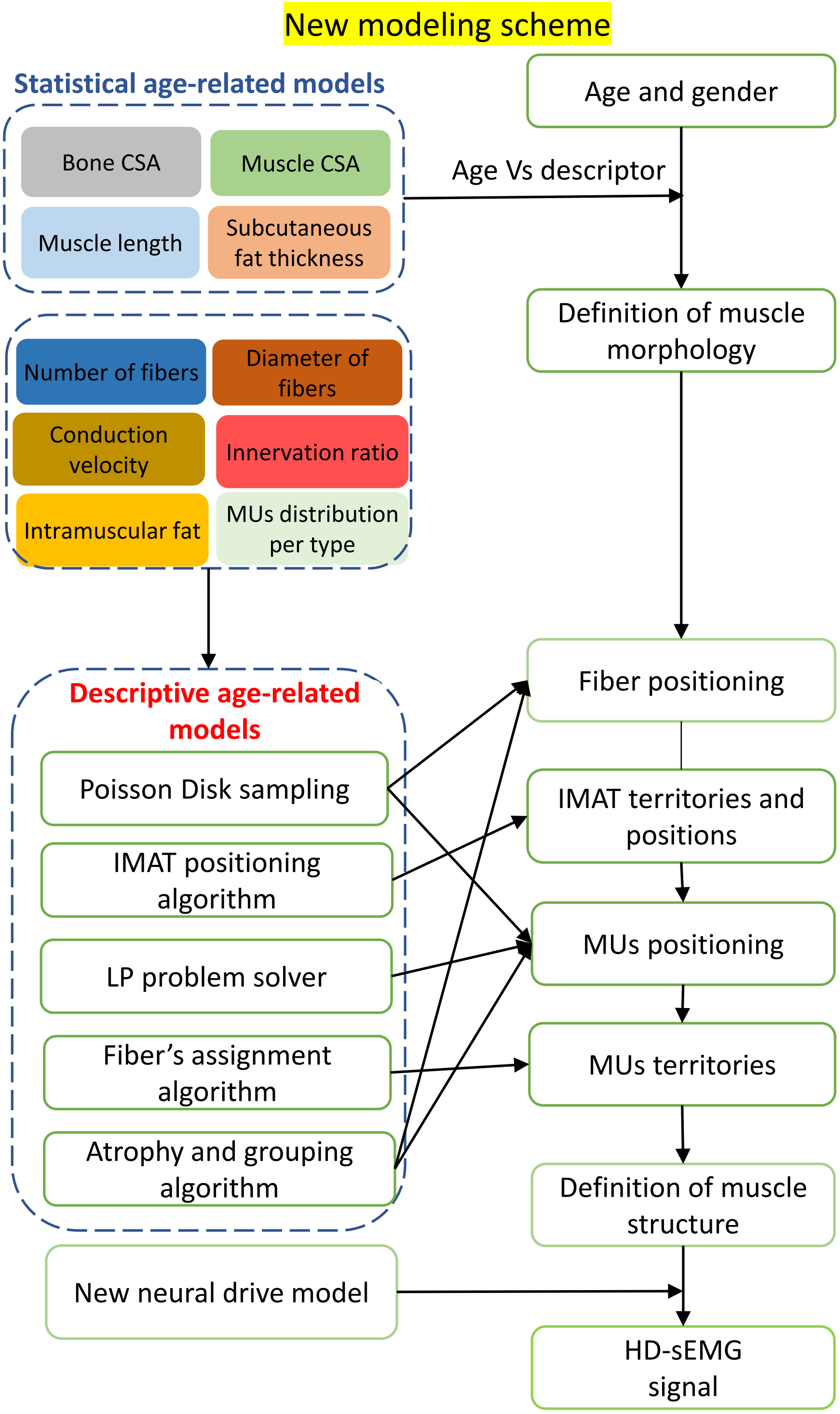

Figure 3.9: New modeling approach diagram. The main input of this model are the age and gender of the subject. All anatomical and neural parameter need in model workflow are estimated based on statistical and descriptive model (experimental values reported from literature).

These models, through vario¨us algorithms, will insure:

1. Homogeneous and close-knit fiber positioning within BB muscle: A Poisson Disk Sampling (PDS) will fill the enclosed muscle domain by iteratively adding fibers that are distant in respect to their radius. This algorithm will generate a realistic number of fibers per muscle with more physiologically correct arrangement in

reduced computation time (few seconds).

2. Infiltration of intramuscular fat (IMAT) within BB muscle: IMAT total area will be estimated, in respect to age input, using a statistical model. Then, the IMAT positioning algorithm will split this total area into polygons, randomly shaped and positioned in the muscle.

3. After fiber deletion from IMAT areas, the innervation ratio for each type of MU will be estimated. Then, the total number of MUs can be predicted. Finally, we can place centers of MUs using PDS algorithm. However, a Linear Programming Problem (LPproblem) solver will be used to place most of slow MUs in the innermost muscle layers, and faster MUs near the surface.

4. Assignment of positioned fibers to MUs using a randomized procedure (fibers are going to have same phenotypic as MUs): The assignment will be consistent with the innervation ratio, fiber's proximity to centers of MUs, and presence of neighboring fibers already assigned. This step promotes a realistic MUs territories else the circular simplified forms that exist in literature. In fact, the territory of each MU is defined as a convex hull of their assigned fiber's (convex hull algorithm).

5. Once the muscle structure is defined, a new neural drive will be employed. This neural model can personalize the spatial and temporal recruitment for each type of MU, in respect to the age input.

Once all these stages have been overcome, the MUAPs generation, propagation, extinction, and detection by the HD-sEMG grid will be performed as aforementioned in section 3.2. In the next sections, we will mathematically describe the statistical, descriptive, and neural models.

3.4 Statistical aging models

The muscle and conducting volume are composed of three layers: the Biceps Brachii (BB) muscle, the subcutaneous fat, and the skin. However, the bone (Humerus) radius is needed to compute the muscle radius. The biceps brachii (BB) muscle consists of a long and a short head, which have two different origins (the supraglenoid and tubercle) and a common insertion (the radial tuberosity). Thus we consider the BB muscle as a unique entity when reporting its morphological characteristics from literature. The muscle membrane enumerates many morphological changes from early adulthood to old age including muscle size (cross-sectional area) and length; bone size; and layer thickness (skin and subcutaneous fat).

Thus, we will report experimental data for these two age categories and propose their most appropriate age-related statistical models. Our approach, in this paragraph, will employ regression analysis, curve-fitting, or trend-lines.

The work below is divided into three parts: 1) reporting morphological parameter values for each subject category (young and elder, male and female), 2) experimental data preprocessing based on strict inclusion and exclusion criteria (high standard deviation, adequacy of the measurement protocol,etc.), 3) regression analysis by detecting and quantifying the relationship between aging and parameter values. Four growth model will fitted from experimental data and tested to detect dynamics of these relationships : linear, exponential, logistic and Gompertz model.

- Linear growth: the parameter evolution with aging can be modeled with a linear equation:
  $$p(x) = a.x + p_0 \tag{3.1}$$
  Where p is the muscle parameter at age x, a is the growth rate, p_0 the initial parameter value.

- Exponential growth: the parameter growth rate increases over ages, in proportion to the parameter values, getting larger or smaller. The general form of this model is:
  $$p(x) = p_0.e^{a.x} \tag{3.2}$$
  Where $p(x)$ is the muscle parameter at age x, a is the growth factor, p_0 the initial parameter value.

- Logistic growth: In logistic growth, a parameter growth rate gets smaller and smaller (or larger) as it approaches an imposed maximum (or minimum) value, known as the carrying capacity. The general form of this model:
  $$p(x) = \frac{k.p_0}{p_0 + (k - p_0).e^{-a.x}} \tag{3.3}$$
  Where $p(x)$ is the muscle parameter at age x, a is the growth factor, k is the carrying capacity, and p_0 the initial parameter value. It exists related forms of this logistic model. In particular, the Log-Logistic model which is defined by the following equation:
  $$p(x) = p_0 + (p_0 - p_f)/(1 + (x/a)^{-k}) \tag{3.4}$$
  Where $p(x)$ is the muscle parameter at age x, a is the growth factor, k is the carrying capacity, p_0 the minimum asymptote, and p_f the maximum asymptote.

- Gompertz growth: It is a sigmoid function at which the parameter evolution with aging being slowest or fastest at a given age. The asymptote of the function is approached much more gradually by the curve than the left-hand or lower/higher valued asymptote. This is in contrast to the simple logistic function in which both asymptotes are approached by the curve symmetrically. The general form of this model is:
  $$p(x) = c.e^{-e^{b-a.x}} \tag{3.5}$$
  Where $p(x)$ is the muscle parameter at age x, a is the growth factor, b is the halfway point, and c is an asymptote, since $\lim_{x \to +\infty} c.e^{-e^{b-a.x}} = c$.

The equations 3.1, 3.2, 3.3, and 3.5 are re-framed for each muscle parameter according to the experimental data trends. Then, each model equation parameters are estimated using the Levenberg-Marquardt algorithm (non-linear least squares optimization function) [287]. We will name the models in this section as statistical models of muscle morphology changes with aging.

3.4.1 Changes of muscle cross-sectional area with aging

The Cross-Sectional Area (CSA) values of BB muscle are rarely reported in the literature. In fact, the most reported CSA values include the BB muscle with neighbor muscles, e.g., the Brachialis and the Triceps. Terms like Anatomical Cross-Sectional Area (ACSA) and Physiological Cross-Sectional Area (PCSA) are also frequently matched in these studies. ACSA design the muscle CSA measured in the plane perpendicular to its tendons (the longitudinal axis), commonly recorded at the widest point along the muscle. PCSA is the muscle CSA measured in the plane perpendicular to the muscle fibers. It is obtained by dividing the muscle volume by its true fiber length. The Table 3.2 shows CSA values of BB muscle with the condition: elbow flexors positioned at 90°. To propose an estimated behavior law of the muscle CSA evolution versus aging, we first eliminate experimental data with high standard deviation (scatters in red color, Fig. 3.10). Then we have applied a regression using growth equations of Table 3.3. Four curves of CSA decline are estimated (Fig. 3.11). According to the results, the linear and Gompretz-Weibull equations are more suitable to fit the experimental data of Table 3.2. We will use the Gompretz-Weibull equation to obtain muscle CSA at each age in the personalized aging model.

Table 3.2: CSA reported values of BB muscle (YM: Young Men; OM: Older Men; YW: Young Women; OW: Older Women). (*) CSA for BB and brachialis muscle together.

Subject	Age (y_r)	CSA (cm^2)	Reference
YM	23.3±3	12.7±2.3	[288]
	23.3±1.3	12.4±1.2	[289]
	22.4±3.7	11±8.1	[290]
	28±0.1	15.3±2.5	[181]
	27.5±1.9	12.5±6.3	[291]
	12∼25	11.8±2.7	[292]
YW	25.0±1.4	7.5±0.5	[289]
	21.7±3	6.9±0.3	[290]
OM	81±13	9.1±1.7	[288]
	68±0.5	12.5±3.3	[181]
OW	68.5±3.7	9.7±1.2 *	[293]

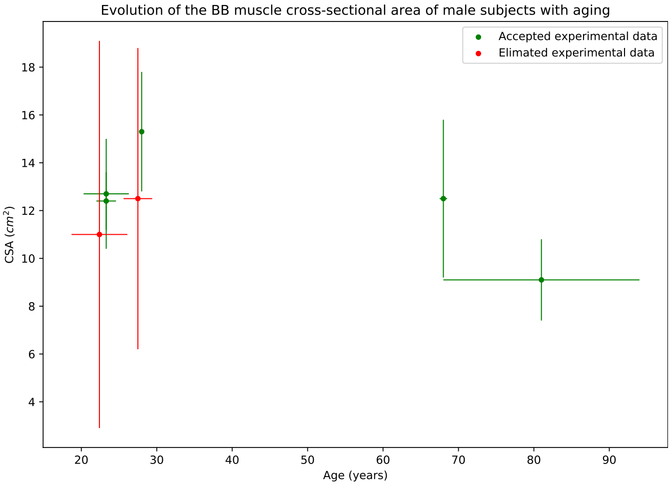

Figure 3.10: The CSA experimental data of male subjects. Scatters in red color are excluded due their high standard deviation.

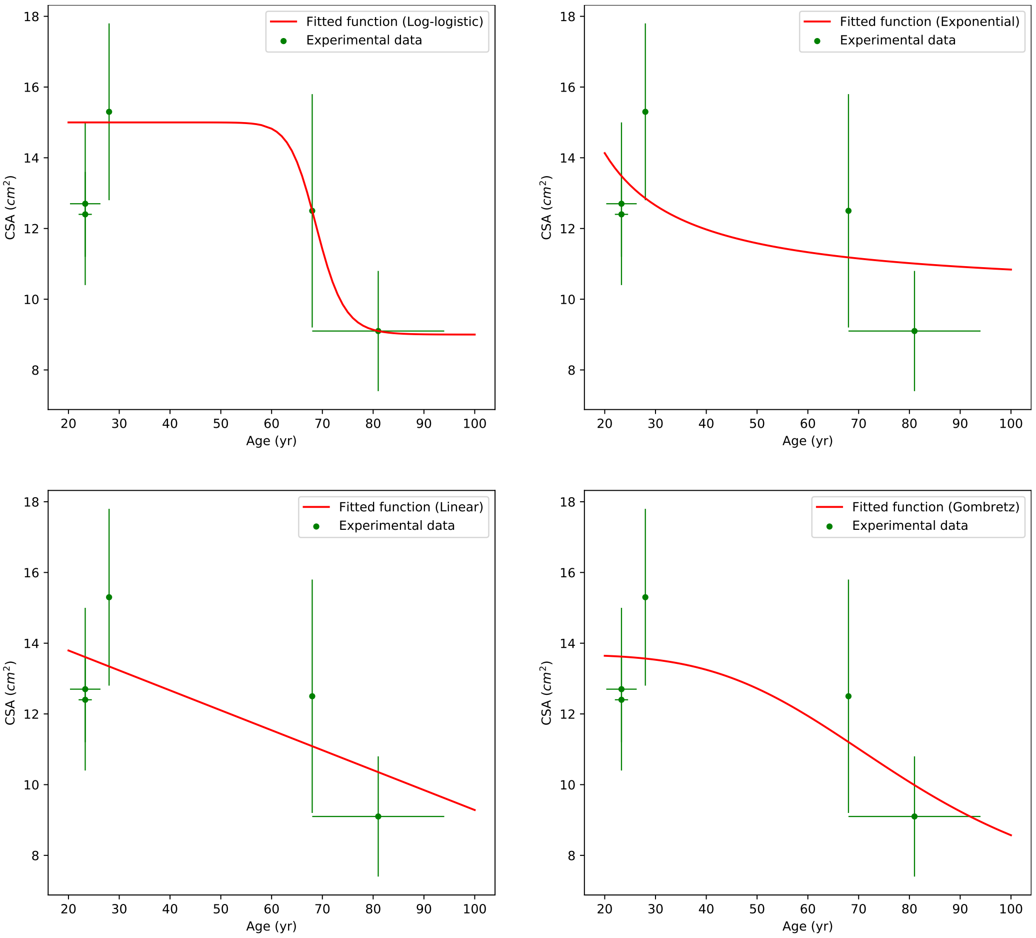

Figure 3.11: The CSA fitted functions for male subjects.

Table 3.3: Estimated parameters of BB CSA model during aging.

Model	equation	estimated parameters
Linear	$p(x) = a.x + p_0$	$p_0 = 14.92$; $a = -0.05$
Exponential	$p(x) = p_0.e^{\frac{a}{x}}$	$p_0 = 10.14$; $a = 6.63$
Log-Logistic	$p(x) = p_0 + (p_0 - p_f)/(1 + (x/a)^{-k})$	$p_0 = 15.2$; $p_f = 9$ $a = 68.91$; $k = 25.23$
Gompretz-Weibull	$p(x) = p_0 + (p_0 - p_f)e^{-e^{-a.(logx - logk)}}$	$p_0 = 50$; $p_f = 2$ $a = 5.18$; $k = 13.56$

3.4.2 Changes of muscle radius with aging

The BB muscle is attached to the Humerus bone. The bone radius parameter is used to compute the muscle radius using the following equation 3.6:

$$CSA_{BB} = \alpha.(\pi.r_{BB}^2 - \pi.r_{bone}^2) \tag{3.6}$$

Where r_{BB} is the BB radius, r_{bone} is the bone radius, and α is an adjustment factor for muscle ($\alpha = \frac{160}{360}$ in our case).

The Table 3.4, shows no significant difference in the bone radius between young and elder subjects, with a slight increase with aging. However, this increase is more observed for elder women compared to youngest.

The Table 3.5 shows the estimated muscle radius for young and elder male/female subjects, using equation 3.6 and tables 3.4, and 3.2.

Table 3.4: Humerus CSA reported value (YM: Young Men; OM: Older Men; YW: Young Women; OW: Older Women). The bone radius was estimated using $CSA_{bone} = \pi r_{bone}^2$.

Subject	Age (y_r)	Bone CSA (mm^2)	Bone radius (mm)	Bone length (mm)	Reference
YM	21±1	412±64	11.45±4		[294]
	23±3	392±40	11.2±3	327±16	[288]
	31±4	520±43	12.8±3		[295]
	25±5	438±39	12.5±0.7	332.5±13	[232]
OM	78±4.9	416±45	11.5±3.7		[294]
	77±1	455±53	12.03±4.1	335±18	[288]
	86±4	454±42	12.02±3.6	332±26	[288]
	74±7	530±60	13.0±4.3		[295]
OW	21±3	367±37	10.7±0.7	302.7±14	[232]
OW	43±5	354±38	11.25±0.7	304.7±8	[232]

Table 3.5: The estimated values of BB muscle radius.

Subject	BB muscle radius (mm)
YM	42,5±3.1
OM	38.7±2.7
YW	36.2±4.5
OW	34±5.1

3.4.3 Changes of muscle length with aging

The muscle length is different from fiber length, and different from fascicule length. The optimal fiber length is defined as the length at which the muscle can generate its maximal isometric force. The measurement of muscle length in vivo is rarely exploited for human skeletal muscles. One of rare study revealing this parameter in [296]. The study measures the long head and short head of biceps lengths with cadaver of male and female subjects. It reports that the short head muscle length is 13.6±2.4 (cm), and the long head length is 15±0.4 (cm). This study indicates that subject ages vary from 23 to 74 years old without precising their gender. A more recent study reports the muscle lengths as equal to 13.98±0.75 (cm) for women and 13.8±1.1 (cm) for men respectively [290] (young subjects). Unfortunately, muscle length is not reported for elder subjects in this study. However, the study [291] correlated the changes of muscle CSA to muscle length of BB. This study evaluates muscle CSA during aging based on MRI technique. It reports that 10% change in muscle length could result in a 21% change in muscle area. Based on this observation, we can generate muscle length for aged category using CSA values of Table 3.2. The Table 3.6 shows BB muscle lengths for the subject categories according to age and gender, and the Fig. 3.12 shows the regression of these experimental data using growth equation of Gompertz (eq. 3.5).

Table 3.6: The estimated values of BB muscle length.

Subject	age (years)	muscle length (cm)
YM	23 ± 4	13.8±1.1
YW	22 ± 3	13.98±0.75
OM	81 ± 13	12.4±1.1
OM	68 ± 0.5	12.9±1.1
OW	68 ± 3.7	13.1±0.75

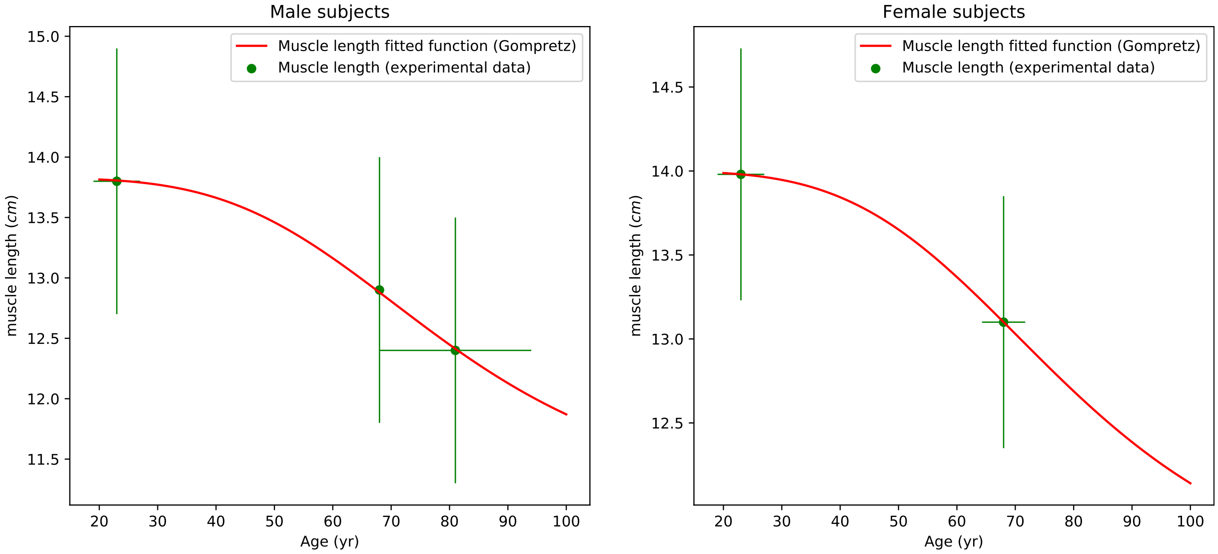

Figure 3.12: Muscle length fitted curve using Gompretz function for male (left) and female (right) subjects.

3.4.4 Changes of fat thickness and infiltration with aging

In the last twenty years, a rapid expansion of understanding of fat tissue organ role has occurred. Fat tissue is not anymore an inert storage depot for excess calories. It was proved that adipose cells expresses and secretes a multitude of hormones and proinflammatory cytokines thereby acting in an autocrine, paracrine, and endocrine manner signaling the heart, musculoskeletal, central nervous, and metabolic systems [122]. It was observed that the increase of adipose tissue ratio is associated with the decrease of strength and mobility in older adults [123, 297, 298, 299, 124]. The study [125] indicates that the change in echo intensity of BB muscle starts from the middle age, and that this change occur prior to the change in muscle thickness. It indicates that the increase of adipose and connective tissue within this muscle is associated with the decrease of contractile tissue and muscle strength since middle age. Therefore, we decide to incorporate efficiently the adipose tissues infiltration through the muscle into the aimed personalized aging model.
Two kind of fat tissues are identified: 1) Inter/inramuscular fat (IMAT), is generally considered to be any adipocyte deposition located between muscle fibers or between muscle groups; 2) Subcutaneous fat (SF) is the fat between muscle and skin.
Advancing age results in a redistribution of fat, with IMAT tending to increase more than the subcutaneous fat [300, 301].
Experimental measures of muscle fat have been achieved with a variety of imaging (MRI, CT) and biochemical techniques. However, measures for BB muscle are rarely reported

compared to lower arm muscles (vastus lateralis (VL), biceps femoris (BF), etc.). Moreover, the reporting of subcutaneous fat from literature is more easy (Table 3.7 than the intramuscular fat, which is totally missed for age and gender subject categories.
Therefore, to follow the evolution IMAT areas during aging, we have inspired from two studies:

- The first study [122] reports that IMAT represents 8% to 10% of the total fat body tissue. However, the fat body tissue is given in (Kg) or $(Kg.m^{-2})$ which makes its conversion to surface areas within BB muscle not evident.

- From the second study [302] we have observed that IMAT fat represents from 5 to 8% of subcutaneous fat (SF) for young subjects, and 20% of subcutaneous fat (SF) for elderly people aged from 70 to 79 years old (48% for sarcopenic men and +29% for sarcopenic women). This approach can be more adequate for the personalized aging model proposed in this chapter. In fact, using the muscle radius (computed in section 3.4.2 with $\alpha = 1$) with the hypothesis that all muscle share the same IMAT percentage of the subcutaneous fat, we can generate IMAT area of BB muscle using the following equation:

  $$Area_{IMAT} = \beta.(\pi.r_{SF}^2 - \pi.r_{BB}^2) \tag{3.7}$$

  Where r_{SF}^2 is the subcutaneous fat radius obtained from Table 3.7, r_{BB}^2 is the muscle radius obtained form Table 3.5, and β is an age regulation factor ($\beta \approx 0.05$ for young subjects, $\beta \approx 0.2$ for elder subjects).

The Table 3.7 and Fig. 3.13 show the experimental data of SF and its regression using Gompretz equation (eq. 3.5) for age and gender subject categories. The Table 3.8 and Fig. 3.14 show the experimental data of IMAT fat and its regression using Gompretz equation (eq. 3.5) for age and gender subject categories.

Table 3.7: The estimated BB subcutaneous muscle fat.

Subject	age (years)	Subcutaneous fat thickness (cm)	Reference
OM (non-sarcopenic)	65-77	mean=0.26 (0.18, 0.33)	[143]
OM (sarcopenic)	74-83	mean=0.20 (0.14, 0.25)	[143]
OW (non-sarcopenic)	64-76	mean=0.35 (0.26, 0.42)	[143]
OW (sarcopenic)	74-82	mean=0.23 (0.19, 0.31)	[143]
YM	29-50	0.43±0.06	[235]
YW	21-44	0.54±0.06	[235]
OM	62-83	0.46±0.03	[235]
OW	62-85	0.6±0.08	[235]

Table 3.8: The estimated BB muscle IMAT fat.

Subject	age (years)	IMAT fat area (cm^2)
YM	29-50	0.31±0.06
YW	21-44	0.55±0.09
OM	62-83	1.2±0.1
OW	62-85	1.78±0.2

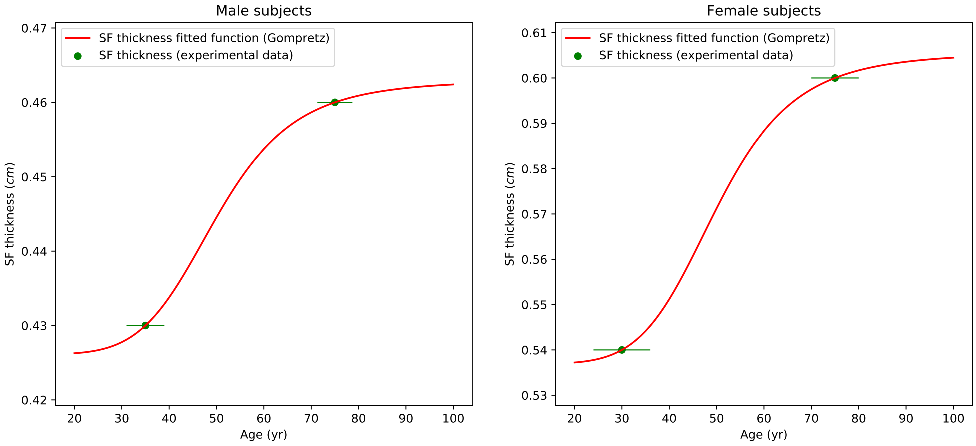

Figure 3.13: Subcutaneous fat thickness fitted curve using Gompretz function for male (left) and female (right) subjects.

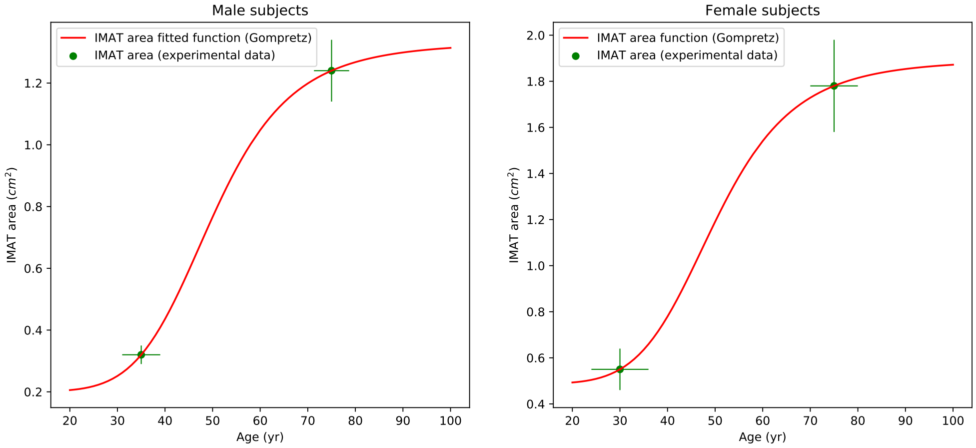

Figure 3.14: IMAT fat areas fitted curve using Gompretz function for male (left) and female (right) subjects.

3.4.5 Changes of skin thickness with aging

The effect of age on the thickness of skin is one of the more controversial topics among dermatological researchers. Comparing measures of skin layer thickness between individuals (and between studies) is especially challenging because of significant variation in measurements between individuals and between sites within each individual [303]. Microscopic appearance of aged skin reveals a thinner epidermis than young skin [304, 305]. Moreover, male skin is thicker than women's, and a full exposed skin is thinner than full protected skin [306]. However, the difference between skin thickness is not significant across the literature, and this slight variation of this parameter values shouldn't have an important impact on the force and sEMG generated bu BB muscle. Despite extensive data, it is difficult to define the effects of aging on whole skin thickness. In the most of cases, studiesimposant reveals only the external layers thickness of the whole skin (epidermal, superficial dermis). In this chapter, we decide to work with a mean skin thickness ranged from 0.6 to 3.00 *mm* in respect to the fact that aged skin is thinner than young skin and male skin is thicker than female skin.

3.4.6 Changes of fibers number with aging

The efficient-standard measurement of fiber loss is the direct anatomical estimation obtained from cadaveric studies, although for obvious reasons these studies are rare [82, 64, 78]. It was observed among these studies that: (i) the total number of fibers within a muscle decrease with aging (apoptosis phenomena), (ii)human muscles are affected by this loss differently: lower limbs are most affected than upper limbs [50], (iii), fast fibers are more concerned by this loss than the slower fibers, in particular, for very elder persons [307]. For the BB muscle, the gap between the number of fibers for young and elder people is between 7% and 10% [78]. This loss can reach 55% of the total fibers number for other muscles [78, 50]. The studies [79, 231] have reported a decrease of 15% to 30% in the number of fibers type IIb. This decrease may be due to the fact that fibers of type II are more vulnerable to apoptosis (denaturation of mitochondria or stem cells), or to "the fast-to-slow" fiber type transformation. Few studies in literature have reported the total number of fibers for BB muscle, and much more rarely for different subject categories (young, elder, male, and female). The Table 3.9 summarize values reported in literature for N_{fibers}. The most relevant and recent study reported in literature is the Klein et al. study [78]. It estimates the N_{fibers} of BB muscle by combining two reliable techniques: MRI and biopsy. The main downside of this study is the little size of the studied sample (6 subjects). Two other studies have reported the N_fibers for young population (either male and female, trained and untrained subjects): [289, 308]. These two studies are using the same approach to compute N_{fibers} but with combining two other techniques: Computerizing tomography(CT) and needle biopsy. The N_{fibers} is given, for these studies, by the following equation:

$$N_{fibers} = \frac{Maximal\ area\ of\ BB\ (obtained\ by\ MRI/CT)}{Mean\ fiber\ area\ of\ BB\ (obtained\ by\ (needle) biopsy)} \tag{3.8}$$

We should note that the difference between the number of fibers is not significant between subject categories in the same study. In contrary, the gap is clearly observed if we compared this number for the same category in different studies. For that reason, we have decided to fit the model of fiber's number using data reported in [78] (see Fig. 3.15).

Table 3.9: Number of fibers of BB muscle reported in literature. Y: Young; O: Older; M: Male; F: Female; U: untrained subjects; T: Trained subjects

Number of fibers	Gender	Age(y_r)	sport	Reference
253.6±40.4	M	Y (21.2±1.9)	U	[78]
234.3±67.4	M	O (82.3±4.3)	U	[78]
180.6±50.1	M	Y (23.3±1.3)	U	[289]
156.8±25.5	F	Y (25.0±1.4)	U	[289]
290.7±72.2	M	Y (23.7±1.2)	T	[308]
278.5±60.7	M	Y (22.5±0.5)	U	[308]
293.2±61.5	M	Y (18∼25)	U	[292]

3.4.7 Changes of fiber diameters with aging

In BB muscle it was found four fiber types and subtypes (I (slow: S), IIc (fast intermediate: FI), IIa (fast resistant: FR), and IIb (fatigable fast: FF)) with different repartition

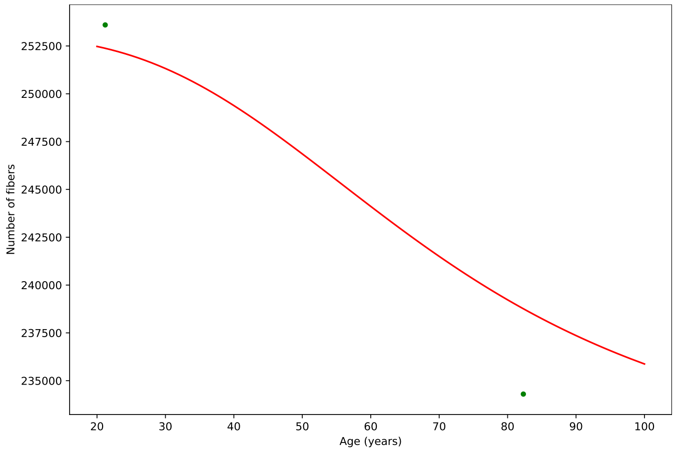

Figure 3.15: The number of fibers fitted curve using Gompretz function for male subjects.

ratios between superficial and deep muscle layers [119]. Contrary to the fiber's number within BB muscle, the size of fibers, all type included, is much more altered by the aging process. The diameters of type IIb fibers can decrease by more than -30% for BB muscle (see Tables 3.10 and 3.11). Few studies in literature have reported the size of fibers for BB muscle, and much more rarely for different subject categories (young, elder, male, and female). We have reported these values in Table 3.10.
Thus, the statistical model describing this decrease in fiber diameters is depicted in Fig. 3.16. Among the four fitted curves depicted in this figure, the Gompretz-Weibull equation seems to be more adapted for experimental data of Table 3.10.

Table 3.10: Comparison between fiber diameters per type of BB muscle (YM: Young Men; OM: Older Men; YW: Young Women; OW: Older Women.)

Subject	Age (year)	Type I (μm)	Type IIa (μm)	Type IIb (μm)	Type IIc (μm)	Type IIab (μm)	Ref.
YM	19∼25	66.2±9.5	76.4±15.8	73.8±15.2	67.8	73.8±15.1	[233]
	17∼30	50.5	55.8 (muscle surface layer)				[309]
	17∼30	49.8	52.1 (muscle surface layer)				[309]
	26∼36	52.03±7.3	57.3±9.2				[310]
	21.2±1.9	65.4±7.6	71.5±7.1				[78]
YW	24∼41	45.7±0.4	37.3±2.2				[311]
	35∼42	45.2±7	46.2±7.2				[310]
OM	74	51.7±6.7	60.4±11.9	51.5±15.8	27.8±15.3	56.1±13.6	[79]
	82.3±4.3	58.4±5.2	60.9±5.5				[78]
	72∼88	43.9±10.1	42.4±9.7				[81]
OW	45∼82	43.8±1.4	35.2±0.8				[311]

In fact, the curve behavior, with a slow decrease of fiber diameters during young/middle age and accelerated rate after 50 years old, seems to be consistent with reported observations in literature (see chapter 1, section 1.4). Moreover, we observe that model describe with accuracy the accelerated atrophy of type IIb fast fibers (red curves) after the age of 75 years, compared to type I atrophy during aging. This statement was demonstrated in many studies (e.g., in [312]). To note, we didn't found relative data for sarcopenic BB muscle in literature. However, the study [312] shows that type-II fiber diameters for sar-

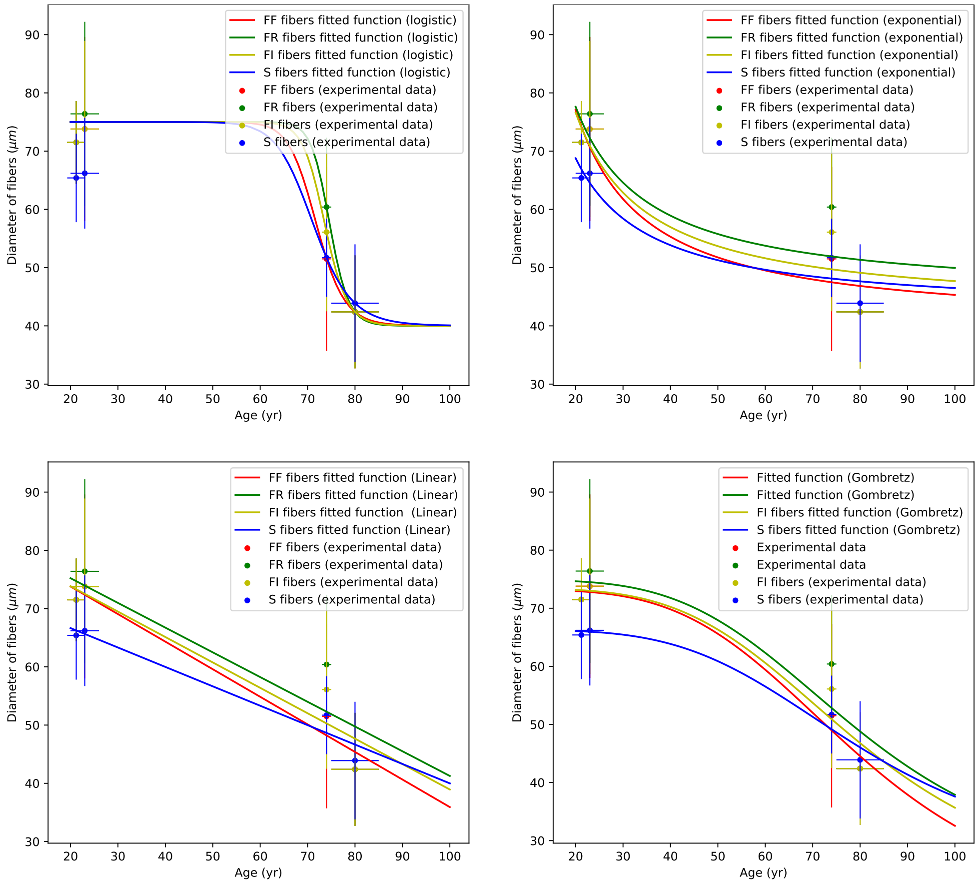

Figure 3.16: Four statistical models estimating the fiber diameters during aging for BB male muscle.

copenic men are significantly below the average range of non sarcopnic ones (the studied muscle was the vastus lateralis (VL)).

Table 3.11: The fiber diameter decline with aging (unit = %). Estimations were obtained using values reported in Table 3.10.

Fiber sizes decline between	Ref. young	Ref. elder	Type I	Type IIa	Type IIb	Type IIc	Type IIab
YM and OM (%)	[233]	[79]	21.9	20.9	30.2	58.9	23.9
YM and OM (%)	[78]	[78]	10.7	14.8			
YM and very OM (%)	[233]	[81]	33.6	44.5	42.5	37.4	42.5
YW and OW (%)	[311]	[311]	4.1	5.6			

3.4.8 Changes of fiber ratio per type with aging

We provide the distribution of fibers according to their types in Table 3.12. There is no need for a statistical model for this parameter as it is not included in this modeling scheme. However, it will be useful when estimating the distribution of MUs latter.

Table 3.12: Distribution of fibers of BB muscle according to type. YM: Young Men; OM: Older Men; YW: Young Women; OW: Older Women

Subject	Age(y_r)	Type I(%)	Type IIa(%)	Type IIb(%)	Type IIc(%)	Type IIab(%)	Ref
YM	28±0.1	49±2	25±6	26±7	0±0		[181]
	19∼25	41.7±8.5	19.4±6.3	29.0±11.2	0.5	9.4±11	[79]
	17∼40	39.1±2.1	36.5±3	20.3±2.6	3.9±0.7		[119]
	21.8±5	42.3±7	57.7±7 (muscle surface layer)				[313]
	21.8±5	50.5±9	49.5±9 (muscle deep layer)				[289]
YW	25.0±1.4	49±2	25±6	26±7	0±0		[289]
OM	68±0.5	52±8	20±4	26±7	2±0		[181]
	77±0.4	51.8±2.3	30.6±2.3	16.9±2.4	0.9±0.3		[314]
	74	49.4±11.2	24.1±8	15.6±18.1	0.1±0.1	10.8±9.7	[79]
	78∼81	58.5±5.9	26.4±4.1	15.5±4.0	0.4±0.3		[307]
OW	78∼81	53.3±2.9	23.7±2.2	23.0±3.0	0.1±0.1		[307]

3.5 Fibers positioning model with aging

Once the parameters of muscle morphology are computed using statistical models as depicted in 3.4, the fiber positioning model can be employed. Three main fiber aspects are outstanding during aging over the literature: 1) the loss of fibers, 2) the decrease of fiber sizes, 3) the changes in the ratio of fiber types . We will model at first the number, size and distribution ratios if fibers. Then we will place the fibers in muscle area using Fast Poisson Disk Sampling (FPDS) algorithm (see Fig. 3.17).

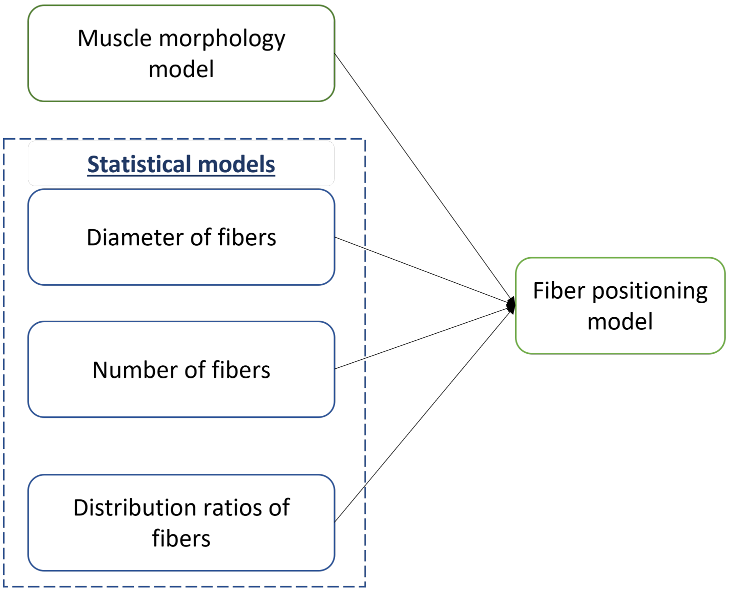

Figure 3.17: Diagram of steps to build the fiber's model with aging.

Previous models of sEMG signals have not specifically developed a realistic density and distribution of fibers within the muscle. Authors have worked on modeling the electric signal produced by a single contraction of a single muscle. The sEMG signal simulated at the skin surface is the summation of all these single fiber action potentials filtered through a conductor volume transfer function. The reliability and the impact of fiber distribution and density according to their contractile properties on the simulated EMG signal is not assessed. The model [44] estimates the number of fibers within muscle according to its cross-sectional area and the all fibers area. Then, the number of fibers for each of the 120 MUs was calculated using an exponential equation. To note, the excitation thresholds of the MUs were determined similarly in the same study. Then, motor unit territories were placed randomly in the simulated muscle without exceeding muscle boundary. To activate the muscle, an excitatory drive was sent to the motor neuron pool, activating any MU whose excitation threshold was exceeded.

The modeling approach depicted in [1], and used in this study, follows the same vein as in [44]. However, it changes the algorithm of MUs and fibers positioning (see section 3.2.2 for algorithms explanation and limitations).

In order to simulate physiologically correct number and density of fibers, we propose an alternative approach that consists of using the FPDS algorithm. The FPDS is part of a family of algorithms that fill an enclosed 2D domain by iteratively adding points that are maximally distant from the previously added ones (known as Poisson sampling disk) [315, 316, 317]. The best candidate (BC) that [1] has performed, is part if this algorithms family. However, authors in [1] have imposed a fixed number of MUs to fulfill in the muscle domain. Which can lead to break the constraint on maximal distance between center of MUs and/or increase the computation time. Moreover, the BC algorithm is not performed when positioning fiber into the MUs domains. As consequence, we obtained inconsistent number of fibers per muscle and unreliable placement of fibers (see Table 3.1 and Fig. 3.8 in section 3.2.2).

The new algorithm maximally disperse the fibers territories in the muscle cross sectional area. At the same time, the generated fiber centers are quasi-random (Fig. 3.18).

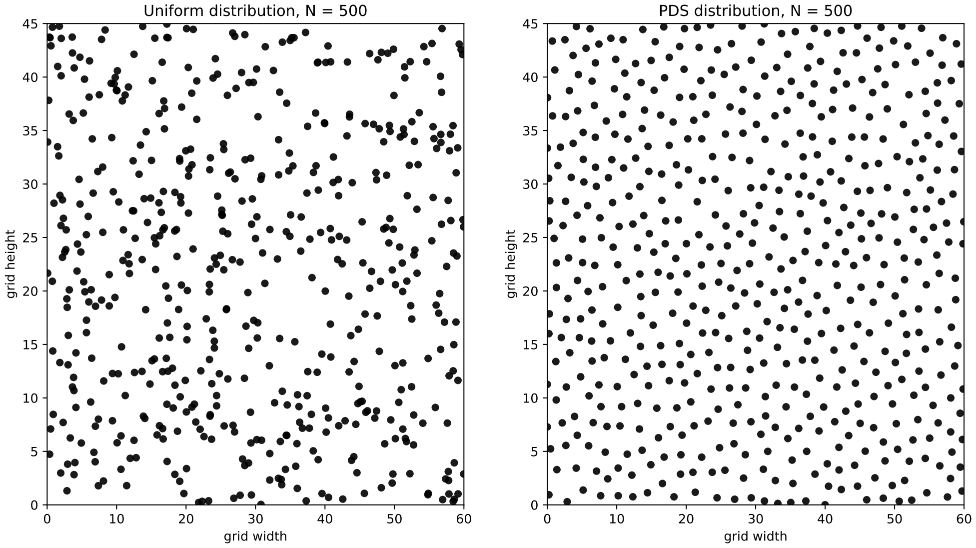

Figure 3.18: Example of 500 points drawn from the uniform distribution (a) and generated by the PDS (b). An even quasi-random arrangement of the points, such as the one provided by the PDS, is not achievable when using the uniform distribution.

The simplified PSD algorithm pattern is based on: 1) generating randomly point/fiber; 2) verifying that the point is not too close to any existing point; 3) repeating k times. Nonetheless, this pattern consume high computational time [318]. However, if the minimum distance between points was known *a prior*, we can use more enhanced and faster

algorithm: the Fast Poisson disk sampling (FPDS) [317]. In fact, this method cut down dramatically the computational time by performing pre-initialized background grid (using predefined minimum distance between points, r). Each grid cell can only receive one point (the edge of cell $= r/\sqrt{2}$). Thus, at each new point, only points indexed in grid cells need to be checked (see Algorithm 1).
Tp perform this FPDS algorithm, we have fixed two ages: 25 years and 82 year old of male subjects. The statistical model (depicted in 3.4.7) have computed the related diameter of fibers for each subject and deliver the corespondent radius to fiber positioning algorithm.

Algorithm 1 Fast Poisson Disc Sampling (FPDS) algorithm

```
Require: Fiber radius ($r$), muscle radius ($r_{muscel}$)
    Step 0. Initialize an 2-dimensional background grid for storing samples and accelerating spatial searches. We pick the cell size to be bounded by $r/\sqrt{2}$, so that each grid cell will contain at most one sample, and thus the grid can be implemented as a simple 2-dimensional array of integers: the default $-1$ indicates no sample, a non-negative integer gives the index of the sample located in a cell
    Step 1. Select the initial sample, $x_0$, randomly chosen uniformly from the domain. Insert it into the background grid, and initialize the "active list" (an array of sample indices) with this index (zero).

Ensure: $x_0$ in 2-dimensional grid

    while active list is not empty do
    Step 2. choose a random index from it (say i). Generate up to k points chosen uniformly from the spherical annulus between radius $r$ and $2r$ around $x_i$. For each point in turn, check if it is within distance r of existing samples (using the background grid to only test nearby samples). If a point is adequately far from existing samples, emit it as the next sample and add it to the active list. If after $k$ attempts no such point is found, instead remove i from the active list.
    end while
```

The Fig. 3.19 shows the morphology of BB muscle for young men (age = 25 yrs) and elderly men (age = 82 yr). The Table 3.13 shows that FPDS have produced realistic number of fibers for young and elder muscle (250698 and 211798 respectively). These produced number of fibers are consistent with reported values in literature and depicted in Table 3.9. The computational time to generate these anatomies and store fiber positions in cylindrical coordinate is lower than 35s.

Table 3.13: The number of fiber estimated by FPDS algorithm and its related computational time for YM (young men) and OM (older men).

Subject	age (years)	Number of fibers	Computational time (s)
YM	25	250698	31.08
OM	82	211798	28.71

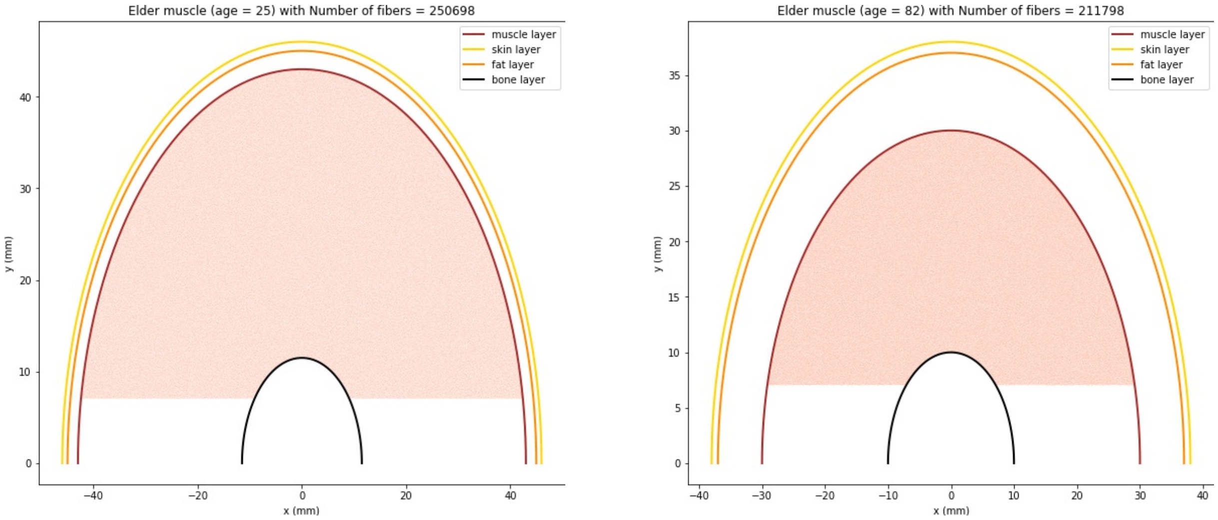

(a) (b)

Figure 3.19: Muscle morphology with fibers placed according to FPDS algorithm for (a) young, and (b) elder male subject.

3.6 IMAT model with aging

We have simulated in section 3.4.4 the evolution of the total IMAT area in BB muscle with aging (see eq. 3.7). However, in this section, we develop an algorithm to disperse this total area into small adipocyte depositions located between muscle fibers.

For that purpose, we require the parameters of muscle morphology (the muscle and bone radius), the fiber coordinates (computed in the previous section), and the total surface of IMAT within BB muscle (computed in section 3.4.4) (Fig.3.20).

The algorithm of IMAT is based on positioning of micro random polygons (0.4 to 1.5 mm of width and height) in the BB muscle. The algorithm will be stopped when the sum of polygon areas reach the total estimated area of IMAT. Then the fibers situated inside these polygon areas will be deleted. The description of this algorithm is depicted in 2.

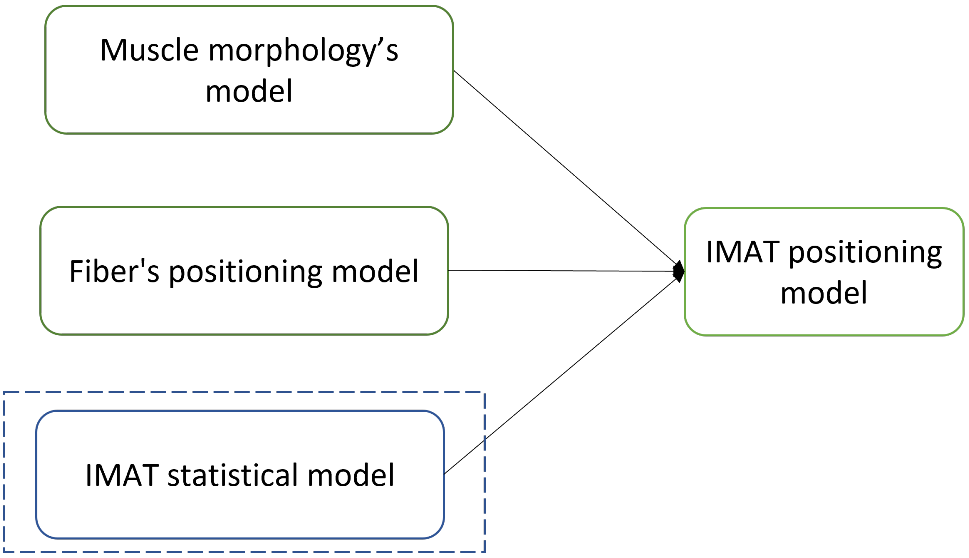

Figure 3.20: Diagram of steps and requirements needed to build the IMAT model with aging.

Algorithm 2 Positioning of adipocyte depositions algorithm

```
Require: muscle radius ($muscle_r$), bone radius ($b_r$), total IMAT area $Total_{IMAT\_area} = f(age)$, the coordinate of fibers
  Step 0. Positioning of the first adipocyte deposition
  1. Generate the first polygon center, randomly located in the muscle surface (between $muscle_r$ and $b_r$). The center coordinates are defined as $c_{px}$ and $c_{py}$.
  2. Define the shape/size of polygon (adipocyte deposition size). The width ($d_w$) and height ($d_h$) are selected randomly between 0.4 and 1 mm for young subjects, and between 0.5 and 1.5 mm for elderly subjects.
  3. Define the number of polygon vertices $n_v$ : randomly selected between 3 and 7.
  4. Split the width and the height of polygon into $n_v$ segments: $d_w$ gives $x_i$ segments with i = 1 to $n_v$, and $d_h$ gives $y_i$ segments with i = 1 to $n_v$.
  5. Compute the polygon angles using $x_i$, $y_i$, $c_{px}$, $c_{py}$ and the equation: $angles = \arctan 2(x_i - c_{px}, y_i - c_{py})$
  6. Form/plot the polygon using: $angles$, center coordinates ($c_{px}, c_{p_y}$), and vertices $n_v$.
  7. Compute the polygon area using Shoelace formula:
      $P^0_{area} = \frac{1}{2} | \sum_{i=1}^{n_v - 1} x_i y_{(i+1)} + x_{n_v} y_1 - \sum_{i=1}^{n_v - 1} x_{(i+1)} y_i - x_1 y_{n_v} |$      (3.9)
  Step 2. Generate many polygons $P^k$ with the same manner as in step 0. We break the loop when the sum of all generated $P^k$ areas reaches the $Total_{IMAT\_area}$
  $P^{total}_{area} \leftarrow P^0_{area}$:
  $k \leftarrow 0$
  while $P^{total}_{area} < Total_{IMAT\_area}$ do
      $k \leftarrow k + 1$
      $P^{total}_{area} \leftarrow P^{total}_{area} + P^k_{area}$
  end while
  Step 3. Remove all fibers located within polygon areas knowing the fiber and polygon coordinates.
```

We perform this algorithm on young subject (age = 25 years) and elder subject (age = 82 years). The muscle morphology and fibers positioning are computed according to these ages using results of previous sections. We observe that IMAT model has generated 54 adipocyte zones for young male with a mean area equal to 0.41 mm^2. Whereas, for elderly subject, the number and size of these adipocyte zones increase to reach 127 and 0.7 mm^2 respectively (see Table 3.14). To note, the sizes and number of these adipocyte zones can be managed for more realism using experimental imaging technique.

Table 3.14: The number of adipocyte zones (polygons) estimated by Algorithm 2 and their relative areas for young (YM) and older male (OM). The computation time of the Algorithm 2 is negligible (few ms).

Subject	Age (years)	Total IMAT area (cm^2)	Adipocyte number	Adipocyte area (mm^2)
YM	25	0.22	54	0.41
OM	82	1.28	127	0.70

The Fig. 3.21 shows the total IMAT area for young and elderly subject simulated as circle with a radius equal to $\sqrt{\frac{Total_{IMAT\_area}}{\pi^2}}$. From this configuration, and performing the algorithm 2, we obtain the dispersion of IMAT adipocyte zones as depicted in Fig. 3.22. However, after deleting the fibers from the adipocyte zones, we have obtained a lower number of fibers for elderly subject, compared to the value reported in [78] (see Table 3.15). This can be explained by an overestimation of this value, for aged category, in the study [78]. In fact, authors in [78] have estimated the number of fibers per muscle by dividing the maximal area of BB (obtained by MRI technique) by the mean fiber area (obtained by biopsy) (see eq. 3.8). By overlooking the notable IMAT infiltration factor in elderly people, they may overestimate the number of fibers for this aged category.

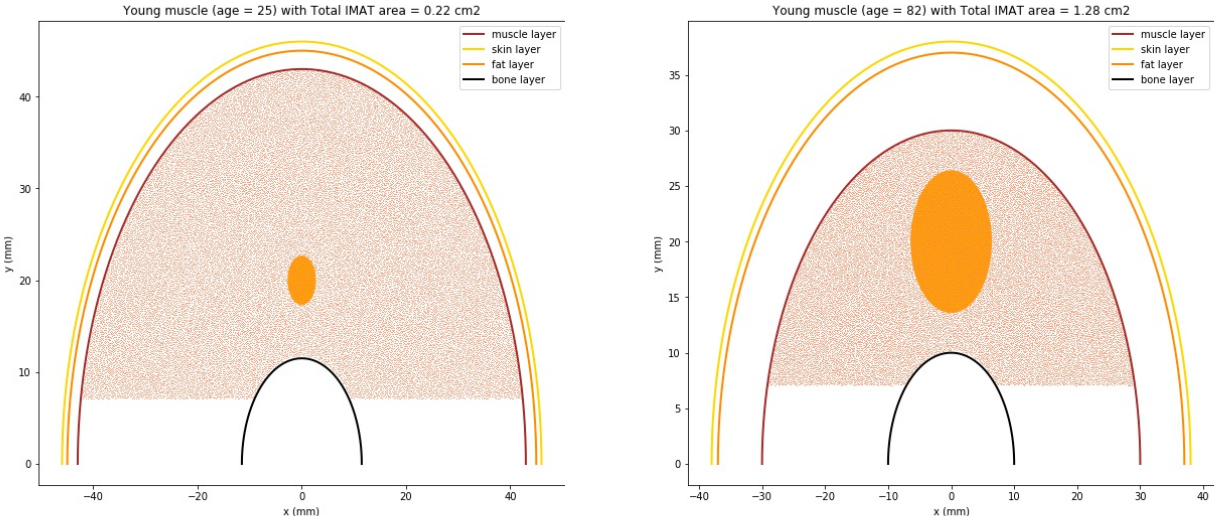

(a) (b)

Figure 3.21: The total IMAT area for (a) young and (b) elderly subject simulated as circle (orange) with a radius equal to $\sqrt{\frac{Total_{IMAT\_area}}{\pi^2}}$.

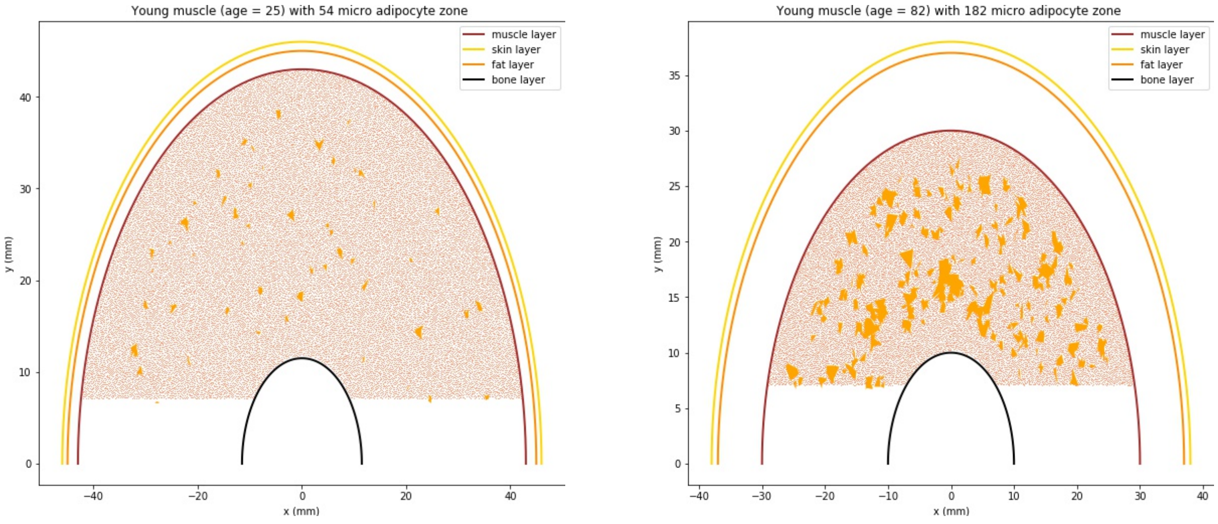

(a) (b)

Figure 3.22: The dispersion of IMAT adipocyte zones after performing the IMAT positioning algorithm for (a) young and (b) older subject.

Table 3.15: The difference the number of fibers estimated by FPDS algorithm, the number of fibers after removing fibers located inside the adipocyte zones, and the number of fibers reported in the literature for young (YM) and older (OM).

Subject	Age (years)	Estimated Nb of fibers	Nb of fibers after IMAT modeling	Nb of fibers in literature (thousand)
YM	25	250698	239117	253.6±40.4
OM	82	211798	148695	243.3±67.4

3.7 Motor units model with aging

The Motor unit structure and morphology still nowadays a critical issue to resolve [285]. The related anatomical parameters: the number, the innervation ratio (number of fibers per MU), the territories, and the fiber density (fibers/area) are rarely reported in literature for all muscles including the BB muscle. Moreover, the rare experimental data reported in literature are confused. It was reported, in the review [99], that the number of MUs varies between 118 and 398 for BB muscle using EMG estimation techniques. Other studies, based on counting of Motoneuron MN axons, have reported a number between 500 and 2000 (mean equal to 774 MUs for the BB muscle in [40] without age and gender clarification). However, this value can be overestimated due to high similarities between α-motoneuron axons and sensory somatic motoneuron axons. Moreover, no information concerning the number of MUs per type (S, FI, FR, and FF) was reported in these studies. Other parameter remains unavailable in literature which is the MU size and shape. None of these techniques (EMG and in *in vitro*) have directly measure these parameters. Expect a recent study [39], using MRI technique, has estimated the maximum and minimum MU dimensions at 10.7 ± 3.3 mm and 4.5 ± 1.2 mm respectively. Authors in [39] have observed that the MUs have an elliptical or crescent-shaped outline, and some MUs have a "split" territories. However, the cited study was performed on VL muscle. Likewise, the other structural parameters of MUs show the same confusion (e.g., the estimation of the innervation ratio [285]).

Based on the fact that MU size is a critical determinant of its physiological action, and understanding changes in MU structure in the setting of neuromuscular diseases is of fundamental importance in the interpretation of diagnostic clinical sEMG, we will try, in this section, to propose a MUs model for BB muscle. This model will place centers of MUs with a maximal dispersion in the muscle cross-section. Then, we will assign fibers (simulated in section 3.5) to the α-motoneurons (centers of MUs).

We assume that MUs centers are distributed uniformly in the muscle cross-section. This assumption was also made in previous works on sEMG simulation [319, 44]. We propose to use the FPSD algorithm to distribute uniformly centers of MUs for each type. For that purpose, we "split" the muscle area into three zones: the deep layers of muscle are mainly populated by slow MUs, the intermediate layers are populated by FI and FR MUs, and we place FF MUs in surface layers of muscle. This positioning is base on observations in literature [119] that confirm this behavior. The Fig. 3.23 shows the positioning of MUs centers using the FPSD algorithm.

Then, we estimate the innervation ratio (number of fibers) for each MU using the results of FPSD algorithm (number of MUs and ratio). Finally, fibers are attributed to α-motoneurons according to: the estimated innervation ratio, the proximity of fibers to the MU center and presence of neighboring fibers already attributed to that α-motoneuron.

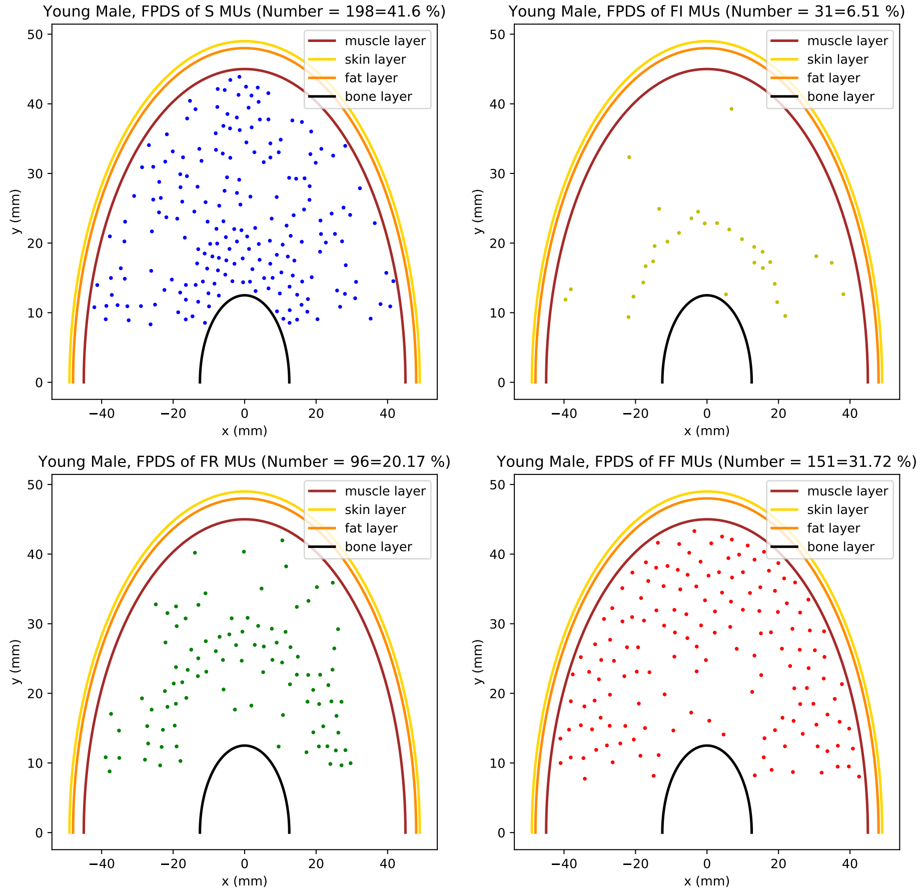

Figure 3.23: Positioning of MUs according to their type and using FPSD algorithm (Young Male subjects).

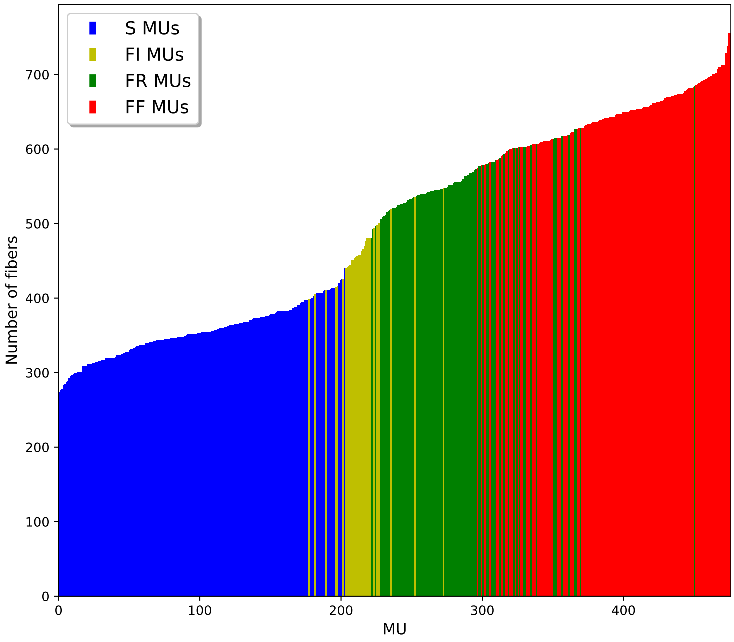

Figure 3.24: The estimated number of fibers innervated by each MN for a BB muscle with 45 mm of radius, and 250698 fibers. The number of MUs is equal to 476 (Young male subject).

For each neuron-fiber pair, the probability of assignment is represented by a score $W_f(n)$ that combines influences of each of these factors.

Algorithm 3 Fiber neuron assignment algorithm

```
Require: Number of fiber $n_{fiber}$
  Number of MU $n_{MU}$
  Fiber coordinates $(\rho_f,\theta_f)$
  MUs coordinates $(\rho_{MU},\theta_{MU})$
  while Not all fiber are assigned do
      for n in $n_{MU}$ do
          $w \leftarrow W_f(n)$
      end for
  end while
```

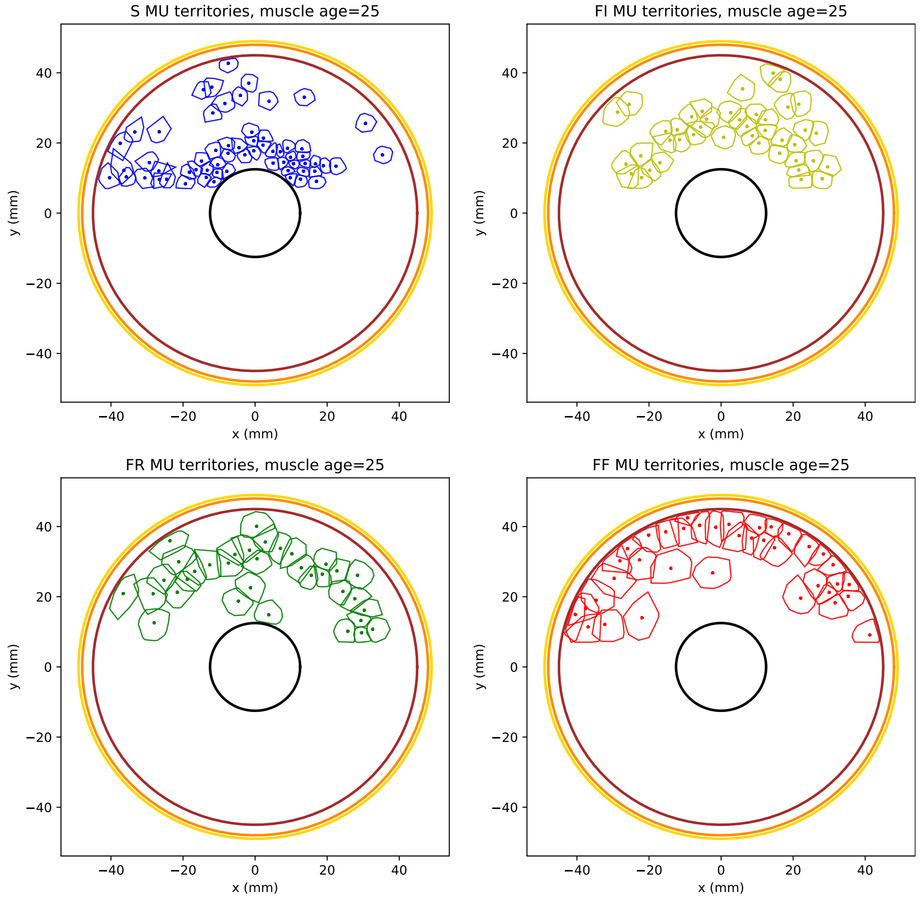

Figure 3.25: Centers of MUs across the cross sectional area of the muscle; The FPDS method allows an even distribution of not only the centers, but also of the sizes of MUs (Young male subjects).

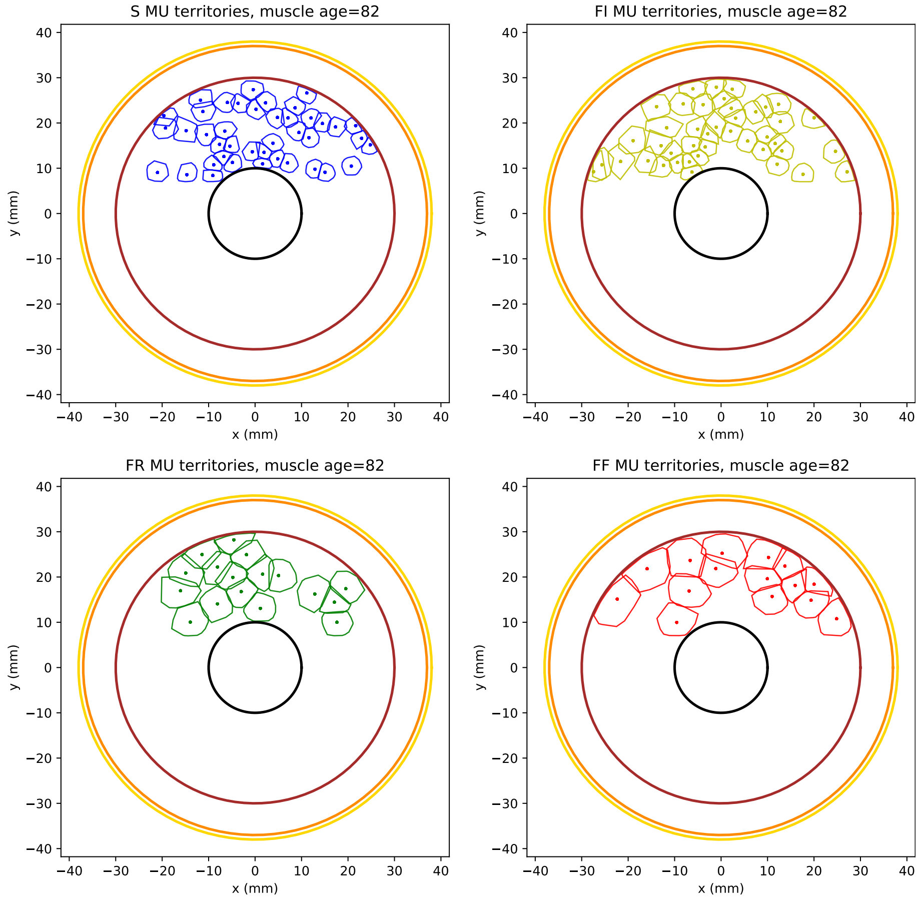

Figure 3.26: Territory centers of MUs across the cross sectional area of the muscle (Elder male subject).

3.8 Neural drive model with aging

The model [1, 11] is a multi-components system. It simulates the force and the HD-sEMG generated by BB muscle during isometric contractions. The recruitment pattern component simulates the MUs recruitment, activation and firing rate according to the size principle [43] and using the MN pool model depicted in [44]. The MUAPs are computed with high-fidelity to the fibers and MUs sizes of BB muscle. However, the variability in cell properties (S, FI, FR and FF type) is not incorporated in the MN pool model [44]. In fact, published computational models of MN pool [44, 320, 213, 321, 322] have considered a continuum form of the MUs electrical properties, although the evidence of its distinct morphological, structural and functional properties. In these models, all MUs of different types are recruited at the same ETh. The Fuglevand Motoneuron (MN) pool model [44], used in the HD-sEMG/force model [1, 11], operates with homogeneous MN pool according to the size-principle [43]. However, the conductor volume, the MUAPs and the force components are personalized to the types of MUs sources. Furthermore, the Fuglevand model capacity to mix or reverse MUs recruitment is limited [213]. A previous study [323] has evoked the limited capacity of this model to recruit FF MUs at high contraction levels for aged-subject categories. The study [213] has modified the Fuglevand model by assigning MN by cell index to be adapted for mixed or reversed recruitment.

In this study, 1) we will investigate the capacity of Fuglevand model to recruit fast fatigable (FF) MUs at 60% of MVC for real cases (young and aged subjects), and 2) we will propose a discrete type-scaled recruitment model. The new approach follows the size-principle and respects MU type variability. and its different recruitment ranges.

3.8.1 Fuglevand model

Since the publication of Fuglevand model in 1993 [44], it has been considered as the major increment in the modeling of MUs recruitment. In this model, MUs are recruited according to the size-principle [43] and to the force level developed. Each MU is recruited according to a minimum excitation threshold needed to initiate the discharge moments of MU action potential. This excitation threshold is described as depicted in [44] by the following expression:

$$Th_i = e^{i\frac{\ln(R)}{N}} \tag{3.10}$$

where Th_i is the excitation threshold to initiate repetitive discharge moments of the i^{th} MU, R is the force level (% of MVC) to recruit all MUs, and N is the total number of MUs within muscle. The number of muscle MUs N and its recruitment range r are muscle specific parameters and usually are not easily achievable experimentally. It was reported [324, 211] that for larger proximal muscle, such as the BB muscle, the MUs recruitment plays more important role in force modulation than its firing rate. The R of BB muscle according to [324] varies from 0 to 0.88. This range was estimated based on sEMG signal during isometric contractions. The study [320] has proposed a more adapted Fuglevand recruitment scheme for such muscles with a gradual slope:

$$Th_i = \frac{ai}{N} e^{i\frac{\ln(\frac{R}{a})}{N}} \tag{3.11}$$

However, authors in [323] have mentioned that the equations: (3.10) and (3.11) are not able to recruit FF MUs types at 60% of MVC for aged categories: elder men and elder women. In fact, the study [323] has applied a sensitivity analysis to evaluate recruitment model performance at a large variation ranges of Fuglevand and De Luca model [211] parameters for different age and gender categories. To verify this statement, we will apply the models (equations (3.10) and (3.11)) on a realistic distribution of MUs for young and elder BB muscle (Table 3.16). At 60% of MVC with orderly size recruitment, all types of MUs should be recruited. Such force level need FF MUs to be exerted.

Table 3.16: Number of MUs of the BB muscle for young and aged subjects. Relative number of S, FI, FR, FF MUs are reported in [79]

Age Category	MUs Number	**MU ratio per type**[a] **(%)**			
		S	***FI***	***FR***	***FF***
Young males	300	47	9	15	29
Elder males	250	55	15	20	10

[a] Data reported in [79].

3.8.2 New recruitment model adapted to aging

The electrical activity generated by the muscle during contraction depends of the fiber/MUs type composition as well as its number within the muscle. Nevertheless, the wide variability of the electrical activity is also due to the limb anatomy (muscle/MUs, blood vessel, adipose and skin tissues) with its different physiological properties. To achieve that on the MN pool, we first developed a type-scaled, high-fidelity computational recruitment model including its respective MUs types: Small (S), Fast-Intermediate (SI), Fast-Resistant (FR), and Fast-Fatigable (FF) types. Each type is simulated using equation (3.12) with its relative parameters. The model simulating global motoneuron pool recruitment is given by equation (3.13) which is the summation of type-scaled models.

$$Th_{\{type\}i} = A_{\{type\}} + e^{i\frac{\ln(R_{\{type\}})}{N_{\{type\}}}} \tag{3.12}$$

$$Th_{\{Global\}} = \sum_{k=S,FI,FR,FF} Th_{\{type\}k} \tag{3.13}$$

An aged muscle consisted of 250 MUs cells (Table 3.16 and 3.17) is performed to simulate the recruitment of MUs using the new modeling approach. This muscle includes: 137 cells ($\sim$ 55%) of S type, 38 cells ($\sim$ 15%) of FI type, , 50 cells ($\sim$ 20%) of FI type,and 25 cells ($\sim$ 10%) of FF type (Table 3.17). This repartition matches the relative distribution of MUs types reported experimentally from the BB muscle [79]. The MUs size and type are strongly correlated, but the correlation ratio is not one [325]. This makes application of the size principle to predict motoneuron/MU type recruitment not totally correct and reliable. A mixed (recruitment of several motoneuron types at the same time) or reverse (FF>FR>FI>S) recruitment should be investigated mathematically and experimentally. The wide overlap between physiological properties of MUs (sizes overlap cross the MUs types) and the large biological variability of MN observed experimentally, are a supported arguments to make these investigations. However, this model (equations (3.12) and (3.13)) was originally developed to work with a homogeneous sub-models (MUs type models), as with Fuglevand model. Only the global model (equation (3.13) is heterogeneous. To make it more compatible with mixed and reversed type recruitment, we have modified the assignment of MUs to be by cell indexes and sizes both. To investigate the performance of Fuglevand model, we apply its recruitment scheme on young and aged muscle with realistic distribution of MUs types (Table 3.16). The Fig. 3.27 represents the RTE function according to recruited MUs (orderly sizes recruitment). In this figure, we observe that, for aged categories (Fig. 3.27(b)), no FF MUs at 60% of MVC are recruited. Such force level needs FF MUs to be exerted for biceps brachii muscle. This observation

Table 3.17: New model parameters: Number, recruitment range *RR*, and initial threshold *A* for each type of MUs (equation (3.12)). Type's percentage data are reported in [79] for aged muscle.

Model Parameters	**MUs type**[a]			
	S	***FI***	***FR***	***FF***
RR	25	35	50	88
A	0	24	34	49
N	137	38	50	25

[a] type percentage data reported in [79].

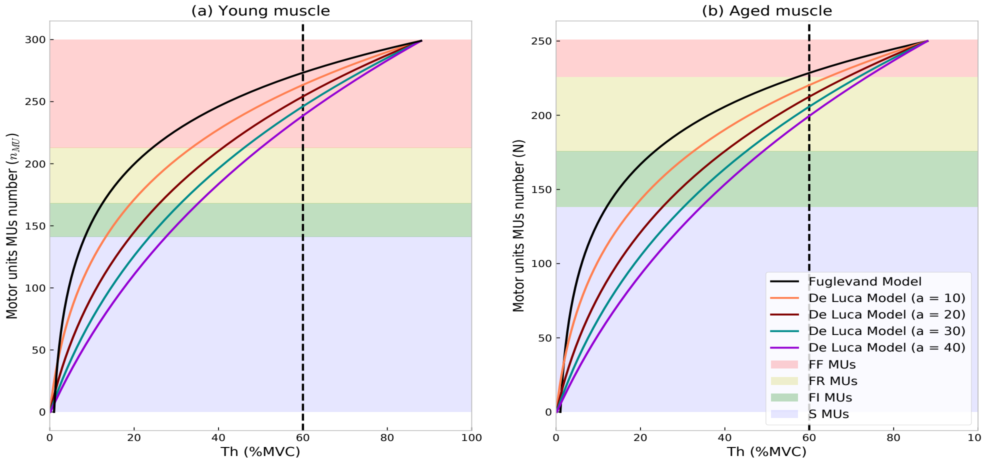

Figure 3.27: The recruitment threshold function for (a) young muscle and (b) aged muscle. The $RR = 88$ for both young and elder muscle, and for Fuglevand and De luca model (equations (3.10) and (3.11)). The sizes of MUs respect that S(blue)<FI(green)<FR(yellow)<FF(red).

is valid for Fuglevand and De Luca model both. Changing the slope value a or the RR do not ameliorate the results. The model described in equations (3.10) and (3.11) is not appropriate for such muscle configuration, even when considering that the size orderly recruitment is valid. The Fig. 3.28 shows the recruitment behavior of Fuglevand model (continuum black line) and the new modeling approach (colored scatters: S (blue), FI (green), FR (yellow), FF (red)). The new approach is applied on the same aged muscle of Fig. 3.27(b) and simulated with parameter values depicted in Table 3.17. We observe that the new recruitment threshold function is able to recruit FF MUs with a strict orderly size recruitment, which is not the case for Fuglevand model. Moreover, the curve behavior of the new personalized recruitment model to MUs type is very close to the recruitment scheme fitted from experimental data depicted in the study [213].

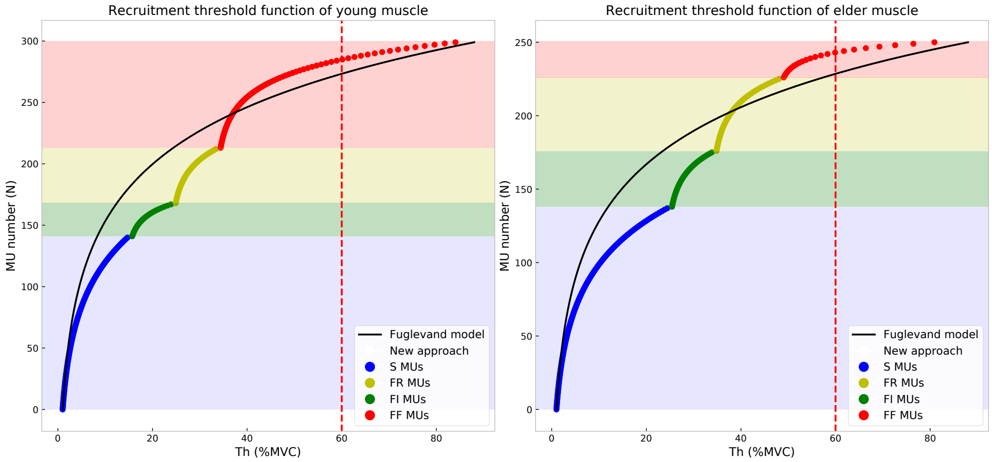

Figure 3.28: The recruitment threshold function for aged muscle: Fuglevand model (black line) versus the new type-scaled recruitment model (scatter plot with S-type (blue scatters),FI-type (green scatters),FR-type (yellow scatters),and FF-type (red scatters)). The recruitment range is $RR = 88$.

For mixed and reverse recruitment, experimentally proved (in [213]), we have assigned the MUs force according to cell indexes. The new indexation makes MUs with the same order sizes following the same recruitment scaled-type scheme. The Fig. 3.29 shows a mixed and reverse recruitment using the new modeling approach.

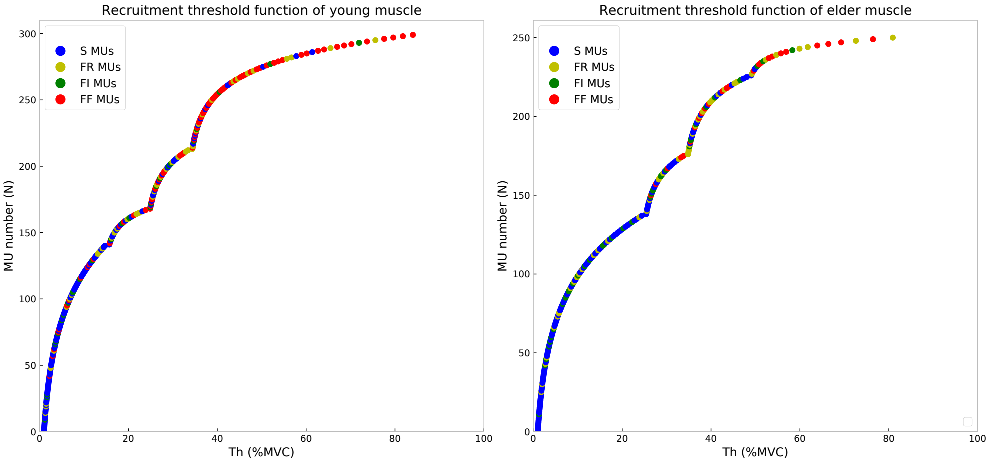

Figure 3.29: A mixed recruitment threshold function for aged muscle.

However, this scheme should be improved, in future work, using more advanced and appropriate equations, e.g., applying a sigmoid functions for type-scaled model instead of exponential recruitment evolution. Such recruitment behavior (sigmoid-shaped curve) can promote small recruitment rate of FF MUs at low Th and an important one at high Th. Furthermore, the strictly size indexation of MUs will be compatible for a mixed and reversed recruitment using sigmoid-shaped functions.

To resume, our results indicate that generic and homogeneous recruitment models confusing size and type of MUs can deliver a non-realistic recruitment behavior for elderly people. FF MUs for aged biceps brachii muscle are not recruited at higher contractions with these models. This aspect impacts the prediction reliability of simulated sEMG and force. An adjustable, discrete, and scaled-type computational model was investigated in the present study. The new proposed approach offers a mixed and reversed recruitment with the ability to recruit FF MUs at high contraction for aged healthy subjects.

3.9 Simulations with the HD-sEMG model

To evaluate the proposed changes, in the modeling approach, we decided to simulate HD-sEMG signals over a 16×16 electrode grid and to compute sEMG signal features on the recorded signals. Four signals are computed on the signals amplitude (RMSA), on the probability density function (Kurtosis and Skewness), and on the estimated mean frequency (MNF) of these signals.

For this purpose, we simulated a potential map of seven anatomies aged between 25 years and 85 years old, at low and high contraction levels (20 and 60% of the Maximal voluntary contraction (MVC)) during 5s of holding contraction. The seven anatomies are generated by introducing only the age and the gender of subjects as inputs to the new proposed modeling approach. The grid position is the same for all simulations. The features are computed at each grid electrode and then averaged over the 64 channels. The Table 3.18 shows the values of main parameters defining the structure and morphology of BB muscle, estimated by statistical and phenomenological modeling approach described in the previous sections. We observe a decrease in the estimated percentage of fast fatigable MUs: more than 50% of MUs are lost, from 31% at age 25 years to 14% at 85 years old. However, the other types of MUs are not impacted by the same way with muscle (e.g., the percentage of slow MUs increase but not considerably as the decrease of FF ones).

This tendency of MUs loss is consistent with reported observations [100, 97] underlying a loss of MUs by 50% for very elder peoples ($> 75 years$). To note, these studies [100, 97] have not mentioned which type of MUs is affected by this loss.
Moreover, the proposed model expects a large expansion of "survived" MUs territories. This expansion, regarding mainly the FF MUs, is a consequence of the large MUs loss against the small loss of fibers with aging (see related parameters in Table 3.18). In the same vein, The HD-sEMG signals simulated according to estimated parameters depicted in Table3.18 show similarities with behaviors reported in literature. In fact, in the Fig. 3.30, we observe that the root mean square of signal amplitudes (RMSA) is significantly reduced with aging at maintaining high level of contractions (60% of the maximal voluntary contraction (MVC)). In particular between the age 40 and 50 years old. However, by maintaining low force strength (20% of MVC), the RMSA decrease slightly with aging. The same trends were observed in literature [199, 201]. The structural changes of muscle with aging, in addition of changes in recruitment pattern, can explain this behavior. In fact, the aged muscle is dominantly populated by slow MUs. Thus the capacity to maintain a low level of contractions (such at 20% of MVC) is accurately preserved until advanced ages [326, 327]. However, the comparison between young and elderly subjects using the absolute values of sEMG amplitude should be applied with caution. The higher subcutaneous adipose tissue usually detected in elderly compared with young can affect the measurements with misleading findings [199].

Table 3.18: The estimated morphological and structural parameters using the proposed aging model. SAT: Subcutaneous adipose tissue. * *mean value.*

Parameter	Subject 1	Subject 2	Subject 3	Subject 4	Subject 5	Subject 6	Subject 7
Age (yrs)	25	35	45	55	65	75	85
Muscle CSA (cm^2)	13.6	13.41	13.01	13.35	11.48	10.53	9.64
Muscle length (cm)	13.99	13.9	13.75	13.51	13.2	12.85	12.53
SAT (cm)	0.42	0.42	0.43	0.44	0.45	0.46	0.47
IMAT area (cm^2)	0.21	0.31	0.59	0.92	1.13	1.24	1.28
Nb of fibers	251199	250444	248172	245487	239773	228314	200242
Nb of MUs	531	557	479	401	338	271	181
S MUs (%)	42	43	45	46	49	52	56
FI MUs (%)	8	4	10	13	15	19	19
FR MUs (%)	19	18	16	13	12	11	11
FF MUs (%)	31	35	29	28	24	16	14
Innervation ratio*	507	490	589	711	964	1255	1618
Area of S MUs* (mm^2)	9.7	8.6	10.4	12.6	14.9	17.1	19.0
Area of FI MUs* (mm^2)	14.4	17.5	20.9	24.7	27.0	29.0	33.6
Area of FR MUs* (mm^2)	34.1	31.6	40.2	47.1	55.0	64.7	75.3
Area of FF MUs* (mm^2)	46.8	44.9	50.0	69.5	83.5	92.8	106.1

In the frequency domain, we evaluate the HD-sEMG signals with Mean frequency (MNF). the Fig. 3.31 shows the variation of this signal feature in relation of aging and force produced. We observe, as expected with literature reports (e.g., in [190]), a decrease in MNF values with aging at 60% of MVC [190]. However, at 20%of MVC, we don't observe the fast decline in MNF but a slight increase. Such aspect should be confirmed with a comparative study between young and elder population (one of the perspective of this

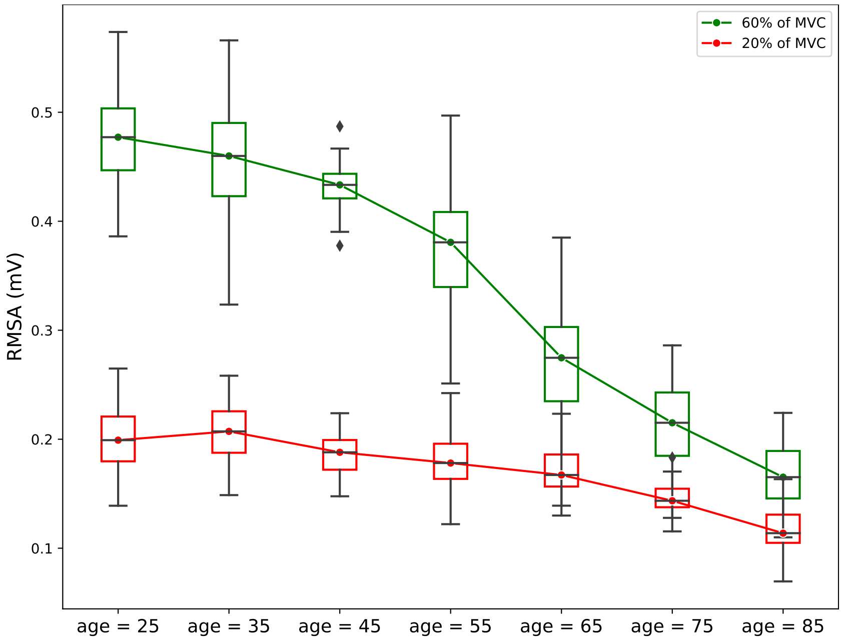

Figure 3.30: The variation of the Root mean square of Amplitude (RMSA) values (in mV) relative to the subjects ages of the different simulations. (Green) RMSA of HD-sEMG signal at high contractions. (Red) RMSA of HD-sEMG signal at low contractions.

work). To note, this MNF signal feature was recently used as biomarker of early signs of Sarcopenia (muscle aging disease) [9]. The Fig. 3.32 and 3.33 show the kurtosis and skewness features for the 7 aged subjects. We observe an increase of these value with aging and MVC level both. However, we find that kurtosis and skewenes values are slightly higher than expected and than observed in literature.

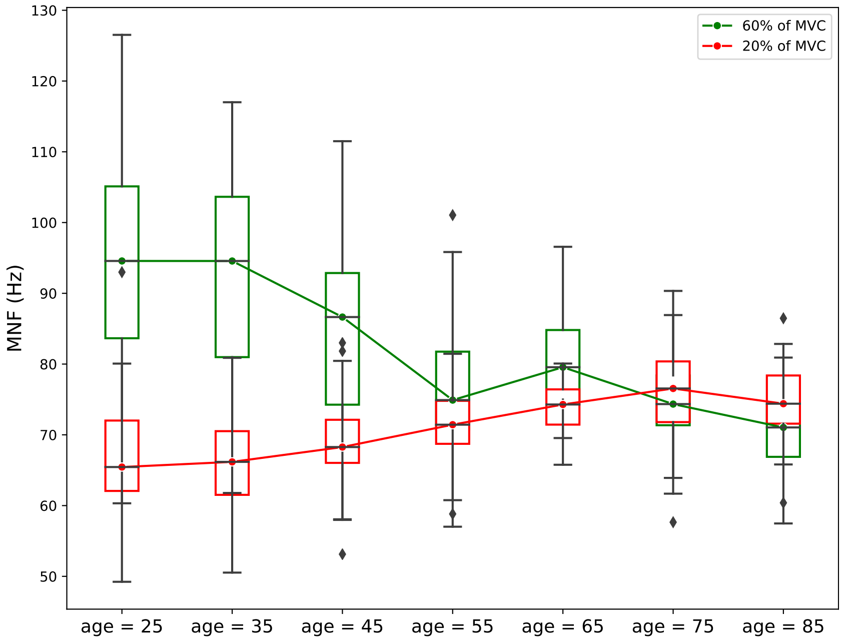

Figure 3.31: The variation of the Mean frequency (MNF) values (in Hz) relative to the subjects ages of the different simulations. (Green) MNF of HD-sEMG signal at high contractions. (Red) MNF of HD-sEMG signal at low contractions.

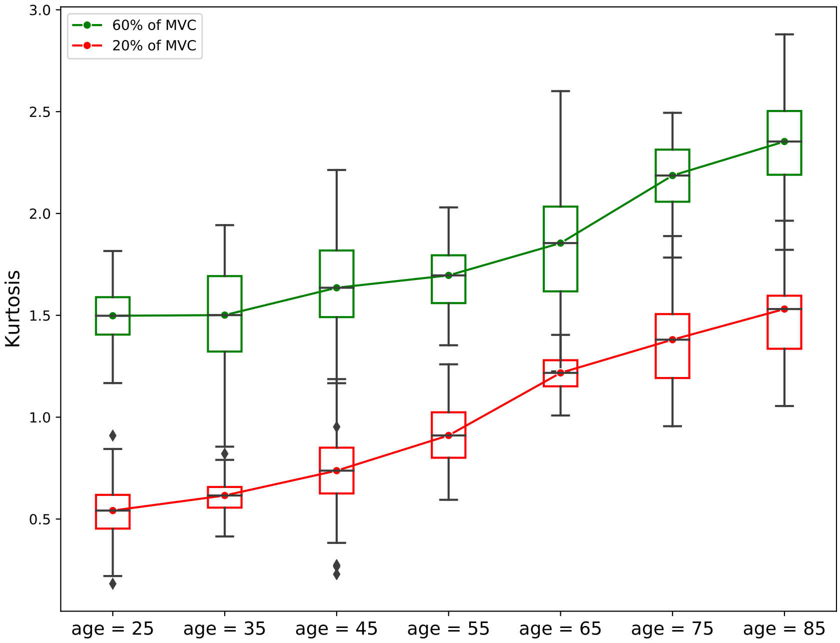

Figure 3.32: The variation of the Mean frequency (Kurtosis) values relative to the subjects ages of the different simulations. (Green) Kurtosis of HD-sEMG signal at high contractions. (Red) Kurtosis of HD-sEMG signal at low contractions.

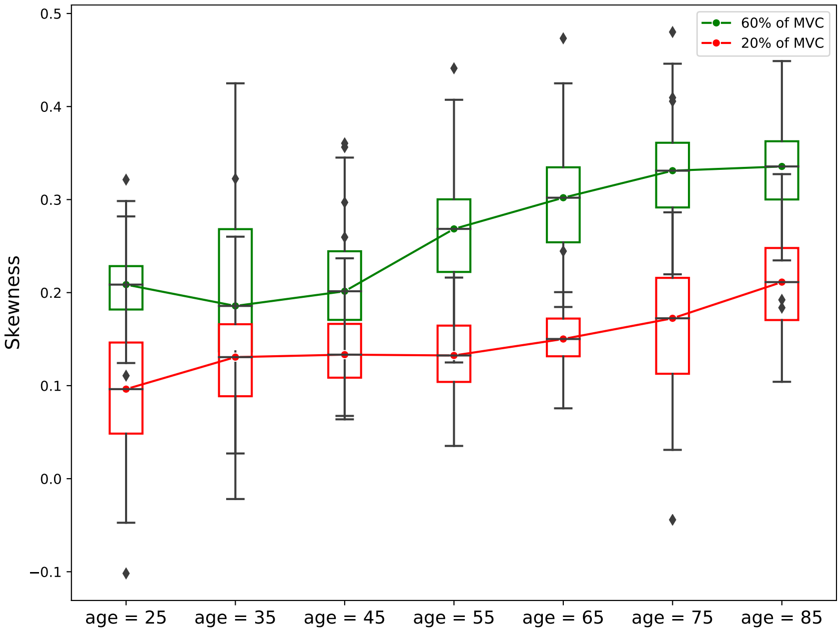

Figure 3.33: The variation of the Mean frequency (Skewness) values relative to the subjects ages of the different simulations. (Green) Skewness of HD-sEMG signal at high contractions. (Red) Skewness of HD-sEMG signal at low contractions.

3.10 Discussion et Conclusion

In this chapter we have proposed to address inconsistency observations in the building of muscle structure, and in the recruitment pattern of MUs using the HD-sEMG model depicted in [1, 11]. In fact the model approach of [1, 11] have placed in first order the MUs according to the Best Candidate (BC) algorithm (proposed by [281]) in the purpose to maximize minimal distances between centers of MUs. Then, authors in [1, 11] have added constraints to disperse the positions of MUs in the muscle volume according to their types as suspected in physiological studies [119] (slow MUs are located in the deep layers of BB muscle, when fast MUs are located near the muscle surface). Finally, authors have fulfilled the MUs by a number of fibers placed randomly inside the circular territories of MUs. The number of MUs, the number of fibers per MU, the percentage of MUs according to their type are defined and introduced as inputs of the MUs positioning algorithm in [1, 11].

We have observed that this strategy can lead to a non realistic number of fibers. In fact, less than 100.000 fibers per muscle for young male subjects are only generated by this algorithm. However, the number of fibers for BB muscle was reported near the value of 250.000 fibers approximately [78]. Moreover, the regionalization of MUs inside the muscle according to their types without a supplement constraint on their sizes or densities can lead to a non homogeneous fiber density inside the muscle volume as depicted in Fig. 3.7. For that reason, we have proposed a new algorithm for fiber and MUs positioning in this chapter. However, to avoid this kind of errors, we have proposed a initialization of the model using only two parameters: the age and the gender. In fact, we have proposed to estimate all the neuromuscular parameters involved in this model using "statistical" regression models. Since the major part of those parameters and their age changes are reported in literature. For that purpose, we have extracted values of these parameters for young, elder, male and female populations. Then, using the regression equations depicted in the section 3.4, we estimate the appropriate model equation and its relative parameter values, in order to better fit reported experimental data. As consequence, we have estimated according to age and gender all model entries such as the muscle radius/length, the subcutaneous fat thickness, and the diameter and percentage of fibers according to their types.

Then, we have placed fibers according to the Fast Poisson Disk Sampling algorithm [316]. The positioning of fibers is based on the their radius and the muscle/bone radius (both estimated from statistical models in section 3.4). Using this algorithm, we have positioned 250698 fibers in the BB muscle of young male subject aged at 25 years old (which is close to the reported value in [78]). The FPDS algorithm is part of family algorithms that fill an enclosed domain by a number of points added iteratively to respect a fixed minimal radius [315, 316, 317]. However, the use of these methods in the biophysical models simulating sEMG signals are limited to only the MUs positioning (few hundred) rather than the positioning of fibers (thousand of hundreds) [328, 319, 282]. The high computational time (from few minutes to few hours) is the main cause of this limitation. In this study, the FPDS has a pre-initialize background grid that minimize the computational time of the algorithm by limiting the iterative check to only the points/fibers indexed in this grid. As consequence, the 250698 was positioned in only 31s.

The second main contribution in this chapter, is the intramuscular adipose tissue (IMAT) infiltration model. To our knowledge, we are the first proposing this model in the simulation of the HD-sEMG signals. The total IMAT area was estimated using a statistical model and then subdivided into small polygons areas dispersed over the BB muscle volume. The fibers located in theses polygon areas are then removed. However, the statistical model of IMAT versus aging needs to be validated or improved by an appropriate experimental data/protocol. In fact, we have proposed this model based on our observations and findings reported in the literature. These finding have suggested a ratio between IMAT and the total body fat tissue (BFT) or subcutaneous fat (SF). These latter parameters are easily measured and well reported in the literature [122, 302]. Nevertheless, these findings have supposed that the total estimated IMAT is equally apportioned to all skeletal muscles. This hypothesis is to verify. Meanwhile, we keep working with this assumption. Moreover, we should note that each layer composing the conductor volume is considered as a homogeneous medium in the model [1, 11]. In this conductor volume, the muscle layer is an anisotropic medium and has higher conductivity along the longitudinal direction than in the other directions. While, the subcutaneous fat and the skin tissues are isotropic. The introduction of IMAT infiltration will changes the muscle layer homogeneity. As consequence, the estimation of the potential distribution over the skin, due to sources in the muscle and based on the solution of the Poisson equation in the spatial frequency domain in the different media [329], should be adapted to the multiple adipose infiltration between fibers. In this study, we didn't address this issue. A reflection about solving this mathematical issue without altering the computation time and complexity of the model [1, 11] should be made.

After fibers and IMAT positioning, we proceed to the positioning of MUs according the FPDS algorithm. For that purpose, we have fixed at first the minimal distance between centers of MUs. This parameter is essential to initiate the FPDS algorithm and can be reported from literature (e.g., in)[40]). However, the particularity of this study, is to not use this parameter as the radius that define the circular territory enclosing the center of the MU. This assumption was made by all studies simulating MUs territories in the biophysical models of sEMG signals (e.g.in [1, 278]), expecting one recent study [319] which define the MUs territories based on the positions of their innervated fibers. Although the similarities between the methodologies of fiber's assignment, we are performing a different positioning algorithms (farthest point sampling in [319] and FPDS in this study). In this chapter, we follow the same algorithm in order to define MUs territories. The fibers are assigned to these centers according to: the estimated innervation ratio (statistical model), their proximity of MU center, and the presence of neighboring fibers already attributed to MU center. Each MU territory is then defined by the area of the convex hull enclosing all fibers assigned to its center. The average area of these convex hulls for each type of MUs is depicted in Table 3.18. This model can place centers of large MUs (FF-type) near the surface muscle layer as suspected in [119] and, at the same time, guarantee a large area/size of the positioned MU. This can not be ensured with circle territories. However, the impact of this approach should evaluated on the simulated HD-sEMG signals.

The last phenomenological model proposed, was a computational recruitment model of MUs. In fact, the recruitment thresholds of MUs in a muscle appear to follow a continuous distribution with many MUs attaining a small recruitment threshold, and few large MUs only being recruited at high activation levels [278]. This behavior is captured well by the exponential model proposed by [44] and used by in [1, 11]. However, we have demonstrated the limited capacity of this model to recruit FF MUs at high contraction levels for aged-subject categories. To overcome this limitation, we have proposed an extended version of the MUs recruitment model depicted in [44]. In this extended version, we have attributed a gradual slope of MUs recruitment according to MVC level and type of MUs both.

Finally, we have illustrated the HD-sEMG signals resulting from these modifications. The features of HD-sEMG signals are computed over the 64 channels of the recording system and then averaged. The evolution of feature values was presented according to 7 different subject ages (Table 3.18) and two contraction levels (60% and 20% of MVC). However, these simulations are preliminary illustrations of HD-sEMG signals in order to compare general behavior trends to those reported in literature. Future work should statistically explore these trends among a large sample of young and elderly population and with more features.

General conclusion

In this general conclusion, we will run through the essential points that were addressed and developed within this thesis. Then, we will mention some of the limitations of the proposed models and we will finish by elaborating the perspective of future works. As previously explained, this thesis aims at helping in the detection of the premature motor decline with aging by using identification procedure performed on a multi-physic, multi-scale model describing the skeletal muscle during isometric contractions [1]. For this purpose, we are faced with several steps of applied mathematics, physiology, and signal processing to finally model the structural and morphological changes of skeletal muscle with aging.
The first contribution was the application of sensitivity analysis method on the model [1]. This method aims for defining the neuromuscular parameters with large and negligible impacts on the simulated sEMG signals, in the target of a subsequent identification of those parameters based on experimental HD-sEMG signals. However, the requested task is not evident. In fact, This model have a complex design with a large number of inputs, more than 50 parameters, and marked by switching between behaviors according to threshold concepts. In addition, many of these parameters are associated to large uncertainties due to the lack of knowledge and/or the measurement errors. Based on a bibliographic research, the Morris Sensitivity Analysis (MSA) come forth as the method with acceptable compromise between its computation time and the model complexity. It screens the most and least sensitive parameters with the fewer number of model simulations. In fact, the MSA varies one input at a time and computes the Elementary Effect (EE) of this variation on the model output.This computation is repeated several times for each input by following different trajectories T in the input space. The mean μ^* and the standard deviation σ of these EEs for each input are considered as the MSA indices. The input's impact is assessed based on values and rankings of these indices. The primary sensitivity analysis tests with MSA method have displayed an unstable parameter ranking even if increasing the number of trajectories T (i.e., number of model evaluations). In fact, the mean μ^* is inappropriate estimator of asymmetric an non-normal distributions of EEs. Moreover, the standard deviation σ is highly sensitive to extreme outlier. However, the EEs computed using MSA method on complex systems are frequently asymmetric and with large outliers. As consequence, we have proposed an extension of MSA by suggesting the use of two more robust estimators of EEs: the absolute median χ^* and the median absolute deviation ρ. Furthermore, we have improved the efficacy of these estimators in enhancing stability of rankings, in screening the parameter effects with extended information (linear, (non)monotonic, and non linear and/or with parameter interaction effects), and in reducing the computation time of the method. The assessment and the comparison between the MSA method and the proposed Improved Sensitivity Analysis (IMSA) method are presented in the first section of chapter 1. Then, the IMSA was employed on the neuromuscular model [1] simulating the electrical activity of Biceps Brachii muscle

during isometric contractions. For that purpose, we have decided to perform the sensitivity analysis according to the parameter variation ranges of two age categories: Young and Elder population, and at high and low maintained isometric force (High Contraction (HC) = 60% of Maximal Voluntary contraction (MVC), and Low Contraction (LC) = 20% of MVC). The HD-sEMG signals are computed and monovariate and bivariate features of signals are calculated (the total number if feature studies w=is 23, e.g., feature in time domain and features in frequency domain). The final step in this first contribution was the building of sensitivity matrixes relating each HD-sEMG (High Density surface Electromyography) signal feature to their most influential parameters. This step is useful for the subsequent identification of those influential neuromuscular parameters. However, when dealing the HD-sEMG signals by the sensitivity analysis method, we have state many limitations of the model [1]. Which lead to the second contribution on this thesis work.

The second contribution was the model personalization to muscle aging. In fact, to generate young and elderly simulated HD-sEMG signals, users need calibrate/adjust manually the values of around 50 neuromuscular parameters (entries of the model). This calibration needs some expertise and a well-known of the variation ranges of all these parameters for young and elderly subjects. Moreover, users must have a deep understanding of the workflow, the building and the solving process of the model to avoid introducing contradictory values of model entries (e.g., the number and sizes fibers must be consistent with the size correspondent Motor Unit and muscle volume). Which can be an obstacle in the perspective of developing a model aided diagnosis tool. Furthermore, many aged muscle characteristics are not included in the model [1], e.g., the Intramuscular Adipose Tissue (IMAT) infiltration and the expansion of MUs. However, these important aging changes contribute to the diagnosis of muscle aging [133, 8]. For that purpose, we have modified the model schema implementation to be more easy to manipulate (i.e., user-friendly), with less error and inconsistency risks. Only the age and the gender of subject became needed as model entries to initiate a simulation of HD-sEMG signals. All other parameters necessary in simulations are then estimated through "statistical" models. The statistical models employ regression analysis to estimate the relation Parameter *Vs* Age. A bibliographic research reporting these morphological and structural changes according to age, gender, and BB muscle was done. Once built, we have developed phenomenological models for the purpose of positioning fibers, IMAT and MUs. In fact, we have placed fibers using Fast Poisson Disk Sampling (FPDS) method for homogeneous and dense fibers for more realism muscle structure. As an example, we have placed *250689* and *211798* of fibers into young and aged statistically estimated. The computational time of this algorithm is 30s. Then, we have performed an algorithm/model to place small (micro) adipose depositions between fibers. This model splits the total area of IMAT (estimated by statistical models) into random polygons with the constraint of that their sizes do not exceed the IMAT area. The adipose depositions were placed within the BB muscle and emptied from fiber pre-placed in the previous step. Then a positioning of MUs centers was done and fibers were assigned to these centers according to: the estimated innervation ratio (statistical model), their proximity of MU center, and the presence of neighboring fibers already attributed to MU center. The last phenomenological model proposed, was a computational recruitment model of MUs. It is an extended version of the famous *Fuglevand* recruitment model [44], where the recruitment threshold was adapted to aged muscle structure. In fact, we have attributed a gradual slope of MUs recruitment according to MVC level and type of MUs both. Finally, we enclose the chapter 3 that contain these modeling approach by simulating HD-sEMG signals with model incorporating these changes. The features of HD-sEMG signals are computed over the simulated electrode channel and the computation scheme proposed in [1]. The evolution of feature values was presented according to 7 subject ages {25 yrs, 35 yrs, 45 yrs, 55 yrs, 65 yrs, 75 yrs, 85 yrs}, and two contraction levels {60% and 20% of MVC}. However, these simulations are preliminary illustrations of HD-sEMG signals in order to compare general behavior trends to those reported in literature. Future work should statistically explore these trends among a large sample of young and elderly population.

After improving the sensitivity analysis method, and developing the personalized muscle model with aging, the next stage of the work will be dedicated to the neuromuscular parameter identification using inverse method. A preliminary work of parameter identification was initiated using simple method (Gradient descent) and one and/or two muscle parameters was identified in a reduced time (This work is not included in this thesis manuscript). These parameters, identified from sEMG signals, can be used to detect an early decline of muscle aging. In fact, the diagnosis of muscle aging as a disease entity (known with the name of Sarcopenia) respects diagnosis criteria fixed by the different group of works on this disease (e.g., [8] and [133]). These diagnosis criteria are limited to measure macroscopic age changes such as the muscle mass and strength loss. However, it is more interesting to evaluate muscle aging at inner(fiber and MU) muscle scales. Parameters such as the increase of IMAT proportions in the muscle, the disorder in the neural recruitment of MUs, or the increase of MUs sizes detected by sEMG signals should offering a safe and rapid diagnosis of pre stages of sarcopenia or an accelerated muscle aging. The sEMG can provide objective answers to many unresolved neuromuscular issues. Nonetheless, the sEMG technique still until today a widely used technology to assess neuromuscular outcomes but only in the scoop of research fields.

The clinical application of this technique suffers of many technical and administrative barriers [330, 331]. In this thesis work, we have tried to boost the use of sEMG technique in clinical environment in the focus of developing a Model Aided Diagnosis (MAD) of muscle aging at short-mid term. We have take into consideration: the reducing of complexity when dealing with the model (user-friendly, only the age and gender is needed as entries); focusing the modeling approaches toward a precise objective/phenomenon (muscle aging: morphological and structural changes); finding a compromise between reliable mathematical methods and time of computation (screening sensitivity analysis indeed of high cost computational methods with more information on the parameter interactions); and tacking advantages of all accumulated expertise through past years in the evaluation of muscle changes with aging using sEMG technique (statistical models).

However, the work presented in this thesis, concerning the aging model, needs more adjustment and validation process. Meanwhile, we will try at the end of this work, as a perspective, to plot/imagine/propose a decision tree/scenario to evaluate/diagnosis the muscle aging using a bio-reliable model simulating the electrical and mechanical activity of skeletal muscle (see Fig. 3.34).

The proposed diagnosis decision tree works by acquiring real HD-sEMG signal from a patient, then apply some processing techniques to improve the quality of signal and extract useful features. In parallel, a simulated HD-sEMG signal is generated using a bio-reliable model. This model needs only a primitive and easy accessible information from the patient to generate sEMG signal. Information such as, age, gender, and BMI. Then, using this information and what we call the "offline system", we generate data needed to simulate a realistic sEMG signal personalized to the patient. The real sEMG signal detected at the skin surface of patient is then compared to simulated signal. If the comparison results satisfied a pre-fixed threshold criteria, the HD-sEMG model will be used to identify a predefined anatomical/neural muscle parameter(s). This (these) parameter(s) will be used, by clinicians, as indicator(s)/biomarker(s) of muscle aging. If the simulated sEMG signal is not matching with patient-measured sEMG, the information with signal processing results will be transferred to the "offline system". This system, related to a computational statistical aging models and a data-base, will make a decision by proposing a new set of inputs to compute/simulate a new patient-personalized sEMG signal. This action will be repeated until the comparison result converge into the pre-fixed threshold criteria.

The proposed aided-diagnosis tool is composed of two toolboxes: online and offline toolbox. The online toolbox contains a fast speedup HD-sEMG model, the real equipment measuring sEMG from patient, and a calculation server (computer). In fact this computer will ensure the comparison between simulated and real-time sEMG signals, the computing of the identified muscle aging indicator(s), and the communication with the offline toolbox.

The offline toolbox will incorporate all data and make-decision algorithms ensuring the monitoring and the well execution of the online toolbox. It will contain:

- Data base: containing all data needed to built aging statistical models. Furthermore, this data base will be rewarded permanently by patient-measured sEMG signals and their processing treatments.
- Statistical aging models: all models extracted from litterateur and/or self-developed, correlating anatomical and neural muscle factors to muscle force and sEMG.
- Toolbox tool: containing a package of make-decision algorithms. These algorithms will help in: (1) the building of the cost functions needed in the parameter identification (using pre-computed sensitivity analysis results); (2) the adjustment and calibration of statistical aging models using the results comparing the simulated sEMG to real-measured sEMG; (3) the updating and feeding of the offline database.

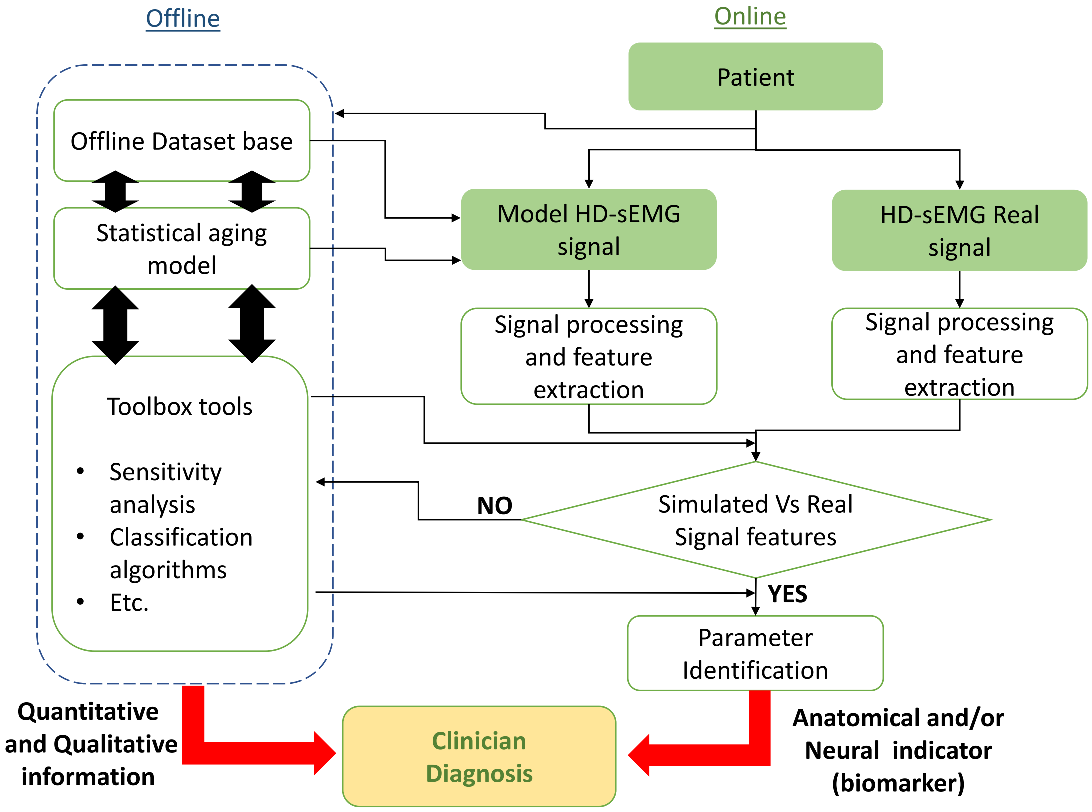

Figure 3.34: Proposed scheme to perform the Model Aided Diagnosis (MAD) of muscle aging.

Sarcopenia is one of the main causes of frailty and inability in elderly people. An aided-diagnosis tool aims to detect early signs of sarcopenia. This will promote the development of innovative personalized therapies (physical exercise, diet) in conjunction with geriatricians.

Bibliography

[1] Vincent Carriou, Sofiane Boudaoud, Jeremy Laforet, and Fouaz Sofiane Ayachi. Fast generation model of high density surface EMG signals in a cylindrical conductor volume. *Computers in Biology and Medicine*, 74:54–68, July 2016.

[2] Kaare Christensen, Gabriele Doblhammer, Roland Rau, and James W Vaupel. Ageing populations: the challenges ahead. *Lancet*, 374(9696):1196–1208, October 2009.

[3] Kashif T. Khan, Kaveh Hemati, and Anne L. Donovan. Geriatric Physiology and the Frailty Syndrome. *Anesthesiology Clinics*, 37(3):453–474, September 2019. Publisher: Elsevier.

[4] Jamie S. McPhee, David P. French, Dean Jackson, James Nazroo, Neil Pendleton, and Hans Degens. Physical activity in older age: perspectives for healthy ageing and frailty. *Biogerontology*, 17:567–580, 2016.

[5] Ian Janssen. Evolution of sarcopenia research. *Applied Physiology, Nutrition, and Metabolism = Physiologie Appliquee, Nutrition Et Metabolisme*, 35(5):707–712, October 2010.

[6] Luigi Ferrucci, Morgan E. Levine, Pei-Lun Kuo, and Eleanor M. Simonsick. Time and the Metrics of Aging. *Circulation Research*, 123(7):740–744, September 2018.

[7] World Health Organization. *International statistical classification of diseases and related health problems.* World Health Organization, 2015.

[8] Alfonso J Cruz-Jentoft, Gülistan Bahat, Jürgen Bauer, Yves Boirie, Olivier Bruyère, Tommy Cederholm, Cyrus Cooper, Francesco Landi, Yves Rolland, Avan Aihie Sayer, Stéphane M Schneider, Cornel C Sieber, Eva Topinkova, Maurits Vandewoude, Marjolein Visser, and Mauro Zamboni. Sarcopenia: revised European consensus on definition and diagnosis. *Age and Ageing*, 48(1):16–31, January 2019.

[9] R. Habenicht, G. Ebenbichler, P. Bonato, J. Kollmitzer, S. Ziegelbecker, L. Unterlerchner, P. Mair, and T. Kienbacher. Age-specific differences in the time-frequency representation of surface electromyographic data recorded during a submaximal cyclic back extension exercise: a promising biomarker to detect early signs of sarcopenia. *Journal of Neuroengineering and Rehabilitation*, 17(1):8, January 2020.

[10] Loubna Imrani, Sofiane Boudaoud, Jeremy Laforet, and Kiyoka Kinugawa. Ageing effect evaluation on HD-sEMG signals using CCA approach. *IRBM*, 42, May 2021.

[11] Vincent Carriou, Sofiane Boudaoud, and Jeremy Laforet. Speedup computation of HD-sEMG signals using a motor unit-specific electrical source model. *Medical & Biological Engineering & Computing*, 56(8):1459–1473, August 2018.

[12] L. M. Verbrugge and A. M. Jette. The disablement process. *Social Science & Medicine (1982)*, 38(1):1–14, January 1994.

[13] S. M. S. Samarakoon, H M Chandola, and B. Ravishankar. Effect of dietary, social, and lifestyle determinants of accelerated aging and its common clinical presentation: A survey study. *Ayu*, 32(3):315–321, 2011.

[14] Laura A. Bardon, Clare A. Corish, Meabh Lane, Maria Gabriella Bizzaro, Katherine Loayza Villarroel, Michelle Clarke, Lauren C. Power, Eileen R. Gibney, and Patricia Dominguez Castro. Ageing rate of older adults affects the factors associated with, and the determinants of malnutrition in the community: a systematic review and narrative synthesis. *BMC Geriatrics*, 21(1):676, December 2021.

[15] J. P. Michel, C. Dreux, and A. Vacheron. Healthy ageing: Evidence that improvement is possible at every age. *European Geriatric Medicine*, 7(4):298–305, July 2016.

[16] Matteo Cesari, Antonio Cherubini, Jack M. Guralnik, Ariel Beresniak, Leocadio Rodriguez-Mañas, Marco Inzitari, and Jeremy Walston. Early detection of accelerated aging and cellular decline (AACD): A consensus statement. *Experimental Gerontology*, 146:111242, April 2021.

[17] Sandra Rodríguez-Rodero, Juan Luis Fernández-Morera, Edelmiro Menéndez-Torre, Vincenzo Calvanese, Agustín F. Fernández, and Mario F. Fraga. Aging Genetics and Aging. *Aging and Disease*, 2(3):186–195, April 2011.

[18] D. Melzer, L. Pilling, and L. Ferrucci. The genetics of human ageing. *Nature Reviews Genetics*, 2019.

[19] Joris Deelen. Searching for the genetic key to a long and healthy life. *eLife*, 9:e57242, April 2020. Publisher: eLife Sciences Publications, Ltd.

[20] Paul R. H. J. Timmers, Evgeny S. Tiys, Saori Sakaue, Masato Akiyama, Tuomo T. J. Kiiskinen, Wei Zhou, Shih-Jen Hwang, Chen Yao, Joris Deelen, Daniel Levy, Andrea Ganna, Yoichiro Kamatani, Yukinori Okada, Peter K. Joshi, James F. Wilson, and Yakov A. Tsepilov. Mendelian randomization of genetically independent aging phenotypes identifies LPA and VCAM1 as biological targets for human aging. *Nature Aging*, 2(1):19–30, January 2022. Number: 1 Publisher: Nature Publishing Group.

[21] Lídia Sànchez-Riera and Nicholas Wilson. Fragility Fractures & Their Impact on Older People. *Best Practice & Research Clinical Rheumatology*, 31(2):169–191, April 2017.

[22] Andrew J. Milat, Wendy L. Watson, Claire Monger, Margo Barr, Michael Giffin, and Michael Reid. Prevalence, circumstances and consequences of falls among community-dwelling older people: results of the 2009 NSW Falls Prevention Baseline Survey. *New South Wales Public Health Bulletin*, 22(3-4):43–48, June 2011.

[23] Y. Rolland, S. Czerwinski, G. Abellan van Kan, J. E. Morley, M. Cesari, G. Onder, J. Woo, R. Baumgartner, F. Pillard, Y. Boirie, W. M. C. Chumlea, and B. Vellas.

Sarcopenia: Its assessment, etiology, pathogenesis, consequences and future perspectives. *The Journal of Nutrition Health and Aging*, 12(7):433–450, September 2008.

[24] Walter R. Frontera and Julien Ochala. Skeletal Muscle: A Brief Review of Structure and Function. *Calcified Tissue International*, 96(3):183–195, March 2015.

[25] Alastair Khodabukus. Tissue-Engineered Skeletal Muscle Models to Study Muscle Function, Plasticity, and Disease. *Frontiers in Physiology*, 12, 2021.

[26] Fabio Demontis, Rosanna Piccirillo, Alfred L. Goldberg, and Norbert Perrimon. Mechanisms of skeletal muscle aging: insights from Drosophila and mammalian models. *Disease Models & Mechanisms*, 6(6):1339–1352, November 2013.

[27] Wayne Scott, Jennifer Stevens-Lapsley, and Stuart Binder-Macleod. Human Skeletal Muscle Fiber Type Classifications. *Physical therapy*, 81:1810–6, December 2001.

[28] Michael Bárány. ATPase Activity of Myosin Correlated with Speed of Muscle Shortening. *The Journal of General Physiology*, 50(6):197–218, July 1967.

[29] D. Pette, H. Peuker, and R. S. Staron. The impact of biochemical methods for single muscle fibre analysis. *Acta Physiologica Scandinavica*, 166(4):261–277, August 1999.

[30] Harald Vikne, Vegard Strøm, Are Hugo Pripp, and Terje Gjøvaag. Human skeletal muscle fiber type percentage and area after reduced muscle use: A systematic review and meta-analysis. *Scandinavian Journal of Medicine & Science in Sports*, 30(8):1298–1317, 2020. _eprint: https://onlinelibrary.wiley.com/doi/pdf/10.1111/sms.13675.

[31] Lee Nowak and Patricio Reyes. Muscle Biopsy: A Diagnostic Tool in Muscle Diseases. *Journal of Histotechnology*, 31, September 2008.

[32] Nicolas Stifani. Motor neurons and the generation of spinal motor neurons diversity. *Frontiers in Cellular Neuroscience*, 8, 2014.

[33] L Larsson and G Salviati. Effects of age on calcium transport activity of sarcoplasmic reticulum in fast- and slow-twitch rat muscle fibres. *The Journal of Physiology*, 419:253–264, December 1989.

[34] Pedro M. Rodríguez Cruz, Judith Cossins, David Beeson, and Angela Vincent. The Neuromuscular Junction in Health and Disease: Molecular Mechanisms Governing Synaptic Formation and Homeostasis. *Frontiers in Molecular Neuroscience*, 13, 2020.

[35] P van Mier and JW Lichtman. Regenerating muscle fibers induce directional sprouting from nearby nerve terminals: studies in living mice. *The Journal of Neuroscience*, 14(9):5672–5686, September 1994.

[36] Lionel A. Tintignac, Hans-Rudolf Brenner, and Markus A. Rüegg. Mechanisms Regulating Neuromuscular Junction Development and Function and Causes of Muscle Wasting. *Physiological Reviews*, 95(3):809–852, July 2015. Publisher: American Physiological Society.

[37] Dario Farina, Francesco Negro, Marco Gazzoni, and Roger M. Enoka. Detecting the Unique Representation of Motor-Unit Action Potentials in the Surface Electromyogram. *Journal of Neurophysiology*, 100(3):1223–1233, September 2008.

[38] Tamás Kapelner, Ning Jiang, Aleš Holobar, Ivan Vujaklija, Aidan D. Roche, Dario Farina, and Oskar C. Aszmann. Motor Unit Characteristics after Targeted Muscle Reinnervation. *PLOS ONE*, 11(2):e0149772, February 2016. Publisher: Public Library of Science.

[39] Matthew G. Birkbeck, Linda Heskamp, Ian S. Schofield, Andrew M. Blamire, and Roger G. Whittaker. Non-invasive imaging of single human motor units. *Clinical Neurophysiology*, 131(6):1399–1406, June 2020.

[40] Fritz Buchthal, Franuesco Erminio, and Poul Rosenfalck. Motor Unit Territory in Different Human Muscles. *Acta Physiologica Scandinavica*, 45(1):72–87, 1959. _eprint: https://onlinelibrary.wiley.com/doi/pdf/10.1111/j.1748-1716.1959.tb01678.x.

[41] Todor I. Arabadzhiev, Vladimir G. Dimitrov, Nonna A. Dimitrova, and George V. Dimitrov. Influence of motor unit synchronization on amplitude characteristics of surface and intramuscularly recorded EMG signals. *European Journal of Applied Physiology*, 108(2):227, September 2009.

[42] L Edström and L Larsson. Effects of age on contractile and enzyme-histochemical properties of fast- and slow-twitch single motor units in the rat. *The Journal of Physiology*, 392:129–145, November 1987.

[43] Elwood Henneman, George Somjen, and David O. Carpenter. Functional significance of cell size in spinal motoneurons. *Journal of Neurophysiology*, 28(3):560–580, May 1965. Publisher: American Physiological Society.

[44] A. J. Fuglevand, D. A. Winter, and A. E. Patla. Models of recruitment and rate coding organization in motor-unit pools. *Journal of Neurophysiology*, 70(6):2470–2488, December 1993.

[45] H. Lee Sweeney and David W. Hammers. Muscle Contraction. *Cold Spring Harbor Perspectives in Biology*, 10(2):a023200, January 2018. Company: Cold Spring Harbor Laboratory Press Distributor: Cold Spring Harbor Laboratory Press Institution: Cold Spring Harbor Laboratory Press Label: Cold Spring Harbor Laboratory Press Publisher: Cold Spring Harbor Lab.

[46] Nicholas Sperelakis, Judith Heiny, and Hugo Gonzalez-Serratos. Chapter 42 - Skeletal Muscle Excitability. In Nicholas Sperelakis, editor, *Cell Physiology Source Book (Fourth Edition)*, pages 729–756. Academic Press, San Diego, January 2012.

[47] H. E. Huxley. The Double Array of Filaments in Cross-Striated Muscle. *The Journal of Biophysical and Biochemical Cytology*, 3(5):631–648, 1957.

[48] Pietro Montesano, Stefano Palermi, Bruno Massa, and Filomena Mazzeo. From “sliding” to “winding” filaments theory: A narrative review of mechanisms behind skeletal muscle contraction. *Journal of Human Sport and Exercise*, 15(Extra 3):806–814, 2020.

[49] Lars Larsson, Hans Degens, Meishan Li, Leonardo Salviati, Young il Lee, Wesley Thompson, James L. Kirkland, and Marco Sandri. Sarcopenia: Aging-Related Loss of Muscle Mass and Function. *Physiological Reviews*, 99(1):427–511, January 2019. Publisher: American Physiological Society.

[50] D. J. Wilkinson, M. Piasecki, and P. J. Atherton. The age-related loss of skeletal muscle mass and function: Measurement and physiology of muscle fibre atrophy and muscle fibre loss in humans. *Ageing Research Reviews*, 47:123–132, November 2018.

[51] Gregory D. Cartee, Russell T. Hepple, Marcas M. Bamman, and Juleen R. Zierath. Exercise Promotes Healthy Aging of Skeletal Muscle. *Cell metabolism*, 23(6):1034–1047, June 2016.

[52] Scott Trappe, David Williamson, and Michael Godard. Maintenance of Whole Muscle Strength and Size Following Resistance Training in Older Men. *The Journals of Gerontology: Series A*, 57(4):B138–B143, April 2002.

[53] Evelien Gielen, David Beckwée, Andreas Delaere, Sandra De Breucker, Maurits Vandewoude, Ivan Bautmans, and the Sarcopenia Guidelines Development Group of the Belgian Society of Gerontology and Geriatrics (BSGG). Nutritional interventions to improve muscle mass, muscle strength, and physical performance in older people: an umbrella review of systematic reviews and meta-analyses. *Nutrition Reviews*, 79(2):121–147, January 2021.

[54] C. Scott Bickel, James M. Cross, and Marcas M. Bamman. Exercise dosing to retain resistance training adaptations in young and older adults. *Medicine and Science in Sports and Exercise*, 43(7):1177–1187, July 2011.

[55] Siân Robinson, Cyrus Cooper, and Avan Aihie Sayer. Nutrition and Sarcopenia: A Review of the Evidence and Implications for Preventive Strategies. *Journal of Aging Research*, 2012:e510801, March 2012. Publisher: Hindawi.

[56] A. Mithal, J.-P. Bonjour, S. Boonen, P. Burckhardt, H. Degens, G. El Hajj Fuleihan, R. Josse, P. Lips, J. Morales Torres, R. Rizzoli, N. Yoshimura, D. A. Wahl, C. Cooper, B. Dawson-Hughes, and for the IOF CSA Nutrition Working Group. Impact of nutrition on muscle mass, strength, and performance in older adults. *Osteoporosis International*, 24(5):1555–1566, May 2013.

[57] Rita Rastogi Kalyani, Mark Corriere, and Luigi Ferrucci. Age-related and disease-related muscle loss: the effect of diabetes, obesity, and other diseases. *The lancet. Diabetes & endocrinology*, 2(10):819–829, October 2014.

[58] Peter Francis, Mark Lyons, Mathew Piasecki, Jamie Mc Phee, Karen Hind, and Philip Jakeman. Measurement of muscle health in aging. *Biogerontology*, 18(6):901–911, December 2017.

[59] Analiza M. Silva, Wei Shen, Moonseong Heo, Dympna Gallagher, Zimian Wang, Luis B. Sardinha, and Steven B. Heymsfield. Ethnicity-Related Skeletal Muscle Differences Across the Lifespan. *American journal of human biology : the official journal of the Human Biology Council*, 22(1):76–82, 2010.

[60] D. Gallagher and S. B. Heymsfield. Muscle distribution: variations with body weight, gender, and age. *Applied Radiation and Isotopes: Including Data, Instrumentation and Methods for Use in Agriculture, Industry and Medicine*, 49(5-6):733–734, June 1998.

[61] Ian Janssen, Steven B. Heymsfield, ZiMian Wang, and Robert Ross. Skeletal muscle mass and distribution in 468 men and women aged 18–88 yr. *Journal of Applied Physiology*, 89(1):81–88, July 2000. Publisher: American Physiological Society.

[62] M. E. Sehl. Senescence, frailty and mortality: mathematical models of aging. *Medicine and Health, Rhode Island*, 84(11):360–364, November 2001.

[63] W. Kyle Mitchell, John Williams, Philip Atherton, Mike Larvin, John Lund, and Marco Narici. Sarcopenia, Dynapenia, and the Impact of Advancing Age on Human Skeletal Muscle Size and Strength; a Quantitative Review. *Frontiers in Physiology*, 3:260, July 2012.

[64] Jan Lexell, Charles C. Taylor, and Michael Sjöström. What is the cause of the ageing atrophy?: Total number, size and proportion of different fiber types studied in whole vastus lateralis muscle from 15- to 83-year-old men. *Journal of the Neurological Sciences*, 84(2):275–294, April 1988.

[65] William J. Evans and Ben F. Hurley. Age, Gender, and Muscular Strength. *The Journals of Gerontology: Series A*, 50A(Special_Issue):41–44, November 1995.

[66] E.M.K. Haynes, N.A. Neubauer, K.M.D. Cornett, B.P. O'Connor, G.R. Jones, and J.M. Jakobi. Age and sex-related decline of muscle strength across the adult lifespan: a scoping review of aggregated data. *Applied Physiology, Nutrition, and Metabolism*, 45(11):1185–1196, November 2020. Publisher: NRC Research Press.

[67] R. S. Lindle, E. J. Metter, N. A. Lynch, J. L. Fleg, J. L. Fozard, J. Tobin, T. A. Roy, and B. F. Hurley. Age and gender comparisons of muscle strength in 654 women and men aged 20–93 yr. *Journal of Applied Physiology*, 83(5):1581–1587, November 1997. Publisher: American Physiological Society.

[68] Marjolein Visser, Bret H. Goodpaster, Stephen B. Kritchevsky, Anne B. Newman, Michael Nevitt, Susan M. Rubin, Eleanor M. Simonsick, Tamara B. Harris, and for the Health ABC Study. Muscle Mass, Muscle Strength, and Muscle Fat Infiltration as Predictors of Incident Mobility Limitations in Well-Functioning Older Persons. *The Journals of Gerontology: Series A*, 60(3):324–333, March 2005.

[69] Annemarie Koster, Jingzhong Ding, Sari Stenholm, Paolo Caserotti, Denise K. Houston, Barbara J. Nicklas, Tongjian You, Jung Sun Lee, Marjolein Visser, Anne B. Newman, Ann V. Schwartz, Jane A. Cauley, Frances A. Tylavsky, Bret H. Goodpaster, Stephen B. Kritchevsky, Tamara B. Harris, and for the Health ABC study. Does the Amount of Fat Mass Predict Age-Related Loss of Lean Mass, Muscle Strength, and Muscle Quality in Older Adults? *The Journals of Gerontology: Series A*, 66A(8):888–895, August 2011.

[70] Serge Beliaeff, Danielle Bouchard, Christophe Hautier, Martin Brochu, and Isabelle Dionne. Association Between Muscle Mass and Isometric Muscle Strength in Well-Functioning Older Men and Women. *Journal of aging and physical activity*, 16:484–93, November 2008.

[71] Fennigje M. Purves-Smith, Nicolas Sgarioto, and Russell T. Hepple. Fiber Typing in Aging Muscle. *Exercise and Sport Sciences Reviews*, 42(2):45–52, April 2014.

[72] J. Lexell and D. Y. Downham. The occurrence of fibre-type grouping in healthy human muscle: a quantitative study of cross-sections of whole vastus lateralis from men between 15 and 83 years. *Acta Neuropathologica*, 81(4):377–381, 1991.

[73] Marco V. Narici and Nicola Maffulli. Sarcopenia: characteristics, mechanisms and functional significance. *British Medical Bulletin*, 95(1):139–159, September 2010.

[74] Rachel Nilwik, Tim Snijders, Marika Leenders, Bart B. L. Groen, Janneau van Kranenburg, Lex B. Verdijk, and Luc J. C. van Loon. The decline in skeletal muscle mass with aging is mainly attributed to a reduction in type II muscle fiber size. *Experimental Gerontology*, 48(5):492–498, May 2013.

[75] Laurence Z. Rubenstein. Falls in older people: epidemiology, risk factors and strategies for prevention. *Age and Ageing*, 35(suppl_2):ii37–ii41, September 2006.

[76] Ana Mattiello-Sverzut, Leila Chimelli, Maria Sílvia de Assis Moura, Silvia Teixeira, and José Oliveira. The effects of aging on biceps brachii muscle fibers - A morphometrical study from biopsies and autopsies. *Arquivos de neuro-psiquiatria*, 61:555–60, October 2003.

[77] S. Kirkeby and C. Garbarsch. Aging affects different human muscles in various ways. An image analysis of the histomorphometric characteristics of fiber types in human masseter and vastus lateralis muscles from young adults and the very old. *Histology and Histopathology*, 15(1):61–71, January 2000.

[78] Cliff S. Klein, Greg D. Marsh, Robert J. Petrella, and Charles L. Rice. Muscle fiber number in the biceps brachii muscle of young and old men. *Muscle & Nerve*, 28(1):62–68, 2003.

[79] M Monemi, P. O Eriksson, A Eriksson, and L. E Thornell. Adverse changes in fibre type composition of the human masseter versus biceps brachii muscle during aging. *Journal of the Neurological Sciences*, 154(1):35–48, January 1998.

[80] P. O. Eriksson, A. Eriksson, M. Ringqvist, and L. E. Thornell. Histochemical fibre composition of the human digastric muscle. *Archives of Oral Biology*, 27(3):207–215, 1982.

[81] E. Nygaard and J. Sanchez. Intramuscular variation of fiber types in the brachial biceps and the lateral vastus muscles of elderly men: how representative is a small biopsy sample? *The Anatomical Record*, 203(4):451–459, August 1982.

[82] J. Lexell, K. Henriksson-Larsén, B. Winblad, and M. Sjöström. Distribution of different fiber types in human skeletal muscles: effects of aging studied in whole muscle cross sections. *Muscle & Nerve*, 6(8):588–595, October 1983.

[83] T. Lang, T. Streeper, P. Cawthon, K. Baldwin, D. R. Taaffe, and T. B. Harris. Sarcopenia: etiology, clinical consequences, intervention, and assessment. *Osteoporosis International*, 21(4):543–559, 2010.

[84] F. G. I. Jennekens, B. E. Tomlinson, and J. N. Walton. Histochemical aspects of five limb muscles in old age An autopsy study. *Journal of the Neurological Sciences*, 14(3):259–276, November 1971. Publisher: Elsevier.

[85] Dirk Pette and Robert Staron. Myosin isoforms, muscle fiber types, and transitions. *Microscopy research and technique*, 50:500–9, September 2000.

[86] Russell T. Hepple and Charles L. Rice. Innervation and neuromuscular control in ageing skeletal muscle. *The Journal of Physiology*, 594(8):1965–1978, April 2016.

[87] Peter Höök, Xiaopeng Li, John Sleep, Simon Hughes, and Lars Larsson. In vitro motility speed of slow myosin extracted from single soleus fibres from young and old rats. *The Journal of Physiology*, 520(Pt 2):463–471, October 1999.

[88] Giuseppe D'Antona, Maria Antonietta Pellegrino, Raffaella Adami, Rosetta Rossi, Carmine Naccari Carlizzi, Monica Canepari, Bengt Saltin, and Roberto Bottinelli. The effect of ageing and immobilization on structure and function of human skeletal muscle fibres. *The Journal of Physiology*, 552(Pt 2):499–511, October 2003.

[89] Lisa S. Krivickas, Dongwon Suh, John Wilkins, Virginia A. Hughes, Ronenn Roubenoff, and Walter R. Frontera. Age- and Gender-Related Differences in Maximum Shortening Velocity of Skeletal Muscle Fibers. *American Journal of Physical Medicine & Rehabilitation*, 80(6):447–455, June 2001.

[90] M. Fragala, A. Kenny, and G. Kuchel. Muscle Quality in Aging: a Multi-Dimensional Approach to Muscle Functioning with Applications for Treatment. *Sports Medicine*, 2015.

[91] Jamie S. McPhee, Jean-Yves Hogrel, Andrea B. Maier, Enn Seppet, Olivier R. Seynnes, Sarianna Sipilä, Roberto Bottinelli, Yoann Barnouin, Astrid Y. Bijlsma, Helena Gapeyeva, Thomas M. Maden-Wilkinson, Carel G. Meskers, Mati Pääsuke, Elina Sillanpää, Lauri Stenroth, Gillian Butler-Browne, Marco V. Narici, and David A. Jones. Physiological and functional evaluation of healthy young and older men and women: design of the European MyoAge study. *Biogerontology*, 14(3):325–337, June 2013.

[92] Tom Maden-Wilkinson, Jamie Mcphee, David Jones, and Hans Degens. Age Related Loss of Muscle Mass, Strength and Power and their Association With Mobility in Recreationally Active UK Older Adults. *Journal of aging and physical activity*, 23, July 2014.

[93] Lauri Stenroth, Elina Sillanpää, Jamie S. McPhee, Marco V. Narici, Helena Gapeyeva, Mati Pääsuke, Yoann Barnouin, Jean-Yves Hogrel, Gillian Butler-Browne, Astrid Bijlsma, Carel G. M. Meskers, Andrea B. Maier, Taija Finni, and Sarianna Sipilä. Plantarflexor Muscle–Tendon Properties are Associated With Mobility in Healthy Older Adults. *The Journals of Gerontology: Series A*, 70(8):996–1002, August 2015.

[94] M. J. Campbell, A. J. McComas, and F. Petito. Physiological changes in ageing muscles. *Journal of Neurology, Neurosurgery, and Psychiatry*, 36(2):174–182, April 1973.

[95] B. E. Tomlinson and Dorothy Irving. The numbers of limb motor neurons in the human lumbosacral cord throughout life. *Journal of the Neurological Sciences*, 34(2):213–219, November 1977.

[96] Kenichiro Oda. Age changes of motor innervation and acetylcholine receptor distribution on human skeletal muscle fibres. *Journal of the Neurological Sciences*, 66(2):327–338, November 1984.

[97] Mathew Piasecki, Alex Ireland, David Jones, and Jamie Mcphee. Age-dependent motor unit remodelling in human limb muscles. *Biogerontology*, 17, June 2016.

[98] Jasper R. Daube. Motor unit number estimates—From A to Z. *Journal of the Neurological Sciences*, 242(1):23–35, March 2006. Publisher: Elsevier.

[99] Clifton L. Gooch, Timothy J. Doherty, K. Ming Chan, Mark B. Bromberg, Richard A. Lewis, Dan W. Stashuk, Michael J. Berger, Michael T. Andary, and Jasper R. Daube. Motor unit number estimation: a technology and literature review. *Muscle & Nerve*, 50(6):884–893, December 2014.

[100] Chris J. McNeil, Timothy J. Doherty, Daniel W. Stashuk, and Charles L. Rice. Motor unit number estimates in the tibialis anterior muscle of young, old, and very old men. *Muscle & Nerve*, 31(4):461–467, 2005. _eprint: https://onlinelibrary.wiley.com/doi/pdf/10.1002/mus.20276.

[101] Chris J. McNeil and Charles L. Rice. Neuromuscular adaptations to healthy aging. *Applied Physiology, Nutrition, and Metabolism*, 43(11):1158–1165, November 2018. Publisher: NRC Research Press.

[102] M. Piasecki, A. Ireland, J. Piasecki, D. W. Stashuk, A. Swiecicka, M. K. Rutter, D. A. Jones, and J. S. McPhee. Failure to expand the motor unit size to compensate for declining motor unit numbers distinguishes sarcopenic from non sarcopenic older men. *The Journal of Physiology*, 596(9):1627–1637, May 2018.

[103] TM Manini, SL Hong, and BC Clark. Aging and muscle: a neuron's perspective. *Current opinion in clinical nutrition and metabolic care*, 16(1):10.1097/MCO.0b013e32835b5880, January 2013.

[104] Martin V. Sale and John G. Semmler. Age-related differences in corticospinal control during functional isometric contractions in left and right hands. *Journal of Applied Physiology*, 99(4):1483–1493, October 2005. Publisher: American Physiological Society.

[105] Geoffrey A. Power, Brian H. Dalton, and Charles L. Rice. Human neuromuscular structure and function in old age: A brief review. *Journal of sport and health science*, 2(4):215–226, December 2013.

[106] G. Scaglioni, A. Ferri, A. E. Minetti, A. Martin, J. Van Hoecke, P. Capodaglio, A. Sartorio, and M. V. Narici. Plantar flexor activation capacity and H reflex in older adults: adaptations to strength training. *Journal of Applied Physiology*, 92(6):2292–2302, June 2002. Publisher: American Physiological Society.

[107] V. Ramírez and B. Ulfhake. Anatomy of dendrites in motoneurons supplying the intrinsic muscles of the foot sole in the aged cat: Evidence for dendritic growth and neo-synaptogenesis. *Journal of Comparative Neurology*, 316(1):1–16, 1992. _eprint: https://onlinelibrary.wiley.com/doi/pdf/10.1002/cne.903160102.

[108] Susanna Kullberg, Vania Ramírez-León, Hans Johnson, and Brun Ulfhake. Decreased Axosomatic Input to Motoneurons and Astrogliosis in the Spinal Cord of Aged Rats. *The Journals of Gerontology: Series A*, 53A(5):B369–B379, September 1998.

[109] Tessa Gordon, Janka Hegedus, and Siu Lin Tam. Adaptive and maladaptive motor axonal sprouting in aging and motoneuron disease. *Neurological Research*, 26(2):174–185, March 2004. Publisher: Taylor & Francis _eprint: https://doi.org/10.1179/016164104225013806.

[110] Jacques Duchateau and Stéphane Baudry. Maximal discharge rate of motor units determines the maximal rate of force development during ballistic contractions in human. *Frontiers in Human Neuroscience*, 8:234, April 2014.

[111] S. D. Harridge, A. Kryger, and A. Stensgaard. Knee extensor strength, activation, and size in very elderly people following strength training. *Muscle & Nerve*, 22(7):831–839, July 1999.

[112] Jennifer E. Stevens, Scott K. Stackhouse, Stuart A. Binder-Macleod, and Lynn Snyder-Mackler. Are voluntary muscle activation deficits in older adults meaningful? *Muscle & Nerve*, 27(1):99–101, January 2003.

[113] Anita Christie and Gary Kamen. Doublet Discharges in Motoneurons of Young and Older Adults. *Journal of Neurophysiology*, 95(5):2787–2795, May 2006. Publisher: American Physiological Society.

[114] Gary Kamen. Aging, resistance training, and motor unit discharge behavior. *Canadian Journal of Applied Physiology = Revue Canadienne De Physiologie Appliquee*, 30(3):341–351, June 2005.

[115] R. M. Girts, J. A. Mota, K. K. Harmon, R. J. MacLennan, and Matt S. Stock. Vastus Lateralis Motor Unit Recruitment Thresholds are Compressed Towards Lower Forces in Older Men. *The Journal of Frailty & Aging*, 9(4):191–196, October 2020.

[116] K. Häkkinen and A. Häkkinen. Neuromuscular adaptations during intensive strength training in middle-aged and elderly males and females. *Electromyography and Clinical Neurophysiology*, 35(3):137–147, May 1995.

[117] Zeynep Erim, M. Faisal Beg, David T. Burke, and Carlo J. de Luca. Effects of Aging on Motor-Unit Control Properties. *Journal of Neurophysiology*, 82(5):2081–2091, November 1999. Publisher: American Physiological Society.

[118] Scott Rubinstein and Gary Kamen. Decreases in motor unit firing rate during sustained maximal-effort contractions in young and older adults. *Journal of Electromyography and Kinesiology*, 15(6):536–543, December 2005.

[119] Raja Dahmane, Srdjan Djordjevič, Bostjan Šimunič, and Vojko Valenčič. Spatial fiber type distribution in normal human muscle: Histochemical and tensiomyographical evaluation. *Journal of Biomechanics*, 38(12):2451–2459, December 2005.

[120] Chet T. Moritz, Benjamin K. Barry, Michael A. Pascoe, and Roger M. Enoka. Discharge Rate Variability Influences the Variation in Force Fluctuations Across the Working Range of a Hand Muscle. *Journal of Neurophysiology*, 93(5):2449–2459, May 2005. Publisher: American Physiological Society.

[121] Brian L. Tracy, Katrina S. Maluf, Jennifer L. Stephenson, Sandra K. Hunter, and Roger M. Enoka. Variability of motor unit discharge and force fluctuations across a range of muscle forces in older adults. *Muscle & Nerve*, 32(4):533–540, 2005. _eprint: https://onlinelibrary.wiley.com/doi/pdf/10.1002/mus.20392.

[122] Odessa Addison, Robin L. Marcus, Paul C. LaStayo, and Alice S. Ryan. Intermuscular Fat: A Review of the Consequences and Causes. *International Journal of Endocrinology*, 2014:e309570, January 2014. Publisher: Hindawi.

[123] Robin A McGregor, David Cameron-Smith, and Sally D Poppitt. It is not just muscle mass: a review of muscle quality, composition and metabolism during ageing as determinants of muscle function and mobility in later life. *Longevity & Healthspan*, 3:9, December 2014.

[124] Hadi Rahemi, Nilima Nigam, and James M. Wakeling. The effect of intramuscular fat on skeletal muscle mechanics: implications for the elderly and obese. *Journal of the Royal Society Interface*, 12(109):20150365, August 2015.

[125] Yoshihiro Fukumoto, Tome Ikezoe, Yosuke Yamada, Rui Tsukagoshi, Masatoshi Nakamura, Yui Takagi, Misaka Kimura, and Noriaki Ichihashi. Age-Related ultrasound changes in muscle quantity and quality in women. *Ultrasound in Medicine and Biology*, 41(11):3013–3017, November 2015. Accepted: 2018-05-25T00:45:25Z Publisher: Elsevier USA.

[126] Dennis Taaffe, Tim Henwood, Michael Nalls, Duncan Walker, Thomas Lang, and Tamara Harris. Alterations in Muscle Attenuation following Detraining and Retraining in Resistance-Trained Older Adults. *Gerontology*, 55:217–23, March 2009.

[127] J E Morley. Anorexia of aging: physiologic and pathologic. *The American Journal of Clinical Nutrition*, 66(4):760–773, October 1997.

[128] R. Roubenoff. Sarcopenia and its implications for the elderly. *European Journal of Clinical Nutrition*, 54(3):S40–S47, June 2000. Number: 3 Publisher: Nature Publishing Group.

[129] Hayley J Denison, Cyrus Cooper, Avan Aihie Sayer, and Sian M Robinson. Prevention and optimal management of sarcopenia: a review of combined exercise and nutrition interventions to improve muscle outcomes in older people. *Clinical Interventions in Aging*, 10:859–869, May 2015.

[130] Oliver Chaudry, Andreas Friedberger, Alexandra Grimm, Michael Uder, Armin Michael Nagel, Wolfgang Kemmler, and Klaus Engelke. Segmentation of the fascia lata and reproducible quantification of intermuscular adipose tissue (IMAT)

of the thigh. *Magnetic Resonance Materials in Physics, Biology and Medicine*, 34(3):367–376, June 2021.

[131] Irwin H. Rosenberg. Sarcopenia: Origins and Clinical Relevance. *The Journal of Nutrition*, 127(5):990S–991S, May 1997.

[132] Alfonso J. Cruz-Jentoft, Jean Pierre Baeyens, Jürgen M. Bauer, Yves Boirie, Tommy Cederholm, Francesco Landi, Finbarr C. Martin, Jean-Pierre Michel, Yves Rolland, Stéphane M. Schneider, Eva Topinková, Maurits Vandewoude, and Mauro Zamboni. Sarcopenia: European consensus on definition and diagnosis. *Age and Ageing*, 39(4):412–423, July 2010.

[133] IWGS. Sarcopenia: An Undiagnosed Condition in Older Adults. Current Consensus Definition: Prevalence, Etiology, and Consequences. *Journal of the American Medical Directors Association*, 12(4):249–256, May 2011.

[134] John E. Morley, Angela Marie Abbatecola, Josep M. Argiles, Vickie Baracos, Juergen Bauer, Shalender Bhasin, Tommy Cederholm, Andrew J. Stewart Coats, Steven R. Cummings, William J. Evans, Kenneth Fearon, Luigi Ferrucci, Roger A. Fielding, Jack M. Guralnik, Tamara B. Harris, Akio Inui, Kamyar Kalantar-Zadeh, Bridget-Anne Kirwan, Giovanni Mantovani, Maurizio Muscaritoli, Anne B. Newman, Filippo Rossi-Fanelli, Giuseppe M. C. Rosano, Ronenn Roubenoff, Morris Schambelan, Gerald H. Sokol, Thomas W. Storer, Bruno Vellas, Stephan von Haehling, Shing-Shing Yeh, and Stefan D. Anker. Sarcopenia With Limited Mobility: An International Consensus. *Journal of the American Medical Directors Association*, 12(6):403–409, July 2011.

[135] Liang-Kung Chen, Li-Kuo Liu, Jean Woo, Prasert Assantachai, Tung-Wai Auyeung, Kamaruzzaman Shahrul Bahyah, Ming-Yueh Chou, Liang-Yu Chen, Pi-Shan Hsu, Orapitchaya Krairit, Jenny S. W. Lee, Wei-Ju Lee, Yunhwan Lee, Chih-Kuang Liang, Panita Limpawattana, Chu-Sheng Lin, Li-Ning Peng, Shosuke Satake, Takao Suzuki, Chang Won Won, Chih-Hsing Wu, Si-Nan Wu, Teimei Zhang, Ping Zeng, Masahiro Akishita, and Hidenori Arai. Sarcopenia in Asia: Consensus Report of the Asian Working Group for Sarcopenia. *Journal of the American Medical Directors Association*, 15(2):95–101, February 2014. Publisher: Elsevier.

[136] Alfonso J. Cruz-Jentoft, Francesco Landi, Stéphane M. Schneider, Clemente Zúñiga, Hidenori Arai, Yves Boirie, Liang-Kung Chen, Roger A. Fielding, Finbarr C. Martin, Jean-Pierre Michel, Cornel Sieber, Jeffrey R. Stout, Stephanie A. Studenski, Bruno Vellas, Jean Woo, Mauro Zamboni, and Tommy Cederholm. Prevalence of and interventions for sarcopenia in ageing adults: a systematic review. Report of the International Sarcopenia Initiative (EWGSOP and IWGS). *Age and Ageing*, 43(6):748–759, November 2014.

[137] Valéria Pagotto and Erika Aparecida Silveira. Methods, Diagnostic Criteria, Cutoff Points, and Prevalence of Sarcopenia among Older People. *The Scientific World Journal*, 2014:231312, 2014.

[138] Hee-Kyung Chang, Ji-Yeon Lee, Cho-Rong Gil, and Mi-Kyoung Kim. Prevalence of Sarcopenia in Community-Dwelling Older Adults According to Simplified Algorithms for Sarcopenia Consensus Based on Asian Working Group for Sarcope-

nia</p>. *Clinical Interventions in Aging*, 15:2291–2299, December 2020. Publisher: Dove Press.

[139] Lara Bianchi, Pasquale Abete, Giuseppe Bellelli, Mario Bo, Antonio Cherubini, Francesco Corica, Mauro Di Bari, Marcello Maggio, Giovanna Maria Manca, Maria Rosaria Rizzo, Andrea P Rossi, Francesco Landi, Stefano Volpato, and for the GLISTEN Group Investigators. Prevalence and Clinical Correlates of Sarcopenia, Identified According to the EWGSOP Definition and Diagnostic Algorithm, in Hospitalized Older People: The GLISTEN Study. *The Journals of Gerontology: Series A*, 72(11):1575–1581, October 2017.

[140] Jacob Pacifico, Milou A. J. Geerlings, Esmee M. Reijnierse, Christina Phassouliotis, Wen Kwang Lim, and Andrea B. Maier. Prevalence of sarcopenia as a comorbid disease: A systematic review and meta-analysis. *Experimental Gerontology*, 131:110801, March 2020.

[141] Emanuela A. Greco, Peter Pietschmann, and Silvia Migliaccio. Osteoporosis and Sarcopenia Increase Frailty Syndrome in the Elderly. *Frontiers in Endocrinology*, 10:255, April 2019.

[142] Jack M. Guralnik, Eleanor M. Simonsick, Luigi Ferrucci, Robert J. Glynn, Lisa F. Berkman, Dan G. Blazer, Paul A. Scherr, and Robert B. Wallace. A Short Physical Performance Battery Assessing Lower Extremity Function: Association With Self-Reported Disability and Prediction of Mortality and Nursing Home Admission. *Journal of Gerontology*, 49(2):M85–M94, March 1994.

[143] Shumin Li, Hanyu Li, Ying Hu, Shaoming Zhu, Zherong Xu, Qin Zhang, Yunmei Yang, Zhaodi Wang, and Jia Xu. Ultrasound for Measuring the Cross-Sectional Area of Biceps Brachii Muscle in Sarcopenia. *International Journal of Medical Sciences*, 17(18):2947–2953, October 2020.

[144] B. C. Clark and T. M. Manini. Sarcopenia Vs Dynapenia. *The Journals of Gerontology Series A: Biological Sciences and Medical Sciences*, 63(8):829–834, August 2008.

[145] Virginia A. Hughes, Walter R. Frontera, Michael Wood, William J. Evans, Gerard E. Dallal, Ronenn Roubenoff, and Maria A. Fiatarone Singh. Longitudinal Muscle Strength Changes in Older Adults: Influence of Muscle Mass, Physical Activity, and Health. *The Journals of Gerontology: Series A*, 56(5):B209–B217, May 2001.

[146] Kuen-Cheh Yang, Yin-Yin Liao, Ke-Vin Chang, Kuo-Chin Huang, and Der-Sheng Han. The Quantitative Skeletal Muscle Ultrasonography in Elderly with Dynapenia but Not Sarcopenia Using Texture Analysis. *Diagnostics*, 10(6):400, June 2020. Number: 6 Publisher: Multidisciplinary Digital Publishing Institute.

[147] Jacob Bülow, Stanley J. Ulijaszek, and Lars Holm. Rejuvenation of the term sarcopenia. *Journal of Applied Physiology*, 126(1):255–256, January 2019. Publisher: American Physiological Society.

[148] Jüergen M. Bauer and John E. Morley. Editorial: Body composition measurements in older adults. *Current Opinion in Clinical Nutrition & Metabolic Care*, 23(1):1–3, January 2020.

[149] Carla MM Prado, Jessica R. Lieffers, Linda J. McCargar, Tony Reiman, Michael B. Sawyer, Lisa Martin, and Vickie E. Baracos. Prevalence and clinical implications of sarcopenic obesity in patients with solid tumours of the respiratory and gastrointestinal tracts: a population-based study. *The Lancet Oncology*, 9(7):629–635, July 2008. Publisher: Elsevier.

[150] Koeun Lee, Yongbin Shin, Jimi Huh, Yu Sub Sung, In-Seob Lee, Kwon-Ha Yoon, and Kyung Won Kim. Recent Issues on Body Composition Imaging for Sarcopenia Evaluation. *Korean Journal of Radiology*, 20(2):205–217, February 2019.

[151] Andrea Ticinesi, Tiziana Meschi, Marco V. Narici, Fulvio Lauretani, and Marcello Maggio. Muscle Ultrasound and Sarcopenia in Older Individuals: A Clinical Perspective. *Journal of the American Medical Directors Association*, 18(4):290–300, April 2017. Publisher: Elsevier.

[152] Bas Van Hooren, Panayiotis Teratsias, and Emma F. Hodson-Tole. Ultrasound imaging to assess skeletal muscle architecture during movements: a systematic review of methods, reliability, and challenges. *Journal of Applied Physiology*, 128(4):978–999, April 2020. Publisher: American Physiological Society.

[153] Robert D. Boutin, Lawrence Yao, Robert J. Canter, and Leon Lenchik. Sarcopenia: Current Concepts and Imaging Implications. *American Journal of Roentgenology*, 205(3):W255–W266, September 2015. Publisher: American Roentgen Ray Society.

[154] Mickael Tanter and Mathias Fink. Ultrafast imaging in biomedical ultrasound. *IEEE Transactions on Ultrasonics, Ferroelectrics, and Frequency Control*, 61(1):102–119, January 2014. Conference Name: IEEE Transactions on Ultrasonics, Ferroelectrics, and Frequency Control.

[155] Yan To Ling, Christina Zong-Hao Ma, Queenie Tsung Kwan Shea, and Yong-Ping Zheng. Sonomechanomyography (SMMG): Mapping of Skeletal Muscle Motion Onset during Contraction Using Ultrafast Ultrasound Imaging and Multiple Motion Sensors. *Sensors*, 20(19):5513, January 2020. Number: 19 Publisher: Multidisciplinary Digital Publishing Institute.

[156] Thomas Deffieux, Jean-Luc Gennisson, Mickaël Tanter, and Mathias Fink. Assessment of the mechanical properties of the musculoskeletal system using 2-D and 3-D very high frame rate ultrasound. *IEEE transactions on ultrasonics, ferroelectrics, and frequency control*, 55(10):2177–2190, October 2008.

[157] Robin Rohlén, Erik Stålberg, Karen-Helene Stöverud, Jun Yu, and Christer Grönlund. A Method for Identification of Mechanical Response of Motor Units in Skeletal Muscle Voluntary Contractions Using Ultrafast Ultrasound Imaging—Simulations and Experimental Tests. *IEEE Access*, 8:50299–50311, 2020. Conference Name: IEEE Access.

[158] Michael Peolsson, Tommy Löfstedt, Susanna Vogt, Hans Stenlund, Anton Arndt, and Johan Trygg. Modelling human musculoskeletal functional movements using ultrasound imaging. *BMC Medical Imaging*, 10:9, May 2010.

[159] Fanny Buckinx, Francesco Landi, Ricardo Cesari, Bruno Vellas, and John A. Kanis. Pitfalls in the measurement of muscle mass: a need for a reference standard. *Journal of Cachexia, Sarcopenia and Muscle*, 9(2):269–278, April 2018.

[160] Aldo Scafoglieri and Jan Pieter Clarys. Dual energy xray absorptiometry: gold standard for muscle mass? *Journal of Cachexia, Sarcopenia and Muscle*, 9(4):786–787, August 2018.

[161] Olivia Di Vincenzo, Maurizio Marra, and Luca Scalfi. Bioelectrical impedance phase angle in sport: a systematic review. *Journal of the International Society of Sports Nutrition*, 16(1):49, November 2019.

[162] Elsa Dent, Jean Woo, David Scott, and Emiel O. Hoogendijk. Sarcopenia measurement in research and clinical practice. *European Journal of Internal Medicine*, 90:1–9, August 2021.

[163] Hazel M. Clarkson. *Musculoskeletal Assessment: Joint Range of Motion and Manual Muscle Strength*. Lippincott Williams & Wilkins, 2000. Google-Books-ID: mrDPB1hEca0C.

[164] Masahiro Akishita, Koichi Kozaki, Katsuya Iijima, Tomoki Tanaka, Koji Shibasaki, Sumito Ogawa, and Hidenori Arai. Chapter 1 Definitions and diagnosis of sarcopenia. *Geriatrics & Gerontology International*, 18(S1):7–12, 2018. _eprint: https://onlinelibrary.wiley.com/doi/pdf/10.1111/ggi.13311.

[165] Donja M. Mijnarends, Judith M. M. Meijers, Ruud J. G. Halfens, Sovianne ter Borg, Yvette C. Luiking, Sjors Verlaan, Daniela Schoberer, Alfonso J. Cruz Jentoft, Luc J. C. van Loon, and Jos M. G. A. Schols. Validity and reliability of tools to measure muscle mass, strength, and physical performance in community-dwelling older people: a systematic review. *Journal of the American Medical Directors Association*, 14(3):170–178, March 2013.

[166] Andrea P. Rossi, Sofia Rubele, Alessia D'Introno, Elena Zoico, Piero Bradimarte, Giulia Amadio, Nicole Nori, Paola Gnerre, Gloria Mazzali, Francesco Fantin, and Mauro Zamboni. An update on methods for sarcopenia diagnosis: from bench to bedside. *Italian Journal of Medicine*, 12(2):97–107, June 2018. Number: 2.

[167] Ana Rita Sousa-Santos and Teresa F Amaral. Differences in handgrip strength protocols to identify sarcopenia and frailty - A systematic review. *BMC Geriatrics*, 17, October 2017.

[168] Melissa Benton, Jefferson Spicher, and Amy Silva-Smith. *Validity and Reliability of Handgrip Dynamometry in Older Adults: A Comparison of Two Widely Used Dynamometers*. May 2021.

[169] Masaru Higa, Nozomu Araki, Shintaro Nakatani, and Hideki Toji. Measurements of Isometric Strength and Electromyography of Elbow Flexors under Active and Passive Conditions. *Advanced Biomedical Engineering*, 8:124–129, May 2019.

[170] Tetsuya Kimura, Taku Hamada, Takeo Watanabe, Akifumi Maeda, Tomomichi Oya, and Toshio Moritani. Mechanomyographic responses in human biceps brachii and soleus during sustained isometric contraction. *European Journal of Applied Physiology*, 92(4):533–539, August 2004.

[171] Morufu Olusola Ibitoye, Nur Azah Hamzaid, Jorge M. Zuniga, and Ahmad Khairi Abdul Wahab. Mechanomyography and muscle function assessment: A review of current state and prospects. *Clinical Biomechanics*, 29(6):691–704, June 2014.

[172] Irsa Talib, Kenneth Sundaraj, Chee Kiang Lam, and Sebastian Sundaraj. A systematic review of muscle activity assessment of the biceps brachii muscle using mechanomyography. *Journal of Musculoskeletal & Neuronal Interactions*, 18(4):446–462, December 2018.

[173] Emiliano Cè, Susanna Rampichini, and Fabio Esposito. Novel insights into skeletal muscle function by mechanomyography: from the laboratory to the field. *Sport Sciences for Health*, 11(1):1–28, April 2015.

[174] Andrej Meglic, Mojca Uršič, Aleš Škorjanc, Srđan Đorđević, and Gregor Belušič. The Piezo-resistive MC Sensor is a Fast and Accurate Sensor for the Measurement of Mechanical Muscle Activity. *Sensors*, 19(9):2108, January 2019. Number: 9 Publisher: Multidisciplinary Digital Publishing Institute.

[175] L. Larsson, X. Li, and W. R. Frontera. Effects of aging on shortening velocity and myosin isoform composition in single human skeletal muscle cells. *American Journal of Physiology-Cell Physiology*, 272(2):C638–C649, February 1997. Publisher: American Physiological Society.

[176] Jae-Young Lim and Walter R. Frontera. Single skeletal muscle fiber mechanical properties: a muscle quality biomarker of human aging. *European Journal of Applied Physiology*, March 2022.

[177] Walter Frontera, Ana Zayas, and Natividad Rodriguez. Aging of Human Muscle: Understanding Sarcopenia at the Single Muscle Cell Level. *Physical medicine and rehabilitation clinics of North America*, 23:201–7, xiii, February 2012.

[178] Stuart M. Roche, Jonathan P. Gumucio, Susan V. Brooks, Christopher L. Mendias, and Dennis R. Claflin. Measurement of Maximum Isometric Force Generated by Permeabilized Skeletal Muscle Fibers. *Journal of Visualized Experiments : JoVE*, (100):52695, June 2015.

[179] Dominik Schneidereit, Stefanie Nübler, Gerhard Prölß, Barbara Reischl, Sebastian Schürmann, Oliver J. Müller, and Oliver Friedrich. Optical prediction of single muscle fiber force production using a combined biomechatronics and second harmonic generation imaging approach. *Light: Science & Applications*, 7(1):79, October 2018. Number: 1 Publisher: Nature Publishing Group.

[180] Julien Ochala, Walter R. Frontera, David J. Dorer, Jacques Van Hoecke, and Lisa S. Krivickas. Single Skeletal Muscle Fiber Elastic and Contractile Characteristics in Young and Older Men. *The Journals of Gerontology: Series A*, 62(4):375–381, April 2007.

[181] H. Klitgaard, M. Mantoni, S. Schiaffino, S. Ausoni, L. Gorza, C. Laurent Winter, P. Schnohr, and B. Saltin. Function, morphology and protein expression of ageing skeletal muscle: a cross-sectional study of elderly men with different training backgrounds. *Acta Physiologica Scandinavica*, 140(1):41–54, 1990.

[182] Jamie S McPhee, James Cameron, Thomas Maden-Wilkinson, Mathew Piasecki, Moi Hoon Yap, David A Jones, and Hans Degens. The Contributions of Fiber Atrophy, Fiber Loss, In Situ Specific Force, and Voluntary Activation to Weakness in Sarcopenia. *The Journals of Gerontology Series A: Biological Sciences and Medical Sciences*, 73(10):1287–1294, September 2018.

[183] Lorenza Brocca, Jamie S. McPhee, Emanuela Longa, Monica Canepari, Olivier Seynnes, Giuseppe De Vito, Maria Antonietta Pellegrino, Marco Narici, and Roberto Bottinelli. Structure and function of human muscle fibres and muscle proteome in physically active older men. *The Journal of Physiology*, 595(14):4823–4844, July 2017.

[184] Charlotte Beaudart, Yves Rolland, Alfonso J. Cruz-Jentoft, Jürgen M. Bauer, Cornel Sieber, Cyrus Cooper, Nasser Al-Daghri, Islene Araujo de Carvalho, Ivan Bautmans, Roberto Bernabei, Olivier Bruyère, Matteo Cesari, Antonio Cherubini, Bess Dawson-Hughes, John A. Kanis, Jean-Marc Kaufman, Francesco Landi, Stefania Maggi, Eugene McCloskey, Jean Petermans, Leocadio Rodriguez Mañas, Jean-Yves Reginster, Regina Roller-Wirnsberger, Laura A. Schaap, Daniel Uebelhart, René Rizzoli, and Roger A. Fielding. Assessment of Muscle Function and Physical Performance in Daily Clinical Practice. *Calcified Tissue International*, 105(1):1–14, July 2019.

[185] Carlos Saez and Sara García-Isidoro. *Prevalence of Sarcopenia According to the Method Used to Determine Physical Performance.* IntechOpen, November 2021.

[186] R. Merletti and S. Muceli. Tutorial. Surface EMG detection in space and time: Best practices. *Journal of Electromyography and Kinesiology*, 49:102363, December 2019.

[187] E. D. Adrian and D. W. Bronk. The discharge of impulses in motor nerve fibres. *The Journal of Physiology*, 67(2):i3–151, March 1929.

[188] A. Del Vecchio, A. Holobar, D. Falla, F. Felici, R. M. Enoka, and D. Farina. Tutorial: Analysis of motor unit discharge characteristics from high-density surface EMG signals. *Journal of Electromyography and Kinesiology*, 53:102426, August 2020.

[189] Maurice Mohr, Tanja Schön, Vinzenz von Tscharner, and Benno M. Nigg. Intermuscular Coherence Between Surface EMG Signals Is Higher for Monopolar Compared to Bipolar Electrode Configurations. *Frontiers in Physiology*, 9, 2018.

[190] Roberto Merletti, Aleš Holobar, and Dario Farina. Analysis of motor units with high-density surface electromyography. *Journal of Electromyography and Kinesiology*, 18(6):879–890, December 2008.

[191] Marco Gazzoni and U. Barone. Multi channel surface EMG detection and conditioning. *NEUROTECHNIX 2013 - Proceedings of the International Congress on Neurotechnology, Electronics and Informatics*, pages 119–125, January 2013.

[192] Hermie J Hermens, Bart Freriks, Catherine Disselhorst-Klug, and Günter Rau. Development of recommendations for SEMG sensors and sensor placement procedures. *Journal of Electromyography and Kinesiology*, 10(5):361–374, October 2000.

[193] Kevin G. Keenan, Dario Farina, Katrina S. Maluf, Roberto Merletti, and Roger M. Enoka. Influence of amplitude cancellation on the simulated surface electromyogram. *Journal of Applied Physiology (Bethesda, Md.: 1985)*, 98(1):120–131, January 2005.

[194] Dick F. Stegeman, Caroline J. Houtman, Bernd G. Lapatki, and Machiel J. Zwarts. Chapter 12 Multichannel surface EMG11Partly adapted from a review paper in Muscle and Nerve. In Erik Stålberg, editor, *Handbook of Clinical Neurophysiology*, volume 2 of *Handbook of Clinical Neurophysiology*, pages 245–268. Elsevier, January 2003.

[195] Christoph Neuwirth, Sanjeev Nandedkar, Erik StåLberg, and Markus Weber. Motor unit number index (MUNIX): A novel neurophysiological technique to follow disease progression in amyotrophic lateral sclerosis. *Muscle & Nerve*, 42(3):379–384, 2010. _eprint: https://onlinelibrary.wiley.com/doi/pdf/10.1002/mus.21707.

[196] Farong Gao, Yueying Cao, Chuan Zhang, and Yingchun Zhang. A Preliminary Study of Effects of Channel Number and Location on the Repeatability of Motor Unit Number Index (MUNIX). *Frontiers in Neurology*, 11, 2020.

[197] Ryan D. Kaya, Masato Nakazawa, Richard L. Hoffman, and Brian C. Clark. Interrelationship between muscle strength, motor units, & aging. *Experimental gerontology*, 48(9):920–925, September 2013.

[198] M. Drey, C. Grösch, C. Neuwirth, J. M. Bauer, and C. C. Sieber. The Motor Unit Number Index (MUNIX) in sarcopenic patients. *Experimental Gerontology*, 48(4):381–384, April 2013.

[199] Gennaro Boccia, Davide Dardanello, Valeria Rosso, Luisa Pizzigalli, and Alberto Rainoldi. The application of sEMG in aging: A mini review. *Gerontology*, 61, December 2014.

[200] Angkoon Phinyomark, Pornchai Phukpattaranont, and Chusak Limsakul. Feature reduction and selection for EMG signal classification. *Expert Systems with Applications*, 39(8):7420–7431, June 2012.

[201] Dario Farina, Roberto Merletti, and Roger Enoka. The extraction of neural strategies from the surface EMG: An update. *Journal of applied physiology (Bethesda, Md. : 1985)*, 96:1486–95, May 2004.

[202] Mariam Al Harrach, Vincent Carriou, Sofiane Boudaoud, Jeremy Laforet, and Frederic Marin. Analysis of the sEMG/force relationship using HD-sEMG technique and data fusion: A simulation study. *Computers in Biology and Medicine*, 83:34–47, April 2017.

[203] Dick F. Stegeman, Joleen H. Blok, Hermie J. Hermens, and Karin Roeleveld. Surface EMG models: properties and applications. *Journal of Electromyography and Kinesiology*, 10(5):313–326, 2000.

[204] Alessandro Musesti, Giulio G. Giusteri, and Alfredo Marzocchi. Predicting Ageing: On the Mathematical Modelization of Ageing Muscle Tissue. *Active Ageing and Healthy Living*, pages 185–192, 2014. Publisher: IOS Press.

[205] C. J. Heckman and M. D. Binder. Computer simulation of the steady-state input-output function of the cat medial gastrocnemius motoneuron pool. *Journal of Neurophysiology*, 65(4):952–967, April 1991.

[206] Jakob Dideriksen, Dario Farina, and Roger Enoka. Influence of fatigue on the simulated relation between the amplitude of the surface electromyogram and muscle force. *Philosophical transactions. Series A, Mathematical, physical, and engineering sciences*, 368:2765–81, June 2010.

[207] Jakob Dideriksen, Dario Farina, Martin Baekgaard, and Roger Enoka. An integrative model of motor unit activity during sustained submaximal contractions. *Journal of applied physiology (Bethesda, Md. : 1985)*, 108:1550–62, April 2010.

[208] Leonardo Abdala Elias and André Fabio Kohn. Individual and collective properties of computationally efficient motoneuron models of types S and F with active dendrites. *Neurocomputing*, 99:521–533, January 2013.

[209] Francesco Negro and Dario Farina. Decorrelation of cortical inputs and motoneuron output. *Journal of Neurophysiology*, 106(5):2688–2697, November 2011.

[210] Anna M. Taylor and Roger M. Enoka. Optimization of Input Patterns and Neuronal Properties to Evoke Motor Neuron Synchronization. *Journal of Computational Neuroscience*, 16(2):139–157, 2004. Place: Germany Publisher: Springer.

[211] Carlo J. De Luca and Emily C. Hostage. Relationship between firing rate and recruitment threshold of motoneurons in voluntary isometric contractions. *Journal of Neurophysiology*, 104(2):1034–1046, August 2010.

[212] Randall K. Powers and C. J. Heckman. Contribution of intrinsic motoneuron properties to discharge hysteresis and its estimation based on paired motor unit recordings: a simulation study. *Journal of Neurophysiology*, 114(1):184–198, July 2015.

[213] John M. Allen and Sherif M. Elbasiouny. The effects of model composition design choices on high-fidelity simulations of motoneuron recruitment and firing behaviors. *Journal of neural engineering*, 15(3):036024, June 2018.

[214] Francesco Negro, Silvia Muceli, Anna Margherita Castronovo, Ales Holobar, and Dario Farina. Multi-channel intramuscular and surface EMG decomposition by convolutive blind source separation. *Journal of Neural Engineering*, 13(2):026027, April 2016.

[215] Renato N. Watanabe and Andre F. Kohn. Fast Oscillatory Commands from the Motor Cortex Can Be Decoded by the Spinal Cord for Force Control. *Journal of Neuroscience*, 35(40):13687–13697, October 2015. Publisher: Society for Neuroscience Section: Articles.

[216] Bertrand Iooss and Paul Lemaître. A review on global sensitivity analysis methods. In C. Meloni and G. Dellino, editors, *Uncertainty management in Simulation-Optimization of Complex Systems: Algorithms and Applications*. Springer, 2015.

[217] Shuangzhe Liu. Global Sensitivity Analysis: The Primer by Andrea Saltelli, Marco Ratto, Terry Andres, Francesca Campolongo, Jessica Cariboni, Debora Gatelli,

Michaela Saisana, Stefano Tarantola. *International Statistical Review*, 76:452–452, February 2008.

[218] Andrea Saltelli, editor. *Sensitivity analysis in practice: a guide to assessing scientific models.* Wiley, Hoboken, NJ, reprinted edition, 2007. OCLC: 254689671.

[219] George Qian and Adam Mahdi. Sensitivity analysis methods in the biomedical sciences. *Mathematical Biosciences*, 323:108306, May 2020.

[220] Max D. Morris. Factorial Sampling Plans for Preliminary Computational Experiments. *Technometrics*, 33(2):161–174, May 1991.

[221] Yanjun Gan, Qingyun Duan, Wei Gong, Charles Tong, Yunwei Sun, Wei Chu, Aizhong Ye, Chiyuan Miao, and Zhenhua Di. A comprehensive evaluation of various sensitivity analysis methods: A case study with a hydrological model. *Environmental Modelling & Software*, 51:269–285, January 2014.

[222] Kevin J. Hughes, John F. Griffiths, Michael Fairweather, and Alison S. Tomlin. Evaluation of models for the low temperature combustion of alkanes through interpretation of pressure–temperature ignition diagrams. *Physical Chemistry Chemical Physics*, 8(27):3197–3210, July 2006.

[223] A. Janse van Rensburg, G. van Schoor, and P. A. van Vuuren. Stepwise Global Sensitivity Analysis of a Physics-Based Battery Model using the Morris Method and Monte Carlo Experiments. *Journal of Energy Storage*, 25:100875, October 2019.

[224] Marc Jaxa-Rozen and Jan Kwakkel. Tree-based ensemble methods for sensitivity analysis of environmental models: A performance comparison with Sobol and Morris techniques. *Environmental Modelling & Software*, 107:245–266, September 2018.

[225] Kathrin Menberg, Yeonsook Heo, and Ruchi Choudhary. Sensitivity analysis methods for building energy models: Comparing computational costs and extractable information. *Energy and Buildings*, 133:433–445, December 2016.

[226] Steffen Petersen, Martin Heine Kristensen, and Michael Dahl Knudsen. Prerequisites for reliable sensitivity analysis of a high fidelity building energy model. *Energy and Buildings*, 183:1–16, January 2019.

[227] S. Sreedevi, T. I. Eldho, C. G. Madhusoodhanan, and T. Jayasankar. Multiobjective sensitivity analysis and model parameterization approach for coupled streamflow and groundwater table depth simulations using SHETRAN in a wet humid tropical catchment. *Journal of Hydrology*, 579:124217, December 2019.

[228] Majdi Awad, Tristan Senga Kiesse, Zainab Assaghir, and Anne Ventura. Convergence of sensitivity analysis methods for evaluating combined influences of model inputs. *Reliability Engineering & System Safety*, 189:109–122, September 2019.

[229] Christopher Spiewak, Md Rasedul Islam, Md Assad-Uz-Zaman, and Mohammad Rahman. A Comprehensive Study on EMG Feature Extraction and Classifiers. *Open Access Journal of Biomedical Engineering and its Applications*, 1, February 2018.

[230] Christoph Neuwirth, Christian Burkhardt, James Alix, José Castro, Mamede de Carvalho, Malgorzata Gawel, Stephan Goedee, Julian Grosskreutz, Timothée Lenglet, Cristina Moglia, Taha Omer, Maarten Schrooten, and Markus Weber. Quality Control of Motor Unit Number Index (MUNIX) Measurements in 6 Muscles in a Single-Subject "Round-Robin" Setup. *PLoS ONE*, 11(5), May 2016.

[231] P. O. Eriksson. Muscle-fibre composition of the human mandibular locomotor system. Enzyme-histochemical and morphological characteristics of functionally different parts. *Swedish Dental Journal. Supplement*, 12 Suppl:1–44, 1982.

[232] Heidi Haapasalo, Harri Sievanen, Pekka Kannus, Ari Heinonen, Pekka Oja, and Ilkka Vuori. Dimensions and estimated mechanical characteristics of the humerus after long-term tennis loading. *Journal of Bone and Mineral Research*, 11(6):864–872, 1996.

[233] P. O. Eriksson and L. E. Thornell. Histochemical and morphological muscle-fibre characteristics of the human masseter, the medial pterygoid and the temporal muscles. *Archives of Oral Biology*, 28(9):781–795, January 1983.

[234] X. Ye, T. W. Beck, and N. P. Wages. Relationship between innervation zone width and mean muscle fiber conduction velocity during a sustained isometric contraction. *Journal of Musculoskeletal & Neuronal Interactions*, 15(1):95–102, March 2015.

[235] Hans G. J. Kortman, Sarah C. Wilder, Tom R. Geisbush, Pushpa Narayanaswami, and Seward B. Rutkove. Age and gender associated differences in electrical impedance values of skeletal muscle. *Physiological measurement*, 34(12):1611–1622, December 2013.

[236] S. Gabriel, R. W. Lau, and C. Gabriel. The dielectric properties of biological tissues: II. Measurements in the frequency range 10 Hz to 20 GHz. *Physics in Medicine and Biology*, 41(11):2251–2269, November 1996.

[237] Yoshie Ishida, Hiroaki Kanehisa, and Tetsuo Fukunaga. Differences in Muscle Thicknesses of Male and Female Japanese Elite Athletes. *Japanese Journal of Physical Fitness and Sports Medicine*, 41(2):233–240, 1992.

[238] Kianoush Nazarpour, Ali Al-Timemy, Guido Bugmann, and Andrew Jackson. A note on the probability distribution function of the surface electromyogram signal. *Brain Research Bulletin*, 90:88–91, January 2013.

[239] S M Pincus. Approximate entropy as a measure of system complexity. *Proceedings of the National Academy of Sciences of the United States of America*, 88(6):2297–2301, March 1991.

[240] J. S. Richman and J. R. Moorman. Physiological time-series analysis using approximate entropy and sample entropy. *American Journal of Physiology. Heart and Circulatory Physiology*, 278(6):H2039–2049, June 2000.

[241] Xu Zhang and Ping Zhou. Sample entropy analysis of surface EMG for improved muscle activity onset detection against spurious background spikes. *Journal of Electromyography and Kinesiology*, 22(6):901–907, December 2012.

[242] Angkoon Phinyomark, Sirinee Thongpanja, Huosheng Hu, Pornchai Phukpattaranont, and Chusak Limsakul. *The Usefulness of Mean and Median Frequencies in Electromyography Analysis.* IntechOpen, October 2012. Publication Title: Computational Intelligence in Electromyography Analysis - A Perspective on Current Applications and Future Challenges.

[243] Mohammadreza Asghari Oskoei and Huosheng Hu. Support Vector Machine-Based Classification Scheme for Myoelectric Control Applied to Upper Limb. *IEEE Transactions on Biomedical Engineering*, 55(8):1956–1965, August 2008. Conference Name: IEEE Transactions on Biomedical Engineering.

[244] Hangfang Zhao and Lin Gui. Nonparametric and parametric methods of spectral analysis. *MATEC Web of Conferences*, 283:07002, 2019. Publisher: EDP Sciences.

[245] P. Welch. The use of fast Fourier transform for the estimation of power spectra: A method based on time averaging over short, modified periodograms. *IEEE Transactions on Audio and Electroacoustics*, 15(2):70–73, June 1967. Conference Name: IEEE Transactions on Audio and Electroacoustics.

[246] Foster B. Stulen and Carlo J. De Luca. Frequency Parameters of the Myoelectric Signal as a Measure of Muscle Conduction Velocity. *IEEE Transactions on Biomedical Engineering*, BME-28(7):515–523, July 1981.

[247] Selda Uzun, Amir Pourmoghaddam, M Hieronymus, and T Thrasher. Evaluation of muscle fatigue of wheelchair basketball players with spinal cord injury using recurrence quantification analysis of surface EMG. *European journal of applied physiology*, 112:3847–57, March 2012.

[248] Sijiang Du and M. Vuskovic. Temporal vs. spectral approach to feature extraction from prehensile EMG signals. In *Proceedings of the 2004 IEEE International Conference on Information Reuse and Integration, 2004. IRI 2004.*, pages 344–350, November 2004.

[249] Amer Zaylaa, Ahmad Diab, Mariam Al Harrach, and Sofiane Boudaoud. Evaluation of HD- sEMG grid misalignment with muscle fibers using nonlinear correlation. In *International Conference on Advances in Biomedical Engineering (ICABME)*, Beirut, Lebanon, September 2015.

[250] Francesca Campolongo, Jessica Cariboni, and Andrea Saltelli. An effective screening design for sensitivity analysis of large models. *Environmental Modelling & Software*, 22(10):1509–1518, October 2007.

[251] Xu Cheng, Guoyuan Li, Robert Skulstad, Pierre Major, Shengyong Chen, Hans Petter Hildre, and Houxiang Zhang. Data-driven uncertainty and sensitivity analysis for ship motion modeling in offshore operations. *Ocean Engineering*, 179:261–272, May 2019.

[252] D. M. King and B. J. C. Perera. Morris method of sensitivity analysis applied to assess the importance of input variables on urban water supply yield – A case study. *Journal of Hydrology*, 477:17–32, January 2013.

[253] Dorleta Garcia, Inmaculada Arostegui, and Raúl Prellezo. Robust combination of the Morris and Sobol methods in complex multidimensional models. *Environmental Modelling & Software*, 122:104517, December 2019.

[254] Alistair D. Rodman and Dimitrios I. Gerogiorgis. Parameter estimation and sensitivity analysis for dynamic modelling and simulation of beer fermentation. *Computers & Chemical Engineering*, page 106665, December 2019.

[255] M. V. Ruano, J. Ribes, A. Seco, and J. Ferrer. An improved sampling strategy based on trajectory design for application of the Morris method to systems with many input factors. *Environmental Modelling & Software*, 37:103–109, November 2012.

[256] D. Garcia Sanchez, B. Lacarrière, M. Musy, and B. Bourges. Application of sensitivity analysis in building energy simulations: Combining first- and second-order elementary effects methods. *Energy and Buildings*, 68:741–750, January 2014.

[257] Muhammad Aslam. Introducing Kolmogorov–Smirnov Tests under Uncertainty: An Application to Radioactive Data. *ACS Omega*, 5(1):914–917, December 2019.

[258] Frank J. Massey. The Kolmogorov-Smirnov Test for Goodness of Fit. *Journal of the American Statistical Association*, 46(253):68–78, 1951.

[259] Jeff Miller. Short report: Reaction time analysis with outlier exclusion: Bias varies with sample size. *The Quarterly Journal of Experimental Psychology Section A*, 43(4):907–912, November 1991.

[260] Frank R. Hampel. The Influence Curve and its Role in Robust Estimation. *Journal of the American Statistical Association*, 69(346):383–393, June 1974.

[261] Christophe Leys, Christophe Ley, Olivier Klein, Philippe Bernard, and Laurent Licata. Detecting outliers: Do not use standard deviation around the mean, use absolute deviation around the median. *Journal of Experimental Social Psychology*, 49(4):764–766, 2013.

[262] Peter J. Rousseeuw and Christophe Croux. Alternatives to the Median Absolute Deviation. *Journal of the American Statistical Association*, 88(424):1273–1283, December 1993.

[263] Alessandro Del Vecchio, Francesco Negro, Francesco Felici, and Dario Farina. Associations between motor unit action potential parameters and surface EMG features. *Journal of Applied Physiology (Bethesda, Md.: 1985)*, 123(4):835–843, October 2017.

[264] Jakob L. Dideriksen, Roger M. Enoka, and Dario Farina. Neuromuscular adjustments that constrain submaximal EMG amplitude at task failure of sustained isometric contractions. *Journal of Applied Physiology (Bethesda, Md.: 1985)*, 111(2):485–494, August 2011.

[265] Alessandro Del Vecchio, Ilenia Bazzucchi, and Francesco Felici. Variability of estimates of muscle fiber conduction velocity and surface EMG amplitude across subjects and processing intervals. *Journal of Electromyography and Kinesiology*, 40:102–109, June 2018.

[266] I. Campanini, A. Merlo, P. Degola, R. Merletti, G. Vezzosi, and D. Farina. Effect of electrode location on EMG signal envelope in leg muscles during gait. *Journal of Electromyography and Kinesiology*, 17(4):515–526, August 2007.

[267] L. Mesin, R. Merletti, and A. Rainoldi. Surface EMG: The issue of electrode location. *Journal of Electromyography and Kinesiology*, 19(5):719–726, October 2009.

[268] Sabrina S. M. Lee, Maria de Boef Miara, Allison S. Arnold, Andrew A. Biewener, and James M. Wakeling. Recruitment of faster motor units is associated with greater rates of fascicle strain and rapid changes in muscle force during locomotion. *The Journal of Experimental Biology*, 216(2):198–207, January 2013.

[269] Alberto Rainoldi. Spectral properties of the surface EMG can characterize/do not provide information about motor unit recruitment strategies and muscle fiber type. *Journal of Applied Physiology (Bethesda, Md.: 1985)*, 105(5):1678, November 2008.

[270] James M Wakeling, Katrin Uehli, and Antra I Rozitis. Muscle fibre recruitment can respond to the mechanics of the muscle contraction. *Journal of the Royal Society Interface*, 3(9):533–544, August 2006.

[271] Gazzoni Marco, Botter Alberto, and Vieira Taian. Surface EMG and muscle fatigue: multi-channel approaches to the study of myoelectric manifestations of muscle fatigue. *Physiological Measurement*, 38(5):R27–R60, May 2017.

[272] Marina Barandun, Vinzenz von Tscharner, Claudia Meuli-Simmen, Vaughan Bowen, and Victor Valderrabano. Frequency and conduction velocity analysis of the abductor pollicis brevis muscle during early fatigue. *Journal of Electromyography and Kinesiology*, 19(1):65–74, February 2009.

[273] Vincent Carriou, Jeremy Laforet, Sofiane Boudaoud, and Mariam Al Harrach. Sensitivity analysis of HD-sEMG amplitude descriptors relative to grid parameter variations of a cylindrical multilayered muscle model. *Biomedical Physics & Engineering Express*, 2(6):064001, December 2016.

[274] Oliver Röhrle, Utku Ş. Yavuz, Thomas Klotz, Francesco Negro, and Thomas Heidlauf. Multiscale modeling of the neuromuscular system: Coupling neurophysiology and skeletal muscle mechanics. *WIREs Systems Biology and Medicine*, 11(6):e1457, 2019. _eprint: https://onlinelibrary.wiley.com/doi/pdf/10.1002/wsbm.1457.

[275] M. M. Lowery. EMG Modeling and Simulation. In *Surface Electromyography : Physiology, Engineering, and Applications*, pages 210–246. John Wiley & Sons, Ltd, 2016. Section: 8 _eprint: https://onlinelibrary.wiley.com/doi/pdf/10.1002/9781119082934.ch08.

[276] Shihan Ma, Chen Chen, Jiamin Zhao, Dong Han, Xinjun Sheng, Dario Farina, and Xiangyang Zhu. Analytical Modelling of Surface EMG Signals Generated by Curvilinear Fibers With Approximate Conductivity Tensor. *IEEE Transactions on Biomedical Engineering*, 69(3):1052–1062, March 2022. Conference Name: IEEE Transactions on Biomedical Engineering.

[277] Hua Cao, Sofiane Boudaoud, Frédéric Marin, and Catherine Marque. Surface EMG-force modelling for the biceps brachii and its experimental evaluation during isometric isotonic contractions. *Computer Methods in Biomechanics and Biomedical Engineering*, 18(9):1014–1023, July 2015. Publisher: Taylor & Francis _eprint: https://doi.org/10.1080/10255842.2013.867952.

[278] Eike Petersen and Philipp Rostalski. A Comprehensive Mathematical Model of Motor Unit Pool Organization, Surface Electromyography, and Force Generation. *Frontiers in Physiology*, 10, 2019.

[279] Diego Pereira Botelho, Kathleen Curran, and Madeleine Lowery. Anatomically accurate model of EMG during index finger flexion and abduction derived from diffusion tensor imaging. *PLoS Computational Biology*, 15:e1007267, August 2019.

[280] L. Mesin, M. Joubert, T. Hanekom, R. Merletti, and D. Farina. A finite element model for describing the effect of muscle shortening on surface EMG. *IEEE Transactions on Biomedical Engineering*, 53(4):593–600, April 2006.

[281] Don P. Mitchell. Generating antialiased images at low sampling densities. In *Proceedings of the 14th annual conference on Computer graphics and interactive techniques*, SIGGRAPH '87, pages 65–72, New York, NY, USA, August 1987. Association for Computing Machinery.

[282] Vincent Carriou, Jérémy Laforêt, Sofiane Boudaoud, and Mariam Al Harrach. Realistic motor unit placement in a cylindrical HD-sEMG generation model. In *2016 38th Annual International Conference of the IEEE Engineering in Medicine and Biology Society (EMBC)*, pages 1704–1707, August 2016. ISSN: 1558-4615.

[283] Jacob A. Mota, Dennis P. Kwon, Mary Kennedy, Eric J. Sobolewski, Youngdeok Kim, Joaquin U. Gonzales, and Matt S. Stock. Compensatory adjustments in motor unit behavior during fatigue differ for younger versus older men. *Aging Clinical and Experimental Research*, 32(11):2259–2269, November 2020.

[284] Lucas B. R. Orssatto, David N. Borg, Linda Pendrith, Anthony J. Blazevich, Anthony J. Shield, and Gabriel S. Trajano. Do Motoneurons' Discharge Rate Slow With Aging? A Systematic Review And Meta-Analysis. Technical report, bioRxiv, December 2021. Section: New Results Type: article.

[285] R. M. Enoka and A. J. Fuglevand. Motor unit physiology: some unresolved issues. *Muscle & Nerve*, 24(1):4–17, January 2001.

[286] I. Gath and E. Stålberg. In situ measurement of the innervation ratio of motor units in human muscles. *Experimental Brain Research*, 43(3-4):377–382, 1981.

[287] Kenneth Levenberg. A METHOD FOR THE SOLUTION OF CERTAIN NON – LINEAR PROBLEMS IN LEAST SQUARES. *Quarterly of Applied Mathematics*, July 1944.

[288] C. S. Klein, B. L. Allman, G. D. Marsh, and C. L. Rice. Muscle size, strength, and bone geometry in the upper limbs of young and old men. *The Journals of Gerontology. Series A, Biological Sciences and Medical Sciences*, 57(7):M455–459, July 2002.

[289] A. E. J. Miller, J. D. MacDougall, M. A. Tarnopolsky, and D. G. Sale. Gender differences in strength and muscle fiber characteristics. *European Journal of Applied Physiology and Occupational Physiology*, 66(3):254–262, March 1993.

[290] Afruna Lizu. *Effect of the biceps Brachii tendon on elbow flexor force steadiness in men and women.* PhD thesis, University of British Columbia, 2015.

[291] Roy Chan, Michael Newton, and Kazunori Nosaka. Measurement of biceps brachii muscle cross-sectional area by extended-field-of-view ultrasound imaging technique. *ECU Publications 2012*, January 2012.

[292] G. McCall, W. Byrnes, A. Dickinson, P. M. Pattany, and S. Fleck. Muscle fiber hypertrophy, hyperplasia, and capillary density in college men after resistance training. *Journal of applied physiology*, 1996.

[293] Ryota Akagi, Yohei Takai, Megumi Ohta, Hiroaki Kanehisa, Yasuo Kawakami, and Tetsuo Fukunaga. Muscle volume compared to cross-sectional area is more appropriate for evaluating muscle strength in young and elderly individuals. *Age and Ageing*, 38(5):564–569, September 2009.

[294] Matti D. Allen, S. Jared McMillan, Cliff S. Klein, Charles L. Rice, and Greg D. Marsh. Differential Age-related Changes in Bone Geometry between the Humerus and the Femur in Healthy Men. *Aging and Disease*, 3(2):156–163, September 2011.

[295] C. L. Rice, D. A. Cunningham, D. H. Paterson, and M. S. Lefcoe. Arm and leg composition determined by computed tomography in young and elderly men. *Clinical Physiology (Oxford, England)*, 9(3):207–220, June 1989.

[296] K. N. An, F. C. Hui, B. F. Morrey, R. L. Linscheid, and E. Y. Chao. Muscles across the elbow joint: A biomechanical analysis. *Journal of Biomechanics*, 14(10):659–669, January 1981.

[297] Yuri Yoshida, Robin L. Marcus, and Paul C. Lastayo. Intramuscular adipose tissue and central activation in older adults. *Muscle & Nerve*, 46(5):813–816, November 2012.

[298] B. H. Goodpaster, C. L. Carlson, M. Visser, D. E. Kelley, A. Scherzinger, T. B. Harris, E. Stamm, and A. B. Newman. Attenuation of skeletal muscle and strength in the elderly: The Health ABC Study. *Journal of Applied Physiology (Bethesda, Md.: 1985)*, 90(6):2157–2165, June 2001.

[299] Marjolein Visser, Stephen B. Kritchevsky, Bret H. Goodpaster, Anne B. Newman, Michael Nevitt, Elizabeth Stamm, and Tamara B. Harris. Leg muscle mass and composition in relation to lower extremity performance in men and women aged 70 to 79: the health, aging and body composition study. *Journal of the American Geriatrics Society*, 50(5):897–904, May 2002.

[300] Min-Yi Ou, Hao Zhang, Poh-Ching Tan, Shuang-Bai Zhou, and Qing-Feng Li. Adipose tissue aging: mechanisms and therapeutic implications. *Cell Death & Disease*, 13(4):1–10, April 2022. Number: 4 Publisher: Nature Publishing Group.

[301] Debra Lynn Waters. Intermuscular Adipose Tissue: A Brief Review of Etiology, Association With Physical Function and Weight Loss in Older Adults. *Annals of geriatric medicine and research*, 23(1):3–8, March 2019.

[302] Matthew J Delmonico, Tamara B Harris, Marjolein Visser, Seok Won Park, Molly B Conroy, Pedro Velasquez-Mieyer, Robert Boudreau, Todd M Manini, Michael Nevitt, Anne B Newman, and Bret H Goodpaster. Longitudinal study of muscle strength, quality, and adipose tissue infiltration123. *The American Journal of Clinical Nutrition*, 90(6):1579–1585, December 2009.

[303] Jeanette M. Waller and Howard I. Maibach. Age and skin structure and function, a quantitative approach (I): blood flow, pH, thickness, and ultrasound echogenicity. *Skin Research and Technology*, 11(4):221–235, 2005. _eprint: https://onlinelibrary.wiley.com/doi/pdf/10.1111/j.0909-725X.2005.00151.x.

[304] Dominique Batisse, Roland Bazin, Thérèse Baldeweck, Bernard Querleux, and Jean-Luc Lévêque. Influence of age on the wrinkling capacities of skin. *Skin research and technology: official journal of International Society for Bioengineering and the Skin (ISBS) [and] International Society for Digital Imaging of Skin (ISDIS) [and] International Society for Skin Imaging (ISSI)*, 8(3):148–154, August 2002.

[305] M. C. Branchet, S. Boisnic, C. Frances, and A. M. Robert. Skin thickness changes in normal aging skin. *Gerontology*, 36(1):28–35, 1990.

[306] S. Richard, J. de Rigal, O. de Lacharriere, E. Berardesca, and J. L. Leveque. Noninvasive measurement of the effect of lifetime exposure to the sun on the aged skin. *Photodermatology, Photoimmunology & Photomedicine*, 10(4):164–169, August 1994.

[307] Gunnar Grimby, Bente Danneskiold-Samsøe, Keld Hvid, and Bengt Saltin. Morphology and enzymatic capacity in arm and leg muscles in 78–81 year old men and women. *Acta Physiologica Scandinavica*, 115(1):125–134, 1982.

[308] J. D. MacDougall, D. G. Sale, S. E. Alway, and J. R. Sutton. Muscle fiber number in biceps brachii in bodybuilders and control subjects. *Journal of Applied Physiology*, 57(5):1399–1403, November 1984.

[309] J. Polgar, M. A. Johnson, D. Weightman, and D. Appleton. Data on fibre size in thirty-six human muscles. An autopsy study. *Journal of the Neurological Sciences*, 19(3):307–318, July 1973.

[310] F.G.I. Jennekens, B.E. Tomlinson, and J.N. Walton. The sizes of the two main histochemical fibre types in five limb muscles in man. *Journal of the Neurological Sciences*, 13(3):281–292, July 1971.

[311] Anastasia Bougea, George Papadimas, Constantinos Papadopoulos, George P. Paraskevas, Nikolaos Kalfakis, Panagiota Manta, and Evangelia Kararizou. An Age-Related Morphometric Profile of Skeletal Muscle in Healthy Untrained Women. *Journal of Clinical Medicine*, 5(11), November 2016.

[312] Fabiana Tanganelli, Peter Meinke, Fabian Hofmeister, Stefanie Jarmusch, Lisa Baber, Stefan Mehaffey, Stefan Hintze, Uta Ferrari, Carl Neuerburg, Christian Kammerlander, Benedikt Schoser, and Michael Drey. Type-2 muscle fiber atrophy is associated with sarcopenia in elderly men with hip fracture. *Experimental Gerontology*, 144:111171, February 2021.

[313] M. A. Johnson, J. Polgar, D. Weightman, and D. Appleton. Data on the distribution of fibre types in thirty-six human muscles. An autopsy study. *Journal of the Neurological Sciences*, 18(1):111–129, January 1973.

[314] Amelie Aniansson, Marita Hedberg, Gull-Britt Henning, and Gunnar Grimby. Muscle morphology, enzymatic activity, and muscle strength in elderly men: A follow-up study. *Muscle & Nerve*, 9(7):585–591, 1986.

[315] Mohamed Ebeida, Anjul Patney, Scott Mitchell, Andrew Davidson, Patrick Knupp, and John Owens. Efficient Maximal Poisson-Disk Sampling. *ACM Transactions on Graphics (Proceedings of ACM SIGGRAPH 2011)*, 30, July 2011.

[316] Nicholas Dwork, Corey Baron, Ethan Johnson, Daniel O'Connor, John Pauly, and Peder Larson. *Fast Variable Density Poisson-Disc Sample Generation with Directional Variation.* April 2020.

[317] Robert Bridson. Fast Poisson disk sampling in arbitrary dimensions. In *ACM SIGGRAPH 2007 sketches*, pages 22–es, New York, NY, USA, August 2007. Association for Computing Machinery.

[318] D. Cline, S. Jeschke, K. White, A. Razdan, and P. Wonka. Dart Throwing on Surfaces. *Computer Graphics Forum*, 28(4):1217–1226, 2009. _eprint: https://onlinelibrary.wiley.com/doi/pdf/10.1111/j.1467-8659.2009.01499.x.

[319] Konstantin Akhmadeev, Tianyi Yu, Éric Le Carpentier, Yannick Aoustin, and Dario Farina. Simulation of motor unit action potential recordings from intramuscular multichannel scanning electrodes. *IEEE Transactions on Biomedical Engineering*, 67(7):2005–2014, July 2020. Publisher: Institute of Electrical and Electronics Engineers.

[320] Carlo J. De Luca and Paola Contessa. Hierarchical control of motor units in voluntary contractions. *Journal of Neurophysiology*, 107(1):178–195, January 2012.

[321] Randall K. Powers, Sherif M. ElBasiouny, W. Zev Rymer, and C. J. Heckman. Contribution of intrinsic properties and synaptic inputs to motoneuron discharge patterns: a simulation study. *Journal of Neurophysiology*, 107(3):808–823, February 2012.

[322] Jim R. Potvin and Andrew J. Fuglevand. A motor unit-based model of muscle fatigue. *PLOS Computational Biology*, 13(6):e1005581, June 2017. Publisher: Public Library of Science.

[323] Ines Douania, Jeremy Laforêt, Sofiane Boudaoud, and Kiyoka Kinugawa. Assessment and sensitivity analysis of a motor units recruitment model during isometric contractions of the Biceps Brachii. In *2019 Fifth International Conference on Advances in Biomedical Engineering (ICABME)*, pages 1–4, October 2019. ISSN: 2377-5688.

[324] C. G. Kukulka and H. P. Clamann. Comparison of the recruitment and discharge properties of motor units in human brachial biceps and adductor pollicis during isometric contractions. *Brain Research*, 219(1):45–55, August 1981.

[325] S. Cullheim, J. W. Fleshman, L. L. Glenn, and R. E. Burke. Membrane area and dendritic structure in type-identified triceps surae alpha motoneurons. *Journal of Comparative Neurology*, 255(1):68–81, 1987.

[326] Takashi Yamada. Chapter 13 - Mechanisms of decline in muscle quality in sarcopenia. In Kunihiro Sakuma, editor, *Sarcopenia*, pages 295–322. Elsevier, January 2021.

[327] H Yamada, M Okada, Toshiaki Oda, S Nemoto, T Shiozaki, T Kizuka, Shinya Kuno, and Tadashi Masuda. Effects of aging on EMG variables during fatiguing isometric contractions. *Journal of human ergology*, 29:7–14, December 2000.

[328] Jason W. Robertson and Jamie A. Johnston. Modifying motor unit territory placement in the Fuglevand model. *Medical & Biological Engineering & Computing*, 55(11):2015–2025, November 2017.

[329] Dario Farina and Alberto Rainoldi. Compensation of the effect of sub-cutaneous tissue layers on surface EMG: a simulation study. *Medical Engineering & Physics*, 21(6–7):487–497, July 1999.

[330] Rakesh Pilkar, Kamyar Momeni, Arvind Ramanujam, Manikandan Ravi, Erica Garbarini, and Gail F. Forrest. Use of Surface EMG in Clinical Rehabilitation of Individuals With SCI: Barriers and Future Considerations. *Frontiers in Neurology*, 11, 2020.

[331] Roberto Merletti, Isabella Campanini, William Z. Rymer, and Catherine Disselhorst-Klug. Editorial: Surface Electromyography: Barriers Limiting Widespread Use of sEMG in Clinical Assessment and Neurorehabilitation. *Frontiers in Neurology*, 12:642257, February 2021.